Development of a 3D bronchial epithelium model for nanotoxicology : analysis of the protein corona formation on silver nanoparticles in the secretome

Daniel Sanchez Guzman

To cite this version:

Daniel Sanchez Guzman. Development of a 3D bronchial epithelium model for nanotoxicology : analysis of the protein corona formation on silver nanoparticles in the secretome. Toxicology. Université Paris Cité, 2021. English. NNT : 2021UNIP5040 . tel-03891067

HAL Id: tel-03891067
https://theses.hal.science/tel-03891067

Université de Paris

École doctorale médicament, toxicologie, chimie et imageries (MTCI, ED 563)

Unité de Biologie Fonctionnelle et Adaptative (UMR 8251-CNRS)

Development of a 3D bronchial epithelium model for nanotoxicology: analysis of the protein corona formation on silver nanoparticles in the secretome

Daniel SANCHEZ-GUZMAN

Thèse de doctorat de Toxicologie

Dirigée par : Armelle BAEZA-SQUIBAN

Présentée et soutenue publiquement le 8 Décembre 2021

Composition du Jury :

Pr. Guillaume GARÇON — PU, Université de Lille	Rapporteur
Pr. Françoise PONS — PU, Université de Strasbourg	Rapporteure
Dr. Marco MONOPOLI — Lecturer, Royal College of Surgeons, Ireland	Examinateur
Dr. Ignacio GARCIA-VERDUGO — MCU, Université de Paris	Examinateur
Pr. Saadia KERDINE-RÖMER — PU, Université Paris Saclay	Examinatrice
Pr. Armelle BAEZA-SQUIBAN — PU, Université de Paris	Directrice de thèse
Dr. Stéphanie DEVINEAU — MCU, Université de Paris	Co-encadrante/Membre invité

Acknowledgements

First of all, I would like to express my deepest appreciation to all the members of the jury for accepting to be part of this special day. Special thanks to **Professor Françoise PONS** and **Professor Guillaume GARÇON** for carefully read and correct my manuscript and giving me the opportunity of improve it. Many thanks to **Professor Saadia KERDINE-RÖMER**, **Doctor Marco MONOPOLI** and **Doctor Ignacio GARCIA-VERDUGO** for challenging me and discussing the results of my thesis project.

To Professor **Jean-Marie DUPRET**, I am deeply indebted to first accepting me to the BC2T M2, which bring me the opportunity to increases my research experiences opening me a larger professional opportunity. Secondly, I would like to thank you also for receiving me as PhD student at the BFA – UMR CNRS 8251 unit, offering me an adapted place to develop my thesis project.

I would like to extend my sincere thanks to my Ecole Doctoral - MTCI and to the European framework BIORIMA for the financial support of this project.

Each scientific project needs the hand, the supervision and the discussion to provide great quality results and without the help, guidance and advice of my two bosses Professor **Armelle BAEZA** and **Doctor Stephanie DEVINEAU** this project would not be done. I would like to express my deepest gratitude to both of you for putting the confidence on me and allowing me to be part of your team. **Armelle,** I would like to thank you for advising me throughout these three years of work and for believing in my abilities. This period has been a great opportunity to learn from you and to increase my knowledge in the lung toxicity. **Stephanie,** I would like also to thank you for your support throughout these three years of thesis. I very much appreciate your valuable advice and for opening for me the field of the protein corona, increasing profoundly my knowledge in nano-field from the chemist point of view.

During my stage in Paris, I have met many people, which have contributed in one way to another to this thesis. I would like to thank the different member of the team 6 at BFA. First to my office mates. **Pascal** et **Valentina**, je vous remercie d'avoir partagé votre bureau avec moi ces 3 dernières années. Ce fut un plaisir de vous rencontrer et travailler avec vous. Je suis sincèrement reconnaissant de vos nombreux conseils expérimentaux et personale lors de mes étapes ici. Un grand merci également pour votre aide dans l'amélioration de mon niveau de français. I also had a great pleasure of working with you **Oliver**, the difficult time had shortened our work together but I am grateful of your suggestion and experience with cell cultures and

with the images analysis. **Sonja,** I would like to acknowledge your help and suggestions you put into this project. Special thanks to **Fernando** for your experience and support in the SEC setting and the extended and great assistance. I would also like to express my sincere thanks to others members of the lab for their advice and support (**Maria**, **Claire**, **Lihn**, **Jérémy**, **Justine**, **Christina**, **Wenchao**, **Rongxing**, **Emile** and **Florent**). Thanks also to **Chloé**, I very much appreciate our time in the lab. I wish you all the best for the new adventure as a PhD student. I would also thanks to **Roseline, Olja, Françoise** and **Jean-Luc** for their technique and administrative assistance and support.

To my master lab, whom give me the opportunity and strength to start this adventure. **Jean-Michel** thank you for your help, guide and support when I first met you. I applied to work with you as “Ingenieur” but you gave me the opportunity to carried out the M2 before started this adventure. **Ignacio** thank you very much for your huge support, caring and guide. It was great working together with you. Also, many thanks to **Berengere**, **Saadé** and **Pierre**, for your time and patience you dedicated me at my arrival to the lab.

To all of collaborator at the Proteomic platform at Institut Jacques-Monod and NICB-DCU for your help, advice and knowledge on Mass spectrometry analysis. Many thanks to our colleagues at Faculté de Pharmacie de Paris. Je remercie tout particulièrement **René** pour son travail et son soutien dans le domaine de la microscopie électronique. Ce fut un grand plaisir de vous rencontrer pendant cette période et de travailler avec toi. T’est un grand professionnel, mais une personne encore meilleure.

I cannot forget the great people I have met during my stage at the RCSI-Dublin. Many thanks to **Marco** for opening the door of your lab and give me many advice even in such a short time. Special thanks to the members of your team **Marko**, **Mahmoud**, **Duong**, **Javier** and **Esperanza,** for the great welcome and making me feel as home but also for all the scientific support and discussion.

To my friends from Cochin, thank you for sharing with me such as great moment making this stage smoother. Thank you, **Ines** and **Minoo** for our Fridays in Harmony, it has been always an enjoyment to be with you.

To my Latin family, the one I found as a rival and became an essential part of my life. I will never regret to lose the position at Curie because instead I got you, la mansa familia Chilena, **Javi** (un poco menos), **Pato** and **Lautaro** and my favorite Argentino-Uruguayo **Jaime**. Thank you for been here, I couldn’t ask for more.

To the family I found in my life. A **José** y **Ana**, muchas gracias por habernos despertado el interés por la ciencia, incluso aunque sea un trabajo poco reconocido, yo sé que hemos elegido algo que nos apasiona y que podremos disfrutar juntos. Muchas gracias también por la personita que habéis creado, nuestro terremoto **Joselito** que ha llegado a nuestras vidas para que no nos aburramos. También quiero agradecer a mi suegra, **Ana**, sé que te robe una parte importante de tu vida, pero te agradezco enormemente que la compartas conmigo. Muchas gracias por todo tu apoyo.

A mi familia, mi **padre** y mi **madre** os quiero agradecer todo vuestro esfuerzo y sacrificio que habéis hecho durante vuestra vida para que nosotros podamos cumplir nuestras metas. Ese esfuerzo siempre se ve recompensado y espero que estéis orgullosos de la familia que habéis creado. Este trabajo tiene una mención especial para ti **MAMA**, todo lo que tu no pudiste estudiar lo estamos haciendo nosotros gracias a tu esfuerzo y dedicación. Quiero que sepas lo mucho que te quiero y que este trabajo es para ti. A mi hermano **David** y a mi hermana **Inma**, muchas gracias por estar siempre ahí en los buenos y en los malos momentos.

I cannot forget my friend, my travel partner and the love of my life, **Paula,** the responsible I got the crazy idea to do a PhD and to move to Paris. I cannot express how glad I am of you. I am extremely grateful of having you. Thank you so much for your emotional support, your compression, your help and your company. We did this adventure together and we are still alive to tell the tale.

Summary

Titre: Développement d'un modèle 3D d'épithélium bronchique pour la nanotoxicologie: analyse de la formation d'une couronne de protéines autour des nanoparticules d'argent dans le sécrétome

Résumé:

Au cours des dernières années, la production et l'utilisation de nanomatériaux (NMs) dans l'industrie ont augmenté de façon exponentielle et les NMs représentent un danger potentiel pour la santé humaine. L'utilisation de modèles in vitro apparait comme une solution pour prendre en charge l'évaluation de la toxicité d'une très grande diversité de NM à tester.

Pour étudier les effets biologiques de nanoparticules d'argent (AgNPs) sur le poumon, nous avons développé un modèle de culture 3D d'épithélium bronchique humain avec la lignée cellulaire Calu-3. Nous avons analysé la composition du sécrétome apical au cours du temps et caractérisé la composition de la couronne de protéines adsorbés autour des AgNPs en présence du sécrétome. Les Calu-3 ont été cultivées à l'interface air liquide (IAL) sur des inserts d'une porosité de 3 μm et avec une supplémentation réduite en sérum foetal bovin. La mesure de la de résistance électrique transépithéliale, la perméabilité du colorant Lucifer Yellow et l'immunomarquage de la protéine zonula occludens-1 associée aux jonctions serrées ont montré que l'intégrité de l'épithélium était maintenue pendant 28 jours à l'ALI. La composition du sécrétome apical des cellules Calu-3 à l'ALI a été analysée par LC-MS/MS et comparée au sécrétome d'épithéliums bronchiques humaines normaux (NHBE) provenant de 3 donneurs différents. Au total, 408 protéines extracellulaires communes ont été identifiées dans les modèles Calu-3 et NHBE. La sécrétion de mucines formant le gel de mucus (MUC5AC, MUC5B), ainsi que de peptides antimicrobiens (lysozyme, lipocaline-2 et clusterine) démontrent la fonctionnalité du modèle Calu-3.

La barrière épithéliale du modèle Calu-3 a été exposée à 10 μg/cm^2 d'AgNPs. Aucun effet sur la viabilité cellulaire n'a été observé pendant 48 heures. Cependant, une surexpression de gènes impliqués dans les voies de défense antioxydante, inflammatoire et métallique telles que l'hème-oxygénase, les cytokines IL-6 et IL-8, et la métallothionéine a été observée.

La composition de la couronne protéique adsorbée sur les AgNPs a été étudiée en présence des cellules ('couronne cellulaire') ou après la collecte du sécrétome ('couronne acellulaire'). Les protéines adsorbées montrent un enrichissement en protéines impliquées dans les processus biologiques, tels que l'activation cellulaire, le transport, la réponse à un stimulus, les processus métaboliques cellulaires et la réponse à un produit chimique, a été observé dans la couronne protéique. Par ailleurs, les AgNPs pré-incubées dans le sécrétome ont induit une réponse pro-inflammatoire différente dans les macrophages dérivés du THP-1 par rapport aux NP nues. La nouvelle identité biologique des AgNPs acquise dans le sécrétome bronchique pourrait favoriser l'activation des cellules immunitaires et faciliter leur absorption par les macrophages.

En conclusion, un modèle fonctionnel in vitro de culture en 3D d'épithélium bronchique humain a été développé. Il est actuellement mis en œuvre pour évaluer la toxicité à long terme des NM in vitro. Les cellules Calu-3 ont produit un sécrétome à fonction protectrice très similaire à celui produit par les cultures de cellules primaires. Ce travail a mis en lumière le rôle majeur de la couronne protéine dans la réponse immunitaire aux NMs dans le poumon.

Mots clefs:

Toxicité pulmonaire, Calu-3, épithélium bronchique, modèle 3D, nanoparticules d’argent, couronne protéique.

Title: Development of a 3D bronchial epithelium model for nanotoxicology: analysis of the protein corona formation on silver nanoparticles in the secretome

Abstract:

Over the last years, the production and use of nanomaterials (NMs) in the industry have increased exponentially and NMs have become a potential hazard for human health. As a large number of NMs need to be tested for toxicity, in vitro models have become essential for NM toxicity assessment.

To investigate the biological effects of silver nanoparticles (AgNPs) on the lung, we have developed a 3D cell culture model of the human bronchial epithelium using the Calu-3 cell line. We analysed the composition of the apical secretome over time and characterized the formation of the protein corona on AgNPs in the mucus. Calu-3 were grown at the air-liquid interface (ALI) on porous inserts with a 3 µm pore diameter and reduced foetal bovine serum supplementation. The measurement of the transepithelial electrical resistance, the permeability of Lucifer Yellow dye and the immunolabelling of the tight-junction associated zonula occludens-1 protein showed that the epithelium integrity was maintained for 28 days at ALI. The composition of the apical secretome of Calu-3 cells at ALI was analysed by LC-MS/MS and compared to the secretome of primary normal human bronchial epithelial (NHBE) cells from 3 different donors. In total, 408 common extracellular proteins were identified in Calu-3 and NHBE models. The secretion of gel-forming mucins (MUC5AC, MUC5B), as well as antimicrobial peptides (lysozyme, lipocalin-2, and clusterin), demonstrates the functionality of the Calu-3 model.

The Calu-3 epithelial barrier was exposed to 10 µg/cm^2 of AgNPs without any effect on the cell viability until 48 hrs. However, overexpression of proteins involved in the anti-oxidant, inflammation and metal defence pathways such as heme-oxygenase, IL-6 and IL-8 cytokines, and metallothionein was observed.

The formation of the protein corona on AgNPs was investigated in the secretome with cells ('cellular corona') or following secretome collection ('acellular corona'). The biological processes associated with the adsorbed proteins such as cell activation, transport, response to stimulus, cellular metabolic process and response to chemical, were enriched in the protein corona. Furthermore, AgNPs pre-incubated in the secretome induced a different pro-inflammatory response in THP-1 derived macrophages compared to bare nanoparticles. The new biological identity of AgNPs acquired in the bronchial mucus may favour the activation of immune cells and facilitate their uptake by macrophages.

To conclude, a functional in vitro 3D cell culture model of the human bronchial epithelium was developed. It is currently implemented to assess the long-term toxicity of NM in vitro. Calu-3 cells produced a secretome with a protective function highly similar to the one produced by primary cell cultures. This work sheds light on the major role of the protein corona in driving the immune response to NMs in the lung.

Keywords:

Lung toxicity, Calu-3, bronchial epithelium, 3D model, silver nanoparticles, protein corona

List of abbreviations

A

A4F	Asymmetric flow-field-flow
AB	Alamar Blue
ACN	acetonitrile
AgNP	Silver nanoparticle
ALI	Air-liquid interface
AM	Airway macrophage
AMP	Antimicrobial peptide
AP-1	Activator protein-1
ASL	Airway surface liquid
ATCC	American Type Culture Collection
AuNP	Gold nanoparticle

B

BCA	Bicinchoninic acid
BPI	Bactericidal/permeability-increasing
BVR	Biliverdin reductase

C

CCL2/MCP-1	Chemokine ligand 2/Monocyte chemoattractant protein-1
CCSP	Club cell secretory protein
CD	Circular dichroism
COPD	Chronic obstructive pulmonary disease
CPI	Consumer products inventory

D

DAMP	Damage-associated molecular pattern
DC	Dendritic cell
DCS	Differential centrifugal sedimentation
DLS	Dynamic light scattering
DMEM	Dulbecco's Modified Eagle Medium

E

ECL	Enhanced chemiluminescence
ELLA	Enzyme-linked lectin assay

F

FBS	Fetal bovine serum
FDR	false discovery rate

G

GO	gene ontology

H

hAEC	human bronchial airway epithelial cells
hBAL	Human bronchoalveolar lavage
HBSS	Hanks Balanced Salt Solution
HCD	Higher-energy C-trap Dissociation
HCS	High-content screening
HMDS	Hexamethyldisilazane
Hmox-1	Heme oxygenase-1

HRP	Horseradish peroxidase
HSA	Human serum albumin
HTBE	Primary human tracheobronchial
HTS	High-throughput screening

I

IL	Interleukin
ISDD	In vitro Sedimentation, Diffusion and Dosimetry

L

LC-MS/MS	Liquid chromatography–mass spectrometry
LDS	Lithium dodecyl sulfate
LPS	Lipopolysaccharide
LY	Lucifer Yellow

M

MEM	Minimum essential media
MMP	Matrix metalloproteinase
MT	Metallothionein
MUC1	Mucin 1
MUC16	Mucin 16
MUC4	Mucin 4
MUC5AC	Mucin 5AC
MUC5B	Mucin 5B

N

NFkB	Nuclear factor kappa-light-chain-enhancer of activated B cells
NHBE	Primary normal human bronchial epithelial cell
NICB	National Institute for Cellular Biotechnology
NM	Nanomaterial
NMR	Nuclear magnetic resonance
NP	Nanoparticle
NRF2	Nuclear factor erythroid-derived 2-like 2
NTA	Nanoparticle tracking analysis

O

Oct-4	Octamer-binding transcription factor 4
OsO4	Osmium oxide

P

PAMP	Pathogen-associated molecular pattern
PC	Principal component
PCA	Principal component analysis
PCL	Periciliary layer
PE	Polyester
PEG	Polyethylene glycol
PET	Polyethylene terephthalate
PFOA	Perfluorooctanoic acid
PLGA	Poly(lactic acid-co-glycolic acid)
PMA	12-O-tetradecanoylphorbol-13-acetate / Phorbol 12-myristate 13-acetate
PRR	Pattern recognition receptor

PVP	Polyvinylpyrrolidone

R

RANTES/CCL5	Chemokine ligand 5
ROS	Reactive oxygen species
RPMI	Roswell Park Memorial Institute
RT-PCR	Reverse transcription PCR
RT-qPCR	Real-time quantitative PCR

S

SAXS	Small-angle X-ray scattering
SEC	Size exclusion chromatography
SEM	Scanning electron microscopy
SLPI	Secretory leukocyte protease inhibitor
SOD-1	Superoxide dismutase type 1
SP	Surfactant-associated proteins

T

TEER	Trans-Epithelial Electrical Resistance
TEM	Transmission electron microscopy
TIMP	Tissue inhibitors of metalloproteinase
TMB	Tetramethylbenzidine
TNF	Tumor necrosis factor

W

WB	Western blot

X

Xeoxs	Xeuss 2.0 high resolution X-ray spectrometer

Z

ZO-1	Zonula occludens 1

Table of Contents

List of figures

List of tables

Context of the study

Nanotechnology is a recent field of research and innovation focused on the design and creation of materials and devices at the nanoscale. Nanomaterials (NMs) exhibit specific properties due to their small size. Their applications cover many areas in chemistry, physics, material science, engineering, computer science, biology, and medicine. Since the 1990s, the development of nanotechnologies has promoted the industrial production and commercialization of consumer products containing NMs. However, little was known at the time about NM toxicity and their potential risk to the environment and human health. In 2004, Britain's Royal Society and the Royal Academy of Engineering published a report entitled "Nanoscience and Nanotechnologies: Opportunities and Uncertainties", which described the potential consequences for the health and the environment of NMs, as well as the social and regulatory issues associated with nanotechnology. In 2005, the European Commission launched a European action plan to support the implementation of a safe, integrated and responsible approach in nanoscience and nanotechnologies.

In this context, the European Union funds research programs to assess NM toxicity and to develop novel methodologies for the risk management of nanomaterials. BIORIMA is one of them and is focused on nanobiomaterials. The research project of this PhD was developed within the framework of the H2020 BIORIMA project. The BIORIMA project aim is to develop and validate new approaches and protocols, which can be applied to identify and assess the potential risks of manufactured nano(bio)materials. The development of advanced *in vitro* models, as an alternative to reduce the use of animals, was investigated in this context to explore new exposure strategies and to follow the fate and the adverse effects of NMs.

Indeed, the toxicity of NMs could be tested *in vitro* using human cell cultures or *in vivo*, usually on small mammals. The advantages of *in vivo* studies are the possibility to investigate the systemic toxicity of NMs and their effects on specific organs. However, it would be impossible to test the toxicity of all the NMs currently produced *in vivo* because of the number of NMs and products developed, the different exposure routes to consider, and the large differences in chemistry, size, shape, functionalization of the NMs synthesized, which can all play a role in their toxicity. Moreover, the species difference must be taken into account, and experiments on animals raise ethical issues. By contrast, the toxicity of NMs to a target organ can easily be tested *in vitro* on a large number of NMs using human cells or cell lines, providing that the *in vitro* model can reproduce most of the biological features of the organ of interest.

In this work, we focused on the lung, which can be exposed to NMs following nanoparticle (NP) inhalation. Human cells isolated from different airway regions can be used to reconstruct the bronchial or alveolar epithelium while keeping their biological characteristics. The use of human cells also avoids the species difference, which is inherent to *in vivo* testing.

The bronchial epithelial barrier can be reformed *in vitro* using human primary cells or human bronchial cell lines, which present different advantages and limitations. For this work, we selected a cell line to develop an accessible and low-cost model to study the long-term toxicity of NMs, compared to primary cell cultures. Advanced and 3D cell models (such as organoids, spheroids, and scaffolds) are considered a realistic approach to implement the “3R principle” (Replacement, Reduction, and Refinement) to reduce animal testing in nanotoxicological studies.

Here, we developed a 3D model of the bronchial epithelium using the Calu-3 cell line to investigate the effects of exposure to NPs at the air-liquid interface on the epithelium. This model has been adapted to meet the challenges of nanotoxicology, including the investigation of NP-mucus interactions, effects on the epithelial integrity barrier and epithelial translocation, as well as the cellular and molecular responses induced by the NPs. In this context, we focused on the study of the NP-protein interactions that occur as soon as the NPs arrive in a biological medium. We used the biological fluid produced by the cells the apical side, which is called the secretome. This biological fluid will provide the first description of NP-airway proteins interactions to assess the role of the protein corona in driving NP-cell interactions.

Chapter 1: Introduction

Nanotechnology is a multi-disciplinary field that deals with the development and the use of nanomaterials (NMs). It is applied to different areas such as chemistry, physics, material science, engineering, computer science, biology, and medicine. A NM is defined by the EU as a natural, incidental or manufactured material containing particles with one or more external dimensions in the size range 1nm -100nm. The development of NPs has led to multiple innovations and applications in cosmetics, electronic devices, and medicine, and nanotechnology is considered as one of the most promising technologies of the 21st century. However, little is known about the toxicity of NMs and the associated risk for the environment and human health (Dagani 2003). The continued growth of the production and use of manufactured nanoparticles (NPs) increases the risk of exposure. NPs may interact with the human body, following intended or unintended exposure, by inhalation, ingestion or application to the skin (Figure 1). Inhalation is an important route of accidental exposure, especially when considering occupational exposure.

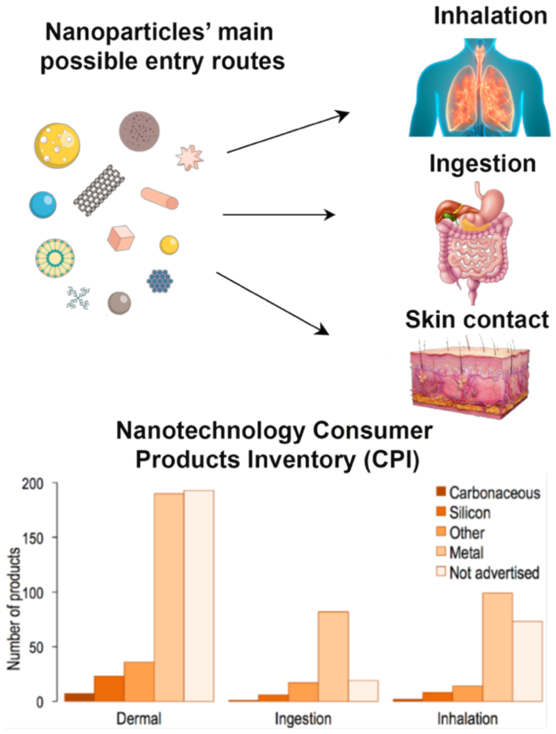

Figure 1: Main routes of nanoparticle entry into the body.

(a*) The 3 principal routes of entry of NPs are inhalation, ingestion and skin contact. (b) The potential exposure pathways from the expected normal use of consumer products grouped by NM composition. Adapted from* (Vance et al. 2015).

1.1 Anatomy and structure of the lung

The organism is protected from the penetration of chemicals, pathogens and other unwanted substances by an epithelial layer that covers the internal and external surfaces of the body. In this study, we focused on the respiratory system as a potential exposure route for NPs. The respiratory tract exhibits a large surface area, about 100 to 150 m^2. It forms a large interface between the tissues and inhaled air, as the daily air volume inhaled by an adult is estimated to 10-15 m^3. The combination of these factors makes the respiratory system one of the main routes of exposure to pollutants, pathogens and atmospheric particles such as nanoparticles. These xenobiotics can be responsible for local toxicity as well as systemic toxicity if they cross the air-blood barrier in the alveoli where gas exchange takes place. The deposition of pollutants depends on their properties and on the structure and defense mechanisms of the respiratory tract.

1.1-1 Description of the respiratory tract

The respiratory tract is divided into two functional zones: the conducting zone, also called airways, which diffuses the inhaled air to the respiratory zone, where gases are exchanged at the level of the alveoli (Figure 2). The airways can be anatomically distinguished into the upper airway, formed by the nasal cavity, the pharynx and the larynx, the lower airway formed by the trachea, bronchi, bronchioles, and the alveolar airway formed by alveolar ducts, and alveoli (Patwa and Shah 2015). Along the respiratory tract, the diameter of the airways decreases as well as the air flow, and the number of bifurcations increases. The respiratory tract is lined with an epithelium that evolves from the upper airways to the deep lung, adapting its shape and cell composition depending on its function (Figure 2):

a) The upper respiratory tract is a complex area associated with the breathing functions. Apart from guiding the air to the lung, the upper airway heats, humidifies and filters the inhaled air, especially in the nose thanks to the nose hair (Pierce and Worsnop 1999). Besides, it is the area where the olfaction function takes place.
b) The lower respiratory tract is delineated by a pseudostratified columnar epithelium mainly formed by ciliated cells and goblet cells. The epithelium is supported, in the upper part (trachea and part of the bronchi), by a collagenous lamina propia containing serous and mucus glands, and by a smooth muscle layer that regulates the airflow. The lamina propia and the smooth muscle become progressively less prominent, and they are absent in the small airways. Furthermore, the epithelium progressively changes to a

thinner , cuboidal cell layer, containing less ciliated and goblet cells, and more club cells (previously called Clara cells) (Bustamante-Marin and Ostrowski 2017).

c) The alveolar region starts after the division of the respiratory bronchioles into alveolar ducts connected the alveolar sacs, which contain the alveoli. The alveoli are the terminal part of the respiratory system, where gas exchange takes place. The closer proximity with the blood capillaries enables gas exchange by diffusion. The alveolar wall acts as a barrier for airborne pollutants. However, if translocation happens, the translocated pollutants directly arrive into the bloodstream with a risk of systemic distribution.

As mentioned above, the lower respiratory tract is formed by a pseudostratified epithelium composed of different types of cells with specific functions. These cells contribute to the mucociliary clearance. This epithelium is also called "mucociliary epithelium". The main cell types are (Figure 2 and Figure 3):

- **Secretory cells** synthesize and secrete the mucin proteins that form the mucus, which lines the surface of the airway epithelium ensuring its lubrication and protection. Depending on their microscopic appearance, we can distinguish goblet cells from Clara and serous cells. They also present different patterns of protein secretion: mucin 5AC (MUC5AC) is mainly secreted by goblet cells, while mucin 5B (MUC5B) secretion is restricted to serous cells (Groneberg et al. 2002). Club cells (or Clara cells) are located in the small airway and the trachea-bronchial axis (Rawlins et al. 2009). Their main functions are i) the synthesis and secretion of surfactant, anti-microbial peptides and other proteins, such as the club cell secretory protein (CCSP), which is important in the lung defense (Arsalane et al. 2000), ii) the detoxification of inhaled xenobiotic and oxidant gases, and iii) the cell renovation and the epithelium protection (Rawlins et al. 2009; Reynolds and Malkinson 2010).
- **Ciliated cells** are characterized by the presence of beating cilia that moves mucus, allowing the removal of trapped pathogens and particles. Cilia is a specialized organelle whose coordinated beating results in the movement of mucus. The ciliary beating of airway epithelial cells constitutes an important part of the mucociliary clearance, allowing mucus sheet to be either expectorated or swallowed.
- **Basal cells** are the progenitor cells of ciliated and secretory cells. They play a critical role in the regeneration of the airway epithelium after an injury and repair.

- **Neuroendocrine cells** are sensorial epithelial cells located in large and small airways. These cells are characterized by their chemosensitivity. They are involved in oxygen sensing and in the immune responses (Noguchi, Furukawa, and Morimoto 2021).

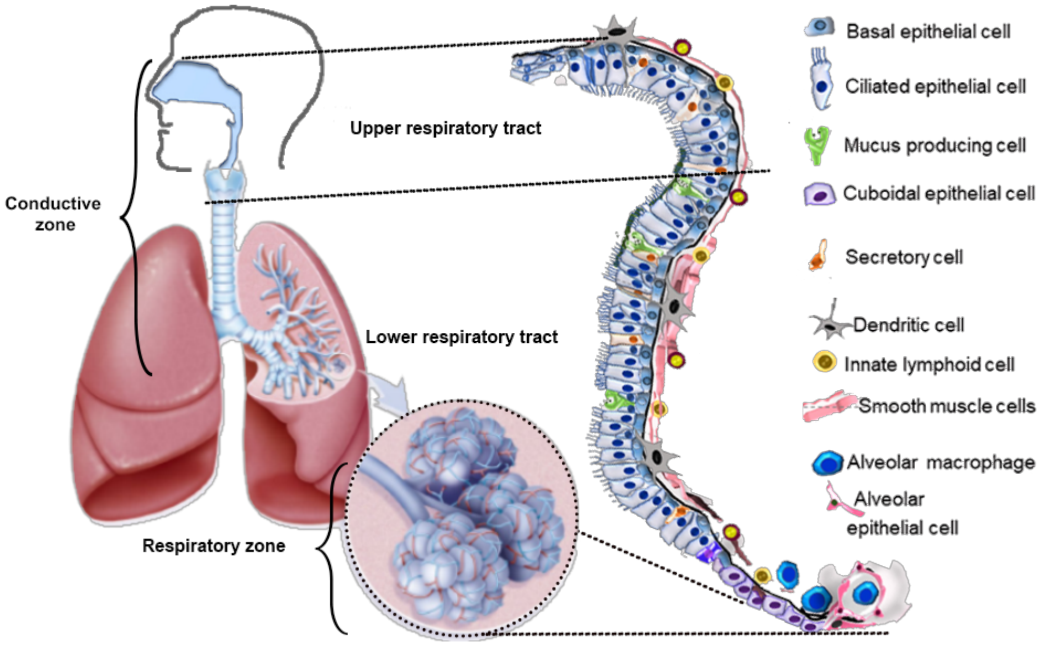

Figure 2: Anatomy of the respiratory tract showing the airways (upper and lower respiratory tract) and the respiratory zone with the alveoli where gas exchange occurs.

The right part shows the evolution of the structure and cell composition of the epithelium that lines the respiratory tract from the upper airways to the alveoli. Adapted from (LeMessurier et al. 2020).

The respiratory zone is lined with a monostratified epithelium composed of two alveolar cell types (Figure 2):

- **Type I alveolar cells** cover 95% of the alveolar surface and form the alveoli. They are flat cells 0.1-0.2 µm thick. They are involved in gas exchange (Morgenroth and Ebsen 2008).
- **Type II alveolar cells** produce the pulmonary surfactant necessary to maintain the alveolar structure during breathing. They also metabolize the inhaled xenobiotics (Castell, Donato, and Gómez-Lechón 2005).

In addition to the epithelial cells, **macrophages** are present in the alveoli regions. They form two distinct populations: 1) alveolar macrophages, which reside in the airway lumen and are in close contact with the alveolar cells; 2) interstitial macrophages, which reside in the interstitial spaces. Alveolar macrophages populate the alveoli shortly after birth and persist over the lifespan. They are critical for tissue homeostasis, host defense, pathogen recognition and clearance, as well as for the phagocytosis of inhaled particles, which leads to their degradation and clearance, and to the presentation of novel antigens to the adaptive immune cells (Hussell and Bell 2014).

The alveolar epithelium is covered by the pulmonary surfactant, which is composed of around 90% lipids (mainly phospholipids) and 10% proteins. The surfactant proteins comprise four specific surfactant-associated proteins (SP): the hydrophilic SP-A and SP-D, and the hydrophobic SP-C and SP-D (Serrano and Pérez-Gil 2006). The main functions of the pulmonary surfactant are to reduce the surface tension at the air-liquid interface avoiding the alveolar collapse during breathing, and to contribute to the host defense.

1.1-2 Protective functions of the airway epithelium and secretions

With each inhalation, the respiratory tract is exposed to inhaled bacteria, viruses and pollutants, such as nanoparticles. These agents do not reach the epithelium directly because it is covered by the airway surface liquid (ASL). The ASL contributes to the defense mechanisms of the airways and participate to the detoxification of the air. The mucociliary clearance is the primary defense mechanism, completed by antimicrobial, anti-oxidant and anti-inflammatory defense mechanisms. These processes rely on the specific properties of the ASL that is composed of salts, water and a variety of biomolecules such as antimicrobial peptides, mucins, and anti-oxidants, among others.

a) Mucociliary clearance

The mucociliary clearance is a protective function of the airways essential for the removal of respiratory pathogens and pollutants (Londino, Collawn, and Matalon 2015). The mucus traps inhaled toxicants and pathogens. Thanks to the ciliary beating, the mucus can be cleared.

The ASL is formed by the periciliary layer (PCL) and the mucus layer (Figure 3):

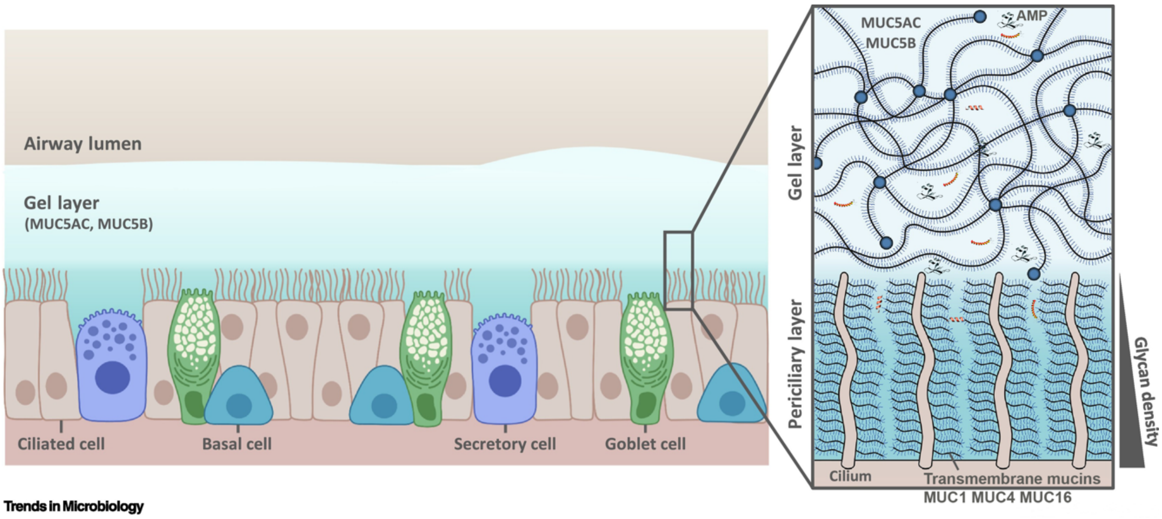

Figure 3: Schematic representation of the bronchial epithelium with airway liquid secretion.

The pseudostratified epithelium of the tracheo-bronchial zone is composed of basal, ciliated and secretory cells. It is covered by an airway surface liquid (ASL) formed by a periciliary layer, which is in close contact with cells in the ciliated zone, and the gel-like mucus layer, containing different types of mucins. From (Wallace et al. 2021).

- The ***periciliary layer*** (PCL) is a 7 µm thick polyanionic mesh in direct contact with the airway surface (Button et al. 2012). The PCL contains molecules such as glycolipids and the membrane-associated mucins, mucin 1 (MUC1), mucin 4 (MUC4) and mucin 16 (MUC16). The membrane-bound mucins contribute to the mechanical properties of the ASL close to the cell surface. MUC4 is expressed on cilia and prevents the penetration of the mucus gel layer. MUC1 is presented on the cell surface and microvilli of ciliated and goblet cells. It modulates the intracellular signaling associated with inflammation and pathogen defense. MUC16 is also expressed by ciliated and secretory cells. It can be cleaved and secreted to the gel layer (Hattrup and Gendler 2008). The main function of the PCL is therefore to provide an efficient lubricating layer for ciliary beating and to prevent mucus layer mixing.
- The ***mucus layer*** is mainly composed of secreted mucins. The gel-forming mucins are mainly MUC5AC and MUC5B, expressed in goblet cells and submucosal glands (Voynow and Rubin 2009). Secreted mucins are large glycosylated proteins with cysteine-rich amino- and carboxy-terminal regions that establish disulfide bonds between polypeptide chains. Furthermore, their central region is rich in serine and threonine, which are the reactive sites of O-glycosylation (Figure 4a). When mucins are secreted into an aqueous solution, they form a tight mesh structured by disulfide bonds, hydrophobic and electrostatic interactions (Wagner, Wheeler, and Ribbeck 2018). This creates a viscous mesh that can trap the inhaled particles either by size exclusion effect or by binding to the mucins or to other mucosal

components (Figure 4b). Smith-Dupont *et al.* reported different diffusion profiles in mucus samples depending on the probes size and surface chemistry (Smith-Dupont et al. 2017). Even when the size of the inhaled particles is small enough to cross the mucus barrier, their diffusion through the gel can be slowed or stopped by the chemical interactions with the mucins.

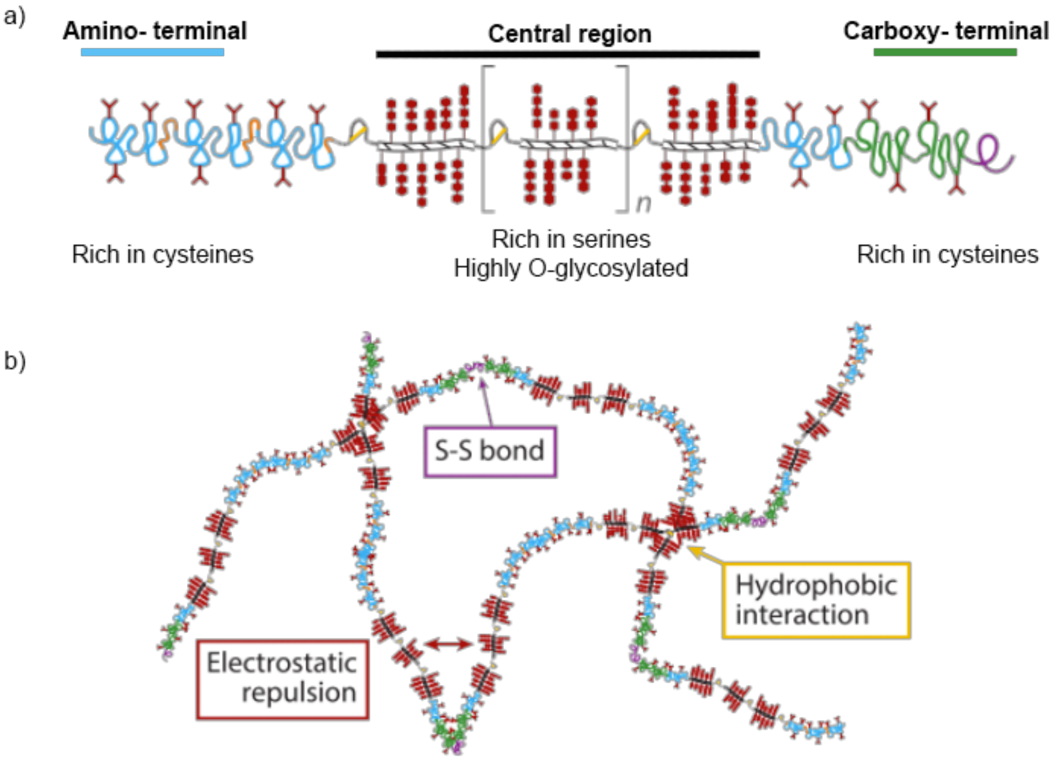

Figure 4: Schematic structure of secreted mucins and the mucus mesh.

(a) General scheme of secreted mucins highlighting the cysteine-rich region and serine-rich regions. (b) Illustration of the mucus mesh established by the secreted gel-forming mucins. Disulfide bonds, hydrophobic and electrostatic interactions maintain the structure and the tightness of the mucus mesh. From (Wagner, Wheeler, and Ribbeck 2018).

b) Other protective functions

When xenobiotics and pathogens cannot be eliminated by the mucociliary clearance, other mechanisms contribute to the epithelial host defense. In addition to mucins, other proteins identified in bronchoalveolar lavages and bronchial epithelium secretions (Jinzhi Chen et al. 2008; Gupta et al. 2019) play an important role in the defense and homeostasis of the ASL. A range of biomolecules identified in the ASL are involved in the aggregation, trapping and killing of microbes/particles, such as metabolic enzymes, lysozyme, β–defensins, lactoferrin, cathelicidin, surfactant proteins, and immunoglobulins (Tecle, Tripathi, and Hartshorn 2010).

Antimicrobial peptides (AMPs):

- The *bactericidal/permeability-increasing (BPI) fold*-containing protein family, which includes BPIFA1 and BPFB1, exhibits a high affinity for many Gram-negative bacterial strains. It contribute to the prevention of biofilm formation (Liu et al. 2013).
- The *lipocalin 2* protein, can bind to bacteria and restrict bacterial growth (Wu et al. 2010).It can also regulate lung inflammation and induce immune cell recruitment during mycobacterial pulmonary infections (Guglani et al. 2012).
- Proteases and antiproteases are secreted by epithelial cells and participate in the lung homeostasis. Modifications of the proteases/antiproteases balance can lead to the development of lung diseases, the disruption of the ASL homeostasis of ASL, and an increasing susceptibility of the epithelium to pollutants and infections.

The respiratory tract produces different families of proteases with unique targets and cellular sources, such as cathepsins, matrix metalloproteinases (MMPs) and type 2 transmembrane serine proteases. These proteases are important for the major histocompatibility complex II formation and antigen presentation (Riese et al. 1996) and for the cleavage of proinflammatory cytokines (Opdenakker, Van Den Steen, and Van Damme 2001). However, a high level of protease activity has been associated with chronic lung diseases, due to the elimination of extracellular matrix components. Antiproteases inhibit proteases and modulate the immune responses in the lung. The ASL contains different families of antiproteases such as *serpin*, which targets serine and cysteine proteases, *tissue inhibitors of metalloproteinases* (TIMPs), which target MMPs, *elafin* and *secretory leukocyte protease inhibitor* (SLPI), which inhibits viral infections and blocks the inflammatory cascades (see review by Meyer and Jaspers, 2015).

Addition mechanisms of defense against adverse effects of inhaled pro-oxidants are provided by an extensive epithelial anti-oxidant system. This system is activated by several mechanisms, including nuclear factor erythroid-derived 2-like 2 (Nrf2)-mediated transcription. Nrf2 is a transcription factor that regulates cellular redox balance, the protective antioxidant and detoxification responses. It is involved in the regulation of enzymes associated with the metabolism of xenobiotics (Kensler, Wakabayashi, and Biswal 2007). This transcription factor regulates the expression of numerous cytoprotective genes involved in the antioxidant and detoxification responses. The expression of heme oxygenase-1 (*hmox-1*) is regulated by Nrf2. It is highly expressed following exposure to nitric oxide, heavy metals, and others. This enzyme works with NADPH P450 cytochrome to catalyze the rate-limiting step in heme degradation, leading to the generation of potent antioxidants and anti-inflammatory molecules such as biliverdin, Fe^{2+} ion and carbon monoxide (Figure 5) (Loboda et al. 2016).

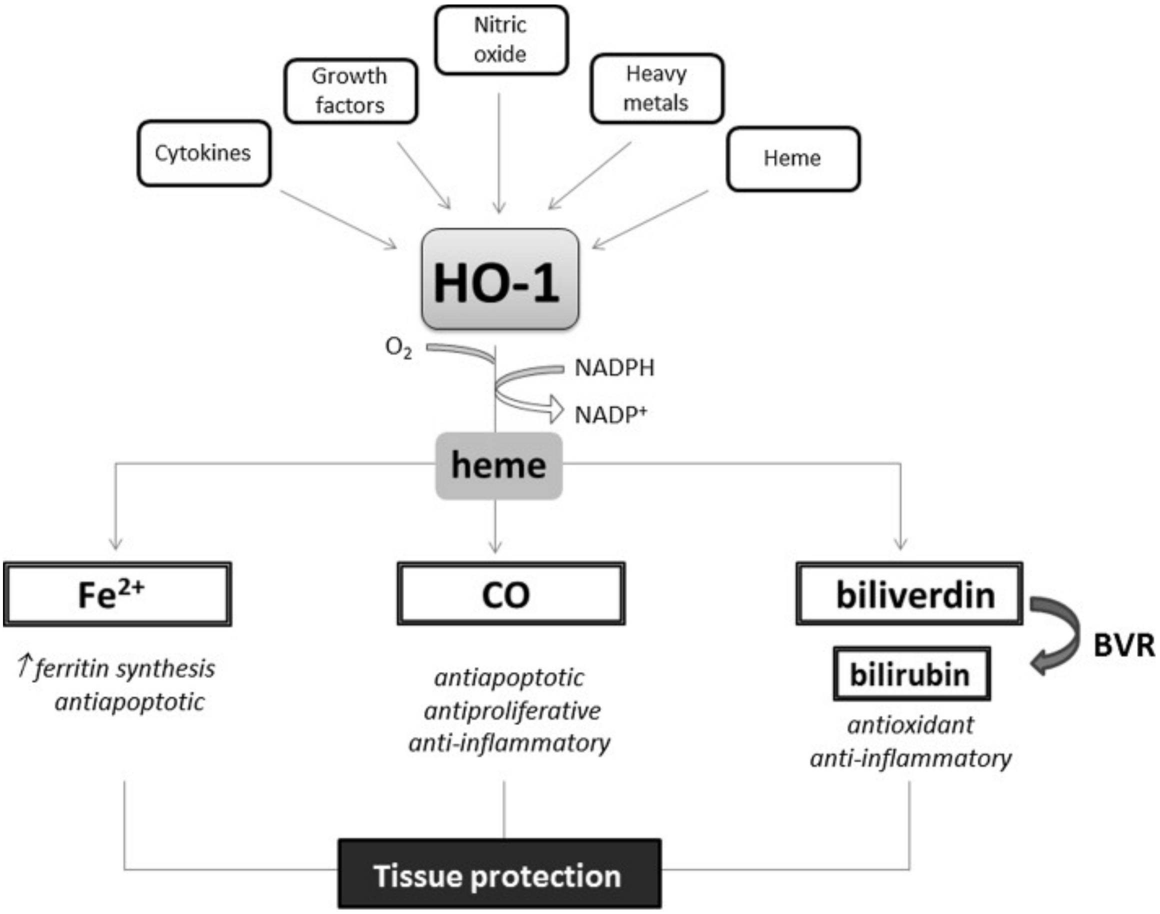

Figure 5: Heme-oxygenase-1 enzymatic pathway.

HMOX-1 is induced by different stimuli such as cytokines, growth factors, nitric oxide and heavy metals. This enzyme works with NADPH P450 cytochrome to degrade heme and produce three bioactive products: Fe^{2+} *ion, carbon monoxide and biliverdin (which is converted to bilirubin by the action of biliverdin reductase (BVR)). The products act as pro-angiogenic, anti-oxidant or anti-inflammatory factors that contribute to the tissue protection. (From* (Loboda et al. 2016)*).*

1.1-3 Innate immunity in the lung

In addition to the physical and biochemical protection provided by the ASL, the pulmonary surfactant and the epithelial cells can be protected from inhaled particles, microbes and toxicants by the innate host defense system. Resident macrophages and dendritic cells of the alveoli react to pathogens, antigens and toxicants, by activating the innate and acquired immunity. In the lung, alveolar macrophages are the most abundant innate immune cells and they play a critical role in the tissue homeostasis, host defense, clearance of surfactant and cell debris, pathogen recognition and elimination, regulation of lung inflammation, and repair of damaged tissue (Joshi, Walter, and Misharin 2018).

The inhaled pathogens, allergens or toxicants, are detected by the pathogen-associated molecular patterns (PAMPs) and/or by the damage-associated molecular patterns (DAMPs) resulting from cell damage and/or cell stress. Both patterns are recognized *via* the membrane associated pattern recognition receptors (PRRs). The binding of ligands to PRRs receptors activates the signaling pathways for cytokines, chemokines and antimicrobial peptide production. The secreted molecules can recruit and activate cells of the innate and adaptive immune systems, such as neutrophiles, eosinophils and monocytes (Figure 6). In addition, during acute inflammation and cytokine secretion by epithelial cells, the alveolar macrophages can also recruit innate immune cells, (McDonald and Kubes 2015), which will in turn differentiate into alveolar macrophages (Dong et al. 2017).

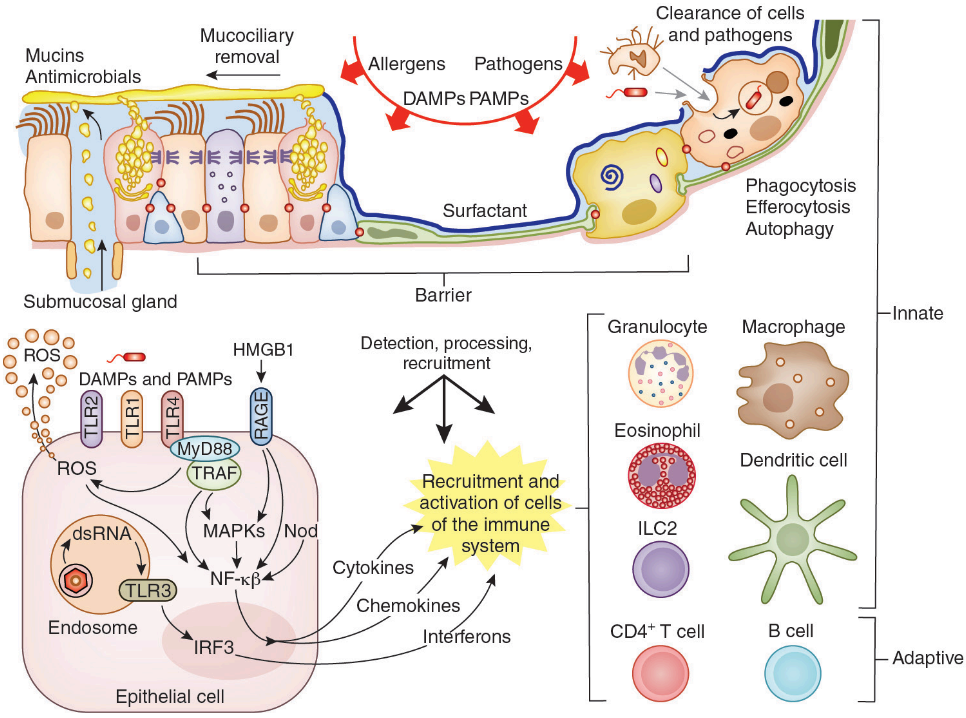

Figure 6: PAMPs and DAMPs signaling cascade activation in the respiratory epithelial cells after inhalation of pathogens, allergens or toxicant.

Pathogen-associated molecular patterns (PAMPs) activated for pathogens and damage-associated molecular patterns (DAMPs) generated from damage and/or cell stress are recognized via membrane associated pattern recognition receptors (PRRs). The binding of ligands to PRRs receptors activate the signaling pathways for the production of cytokines, chemokines and antimicrobial proteins that recruit and activate cells of the innate and adaptive immune systems. From (Whitsett and Alenghat 2015).

1.2 *In vitro* models of the respiratory tract for toxicity testing

The increase of atmospheric pollutants and respiratory infectious diseases an ongoing health concern, which requires the development of new treatments and strategies to prevent these hazards. The potential toxicity of inhaled pollutants and pathogens has been tested in animal models following instillation or inhalation. However, *in vivo* experiments present high costs, uncertainties associated with the extrapolation of the data to humans, as well as ethical issues (Landsiedel et al. 2017). As an alternative, the scientific community has developed *in vitro* lung models using cells from the different segments of the respiratory system. These models have been used to study pulmonary toxicity and related lung diseases to improve our knowledge on molecular and pathophysiological mechanisms (Upadhyay and Palmberg 2018). *In vitro* systems are cost-effective, time-efficient and easy to use. They allow the investigation of detailed cellular and subcellular functions, cell-to-cell communication, and specific molecular mechanisms.

1.2-1 Different *in vitro* models of respiratory epithelium

Cell-based assays have been widely used for toxicological studies using either cell lines or normal cells. Classically, 2D cell cultures have been used to assess the toxicity of a wide range of compounds *in vivo.* Though 2D cultures has shown good results in terms of toxicological assessment, they present several limitations, such as the loss of the tissue architecture, cellular interactions between different cell types, and mechanical constraints, or the lack of the air-liquid interface for respiratory models, which limit their relevance to predict the pulmonary toxicity of nanomaterials. The development of 3D cell culture models, together with the use of primary cells to obtain differentiated tissues, recreates *in vivo* characteristics such as the combination of different cell types, tissue architecture and cell-to-cell interactions that may improve the results of *in vitro* toxicity studies.

a) From 2D to 3D cultures

In vitro lung models were initially developed as 2D cultures generally grown on plastic or plastic-coated surfaces with extracellular matrix components such as collagen and fibronectin. These 2D cultures (Figure 7a) of cell lines have been largely used for toxicity screening studies as well as mechanistic studies, but mainly after unique exposure to investigate short-term effects. Some protocols have been developed to use them for repeated exposures and long-term effects. For example, the bronchial epithelial cell line, BEAS-2B, and the alveolar epithelial cell line, A549, were exposed to vanadium dioxide NPs following different exposure cycles (Xi et al. 2021). However, these cells need frequent passages limiting the number of exposures. Alternatively, the protocol can be adapted with cycles of seeding/exposure/harvest-seeding, which induce additional stress to the cultures and may create artefacts. Moreover, the 2D culture models do not reproduce the tissue-specific architecture, cell-to-cell and cell-to-matrix interactions, and the barrier function of the airway epithelium, which limits their ability to recapitulate *in vivo* cellular differentiation and responses (Bissell, Rizki, and Mian 2003; Cukierman et al. 1998), making them relatively poor airway models.

Efforts have been made to develop 3D cell cultures in order to recreate the 3D environment of cell growth, differentiation and organisation in the body. There is a wide range of 3D cell cultures with advantages and drawbacks. The main models and technologies used are summarized below (see Table 1 for the summary):

- ***Multicellular spheroids***: cell suspension tends to aggregate in culture and go through the process of self-assembly, which can recapitulate the functional phenotype of a tissue (Figure 7d). Spheroids can develop gradients of oxygen, metabolites, nutrients, creating heterogeneous cell populations. Among their advantages, these cultures present a well-defined geometry and allow cell-cell and cell-extracellular matrix interactions. However, technical and biological challenges are associated with the development and maintenance of spheroids of homogeneous size. Spheroids are compatible with co-cultures, but it requires being able to monitor the ratio between the different cell types.
- ***Organoids*** are 3D cultures, which develop real tissue structures. They are derived from stem cells or organ progenitors that differentiate to form an organ-like tissue (Lancaster and Knoblich 2014).
- ***Scaffolds and hydrogels cultures*** use synthetic 3D structures made of different materials with defined porosity and permeability (Figure 7b). They can mimic the microenvironment of a given tissue. Hydrogels such as Matrigel are often used in biological scaffolds to promote good cell attachment and reorganization. Synthetic scaffolds, such as poly(ethylene glycol), poly(vinyl alcohol), poly(2-hydroxy ethyl metharylate), and poly(lactic) (Tibbitt and Anseth 2009), have the advantage of reducing culture variability that can be created by Matrigel batch-to-batch differences (Fang and Eglen 2017).
- ***Organ-on-chip*** refers to an artificial, miniature model of a human organ on a microfluid cell culture chip. These cultures have the potential of mimicking the air and blood flow as well as mechanical and dynamic characteristics of the tissue. The lung-on-a-chip

model is able to mimic breathing by stretching the membrane on which cells are grown (Figure 7c) (Stucki et al. 2018).

- ***3D bioprinting*** uses the 3D printing technology to print cells, biocompatible materials and supporting components into complex 3D living tissues. Such systems have been used to create scaffolds for 3D cultures (Y. S. Zhang et al. 2017).

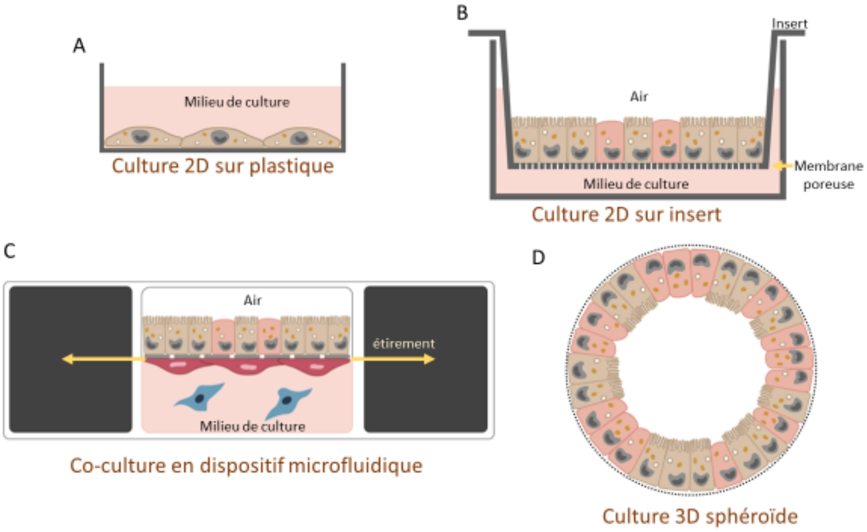

Figure 7: Different strategies for 2D and 3D cell cultures of airway cells.

I will now focus on scaffold-based techniques (Figure 7b), which have been used in this work. Primary cells and cell lines can be grown on polymeric hard material-based supports inside inserts. The inserts are placed in culture wells allowing cell culture both in submerged or air-liquid interface (ALI) conditions. According the chosen condition, the culture develops differently:

- In submerged cultures, cells are covered with a large volume of liquid, usually cell culture medium, that exceeds the volume of the ASL or surfactant, and cannot mimic the physiological features of the respiratory epithelium. This alters the differentiation process, especially for primary bronchial cells that do not produce ciliated cells in this condition. Additionally, using Calu-3 cells, a lower glycoprotein production in submerged cultures compared to ALI cultures was reported (Grainger et al. 2006). Therefore, this condition is unable to address accurately cell-cell and cell-stimulant interactions.
- To obtain a fully differentiate epithelial barrier similar to the one formed *in vivo*, primary human airway epithelial cell must be cultured at the ALI (Gray et al. 1996). For some cell lines, the culture at ALI can also promote differentiation and the development of tissue features. This is the case for the tumoral Calu-3 cell line (Grainger et al. 2006).

Choosing one of the cell culture models can have an impact on toxicological studies. A direct comparison was carried out to investigate the cellular response to xenobiotics in submerged or ALI conditions. Lenz *et al.* investigated the cellular response of the epithelial A549 cell line to zinc oxide NPs in both conditions. ALI cultures exhibited a higher expression level of pro-inflammatory markers than submerged conditions(Lenz et al. 2013), suggesting that ALI models may give more accurate results than submerged cultures due to the direct interaction of the toxic compounds with the cell surface, without any artificial aqueous medium (Ahmad et al. 2014).

Table 1:Advantages and disadvantages of different 3D cell culture techniques.
Adapted from (Fang and Eglen 2017)

Technique	Advantages	Disadvantages
Hard material-based supports	Applicable to microplates ALI cultures High reproducibility Co-culture ability *In vivo*-like architecture when using primary cells Compatible with long-term and repeated exposure	Simplified architecture Static cultures
Spheroids	Easy-to-use protocol Scalable to different plate formats Compliant with HTS/HCS Co-culture ability High reproducibility	Simplified architecture
Organoids	Patient-specific *In vivo*-like complexity *In vivo*-like architecture	High variability Hard to reach *in vivo* maturity Complication in assay Lack key cell types Lack vasculature
Scaffolds/hydrogels	Applicable to microplates Amenable to HTS/HCS High reproducibility Co-culture ability	Simplified architecture Can be variable across lots
Organs-on-chips	*In vivo*-like architecture *In vivo*-like microenvironment, chemical, physical gradients	Lack vasculature Difficult to be adapted to HTS/HCS
3D bioprinting	Custom-made architecture Chemical, physical gradients High-throughput production Co-culture ability	Lack vasculature Challenges with cell/materials Difficult to be adapted to HTS Issues with tissue maturation

HTS: High-throughput screening

HCS: High-content screening

b) Cell lines and primary cultures

Different cell lines have been used to develop models of the *airway epithelium*. They were largely used until the conditions to promote differentiation of primary cells were found. Cell lines are easily accessible, they tolerate a high number of passages without losing cell viability or entering senescence, as occurs with primary cells. Moreover, cell lines are relatively stable, which avoids the effect of donor variability observed with some primary cells. Several available cell lines were obtained either from cancer cells or after immortalized by transfection of viral genes. All airway cell lines do not share the same characteristics. Some have limited capabilities of producing mucus and/or of forming tight junctions, even when grown on inserts and at the air-liquid interface. For example, the bronchial epithelial cell lines, BEAS-2B and NCI-H292, do not develop into a tight epithelium, limiting their use for the study of NP translocation (George et al. 2015). The other bronchial epithelial cell line, 16HBE, which is immortalized, has kept the capability of forming tight junctions, but cannot produce mucus. The only commercially available cell line that can simultaneously form tight junctions and secrete mucus at ALI is the Calu-3 cell line (Kreda et al. 2007). Calu-3 cells differentiate into a functional epithelium, though limited to one cell type. The Calu-3 epithelium exhibits specifics features of the human bronchial epithelium, such as mucus secretion, transporter expression, and cytokine production, making this cell line popular for pharmaco-toxicological studies (Grainger et al. 2006; Kreft et al. 2015; Zhu, Chidekel, and Shaffer 2010; Foster et al. 2013).

In 2013, Walters *et al.* generated an immortalized human airway basal cell (BCi-NS1), which retained characteristics of primary cells after long expansion periods. These cells can differentiate in goblets, Clara and ciliated cells in ALI cultures (Walters et al. 2013). BCi-NS1 have been used in some toxicological studies to evaluate the cell response to smoke extract (Saxena et al. 2021) and to test the biomedical activities of NPs (Wadhwa et al. 2021). BCi-NS1 are a good alternative model to primary cells and reduces donor variability. However, they are not commercially available for the moment, and the complex culture requirements increase their cost, limiting their use.

The *alveolar epithelium* is composed of type I and type II cells. Cell lines have been developed for each cell type. The two main cell lines considered as type-II alveolar cells are A549 and NCI-H441 cell lines, with A549 being the most popular one. A549 cells produce surfactant proteins, but they are not able to produce tight junctions for long periods without dexamethasone, limiting their use for NP translocation studies (B. Rothen-Rutishauser et al. 2008; George et al. 2015). NCI-H441 cells produce surfactant proteins and they can form a polarized tight epithelium, but for a limited period, as observed in our laboratory (Brookes et al., 2021). Recently a type-I alveolar cell line, hAELVi, has been developed to produce a very tight epithelium when grown on ALI (Kuehn et al. 2016). A co-culture of NCI-H441 and hAELVi have been implemented in the laboratory. It forms a tight epithelium that can be maintained for several weeks and which exhibits sustained differentiation markers (Brookes et al. 2021).

Alternatives to cell lines are primary cells isolated from the different airway regions. They can be collected during surgery in hospitals. Biotechnology companies (for instance Lonza, Epithelix etc) also collect and commercialize these cells, reducing interlaboratory differences between protocols. The use of specific cultures conditions (culture at ALI, specific growth factors, presence of retinoic acid) leads to their differentiation into a mucociliary epithelium in few weeks (Rayner et al. 2019). After the *in vitro* differentiation process, the cell cultures represent an epithelium composed of different cell types, including ciliated, goblet and basal cells. An epithelial barrier is obtained, close to the *in vivo* morphology (Cao et al. 2020). Interestingly, such epithelial barrier can be established with cells from healthy donors but also from smokers or from donors with medical conditions such as Chronic Obstructive Pulmonary Disease (COPD) and asthma. It provides the opportunity to investigate the mechanisms involved in the differentiation process in normal or altered conditions, and to evaluate their susceptibility to pharmacological treatments of exposure to toxic compounds. One of the main advantages of this type of epithelial barrier is its sustainability. It represents a good option to evaluate the long-term effects of xenobiotics on the bronchial epithelium.

Table 2: Different cell types used to form airway and alveolar epithelium

Cell name	**Type**	**Culture condition**	**Days in culture**
MucilAir (Commercially available)	Primary bronchial cells	ALI	Up to one year
SmallAir (Commercially available)	Primary bronchial cells	ALI	Up to one year
BEAS-2B	Immortalized cell line	Submerged/ALI	
16HBE140o	Immortalized cell line	Submerged/ALI	
NCI-H292	Tumoral cell line	Submerged	
BCi NS1	Immortalized cell line	ALI	Up to 28 days
Calu-3	Tumoral cell line	Submerged/ALI	Up to 28 days
A549	Tumoral cell line	Submerged/ALI	--
NCI-H441	Tumoral cell line	Submerged/ALI	Up to 30 days
hAELVI	Immortalized cell line	Submerged/ALI	Up to 30 days

Fully differentiated epithelia are also commercialized by several biotechnology companies. The Epithelix Company commercializes fully differentiated epithelium cultures of the upper airway (MucilAir^{TM}) and small airway (SmallAir^{TM}). In addition, MatTek Company recently commercializes a model of the air-blood barrier (EpiAlveolar^{TM}). These companies perform quality controls, which make the cultures ready to use. However, the limitations of primary cultures can be the lack of availability of human tissue, the limited number of isolated cells, a reduced lifespan and donor variability.

c) Co-cultures

To cover the cellular complexity of the lung, co-culture models are used to mimic the interactions between different cell types in the lung. The airway mucosa is a multi-cellular tissue that includes epithelial, endothelial and leucocyte cells *in vivo*. Co-cultures systems have been developed using different human cell lines. A reconstruction of the air-blood barrier of the respiratory tract was developed using a triple co-culture to study particle uptake by Rothen-Rutishauser et al (Figure 8). A549 cells were grown on inserts with human blood monocyte-derived macrophages and dendritic cells in the apical and basal compartment respectively (B. M. Rothen-Rutishauser, Kiama, and Gehr 2005).

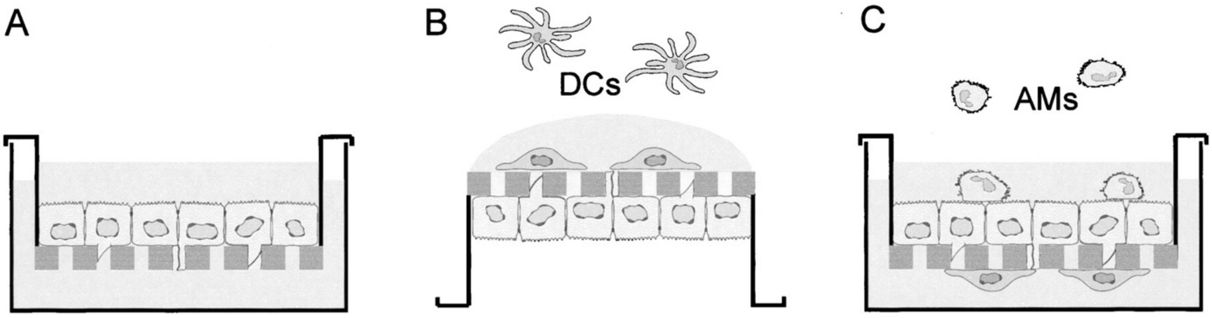

Figure 8: Workflow to setup triple co-culture model.

(a) A549 cells were seeded and grown for 7 days in the apical size of the insert to establish the epithelial barrier. Human peripheral blood monocytes were differentiated into dendritic cells (DCs) or airway macrophage (AMs). (b) Differentiated DCs were added for 2h to the basal side of an inverted inserts (with A549 barrier). (c) Differentiated AMs were added for 2h to the apical side of the insert. Nonadherent DCs or AMs cells were removed during washing. From(B. M. Rothen-Rutishauser, Kiama, and Gehr 2005).

Klein *et al.* (2013) developed another alveolar system consisting of 4 different human cell lines to investigate particle toxicity (Figure 9). They used an endothelial cell line (EA.hy 926) that was seeded in the basolateral side of the inserts. The A549 epithelial cells were seeded on the apical side. Finally, THP-1 macrophages and mast cells (HMC-1) were seeded in the apical side of the insert and adhered to the epithelium (S. G. Klein et al. 2013).

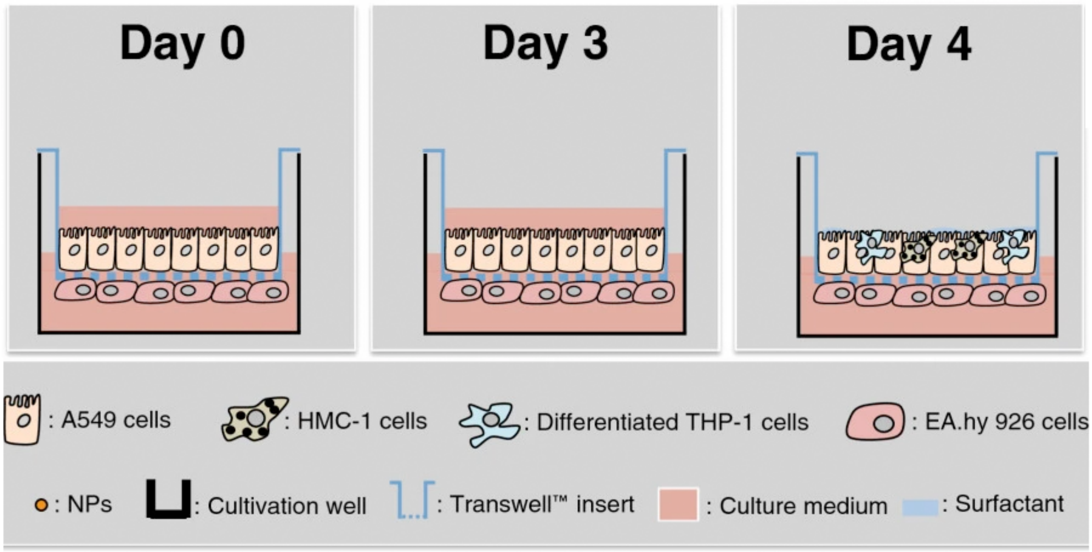

Figure 9: Workflow to setup a co-culture system with 4 cell types.

At day 0 endothelial EA.hy926 cells were seeded in the basolateral side of the insert and A549 epithelial cells were seeded in the apical side of the insert. Cells were kept in culture for 3 days allowing the formation of an epithelial barrier. At day 4, THP-1 macrophages and HMC-1 cells were seeded in the apical side of the. Then the culture was switched to ALI conditions. From (S. G. Klein et al. 2013).

A similar effort has been done to develop co-cultures with bronchial epithelial cells and leucocytes cells. Recently, He *et al*. (2021) has optimized ALI co-cultures with macrophages to estimate the hazard of exposure to an aerosol of lipopolysaccharide (LPS). They tested 4 bronchial epithelial cell lines (Calu-3, 16HBE, NCI-H292 and BEAS-2B) to establish an epithelium at ALI for a long period. Among the bronchial cell lines, only Calu-3 was able to retain a monolayer structure over long periods at ALI. Calu-3 was used to develop co-cultures with THP-1 derived macrophages or human monocyte-derived macrophages, which were viable for up to 6 days. After 6 days, an increase in the number of apoptotic cells was observed (He et al. 2021).

The primary cultures have also been used to develop primary human co-cultures model for the airway barrier. Yonker *et al*. developed a co-culture model using the primary airway basal cells to explore neutrophil transepithelial migration (Yonker et al. 2017). Contrary to conventional cultures, the authors developed the airway barrier in an inverse insert creating the air-liquid interphase in the basal compartments. This strategy allowed the study of neutrophil migration from the apical compartment (submerged) to the epithelial barrier. Additionally, Epithelix sells primary co-cultures of upper and small epithelial cells co-cultured with airway fibroblast (MucilAir^{TM}-HF and SmallAir^{TM}-HF). In these cultures, the two cell types are separated, with the epithelial cells in the apical part and the fibroblast in the basal part of the insert (Figure 10a). MatTek has developed a co-culture of alveolar tissues with both primary alveolar epithelial and fibroblast cells in the apical part, and pulmonary endothelial cells in the basal part of the insert (Figure 10b).

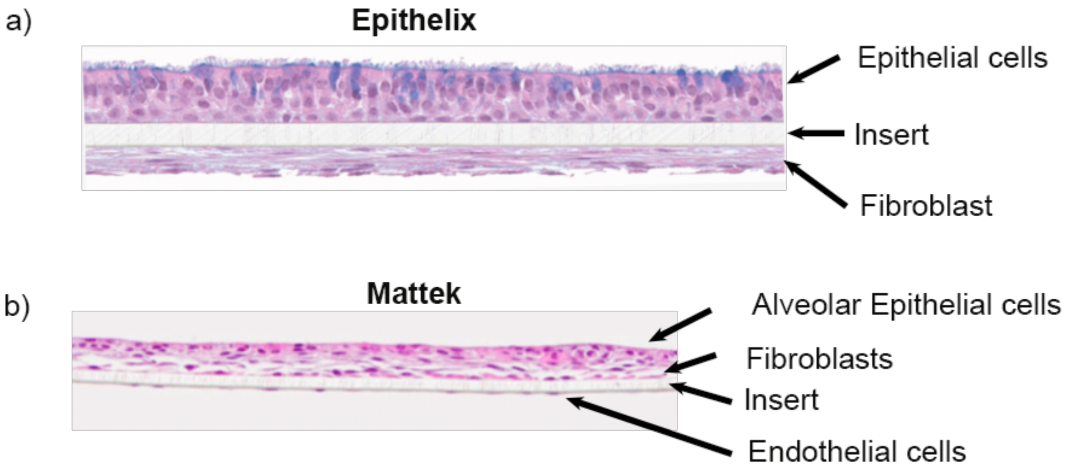

Figure 10: Commercial primary co-cultures of the upper and alveolar airways.
(a) Human upper bronchial epithelial barrier co-cultured with human fibroblast on inserts. (b) Human alveolar barrier co-cultured with fibroblast (in the apical part) and human endothelial cells in the basal part of the insert. (Images from Epithelix and MatTek websites).

The more complex *in vitro* co-culture systems represent a valuable tool to study pulmonary processes and to further evaluate the lung toxicity of NPs. However, differences in culture medium, cell growth rates and cell viability in the cultures, limit their use to short-term exposures.

1.2-2 Exposure system for inhalation toxicology

For *in vitro* inhalation toxicology studies, in addition to have the most relevant culture model, another challenge is to reproduce the exposure to xenobiotics. The lung is exposed to pollutants through their inhalation either as a gas or as an aerosol (liquid or solid particles in suspension in the air). In most of the studies done in submerged cultures, the tested compound is directly added by dilution in the culture medium. The medium may alter the properties of the toxic compound by interaction and binding with medium components such as proteins, thereby modulating the cell response (Gminski, Tang, and Mersch-Sundermann 2010; Dwivedi et al. 2018). It is well known that the serum usually used in culture medium to promote cell growth can reduce the toxicity of some chemicals. To prevent this effect, serum is frequently removed from the culture medium during the treatment period. With the development of cultures at ALI, it has become possible to expose cells to gas or aerosols directly. Specific devices for the exposure of cells at ALI has been developed:

- A vapor exposure system allows the cytotoxicity study of volatile organic chemicals. Dwivedi *et al.* established an exposure chamber system to expose primary bronchial epithelial cells at ALI to aldehydes vapors. The aldehyde concentration in the chamber was monitored during the exposure time by gas chromatography. (Dwivedi et al. 2018).
- A gas/aerosol exposure system allows the exposure of cells cultured at ALI to liquid aerosols clouds. These aerosols can be obtained from dry powders or liquid suspensions. It can also be applied to particle deposition from liquid aerosols. These systems can be coupled to an electrical deposition device to enhance particle deposition.

Advanced aerosol exposure systems are now commercially available, allowing static or dynamic exposure of cells at ALI. These systems can be used either for individual cultures or for several cultures at the same time. The most commonly used systems come from VITROCELL (Mülhopt et al. 2016) and CULTEX (Aufderheide et al. 2017) (Figure 11).

Figure 11: Two of the commercially available exposure systems from Vitrocell and Cultex. The VITROCELL® alpha 12 cloud is used for liquid aerosol. The CULTEX® EDD is used for liquid aerosol and is coupled to an electrical deposition device to enhance particle deposition.

These systems expose the cells inside a cloud. The cloud system nebulizes solutions or particle suspensions to create an aerosol containing the chemicals or particles of interest. The completed exposure cycle takes between 15-60 min. In addition, Vitrocell has developed a dynamic dilution system with a continuous flow exposure. This system is equipped with an entry and an exit nozzle for the aerosol stream, so that the dose and the concentration of the particles in the cloud can be controlled.

Other noncommercial exposure systems, such as XposeALI, have been developed, but they are less accessible to users (Gerde et al. 2004). The advantage of the XposeALI system is that it can create a dry aerosol of particles. This system allows the generation of small batches of dry NP powder using high pressure (Ji et al. 2017). Recently, Vitrocell has also developed a system that implemented dry aerosolized particles.

The aerosol exposure systems are promising to study the toxicity of NPs on the lung, because they reproduce the conditions of lung exposure more realistically. However, a crucial point is to ensure the homogenous distribution of particles over the whole cell surface. Deposition rates exhibit high variation, which is influenced by the nebulization process and the particle properties. The companies have implemented different strategies to quantify the final deposition of particles on the cultures. In the case of Vitrocell, the system measures the dosimetry using a Quartz crystal microbalance, which can measure the deposited mass at a resolution of 10 ng/cm^2. Besides, the formation of droplets and particles agglomeration may also limit the use of these systems due to changes of NP physicochemical properties.

Due to the current technical limitations of the exposure systems and their high cost, conventional protocols developed for the exposure of submerged cultures are employed. In particle toxicology and mainly for NP, the exposure to a liquid particle suspension also shows some limitations. First, the deposited dose depends on the sedimentation of the NPs in solution, so that it may be difficult to evaluate the dose delivered to cells. Models have been developed to determine this delivered dose according to the particle characteristics and the culture medium used, such as the *In vitro* Sedimentation, Diffusion and Dosimetry (ISSD) model (Hinderliter et al. 2010). Second, the dispersion of NMs is done in culture media, which contains a large number of exogenous proteins and biomolecules that can adsorb on NPs to form a biomolecular corona. This corona gives a new identity to NPs and may change its interaction and effect on the cells (Monopoli et al. 2013; Panas et al. 2013). According to the culture medium used, the composition of the corona can profoundly differ, inducing different cellular effects. Culture media without Fetal Bovine Serum (FBS) supplementation can be used during NP exposure to limit this effect. As an alternative to cultures media, salted based buffer, such as PBS or Hanks Balanced Salt Solution (HBSS), can be used for short exposure times. However, in inserts, cells can be exposure to NPs in the apical side for longer periods of time in these buffers, because the nutritional feeding of the cells can be done in the basal compartment (e.g., with 10% FBS supplementation in the culture medium). Lastly, a large effort has been done to compare the different exposure methods and to evaluate their effects on NP toxicity and uptake. Loret *et al.* 2016 compared ALI and submerged exposure of A549 cells to TiO_2 and CeO_2 NPs. They observed significant adverse effects in cultures exposed at ALI to aerosols compared to exposure in submerged conditions (Loret et al. 2016). These differences may also come from the submerged exposure method (Figure 12), where ALI cultures were immersed in media with NPs for long periods to allow NP deposition. An alternative is to prepare a more concentrated NP suspension that can be deposited at ALI in the form of small droplets (a few µL) without losing NPs during the removal of the added buffer or medium. The application of a small volume of liquid will not disturb cultures at ALI and will allow more accurate deposition as no NP will be lost during medium removal.

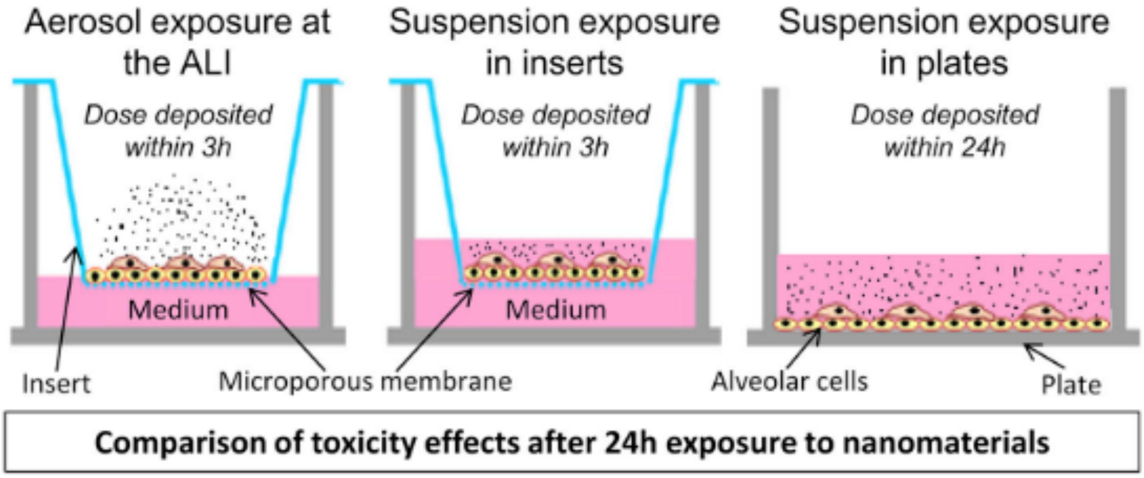

Figure 12:In vitro comparison of cell exposure in submerged conditions or at ALI in inserts or plates.

Alveolar A549 cells were grown in inserts or plates and exposed to an aerosol at ALI (left) or in submerged conditions to NP suspension in a large volume (middle and right).(From (Loret et al. 2016)

1.3 NMs represent a novel hazard for the lung

Exposure to inhaled NPs remains an ongoing health concern. Occupational or accidental exposure may occur. Therefore, the assessment of NP lung toxicity is required.

1.3-1 Importance and interest of NMs

Many different NPs exist, depending on their chemistry, morphology, size and physical chemical properties. The nanoscale size of NPs gives these nanomaterials unique properties compared to microscale and bulk counterparts of same composition (Singh and Nalwa 2007). The new physicochemical properties of NPs compared to bulk materials have opened tremendous opportunities for a wide range of applications in cosmetics, electronics, energy industry, biotechnology, agriculture, pharmaceuticals and medicine among others. Particularly, silver nanoparticles (AgNPs) exhibit strong bactericidal properties, making them interesting materials for a wide range of applications, from washing powder to biomedical applications. There has been an increased interest during the last years for the use of AgNPs in several areas:

- Biomedical applications of AgNPs have been investigated for the development of targeted drug delivery systems (Anandhakumar, Mahalakshmi, and Raichur 2012), tumour-specific therapies, vaccines adjuvant, bone prostheses, and surgical instruments. The antimicrobial properties of AgNPs have favored their use to prevent biofilm formation on medical devices such as catheters (Samuel and Guggenbichler 2004) and to prevent wound contamination, for example in wound dressings (Jiong Chen et al. 2006). Additionally, it was reported that AgNPs enhance the immune response to the influenza using mucosal vaccines *in vivo*, which promotes the production of mucosal antibodies against influenza virus (Sanchez-Guzman et al. 2019). Franco-Molina *et al.* showed a dose-dependent cytotoxic effect of AgNPs that induce the apoptosis of MCF-7 breast cancer cells, without any viability loss in the peripheral blood mononuclear cells (Franco-Molina et al. 2010).
- The industry has taken advantage of the antimicrobial properties of AgNPs, which can be used for their slow release of antimicrobial silver ions. In the food industry, AgNP additives are used to prevent bacterial growth in foods and food packaging (Echegoyen and Nerín 2013). In cosmetic, AgNPs are added to deodorant (Raj et al. 2012).
- In agriculture, commercially available nano-silver based products are available for fertilization, and as fungicides and bug repellent (Servin et al. 2015).

1.3-2 Silver nanoparticles

Silver nanoparticles possess unique physicochemical and biological properties. They have a high electrical and thermal conductivity, catalytic activity, and antibacterial, antifungal, antiviral properties. The Nanotechnology Consumer Products Inventory (2013) listed 1814 consumer products containing nanomaterials. Among these, metal nanoparticles are the most used (Figure 13a), and AgNPs are the most frequently used nanomaterials. 435 products containing AgNPs were recorded on the global market in 2015 (Figure 13b), representing 24% of the total number of commercial products containing NMs (Vance et al. 2015).

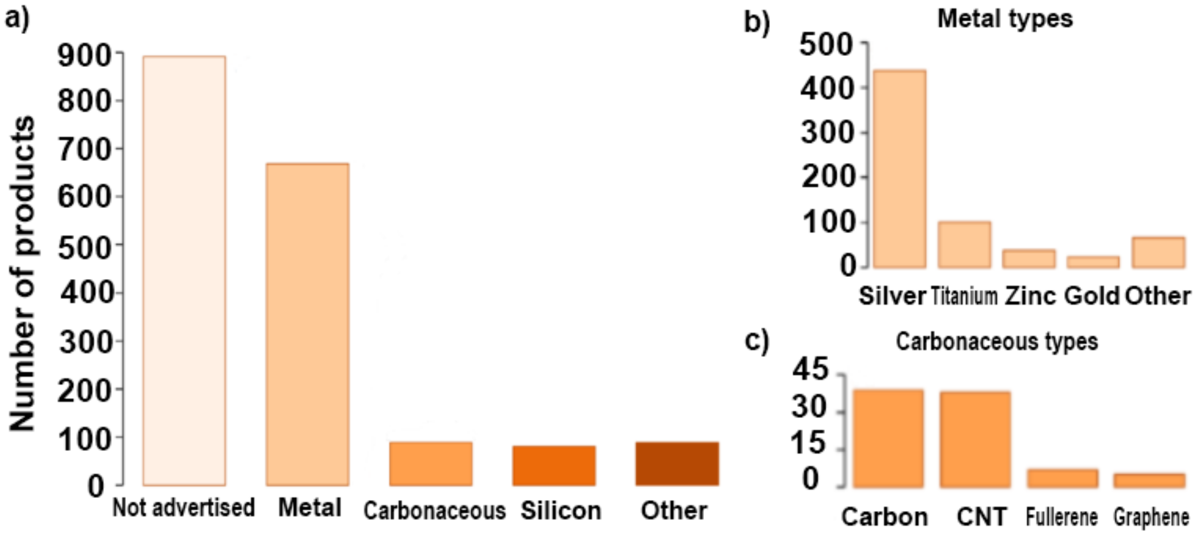

Figure 13: Number of commercial products containing nanomaterials listed by the Consumer Products Inventory (CPI) in 2014.

(a) Nanomaterial chemistry. (b) Elemental composition of metal nanomaterials. (c) Different types of carbonaceous nanomaterials. CNT: carbon nanotubes.

As described above, the use of silver NPs in commercial products increases the risk of exposure by inhalation, ingestion or dermal contact. Thus, AgNPs could present a potential risk to human health because of their known cell toxicity. Their biological and environmental impact must be investigated to minimize a potential detrimental effect of AgNPs.

1.3-3 Lung toxicity of AgNPs

The toxic potential of inhaled NPs is closely related to their ability to penetrate the respiratory tree, which depends on their size (Figure 14). NPs smaller than 100 nm in diameter can reach the bronchi and the alveoli. After deposition, NPs can induce toxicity in two ways. They can locally induce cytotoxicity at the different levels of the airway or they can be translocated and induce systemic effects.

a) Determination of the effective dose deposited in the airways following NP inhalation

Based on mathematical models, the deposition of NPs have been predicted in the respiratory tract (Oberdörster, 2005). This model applies to single particles and not to aggregates. 90% of inhaled particles of 1 µm in diameter are deposited in the nasopharyngeal compartment, 10% in the trachea-bronchial region, and essentially none in the alveolar region. Nanoparticles of 5 nm in diameter will be deposited in equal amounts (30%) in all three regions. Nanoparticles of 20 nm in diameter have the highest deposition efficiency in the alveolar region (50%), whereas in tracheobronchial and nasopharyngeal regions these nanoparticles will deposits with a 15% efficiency only (Figure 14). Moreover, NMs can dissolve or aggregate in biological media. These effects influence their deposition on cells. When studying chemical compounds, it is usually sufficient to know the nominal exposure dose, but this is no longer sufficient for NPs. It is necessary to know the effective dose, that is the amount of NPs that will make contact with the cells, and induce a biological response. Specific methodologies are needed to determine the effective dose for a given NP based on its physicochemical properties in the biological medium of interest.

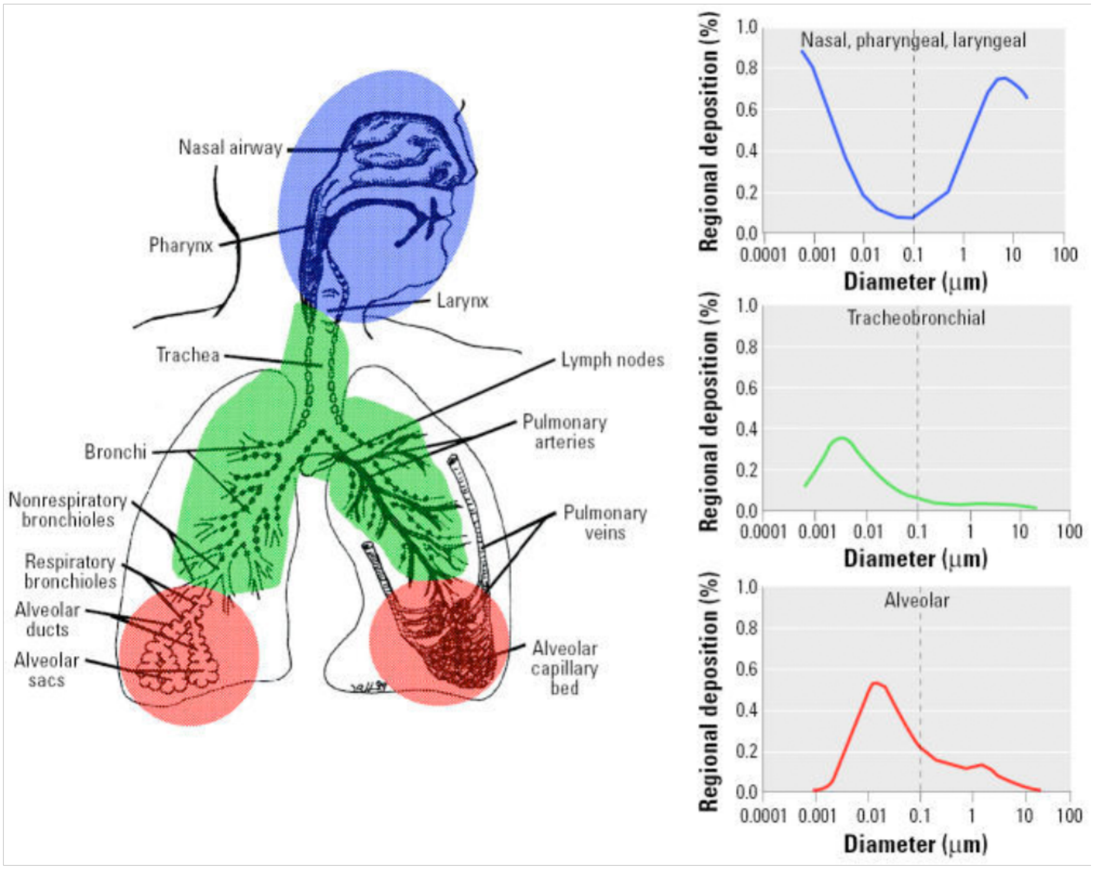

Figure 14: Predicted fractional deposition of inhaled particles in the different regions of the airways.

Inhaled particles of 1 µm in diameter are mainly deposited in the nasopharyngeal region (blue). However, particles with a diameter of 10-100 nm are mostly deposited in the tracheobronchial region (green) and alveolar region (red). From (Oberdörster, 2005).

b) Factors influencing NP toxicity.

The toxicity of NPs can depend on their surface chemistry, size, shape, functionalization and crystallinity (Figure 15). Several studies have investigated the toxic effect of AgNPs on human cells and mammalian organs, especially for the respiratory system. There is a lack of consensus and a high variability in toxicity have been reported. The variability in AgNP synthesis led to different conclusions on the effect of size on AgNP toxicity. Their toxicity also depends on the doses and the exposure.

- **Shape:** It has been shown that different shapes of the same nanomaterial showed different stability *in vivo*. In rodents, filomicelles persisted in circulation up to one week whereas spherical NPs were cleared within two days (Geng et al. 2007).
- **Size:** the size influences the interaction and internalization of nanoparticles. Different mechanism of internalization were observed for microspheres 50-1000 nm in diameter, with no uptake observed for 1000 nm particles (Rejman et al. 2004).
- **Surface charge and chemistry:** The surface charge and the chemistry of nanoparticles also affect the interaction and internalization by the cells. Poly(lactic acid-co-glycolic acid) (PLGA) NPs coated with CS (positively charged NPs) or with PF68 (negatively charged NPs) exhibited differences in internalization by Calu-3 cells. PF68 conferred a hydrophilic surface minimizing hydrophobic entrapment in the mucus (Mura et al. 2011; S. K. Lai, Wang, and Hanes 2009).

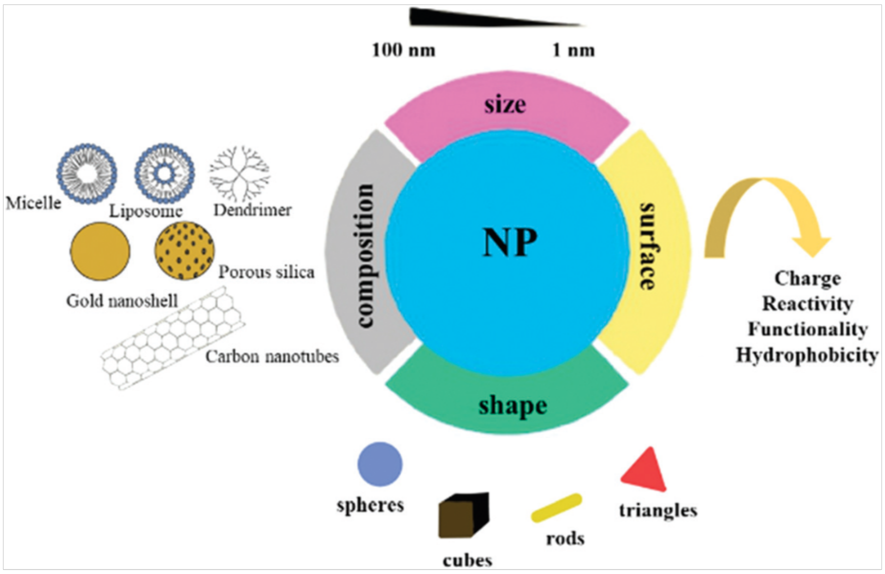

Figure 15: Nanoparticle properties that can influence their toxicity.

The size, surface, shape and composition give unique properties to the NPs, and these characteristics can drive their interaction with the proteins and cells. From (Garcés et al. 2021).

c) Inhalation toxicity of AgNPs

One of the cytotoxic effects of AgNPs comes from their dissolution in the biological medium and the release of toxic silver ions. The dissolution is usually larger for smaller particles. Gliga *et al.* exposed BEAS-2B cells to AgNPs of different sizes for 24 h, and observed a cytotoxic effect only for the smallest NPs (10 nm). The authors found that these NPs released more Ag^+ compared to the larger particles. Besides, the released fraction of Ag ions in the cell medium did not induce toxicity, thus implying that the intracellular Ag ions were responsible for the observed toxicity (Gliga et al. 2014).

To investigate the toxicity of AgNPs at the organ level, and to determine their effects on the respiratory function and inflammation, a wide range of *in vivo* studies using different types of AgNPs have been performed. Botelho *et al.* exposed mice to 15 nm citrate coated AgNPs at low (0.05 µg/g of mouse) or high (5 µg/g of mouse) dose for 1, 3 or 7 days. They reported an increase in the inflammatory markers (Interleukin (IL)-1β, IL-6, Chemokine ligand 2 (CCL2) and IL-10) and the recruitment of immune cells (lymphocytes and macrophages) after 3 days only for the higher dose. After 7 days, the inflammation was no longer detected, but tissue stiffness and resistance significantly decreased, and the surfactant protein D concentration increased. The data demonstrated that AgNP altered the lung response at certain doses (Botelho et al. 2018). Similar results were observed by other authors after one instillation in rats of AgNPs of different size (20 and 110 nm), coating (citrate or Polyvinylpyrrolidone (PVP)), and for different doses (0.5-1 µg/g of rats). In general, an increase in inflammation was observed after instillation, which triggered the recruitment of immune cells such as neutrophils, monocytes and lymphocytes. Significant inflammation was observed with the higher doses only. No significant differences were observed between the different coatings. The authors concluded that 20 nm AgNP produced a strong inflammatory and cytotoxic response after instillation, whereas larger NPs (110 nm) would induce changes in the lung after longer periods (Silva et al. 2015).

As we showed above, sporadic AgNPs inhalation induced inflammation, which is normally resolved in a relatively short period. However, one of the major problems concerning the uses of AgNP is the potential repeated exposure to these NPs. Several *in vivo* studies have investigated the toxicological effects of inhaled AgNPs following repeated exposure. Animals were exposed to AgNPs by inhalation or instillation. Inhalation can best predict AgNP toxicity because it takes into account the different deposition rates of NPs in the different regions of the airways, whereas NPs are directly deposited into the trachea in one bolus by instillation.

Inhalation thus covers the whole airway system. The inhalation experiments of repeated exposure to AgNPs simulated occupational exposure. Jo *et al.* exposed rats to different concentrations of AgNP (0-116 µg/cm^3), 6 h per day, 5 days per week, during 4 weeks. The authors reported a decrease in alveolar macrophages, and the recruitment of neutrophils and monocytes after day 1. Additionally, the authors measured the Ag content in the lung to estimate the clearance kinetics, and suggested it could be the combination of a "fast clearance" (possibly by dissolution of AgNP) and a "slow clearance" (by mucociliary escalator or translocation to the lymphatic system or to the blood of no dissolved NPs) (Jo et al. 2020). Braakhuis *et al.* investigated the effect of different inhalation time per day (45 min, 90 min, 3 h or 6 h) during 4 days, in rats. The authors reported an increase in neutrophils and monocytes 24 h after the first inhalation, as well as an increase in pro-inflammatory cytokines (IL-1β and Tumor necrosis factor (TNF-α) and chemokines (Monocyte chemoattractant protein-1 (MCP-1) and RANTES) in the bronchoalveolar lavage (Braakhuis et al. 2016).

In addition, all the studies highlighted the important role of the innate immune system, which constitutes the first line of defence against inhaled particles and pathogens. The innate immune system is formed in part by phagocytic cells. In the lung, alveolar macrophages internalize inhaled AgNPs to clear the alveolar space. Following the deposition of a large amount of AgNPs, when the local phagocytic defence is overwhelmed, a cascade of recruitment is triggered by the secretion of cytokines and chemokines. In addition, if NPs induce epithelial cell injury and an increase in oxidative stress and inflammation, it also induces the recruitment of neutrophils and lymphocytes to the damaged area (Figure 16).

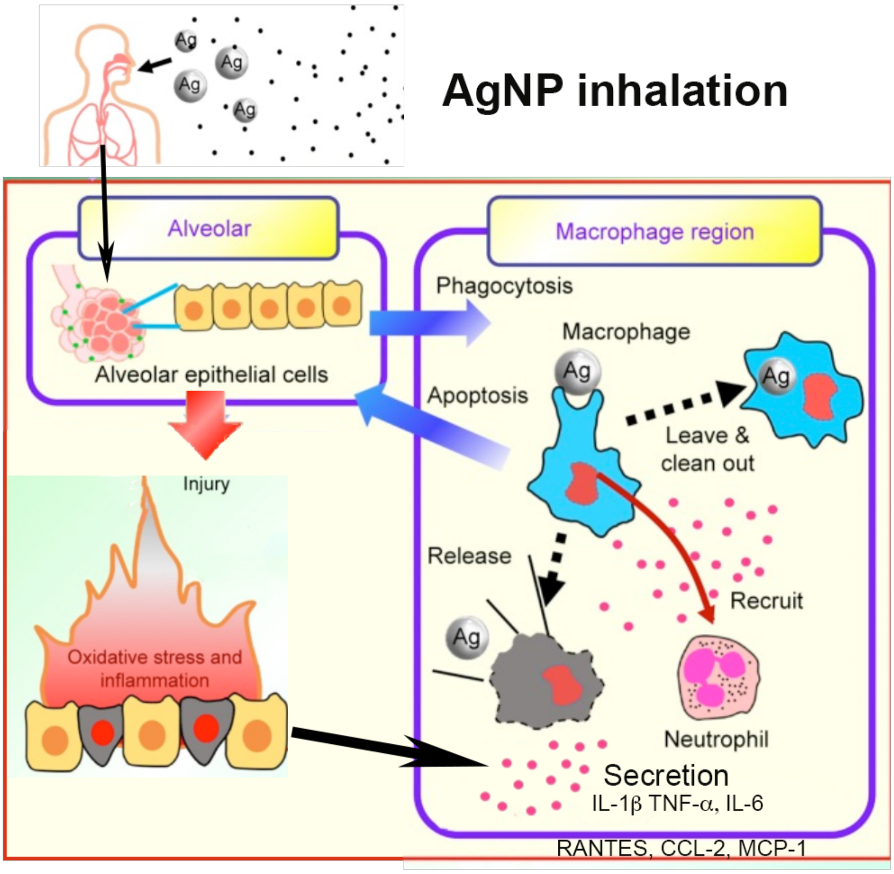

Figure 16: Schematic showing the mechanism of the inflammatory response following AgNP inhalation.

After inhalation, AgNP can arrive at the bronchial or alveolar region. In the alveolar region, the alveolar macrophages phagocyte the NPs to clean out the alveolar space. The activation of these cells induces the secretion of pro-inflammatory cytokines and chemokines, which promote the recruitment of other cell types such as neutrophils. Long NPs exposure derivate in epithelial injury-causing oxidative stress and inflammation. Adapted from (Yang et al. 2019)

1.3-4 Mechanisms of toxicity

In addition to lung inflammation and the activation of the oxidative stress response by AgNPs, damage to specific cells and cellular structures is also actively investigated to identify the mechanisms of toxicity of AgNPs. Acute exposure to AgNPs leads to apoptotic and/or necrotic cell death, characterized by morphological changes, cell membrane permeabilization and cell growth arrest (Wang, Xia, and Liu 2015). The AgNP toxicity can be attributed to several mechanisms including the release Ag ions, AgNP internalization, membrane damage, among others. These effects are associated with the generation of reactive oxygen species (ROS), the disruption of the energy metabolism or enzymatic activities, and gene regulation.

a) ROS generation and oxidative stress

One of the prominent mechanisms of AgNP toxicity is the induction of oxidative stress. *In vivo* and *in vitro* studies have reported an increase in ROS production and the activation of anti-oxidant responses. Different studies reported an accumulation of intracellular ROS in A549 cells after AgNP exposure (Chairuangkitti et al. 2013; Bobyk et al. 2021). High levels of ROS trigger anti-oxidant response. They can also lead to lipid peroxidation, mitochondrial swelling, DNA lesion and lysosomal leakage. Interestingly, Bobyk *et al.* identified oxidative damage to DNA after acute exposure to AgNPs, but no DNA damage after repeated exposure. However, the cell cycle was arrested after repeated exposure only. These results suggest that lower concentrations of AgNPs did not induce DNA damage or that the cell was able to repair DNA during the cell cycle arrest (Bobyk et al. 2021).

b) Disruption of energy homeostasis

AgNP exposure tends to disturb the cellular redox homeostasis. Alteration in respiration and membrane potential was observed in rat liver mitochondria for lethal doses of AgNPs. Teodoro *et al.* reported an impairment of mitochondrial functions due to alteration in the mitochondrial membrane permeability (Teodoro et al. 2011). Reduction in the ATP production led to cell cycle arrest, then to cell death.

In contrast, subtoxic doses of AgNPs could interfere with cellular energy balance, altering cellular metabolism, gene and protein expression, without ROS production or cell death. Chen *et al.* observed a reprogramming of the energy metabolism in HEK293T cells for sublethal concentrations of AgNPs. The cells shift from oxidative phosphorylation-based aerobic metabolism to anaerobic glycolysis to satisfy the cell energy demand (Y. Chen et al. 2014).

Microarray analysis highlighted some molecular and cellular mechanisms involved in the toxicity of AgNPs on epithelial intestinal cells. Böhmert *et al.* observed morphological changes and oxidative stress in Caco-2 cells grown on inserts after exposure to AgNPs. The authors did not observe the induction of apoptosis, instead cells underwent necrosis, which can trigger inflammation. The morphological changes were reflected by the downregulation of tight and adherent junction (tight-junction protein-3, claudin-3 and occludin) genes as well as cell-cell and cell-matrix proteins (actin and tubulin) (Böhmert et al. 2015). Additionally, silver exposure increases the oxidative stress. It participated in the induction of the transcriptional factors like nuclear factor kappa-light-chain-enhancer of activated B cells (NFkB), Nrf2 and the activator protein-1 (AP-1).

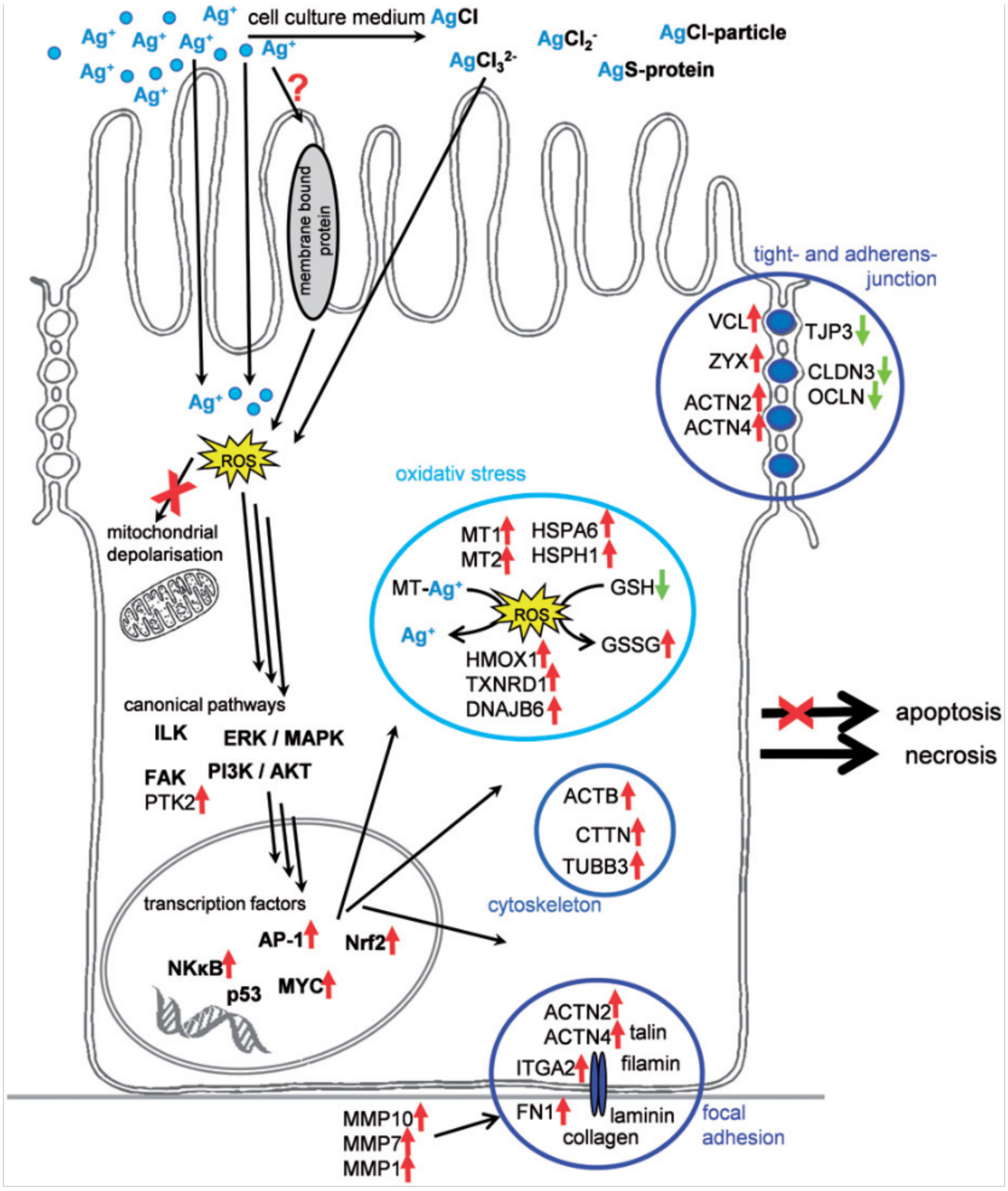

Figure 17: Overview of the effect of AgNP on Caco-2 cells.

The arrows represent upregulation (red) or downregulation (green) of the different genes based on the transcriptomic analysis. AgNP exposure affected Caco-2 cells at different levels. i) Increasing the production of ROS, which induces the activation of the anti-oxidants response through the transcription factors (NKkB, Nrf2 and AP-1). Oxidative stress genes (HMOX1, GSSG), and metal detoxification (MT1 and MT2) were upregulated. Cell morphological changes were reflected by up and downregulation of tight- and adherens-juntions (VCL, ZYX, TJP3n CLDN3, OCLN), cytoskeleton (ACTB, CTTN and TUBB3), and focal adhesion (ACTN2, MMP10, MMP7 and MMP1) genes. From (Böhmert et al. 2015)

The upregulation of metallothioneins was also observed after exposure to AgNPs by Böhmert *et al.* Metallothioneins (MTs) are small, cysteine-rich, metal binding proteins which protect cells from metallic stress. MTs have three main functions in the cells i) metal homeostasis, ii) protection against oxidative damage and iii) detoxification of heavy metals. During heavy metal contamination, the MTs exchange a zinc or copper ion for the heavy metal (Hg, Ag, Cd) which affinity for MT is stronger. The exposure of astrocytes to AgNPs led to a strong upregulation of MTs. The cell viability was not compromised, suggesting that MTs might help in silver detoxification as well (Luther et al. 2012).

1.4 Formation of the Biomolecular corona on NMs

In addition to the physico-chemical properties of the NPs, the adsorption of proteins and other biomolecules on NPs can influence their toxicity. This biomolecular corona may modify their interaction with cells and their fate in the organism (Docter et al. 2015).

1.4-1 Adsorption of proteins on NPs

The phenomenon of protein adsorption on surfaces has been known for more than a century. It was described for example in 1962 by L. Vroman who studied the interactions between hydrophobic solid powders and plasma samples (Vroman 1962). Vroman observed the interaction of a protein with the hydrophobic surface, which then became hydrophilic. Interestingly, different results were observed depending on the type of powder and the type of protein, which indicated that the modification of the wettability of the material was driven both by the presence of plasma proteins and by the physico-chemical properties of the powder. During several decades, different studies were performed to investigate the process of protein adsorption on different types of materials and NMs, emphasizing the need of surface coating to avoid protein coating and to retain the native surface properties of the NMs. Biocompatible polymers have been used to reduce the adsorption of plasma proteins on nanoparticles (Gref et al. 2000), for example after injection in the blood, though it cannot totally block protein adsorption to the surface (here to the polymer chains). The term of “protein corona” was first introduced in 2007 by Cedervall *et al.* who described the process of protein corona formation and the effect of protein-NP interaction *in vivo* (Cedervall, Lynch, Lindman, et al. 2007).

The protein corona is currently described as a dynamic multilayered structure formed by proteins adsorbed on the NP surface following contact with the physiological environment and consequent interaction with proteins (Walkey and Chan 2012). This structure has been schematically divided into two parts known as the “soft” and the “hard” protein corona (Figure 18a). Their exact definition differs between authors. The hard corona, which is preserved after NP separation from the biological medium, is formed by proteins strongly adsorbed to the surface and long-lived equilibrium states between biomolecules and NPs. The soft corona is thought of as the ensemble of more weakly bound proteins, which can be lost during the purification process (Monopoli et al. 2012; Docter et al. 2015). The hard and soft corona can both include protein-NP and protein-protein interactions. The structure and composition of the protein corona is in continuous evolution, with tightly bound proteins exchanged slowly (or no exchanged), while low affinity proteins are expected to be more quickly replaced by high affinity proteins (Milani et al. 2012). Besides, some proteins in the corona may themselves promote the interaction of other proteins, such as chaperonins that can recognize and bind to unfolded adsorbed proteins (G. Klein et al. 2016) (Figure 18b).

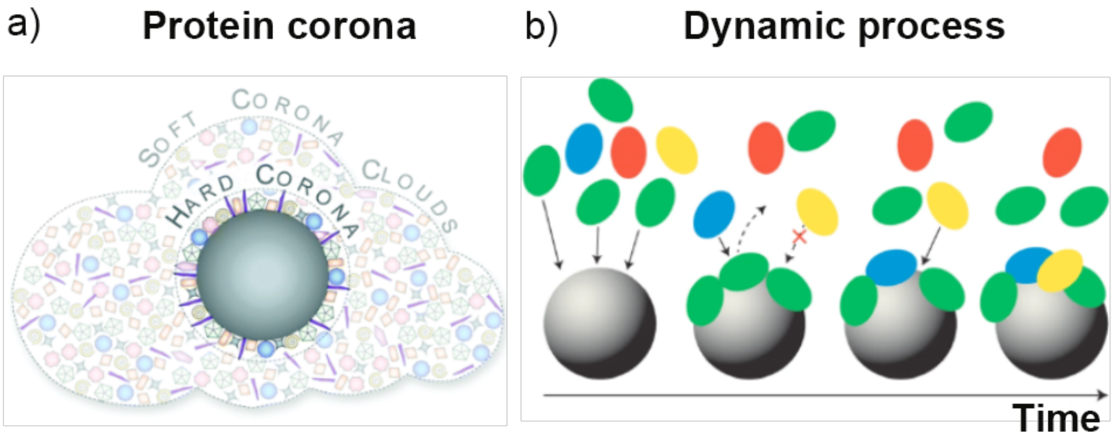

Figure 18: Schematic representation of the protein corona.

(a) Protein corona structures formed by hard corona tightly bound to the NP and the soft corona cloud. (b) Protein corona formation and evolution with time according to the competition model. An initial corona forms by the binding of the most abundant proteins (green). Then the most abundant proteins can be replaced by less abundant proteins which exhibit a higher affinity for the surface (yellow).

The adsorption state can favor or instead limit the aggregation of NPs in solution. It changes the global charge of the NPs and it gives them a biological identity that is distinct from their synthetic identity. Their biological identity determines the physiological response in part by mediating the interaction of the nanomaterial with cells, membranes, and possibly receptors. Uncontrolled nanomaterial-protein interactions can mark a nanomaterial for uptake in off-target cell populations, activate enzymatic cascades and prevent efficient removal from the body (Walkey and Chan 2012).

The protein adsorption depends on several factors, such as the size, shape, surface area and surface charge of the NPs, and the composition of the biological medium.

- **Surface area**: NPs have a larger surface area compared to microparticles due to their small size, which can promote their surface reactivity and nonspecific interactions. Platelet activation was recently shown to depend on the surface area rather than NP size (Zia et al. 2018). Silica and polystyrene NPs of the same size bound different quantity of plasma proteins in the presence of low plasma concentration. By contrast, silica NPs binding capacity was lower in the presence of high concentrations of plasma proteins (Monopoli et al. 2011). The differences in the protein pattern of silica NPs suggest that less abundant proteins whose binding increased at higher plasma concentration, acted as competitive binders and facilitated the desorption of proteins with lower affinity.
- **Shape**: synthesis of NMs with very different shapes (spherical, rod, oval, cubic, triangular, star, needle, cylinder, etc.) has been developed. The binding affinity of human serum albumin was higher for spherical than branched-shaped gold nanoparticles (AuNPs) (Moustaoui et al. 2019). Furthermore, a stronger inhibition of β-galactosidase was observed with pyramid-shape zinc oxide NPs compared to sphere and plate shapes (Cha et al. 2015).
- **Biological fluid**: the NP-protein interactions are mostly driven by non-covalent interactions (ionic interactions, hydrogen bonding, Van der Waals forces and hydrophobic interactions). The biological fluids contain different electrolytes, metabolites, peptides, hormones, lipids, sugars and nucleotides which might deploy different interactions with the surface (Monopoli et al. 2011; Maiorano et al. 2010). AuNPs exhibited different protein coronas when they were incubated in Dulbecco's Modified Eagle Medium (DMEM) or Roswell Park Memorial Institute (RPMI) culture media containing 10% FBS in both cases, highlighting the importance to study protein corona formation on specific fluid. Similarly, the extracellular composition of a biological fluid may change after cell exposure to NPs, triggering the evolution of the protein corona composition (Figure 19). Secretion of metabolites and proteins to the extracellular matrix conditionate the biological fluid, hence new proteins can interact with NPs producing changes in the protein corona. The new protein corona can drive different NP-cell interaction and change the NP aggregation state, resulting in different NP uptake (Albanese et al. 2014).

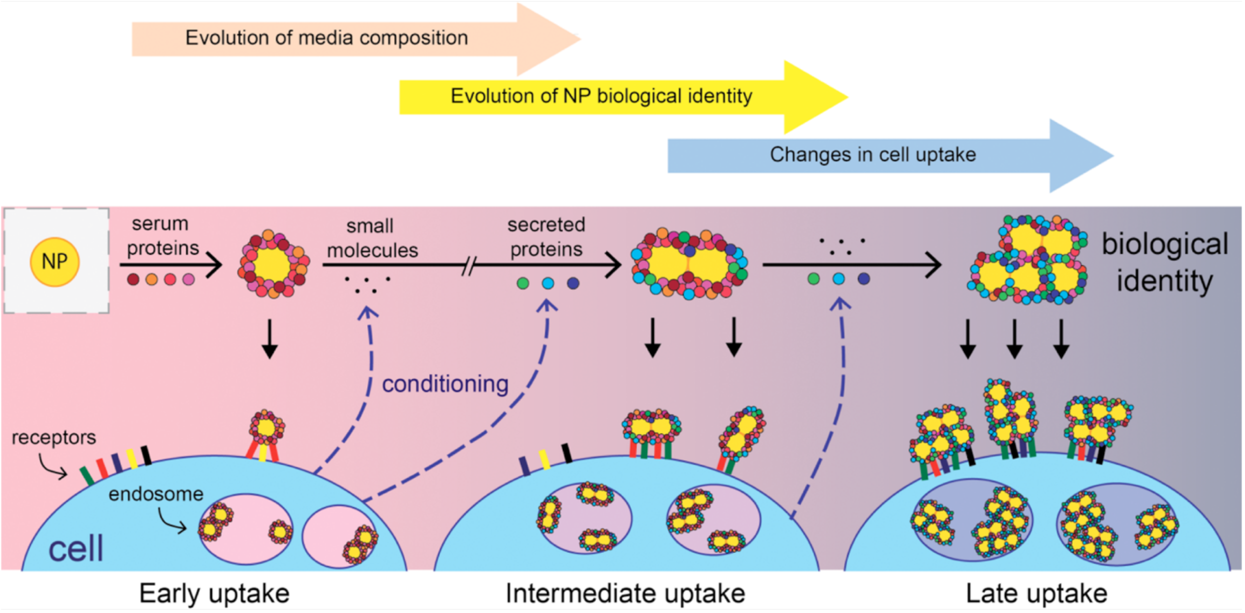

Figure 19: NP evolution in the extracellular environment.

Initial NP exposure created a first protein corona with its biological identity. After NP-cell interaction, cell response led to the secretion of proteins. A new protein corona was formed, and the NP aggregation state was altered. This new biological identity can change NP-cell interaction, for example by increasing NP uptake. From (Albanese et al. 2014)

- **Exposure time**: the protein corona is a dynamic structure, which composition can evolve with time. In most cases, the most abundant proteins are non-specifically adsorbed on the surface of NPs immediately after exposure. These proteins might have low affinity for NPs and can be replaced by less abundant proteins with higher affinity for the surface after a longer exposure time (Baimanov, Cai, and Chen 2019).

1.4-2 Role of the biomolecular corona in NP toxicity

The protein corona can modulate the cellular response to NPs and their toxic effect. It can also induce changes in adsorbed protein structure and activity. It can have an effect on NP internalization. It can trigger the activation of signaling cascades.

- **Structural changes of adsorbed proteins**: the adsorption of proteins on a surface can lead to structural changes of the adsorbed protein, which depends on the type of protein and the type of surface. These changes are biological meaningful, as they can provoke protein function loss. Silica NPs alter hemoglobin secondary structure at biological temperatures, which reduces the oxygen exchange capacities of the protein (Sanchez-Guzman et al. 2020). In addition, conformational changes may trigger protein aggregation and amyloid fiber formation which are known to be more toxic than mature fibrils (Konar, Mathew, and Dasgupta 2019). It can also induce the exposure of hidden epitopes to the immune system. The same protein may exhibit different conformational changes upon binding to different NPs. Human serum albumin (HSA) exhibited a decrease in α-helicity from 68% to 48% after adsorption to AuNPs (Ramezani and Rafii-Tabar 2015). By contrast, citrate-AgNPs failed to induce significant structural changes of HSA (W. Zhang et al. 2015).

- **Modifying cellular uptake**: the presence of different proteins in the corona can promote or limit the internalization of NPs. Imaninezhad *et al.* observed that carbon nanotubes bind to adhesive proteins, like fibronectin present in the culture media, which facilitated NP-cell attachment and internalization (Imaninezhad et al. 2018). Also, AgNPs coated with serum proteins enhanced their uptake and cytotoxicity on embryonic fibroblast. Interestingly, AgNPs coated with an oligo-(ethylene glycol)-alkanothiol to block protein adsorption, reduced serum-corona AgNP uptake, and thus cytotoxicity (Barbalinardo et al. 2018). Opposite effects were observed where the protein corona acts as a shield and reduced the NP uptake by phagocytic cells. The presence of clusterin in the protein corona of silver and silica NPs suppressed their cellular uptake in macrophage-like cells (THP-1) (Aoyama et al. 2016). The authors found that serum- and plasma- protein corona on these NPs significantly reduced the cellular uptake. This effect was stronger with plasma-corona characterized by a higher abundance of clusterin proteins.
- **Cell activation/regulation**: AgNPs regulated development of zebrafish by Octamer-binding transcription factor 4 (Oct-4) expression. *In silico* analysis described a close interaction between Oct-4 transcription factor (involved in the embryo's growth and development) and AgNPs without protein conformational changes (Sarkar et al. 2018). Besides, Verma *et al.* identified a cytotoxic effect of AgNPs, which were synthesized with floral extract, driven by apoptotic factor p53 and the Superoxide dismutase type 1 (SOD-1) enzyme. *In silico* analysis showed an interaction of p53 and SOD1 with residues of Calotropin (from the floral extracts used during NP synthesis) without any binding to AgNPs (Verma et al. 2018).

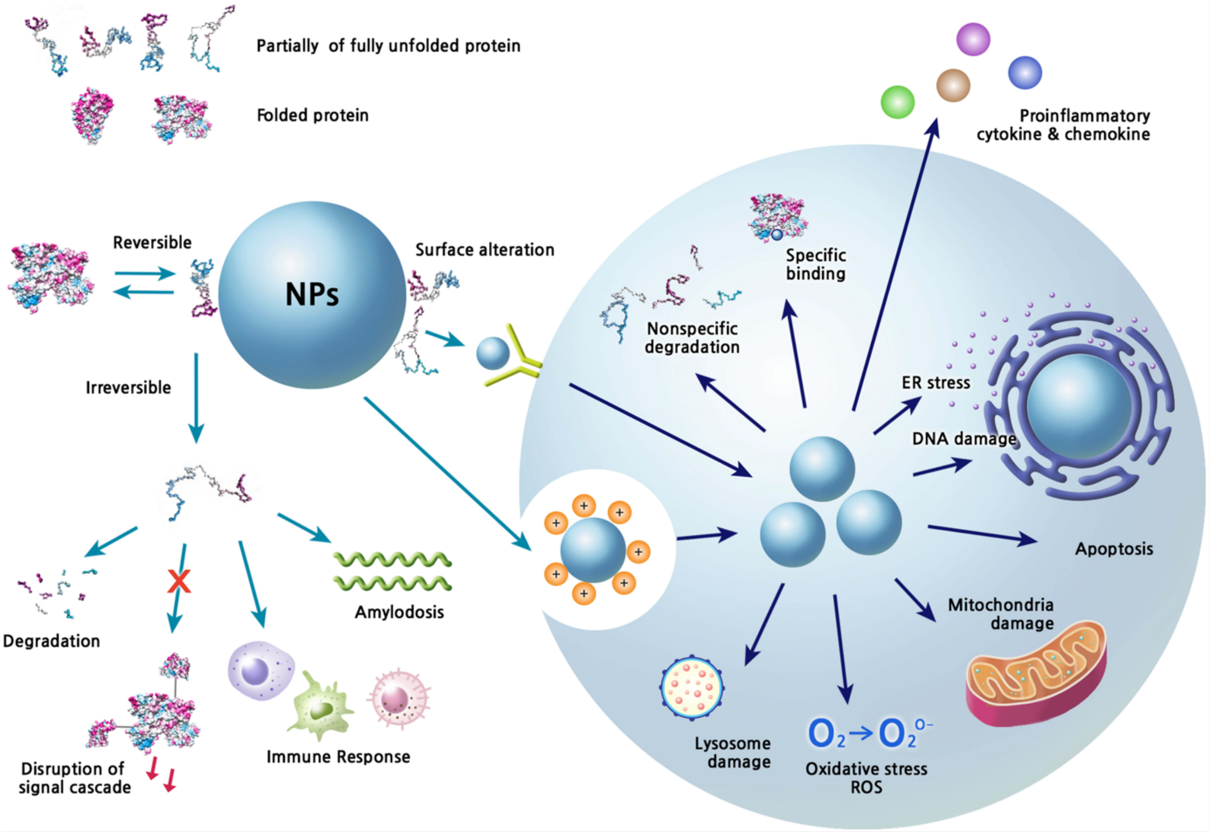

Figure 20: Schematic of the extracellular and intracellular events caused by protein-NP interactions.

The protein-NP interaction can induce changes in the protein structures impairing protein functions. These changes can induce protein degradation, disruption of signal cascade, and immune response activation. Besides, adsorbed protein can interact with membrane receptors and enhance (or shield) the NP uptake, modulating the NP fate and toxic effect (From (Park 2020).

1.4-3 Methodology to study protein corona

A wide range of approaches and techniques has been employed to study the protein corona formation, to determine protein composition, conformational changes, and corona thickness. Importantly, different methodologies were used to isolate NPs with their protein corona from the free proteins of the biological medium.

a) NP isolation

It is important to choose the most appropriate method for the isolation of NPs with their corona from the protein-rich matrix before analysis. The separation step can modify the protein corona. The different methods can produce false positive or false negative results, as a consequence of free protein precipitation or adsorbed protein dissociation during the isolation step. NPs should be isolated without losing bound proteins, while false positive (free proteins) should be omitted. Different methodologies are currently used (Figure 21):

- **Centrifugation**: this is the most common method used for NP separation from the biological medium. This method can lead to false positives if free proteins precipitate at the same time as NPs during the centrifugation steps. False negative results may also occur when adsorbed proteins are lost during the washes or the centrifugation steps. This technique requires an optimization of the protocol for each NP to adjust centrifugation speed and washing cycles (Monopoli et al. 2013).
- **Magnetic separation**: another way to isolate NPs with their corona is to use magnetic forces. The magnetic separation impacts less the protein corona than centrifugation (Bonvin et al. 2017) avoiding false negative results. Its main limitation is that it is restricted to magnetic NPs.
- **Chromatography**: chromatography is less frequently employed due to higher costs, time-consuming aspect and low throughput of samples. This isolation method has a lower impact on the protein corona than centrifugation (Cedervall, Lynch, Lindman, et al. 2007). We can distinguish two main methods, size exclusion chromatography (SEC) and asymmetric flow-field-flow fractionation (A4F). The principle of SEC is that proteins, which are smaller than NPs, interact more with the stationary phase and take more time to pass through the chromatography column. The A4F method can separate analytes in a larger size range. This method is based on a laminar flow that moves the NPs along a porous tube, and the passage through the porous membrane depends on size.

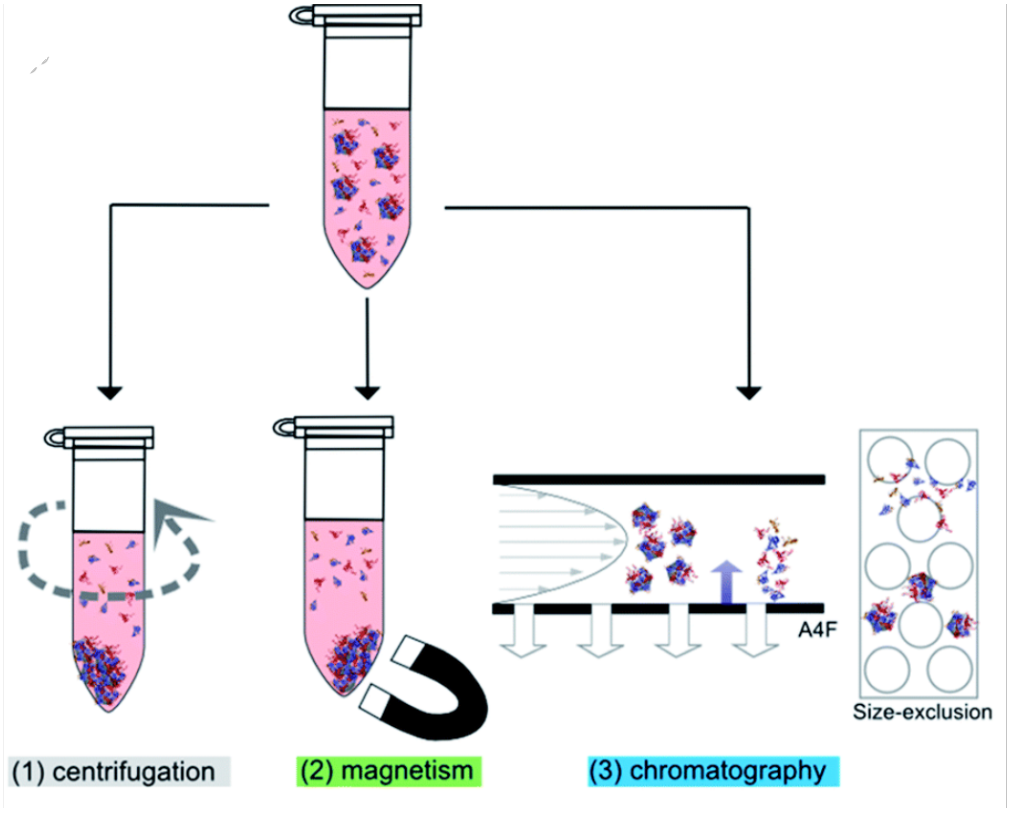

Figure 21: Schematic overview of the different separation methods for NP isolation before the analysis of the protein corona

(1) centrifugation, (2) magnetism separation, (3) chromatography separation by asymmetric flow-field-flow fractionation (A4F) or size exclusion chromatography (SEC). From (Böhmert et al. 2020).

Studies compared the results obtained with the different isolation methods. Pisani *et al.* compared magnetic and centrifugation separation of magnetic silica NPs from the plasma. The authors concluded that the results differ substantially, with different protein abundance in the corona depending on the separation method (C. Pisani et al. 2017). Another study compared the hard corona formed with plasma protein on silica-coated iron oxide NP isolated by either magnetic, centrifugation or size exclusion chromatography. In that case the authors reported similar compositions of the protein corona, independently of the methodology employed (MONOPOLI et al. 2013). Additionally, the type of protein matrix and the type of NPs must be considered when choosing the most appropriate isolation method for the analysis of the protein corona.

b) Protein corona thickness and structure

The structure of protein corona can be evaluated by measuring the increase in NP diameter after incubation with proteins. Several techniques can be used to measure NP size in solution:

- **Dynamic light scattering (DLS)**: DLS can determine changes in the diameter of NPs before and after incubation in a biological fluid. However, in order to obtain reliable results, DLS requires monodisperse population of protein-NP complexes.

- **Differential centrifugal sedimentation (DCS)**: is able to separate NPs based on their density and size. It has been used to determine the thickness of the protein corona on NPs.

c) Protein composition

The composition of the protein corona can be analysed by gel electrophoresis and mass spectrometry.

- SDS-PAGE: One- and two- dimensional gel electrophoresis have been used to separate adsorbed protein according to their molecular weight (one-dimensional) or to their isoelectric point and molecular weight (two-dimensional). This technique provides a first approach to analyse the protein corona. It also provides information on the protein abundance, especially when using 2D gel electrophoresis.

- **Mass spectrometry**: this technique has been used to identify the proteins associated to the NPs. Generally, it can be used after gel electrophoresis separation to analyse specific band or spots. This technique required the enzymatic digestion of the proteins, and the peptide separation by liquid chromatography before the MS injections. Several approaches can be used such as MALDI- MS (Ritz et al. 2015) and LC-MS/MS (Lundqvist et al. 2008; Tenzer et al. 2013). It allows the identification of a larger number of proteins than gel electrophoresis. Qualitative and quantitative analysis can be performed.

d) Protein structure

The changes in protein structure following adsorption on NPs can be investigated with different techniques.

- **Circular dichroism (CD) spectroscopy**: is used to determine the secondary structure of a purified protein (Sanchez-Guzman et al. 2020). This technique provides information on the structural changes resulting from protein adsorption.

- **Nuclear magnetic resonance (NMR) spectroscopy**: provides information about the structure of proteins adsorbed on NPs.

- **Computational simulation**: *in silico* simulation provides information about protein conformation and spatial and temporal resolution to predict protein-NP affinities (Sarkar et al. 2018; Verma et al. 2018) and protein conformation changes (Sanchez-Guzman et al. 2020).

1.4-4 Interaction of nanoparticles with mucus

Inhaled NPs will encounter the mucosal airway epithelium, which is characterized by the presence of a mucus layer. This mucus layer can trap NPs and contribute to their elimination. The interaction of NPs with mucus has gained attention in part due to the increased interest in mucosal administration of drugs, and drug delivery to epithelial surfaces (S. K. Lai, Wang, and Hanes 2009).

The mucus is a viscoelastic hydrogel which impairs the penetration of different NPs. However, liposomes NPs are able to penetrate the mucus layer. In that case, NP size plays an important role in NP penetration in the mucus (Takeuchi, Yamamoto, and Kawashima 2001). In addition to size, the coating of NPs with different polymers can enhance the particle penetration. The hydrophilic and hydrophobic substructure present in polymers such as Polyethylene glycol (PEG) and PLGA can improve particle diffusion by limiting their binding to the mucus (Netsomboon and Bernkop-Schnürch 2016). Mura *et al.* investigated the role of NP surface chemistry and charge on the damage to Calu-3 bronchial epithelial barrier (Mura et al. 2011). The authors exposed Calu-3 cells to PLGA NPs with positive, neutral, and negative surface charge. The negatively charged NPs diffused faster in the mucus layer due to lack of interaction with the mucus mesh. By contrast, positively and neutral NPs were also able to penetrate the mucus layer but with a lower mobility due to enhanced NP interaction with mucus. Furthermore, Fasquelle *et al.* compared the ability of cationic NPs or anionic phospholipid core NPs to interact with mucins and the airway epithelial cells (Fasquelle et al. 2020). The authors showed that the anionic phospholipid core increased NP mobility through a mucin hydrogel by reducing the interaction with mucins.

The surface charge of NPs can improve their penetration in the mucus, facilitating contact with the epithelial barrier. In addition, proteins from the mucus can form a protein corona on NPs, which will in turn affect their penetration in the mucus and their interaction with cells.

Objectives:

The objective of this thesis was to develop a 3D culture model of bronchial epithelium for nanotoxicological studies in acute and sub-chronic conditions. This 3D model could reproduce some of the morphological and functional features of the tissue, including the production of mucus. It allowed us to characterize the NP-protein interaction that takes place after NP inhalation in the airways, which was one of our objectives. In this work, we used Calu-3 cells to establish the epithelial barrier, and silver nanoparticles (AgNPs) as model NPs.

The results of this work are presented in 3 parts (corresponding to chapters 3, 4, and 5) along with a specific discussion and conclusion for each chapter. The objectives of each section are briefly described below:

1- Establishment of a long-term Calu-3 culture model for nanotoxicology. The model must be formed on inserts with a large porosity to allow NP translocation studies. Moreover, reduced fetal bovine serum supplementation was tested to reduce the amount of exogenous proteins, which can interact with NPs during or after exposure.
2- Morphological and functional validation of our Calu-3 model compared to MucilAir™: a commercially available 3D model of the human upper airway epithelium developed with primary cells. The possibility to maintain a tight epithelial barrier for several weeks, the secretion of proteins, and the composition of the secretome, including mucus, were characterized. The evolution of the secretome composition with time was analysed by quantitative mass spectrometry for 18 days in the Calu-3 and MucilAir models.
3- Characterization of the protein corona formed on AgNPs following incubation in the collected secretome or direct exposure to Calu-3 cells. Different methodologies were tested and adapted to NP isolation from the secretome for the analysis of the protein corona. Finally, the role of the protein corona in the cellular interactions of NPs with macrophages was investigated.

Part of this work has already been published. However, we chose not to present this thesis as a collection of articles to better explain the experimental process. The published results are included in chapters 3 and 4 and enriched with additional results and discussion.

Chapter 2: Materials and Methods

2.1- Silver nanoparticles

This thesis was developed in the context of the EU Biorima project. The nanoparticles used were recommended and shared by the consortium. We focused on silver NPs for this project. We have completed their characterization of their physical chemical properties already described by the provider (JRC, EU Joint Research Centre) by analyzing their properties related to the biological media in which we used them.

2.1-1 Details from JRC Scientific and Technical Reports.

The silver nanoparticles used in this study were provided by the European Commission JRC. JRC provides a series of NMs to the scientific community to support the characterization, toxicological and eco-toxicological testing, and risk assessment of NMs. We used the reference NM-300K nano-silver. NM-300K is a colloidal aqueous suspension of silver NPs with a nominal silver content of 10% w/w stabilized with 4% w/w Polyoxyethylene Glycerol Trioleate and Polyoxyethylene (20) Sorbitan mono-Laurant (Tween20). Detailed size distribution characterization is provided in *Table 3*. The size of NM-300K nano-silver was measured by transmission electron microscopy (TEM) in 3 different laboratories (IUTA, VAR and EMPA). The IUTA and VAR laboratories reported two nanoparticle populations with a mean diameter of 3-5 nm and 15-17 nm, respectively. The EMPA laboratory reported a unique NP population with a mean diameter of 17±3.17 nm. In addition, size distribution analysis using scanning electron microscopy (SEM) and nanoparticle tracking analysis (NTA) was performed by IUTA and EMPA laboratories, respectively. The SEM observations showed that particles formed a main population with a mean diameter of 14 nm, while some particles with a diameter up to 66 nm were observed. The NTA analysis reported a mean particle size of 52.3 ± 26 nm. Dynamic light scattering analysis (DLS) was done in several collaborative projects on NM-300K AgNPs. The size distribution of NM-300K was comprised between 50 and 70 nm in water.

Table 3: Size distribution of NM300K.

Data from JRC expressed as average ± standard deviation. Diameters 1 and 2 correspond to the mean diameter of two NP populations identified in the samples.

Technique	Laboratory	Diameter 1 (nm)	Diameter 2 (nm)	Max diameter (nm)
TEM	IUTA	5.2 ± 1.7	15 ± 1.1	32.6
TEM	VAR	3-4	17.3	
TEM	EMPA	17.2 ± 3.2		
SEM	IUTA	14 ± 1.4		66
NTA	EMPA	52.3 ± 26		
DLS	Several	50-70		

TEM: transmission electron microscopy. SEM: scanning electron microscopy. NTA: nanoparticle tracking analysis. DLS: Dynamic Light Scattering. IUTA German institute of Energy and Environmental Technology. VAR: Veterinary and Agrochemical Research Centre (Belgium). EMPA: Swiss Federal Laboratories for Materials Science and Technology.

The stability of the NM-300K suspension was controlled by UV-Vis spectroscopy 12 months after NP synthesis. No changes in the UV-vis spectrum were observed over time (Figure 22a). The dissolution of NM-300K was measured by quantifying silver ions release in the solution following 12 days of incubation in 0.5% nitric acid, in a physiological buffer, or in deionized water. An equilibrium was reached after 5 days of incubation in physiological buffer and water, and no further increase in silver concentration was observed. In nitric acid, the silver concentration increased over time associated with continuous dissolution in acidic conditions over time as compared to physiological buffer and water.

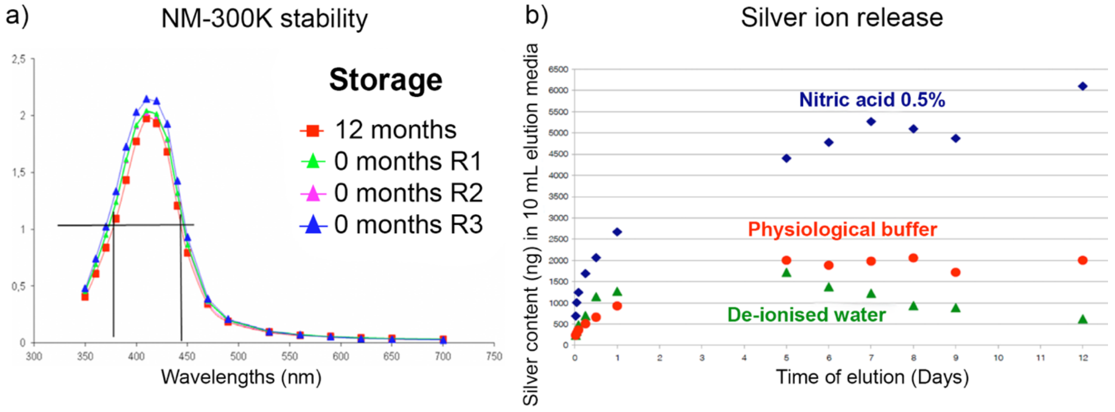

Figure 22: Characterization of NM300K stability (a) and dissolution (b). Data provided by JRC.

(a) UV-Vis spectra of NM-300K after 0 and 12 month storage in the dark at 4°C. The material was preserved in an aqueous dispersion buffer with 4% (v/v) Tween-20 stabilizing agent. (b) Silver concentration (ng/10mL) following dispersion of NM300K in 0.5 % nitric acid, deionized water or physiological buffer. 580 mg of NM-300K was embedded into 460mm^2 of poly-acrylic matrix. The release of Ag$^+$ in the solution was measured during 12 days without removing or changing the elution medium.

2.1-2 Characterization of Ag NPs in biological media

The size of AgNPs was measured by Transmission Electron Microscopy (TEM). The aggregation state and the potential dissolution of NM-300K following incubation at 37°C in the different biological media were analyzed by Dynamic Light Scattering (DLS) and Small-Angle X-ray Scattering (SAXS). The buffers and biological media used in this study were Hanks' Balanced Salt Solution supplemented with Ca^{2+} and Mg^{2+} ($HBSS^{Ca2+/Mg2+}$), Minimum Essential Media (MEM) supplemented with 4% Fetal Bovine Serum (FBS), and the apical secretome of Calu-3 cells (see chapter 3). While TEM analysis is performed on dry particles only, DLS and SAXS can be performed on the particle suspension in the different media. SAXS can be used for the analysis of AgNP size with a higher resolution than DLS, especially in biological media with high protein content. In addition, it allows determining the particle concentration in solution. The samples were prepared for each technique as follow:

a) *Transmission Electron Microscopy*: NM-300K AgNPs were diluted to 0.5 mg/mL in water and a drop was deposited on a Cu-C-Formvar grid. The sample was left for 30 min at room temperature for drying. The excess of liquid was removed with a filter paper. Dilution in $HBSS^{Ca2+/Mg2+}$ was not suitable due to the high salt concentration of this buffer. NPs were imaged with a JEM-100S microscope (Jeol Ltd Tokyo, Japan) operating at 80 kV. Images were acquired with an Orius 200 digital camera (Gatan-Roper Scientific, Evry, France) using Gatan software with a 15,000 x magnification. Automated image analysis developed using ImageJ software was used to reduce noise and to calculate the average NP diameter. The algorithms and parameters used are detailed in Table 4. A total number of 2279 particles were analyzed.

Table 4: ImageJ plugin and parameters used for the automated analysis of TEM images

Algorithm	Parameter
Auto threshold	0 to 113
Watershed	-
Particle analysis	Size = 100 - Infinity nm^2 Circularity = 0.1 - 1

b) *Dynamic Light Scattering*: The size of AgNPs was measured in $HBSS^{Ca2+/Mg2+}$ at 37°C by DLS on a Zetasizer Nano Series (Malvern Instruments) using a particle concentration of 0.01 mg/mL. Each measurement was repeated 3 times. Data analysis was performed using standard procedures. The quality of the fit of the correlation function was checked for each measurement.

c) *Small Angle X-ray Scattering*: AgNP size was also measured in biological media by SAXS. The SAXS experiments were performed by Olivier Taché at NIMBE, CEA Saclay. AgNPs at a concentration of 0.5 mg/mL were incubated in HBSS$^{Ca2+/Mg2+}$, in MEM+4% FBS MEM, or in the apical secretome of Calu-3 cells for 18 days at 37°C. Controls without NPs were incubated in the same conditions for each medium. 100 µL of the solution was transferred to a Kapton capillary for SAXS measurements. The analysis was performed on a on a Xeuss 2.0 high resolution X-ray spectrometer (Xeoxs) using an exposure time of 1h per sample. SAXS data were fitted with a Gaussian polydisperse sphere model using the following parameters: $\rho(Ag) = 10.5$ g/cm^3, scattering length density (SLD) = 9.39×10^{-10} cm^{-2} for water, SLD = 7.76×10^{-11} cm^{-2} for silver. The size distribution was calculated both by curve fitting and by Monte Carlo simulation. The number of particles in the samples was estimated to 7×10^{13} NP/mL after 18 days, in good agreement with the initial concentration of 0.5 mg/mL.

AgNP size distribution was measured by TEM on dry particles and by DLS and SAXS in different media. TEM measurements showed a monodispersed NP population with an average size of 25 ± 5 nm (Figure 23a). Two representative TEM images show the spherical shape of the NM-300K AgNPs with a relatively homogeneous size (Figure 23c-d). DLS results indicated 2 populations in HBSS with a hydrodynamic diameter of 4.5 ± 0.8 and 35 ± 10 nm respectively (Figure 23a). The SAXS results indicated a diameter d = 14.1 ± 0.5 nm in the secretome of Calu-3 cells and d = 15.4 ± 0.2 nm in MEM+4% FBS following 18 days incubation, while aggregation was observed in HBSS at this time point (out-of-range for SAXS analysis) (Figure 23b). The NP size measured at 18 days in the different media was compared to the size measured in the stock solution diluted in water by SAXS in the same conditions: d = 15 ± 0.1 nm. This result suggests that little or no dissolution of AgNPs occurred in the secretome or in MEM+4%FBS at 37°C for this period. Monte Carlo simulation of the particle size distribution indicated that some larger aggregates (around 38-40 nm in diameter) may be present, as observed by DLS. The average ± standard deviation values are indicated in Table 5 for each technique in the different media. SAXS raw data is shown in Figure 24.

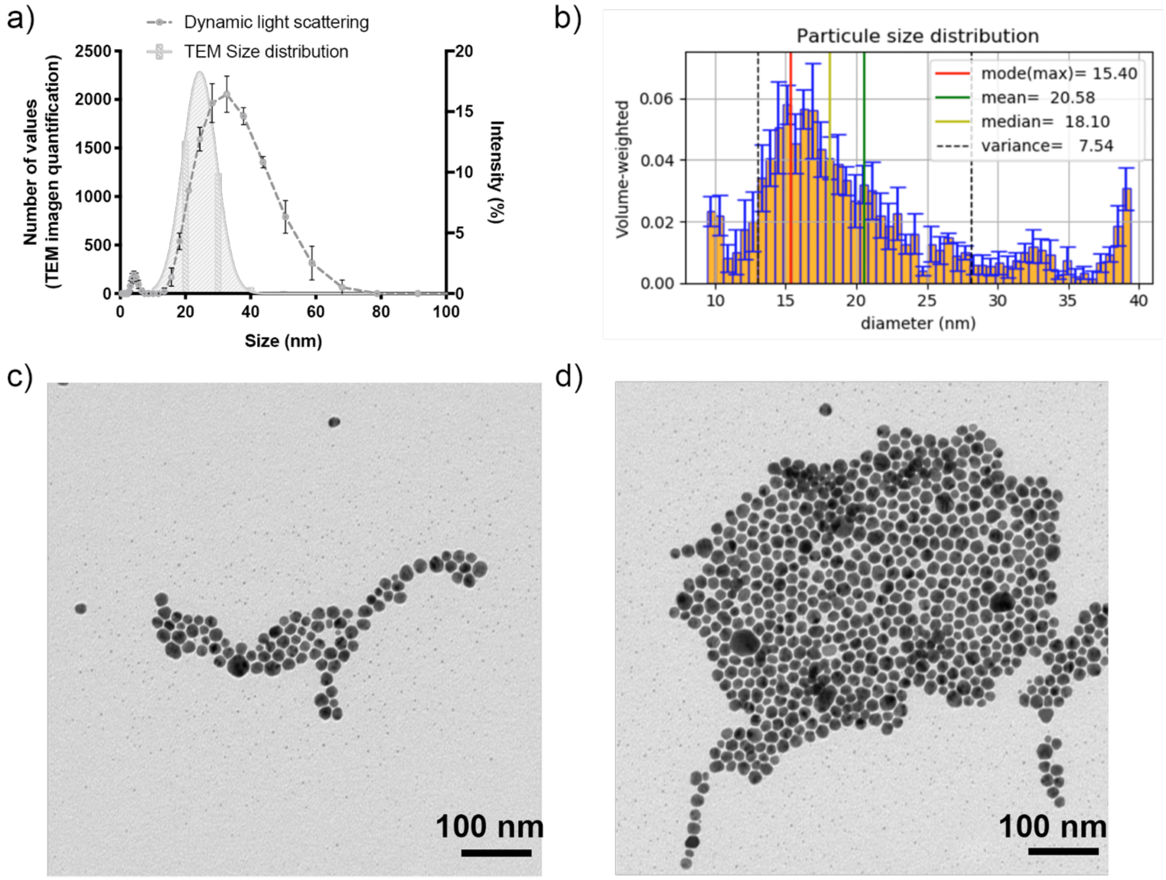

Figure 23: Characterization of AgNPs by TEM, DLS and SAXS in different media.

(a) Size distribution of AgNPs measured by TEM on dried samples (continuous line) and DLS hydrodynamic size distribution in HBSS$^{Ca2+/Mg2+}$ *(discontinuous line). (b) Monte Carlo simulation of particle size distribution in the secretome of Calu-3 cells following 18 days incubation based on the SAXS measurement. (c-d) Representative images of AgNPs by TEM.*

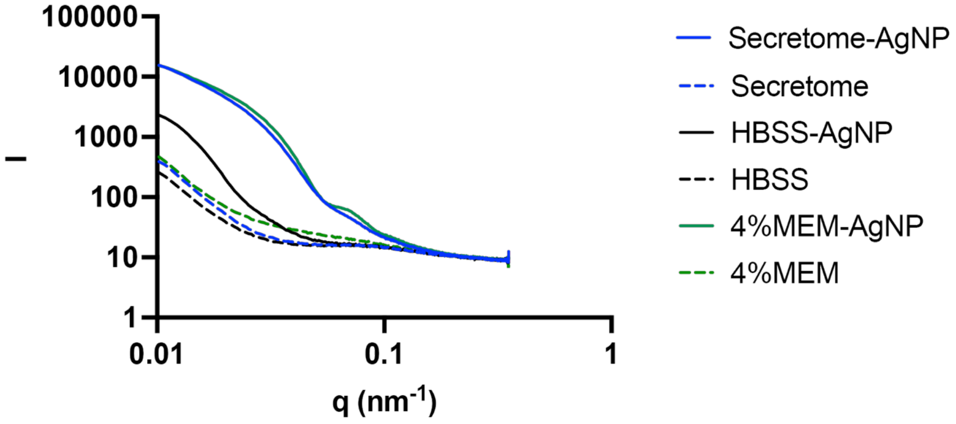

Figure 24: SAXS raw data. SAXS curves represented as the scattering intensity as a function of the structure factor q(1/nm).

AgNPs were incubated in HBSS (black), MEM+4% FBS (green), or the apical secretome of Calu-3 cells (blue) for 18 days at 37°C. The SAXS curves (dot lines) of the media without NPs following 18 days incubation at 37°C are shown.

Table 5: Analysis of AgNP size distribution by TEM, DLS and SAXS.

Techniques	**TEM**	**DLS (HBSS$^{Ca2+/Mg2+}$)**	**SAXS (water)**	**SAXS (MEM+4% FBS @18 days**	**SAXS (Secretome @18 days)**
Size (nm)	d = 25 ± 5 nm	d1 =4.5 ± 0.8 nm d2 =35 ± 10nm	d = 15 ± 0.1 nm	d = 15.4 ± 0.2 nm	d = 14.1 ± 0.5 nm

The SAXS measurements are in line with data reported by JRC for NM-300K batches.

2.2- Cellular models

2.2-1 Calu-3 bronchial epithelial cell line

The human Calu-3 cell line has been widely used for drug screening, infection and toxicological studies (Jeong et al. 2019; Florea et al. 2003; Stentebjerg-Andersen et al. 2011).This cell line has the capacity to simultaneously form a tight epithelium and to secrete mucus when grown at the air-liquid interface (ALI). These features make this cell line an interesting model of the human bronchial epithelium for toxicological assessment.

Calu-3 cells were purchased from the American Type Culture Collection (ATCC® HTB-55™) and used for the experiments between passages 27 and 40. This cell line has been derived from a metastatic human lung adenocarcinoma of a 25-year-old Caucasian man.

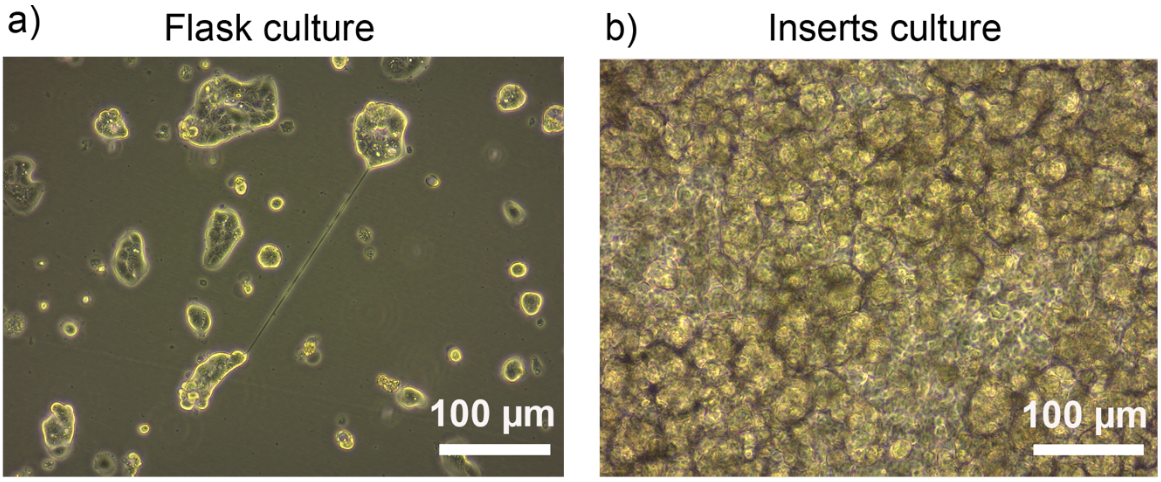

Figure 25: Submerged and air-liquid interface (ALI) cultures of Calu-3 cells

(a) Low-density of Calu-3 cells grown in corning flasks in MEM supplemented with 10% FBS. (b) Calu-3 cells grown on 3µm porous inserts 8 days after ALI in MEM supplemented with 4% FBS.

All products used for cell cultures were provided by Thermo Fisher Scientific unless stated otherwise. Calu-3 cells were cultured in MEM supplemented with 10% FBS (F7524, Sigma-Aldrich), non-essential amino acid 100x (1% v/v), sodium pyruvate (1% v/v), glutamax (1%

v/v), penicillin-streptomycin 100x (1% v/v) and HEPES buffer 100x (1% v/v). The cell cultures were maintained in 25 or 75 cm^2 culture flasks (Corning®) (Figure 25a) at 37°C and 5% CO_2. The culture medium was changed every 2-3 days and cells were passaged weekly before confluence. At each passage, cells were counted and seeded at a density of 40,000 cells per cm^2 in new flasks.

For the establishment of the epithelial barrier, Calu-3 cells were grown on porous inserts (Figure 25b). The culture was established by seeding cells at a density of 500,000 cells/well: 500 µL of cell suspension in MEM+10% FBS was added to the apical compartment and 1.5 mL of MEM+10% FBS was added to the basal compartment (Figure 26a-b). Inserts are commercially available with a membrane porosity ranging from 0.4 to 3 µm in pore diameter. We selected a 3-µm porosity because of its suitability for NP translocation studies. During this project, the inserts were provided by two different suppliers. First, we used Transwell® with a polyester (PE) membrane (pore diameter = 3 µm, surface area = 1.13 cm^2, Corning) from Costar. Then, during the last 6 months of the thesis, we had to change for Millipore inserts due to supply disruption at Costar. The new inserts were Millicell® with a polyethylene terephthalate (PET) membrane (pore diameter = 3 µm, surface area = 1.1 cm^2, Millipore) from Sigma. Although the same pore size was advertised, the pore creation process must be slightly different between suppliers as we found fused pores in Millicell membranes, which were not visible on Costar's inserts (Figure 26c-d). Nevertheless, Calu-3 cell cultures on the two different types of inserts did not show statistical differences in trans-epithelial electrical resistance (TEER), Lucifer Yellow (LY) permeability, growth rates or cell viability at ALI.

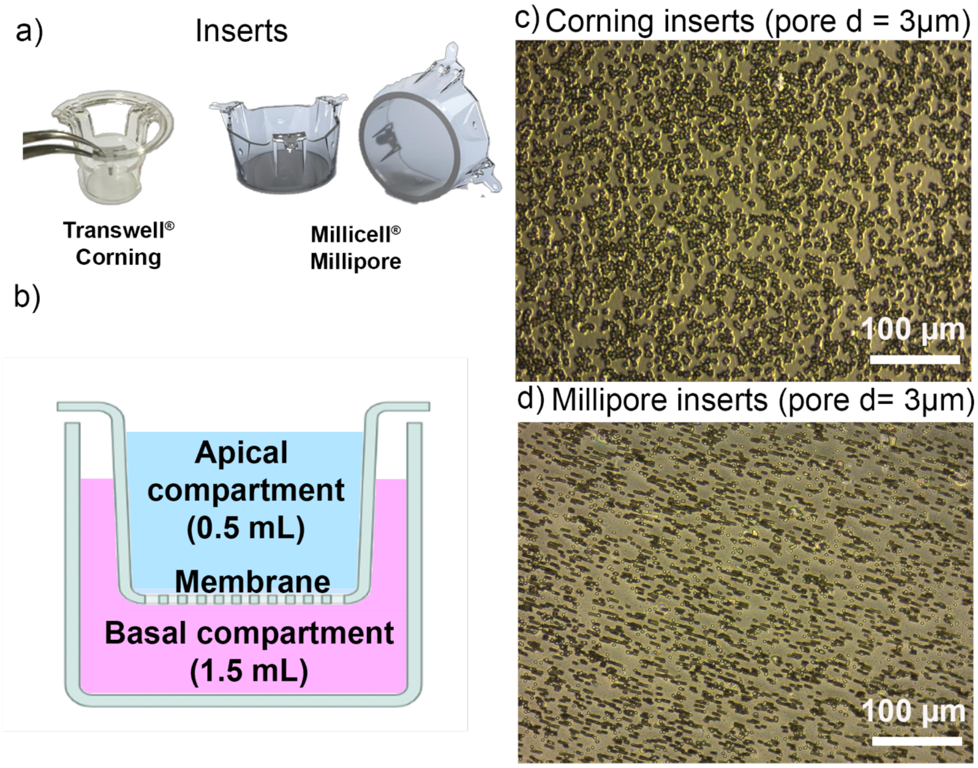

Figure 26: Overview of the inserts.

(a) Images of Transwell® (left) and Millipore® (right) inserts. (b) Schematic insert view in a culture well with the corresponding medium volumes in the insert (in blue, called the apical compartment) and in the receiving well (in pink, called the basal compartment). (c-d) Bright field images of inserts from (c) Corning and (d) Millipore showing the distribution of the 3-µm diameter pores.

The development of the culture on inserts took place in two successive steps:

1. In submerged conditions: Cells were incubated with the culture medium present in both the apical and basal compartments. Cells were kept in submerged conditions in MEM+10% FBS until the TEER reached 700 Ω.cm^2, which usually took 7 to 9 days. During this period, the culture medium was replaced every 2-3 days in both compartments.
2. At the air-liquid interface (ALI): The apical surface of the cells was exposed to the air. ALI was induced by removing the medium from the apical compartment. Cells were kept at ALI with MEM+10% FBS in the basal compartment for one day. Then, the apical and basal compartments were washed with HBSS$^{Ca2+/Mg2+}$ to remove serum proteins. MEM supplemented with different concentrations of serum (0, 2, 4, 8%) was added to the basal compartment only, depending on the experimental conditions. The

TEER was measured at ALI to follow cell differentiation and the formation of a tight epithelium.

During cell differentiation at ALI, the culture medium was changed every 2-3 days in the basal compartment, and the apical secretome was collected. The secretome corresponds to the thin layer of liquid covering cells composed of mucus and proteins secreted by cells. The collection of the apical secretome was performed by incubating cells with 200 µL of HBSS$^{Ca2+/Mg2+}$ at 37°C for 5 min. 3-4 back and forth movements were done with the pipet to detach the viscous mucus and help removing the whole secretome without damaging the cells. Secretomes were stored at -80°C before analysis.

2.2-2 Primary Normal Human Bronchial Epithelial cell (NHBE)

Primary human bronchial epithelial cells were provided by Epithelix (Genève, Switzerland, www.epithelix.com). The system is commercially known as MucilAir™ cultures (Figure 27a). The MucilAir™ 3D lung tissue model is a fully differentiated bronchial epithelium reconstituted from human bronchial airway epithelial cells (hAEC) cultured in Transwell® with a polyester membrane (pore diameter = 0.4 µm, surface area = 0.33 cm^2). NHBE are only available with a 0.4 µm porosity, because NHBE cannot be grown on membranes with larger pores (Figure 27b).

In this study, the MucilAir™ epithelia were derived from the primary cells of 3 non-smoking healthy donors. The donors were two males (15 and 41 years old) and one female (59 years old), all Caucasian (Table 6).

Table 6: Detailed information about the 3 donors and the corresponding MucilAir™ models. Data from Epithelix. TEER: Transepithelial electric resistance. TW: Transwell.

Reception	**Donor**	**Age**	**Sex**	**TEER ($\Omega.cm^2$)**	**Date of seeding on TW (Epithelix)**	**Date of ALI (Epithelix)**	**Days at ALI upon reception**
25/06/19	1 (MD076801)	59	Female	208 ± 4	06/05/19	13/06/19	12
	2 (MD072001)	41	Male	293 ±6	23/04/19	29/04/19	26
	3 (MD067001)	15	Male	207 ± 6	06/05/19	13/06/19	12

MucilAir™ cultures were maintained following the manufacturer instructions. The cells were sent with agar culture medium at 37°C. At reception, agar was removed and the inserts were transferred to a new culture plate with serum-free MucilAir™ culture medium supplemented with penicillin-streptomycin (EP04MM, Epithelix). The cultures were kept for one day at 37°C. Then, the culture medium was changed and the experimental time (as reported in our study) started. In our conditions, cells were kept at ALI with MucilAir^{TM} culture medium. The basal medium and the apical secretome were collected every 2 days and stored at -80°C. Secretomes were collected in the same conditions as for Calu-3 cultures (see 2.1a).

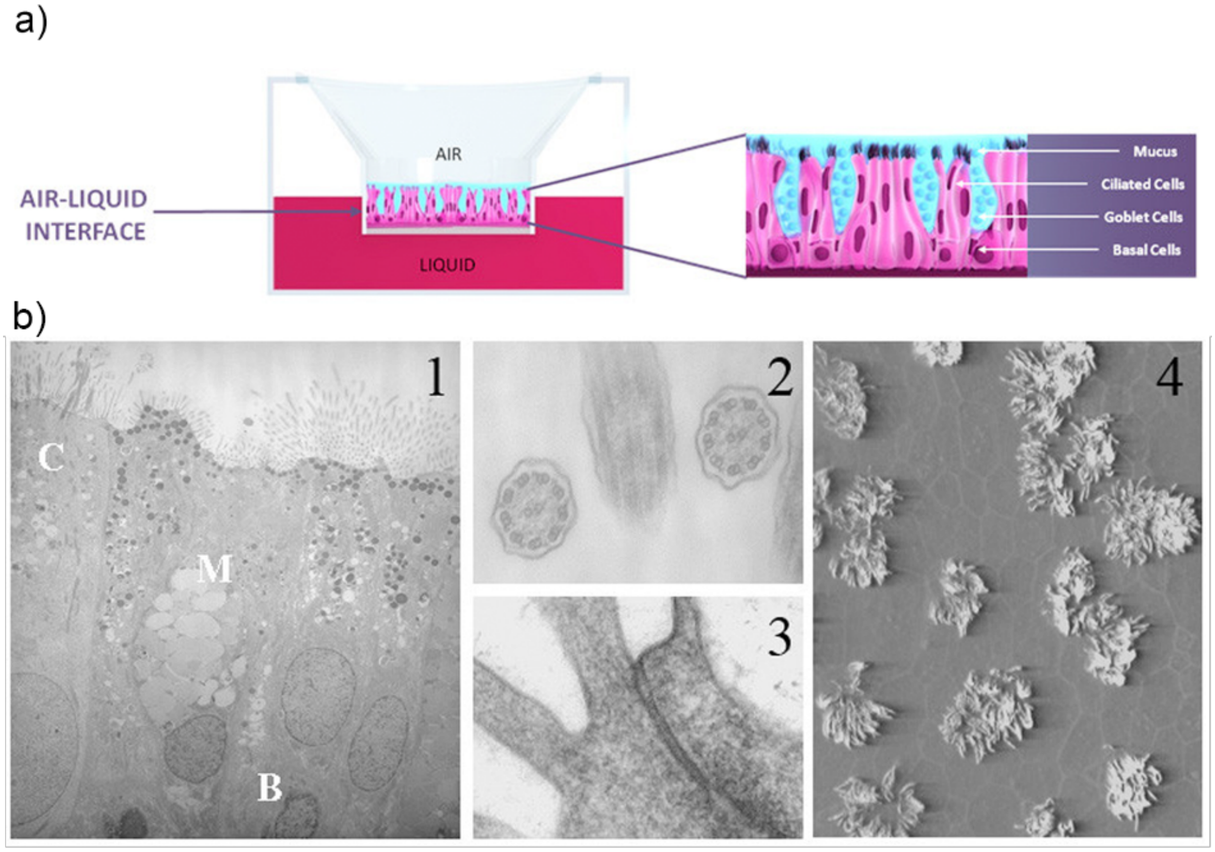

Figure 27: Schematic and representative images of MucilAir^{TM} cultures on Transwell inserts with a 0.4-µm porosity.

(a) Schematic of MucilAir^{TM} with the 3 different cell types: basal, ciliated and goblet cells. b) Transmission and scanning electron microscopy images: 1- Radial section. 2- Cross-section of cilia. 3- Tight junction structures. 4: Beginning of ciliogenesis. (C: ciliated cell, M: Mucus cell and B: Basal cell). Source: Epithelix website.

2.2-3 THP-1-derived macrophages

THP-1 cells were purchased from the American Type Culture Collection (ATCC® TIB202^{TM}). THP-1 is a monocytic cell line derived from human acute monocytic leukemia (Figure 28a). The cells were grown in suspension and differentiated into adherent macrophages by exposure to 12-O-tetradecanoylphorbol-13-acetate (PMA) (P1585, Sigma). The cells were cultured in RPMI 1640 supplemented with 10% FBS, 2 mM Glutamax, 1% v/v NEAA 100x, 1% v/v penicillin-streptomycin 100x, 1% v/v HEPES buffer 100x and 50 µM 2-β-mercaptoethanol. Cells were maintained by adding fresh medium every two days, keeping a cell density lower than 8 x 10^5 cells/mL. Cells were passaged once a week following centrifugation and complete medium changed.

To induce THP-1 differentiation into macrophages, 30 x 10^6 cells were resuspended in 6.25 mL of fresh medium with 500 nM PMA, and incubated at 37°C for 3h under gentle agitation (Figure 28b). Then, PMA was removed by centrifugation, cells were resuspended in fresh RPMI medium + 10% FBS, and finally seeded at a density of 2.35 x 10^5 cell/cm^2. The cells were incubated at 37°C for at least 12h. THP-1 derived macrophages were rinsed with PBS in order to remove dead and non-adherent cells before exposure to nanoparticles.

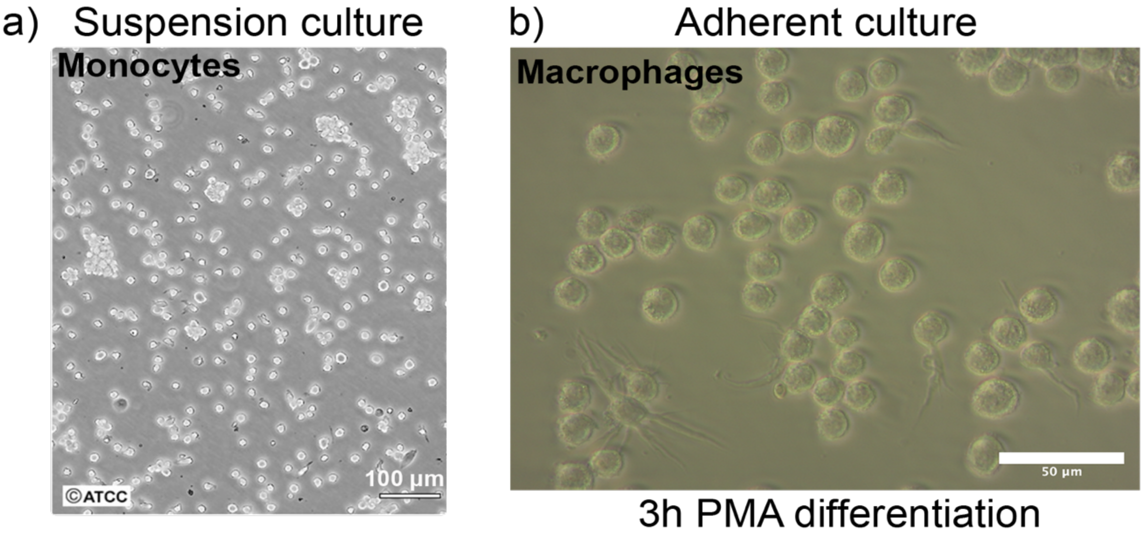

Figure 28: Bright field images of THP-1 cells before and after differentiation into macrophages.

(a) THP-1 monocytic cells (source: ATCC-TIB202) (b) THP-1 derived macrophages following differentiation with PMA.

2.3 Exposure to silver nanoparticles

2.3-1 Preparation of NP suspensions

NM-300K AgNP is a colloidal dispersion with a nominal silver content of 10% w/w. AgNP suspension was diluted in HBSS$^{Ca2+/Mg2+}$ to a concentration of 1 mg/mL. The particle suspension was sonicated for 2x2 min on ice using a cup horn sonicator (450W, 60 Hz, Branson). The NP suspension was further diluted in HBSS$^{Ca2+/Mg2+}$ to a final concentration chosen for the experiments.

2.3-2 Treatments of Calu-3 cells with AgNPs

The AgNPs were delivered to cells grown on inserts at ALI as NP suspension in a reduced volume of liquid, so as not to lose the ALI. 20 µL of AgNP suspension was deposited directly in the apical compartment as 4 droplets of 5 µL each (Figure 29). The control cultures received 20 µL of the HBSS buffer only using the same procedure.

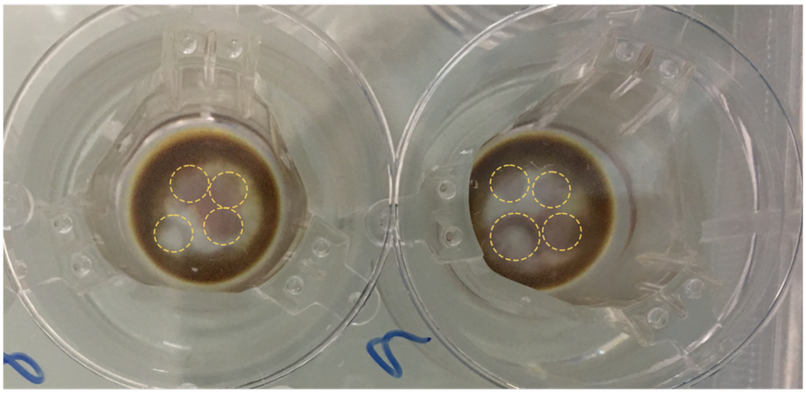

Figure 29: NP deposition strategy.

Pictures of two inserts after deposition of 50 µg AgNPs in the form of 4 droplets (5µL) of AgNP suspension in HBSS directly on Calu-3 cells at ALI. Pictures were taken immediately after deposition. The brown colour comes from AgNPs.

Calu-3 cultures were exposed to AgNPs in a single treatment with approximately 10 µg and 50 µg AgNPs per well, corresponding to 10 and 50 µg/TW. Before each treatment, the apical secretomes were collected and stored at -80°C. Then, cells were exposed to AgNPs as described above for 1 to 48h.

2.3-3 Formation of the acellular protein corona

The adsorption of proteins on NPs was studied by gel electrophoresis and mass spectrometry (see 2.6). The acellular protein corona (protein corona formed in the secretome or culture medium without cells) was formed by mixing the apical secretome of Calu-3, the apical secretome of NHBE cells, or 4% FBS (in average 250 µg/mL) with a known concentration of NPs (see 2.3-1). Generally, 200 µL of apical secretome was mixed with 10 µg of AgNPs and incubated for 1h at 37°C under gentle mixing (Figure 30). This protein/NP ratio was chosen so that it would be identical to the protein/NP ratio in cellular protein corona experiments (protein corona formed in the secretome with cells), where cells are directly exposed to NPs (see 2.3-4).

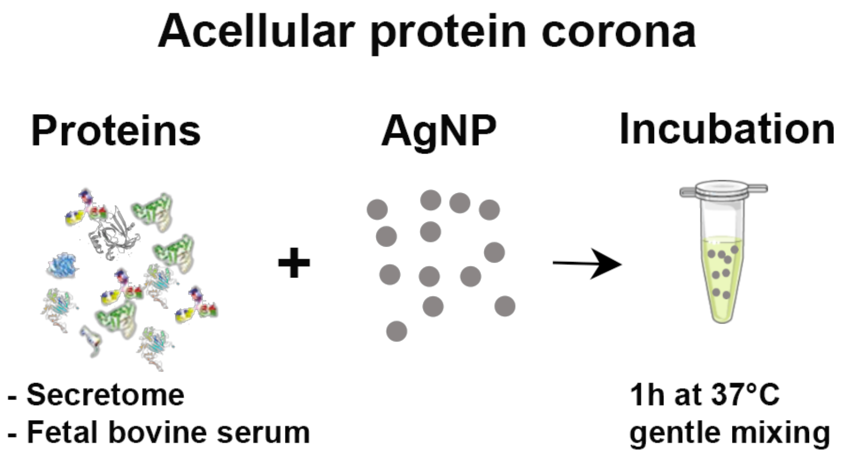

Figure 30: Preparation of the acellular protein corona on AgNPs.

Secretome of Calu-3 or NHBE cells or FBS proteins were mixed with AgNPs in Eppendorf tubes. 200 µL of protein solutions were generally mixed with 10 µg AgNPs and incubated for 1h at 37°C under gentle mixing.

2.3-4 Formation of the cellular protein corona

The formation of the cellular protein corona was investigated by exposing Calu-3 cells at ALI directly to AgNPs. Before exposure, the epithelial integrity and the cell metabolic activity were monitored by measuring the Trans-Epithelial Electrical Resistance (TEER), the Lucifer yellow (LY) permeability and the Alamar Blue (AB) assay (see 2.4-1, 2.4-2 and 2.5-1 respectively). Cells were kept overnight in culture conditions to restore the apical secretome that could have been modified by the manipulation of the cultures. Then, cells were exposed to the chosen concentration of AgNPs as described in section 2.3-2. Following 1h, 24h and 48h treatments, AgNPs with their adsorbed proteins ('cellular protein corona') were collected in HBSS using the same protocol as for secretome collection (Figure 31) (section 2.2-1). Briefly, 200 µL HBSS$^{Ca2+/Mg2+}$ were added in the apical compartment and incubated at 37°C for 5 min. 3-4 back and forth movements were done with the pipet to detach the viscous mucus and help removing the whole secretome with AgNPs. Secretome-AgNP samples were stored at -80°C before analysis.

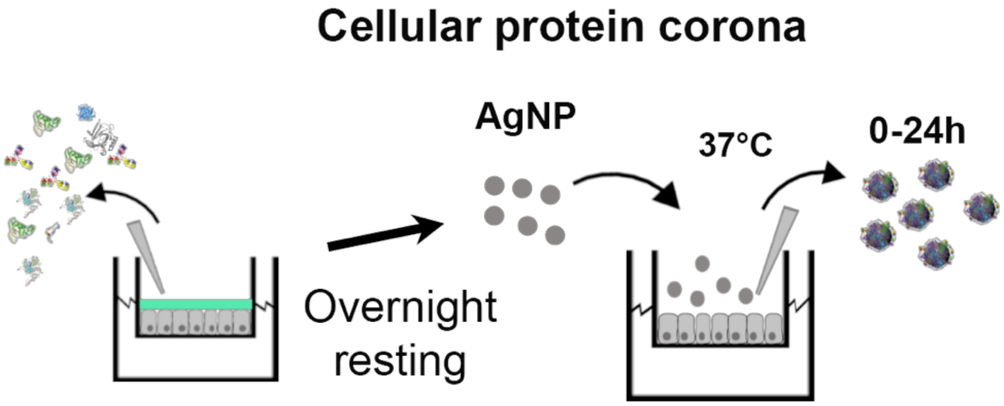

Figure 31: Preparation of the cellular protein corona.

Calu-3 cultures were exposed to AgNPs at 10 or 50 µg/cm² for 1 to 48h. The epithelial barrier integrity was monitored before treatment and cells were kept overnight following TEER measurement to restore the apical secretome. After treatment, secretome-NPs were collected with 200 µL HBSS$^{Ca2+/Mg2+}$ *and samples were kept at -80°C before analysis.*

2.3-5 AgNP isolation for the analysis of the protein corona

All the secretome samples were stored at -80°C for protein corona studies (cellular and acellular protein coronas). A freezing cycle reduced protein sedimentation by centrifugation (see chapter 5). The AgNPs with their adsorbed proteins were isolated from the free proteins in the secretome using two centrifugation steps (Figure 32). All the centrifugations were run for 20 min at 4°C. For the first centrifugation, a low speed of 3,000g was used to precipitate AgNPs, while avoid free protein sedimentation. The supernatant was discarded, and AgNPs were resuspended in 500 µL HBSS $^{Ca2+/Mg2+}$. A second centrifugation step was performed followed by 3 washes in the same buffer. The second centrifugation was done at a higher speed of 14,000g. A cycle of 3 washes was done to remove free or weakly bound proteins from the NPs. The supernatants were discarded and the pellets were always resuspended in 500 µL HBSS $^{Ca2+/Mg2+}$. The final pellet was resuspended in the loading protein buffer used for SDS-PAGE or Liquid chromatography–mass spectrometry (LC-MS/MS) analysis (see 2.6-2).

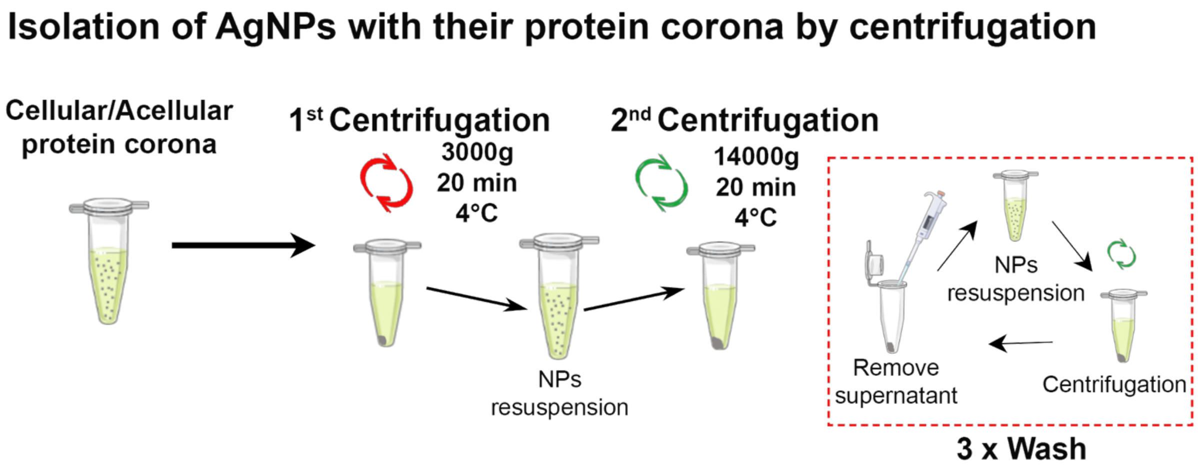

Figure 32: Isolation of AgNPs with their protein corona by centrifugation.

The protocol was adapted for the analysis of the acellular and cellular protein corona formed in the viscous secretome of Calu-3 cells. 2 centrifugation steps, at low speed (3,000g) and at high speed (14,000g) were performed to remove free proteins. The second centrifugation step was repeated 3 times for washing following NP resuspension in 500 µL HBSS. Supernatants were discarded (red square), and the final NP pellet was kept for proteomic analysis.

2.3-6 Treatments of THP-1 cells with AgNPs

Differentiated THP-1 cells were exposed to AgNPs that were incubated with Calu-3 secretome or FBS to form two different protein coronae (see 2.3-3). For the formation of the protein corona in the secretome, the same ratio of protein/NPs as for the cellular protein corona study was used. For the formation of the protein corona in FBS, we used a total protein concentration in FBS identical to the protein concentration in the secretome. The final concentrations of AgNPs applied for THP-1 were obtained by diluting pre-coated AgNP in a mixed HBSS$^{Ca2+/Mg2+}$: serum-free RPMI (v/v) buffer. HBSS and RPMI were mixed because we observed a loss of cell viability of the macrophages when exposed to HBSS alone. No loss of cell viability was observed using HBSS:RPMI buffer during 24h. Before treatment, macrophages were rinsed with PBS to remove dead and detached cells. 200 µL AgNP suspension were added to each well for 4h and 24h.

2.4- Methods to monitor the integrity of the epithelial barrier

2.4-1 Trans-Epithelial Electrical Resistance (TEER) measurement

To assess the integrity of the epithelial barrier formed by Calu-3 or NHBE cells on inserts, the TEER was measured with an EVOM2 ohmmeter (World Precision Instruments, Sarasota, Florida, USA) in combination with an STX2 electrode. The culture medium was replaced by HBSS$^{Ca2+/Mg2+}$ in the basal (1.5 mL) and apical (0.5 mL) compartments. For each experiment, the TEER was also measured in a cell-free insert and the measured value (R_{blank}) was subtracted from the measured TEER value of the cell-seeded inserts (R_{sample}). All TEER values were expressed in Ω.cm^2, multiplying the corrected TEER values by the surface area of the insert (S).

$$TEER_{sample} = (R_{sample} - R_{blank})\ x\ S$$

The epithelial barrier was considered as tight for TEER values higher than 300 Ω.cm^2 (Mura et al. 2011) for Calu-3 cells, and 200 Ω.cm^2 for MucilAir^{TM} (following the manufacturer's recommendations).

2.4-2 Paracellular permeability of Lucifer Yellow (LY)

Lucifer Yellow is a fluorescent dye that crosses the barrier only paracellularly following short incubation time. The formation of tight junctions between epithelial cells impairs the passage of the dye through the paracellular route and indicates the establishment of a tight barrier. 0.5 mL Lucifer yellow (0.1 mg/mL) was added to the apical compartment and 1 mL HBSS$^{Ca2+/Mg2+}$ to the basal compartment followed by 1h incubation at 37°C and 5% CO_2. After incubation, 0.1 mL of apical and basal solutions were transferred to a clear bottom 96-well microplate s (Greiner Item-No. 655090, µClear®) in triplicate. The fluorescence intensity (I) was measured on a FlexStation 3 microplate reader (Molecular Devices) with $\lambda_{exc} = 485$ nm and $\lambda_{em} = 535$ nm. The LY permeability (%) was calculated as follow:

$$LY\ Permeability\ (\%) = \frac{I_{sample} - I_{Blank}}{I_{LY} - I_{Blank}}\ x\ 100$$

A LY permeability smaller than 2% was considered acceptable for a tight barrier (following the manufacturer's recommendations).

2.4-3 Immunohistochemistry and immunocytochemistry

Immunodetection was used to probe tight junctions and mucus production in Calu-3 and NHBE cultures. In addition, specific antibodies were used in NHBE cultures to distinguish between the different cell types. These experiments were performed on whole cultures (immunocytochemistry) as well as on paraffin-embedded sections (immunohistochemistry). In both cases, cells were fixed with 4% paraformaldehyde (Fisher Scientific) for 15 min at room temperature and rinsed 3 times with PBS.

a) Immunohistochemistry on sections

Preparation of paraffin-embedded sections: Following fixation with paraformaldehyde, the inserts were dehydrated with ethanol in a graded series of concentrations: 50% (twice) —70% (twice) —95% (twice) —100% (twice). 100% ethanol was replaced by clearing agent NeoClear^{TM} (64741-65-7, Sigma) allowing the clearing agent to infiltrate the cells and membranes for 10 min twice. Infiltration of the cells was continued by removing the NeoClear^{TM} from the insert and adding liquid paraffin in an oven at 60°C for 1h. Paraffin was changed and replaced with fresh paraffin and incubated for 1h. The insert was then placed at room temperature to allow for the solidification of paraffin. The membrane was cut to remove it from the insert frame and 7-µm thick sections were mounted on glass slides and dried.

Immunohistochemistry: sections were cleared from paraffin with NeoClear^{TM} by 3 bathes of 5 min each. The inserts were hydrated with ethanol in a graded series of concentrations: 100% (twice) —95% (twice) —70% (twice) — 50% (twice) and finally in distilled water. Unmasking of antigens was done by incubating the sections in citrate buffer (1.8 mM citrate acid + 8.2 mM sodium citrate, pH 6) for 40 min at 95°C in a water bath. Following washes with PBS, cells were permeabilized with 0.02% Triton X-100 and blocked with 2% BSA (A7906, Sigma) in PBS. After washing, cells were incubated with the primary antibodies at 4°C overnight (Table 7). After washing with PBS, the secondary antibodies were incubated for 45 min at room temperature (Table 7). Actin filaments were stained with phalloidin conjugated to AF488. The incubation with phalloidin and the secondary antibodies were done at the same time.

Cells were mounted with Fluoroshield^{TM}, which contains DAPI (F6057, Sigma-Aldrich), before imaging on a confocal ZEISS LSM 700 fluorescence microscope with a 63x objective. Version 2.3 of the ZEISS ZEN software was used. Image analysis was performed with ImageJ (http://rsbweb.nih.gov/ij/)

b) Immunocytochemistry on cultures at ALI

After fixation, the membrane of the insert was cut and divided into 4 pieces for multiple antibodies testing. The membrane was incubated for 30 min at room temperature in 0.02% Triton X-100 (Sigma-Aldrich) and 2% BSA (A7906, Sigma-Aldrich) that allows the permeabilization of the plasmic membrane, antibody penetration, and reduction of nonspecific binding respectively. Information about primary and secondary antibodies used in this study are provided in Table 7.

Table 7: List of primary and secondary antibodies used for immunohisto/cyto-chemistry. MUC5AC: mucin 5AC; ZO-1: zonula occludens 1.

Antibody	Type	Specie	Dilution	Reference
Anti-MUC5AC	Primary	Mouse	1/500	ThermoFisher (45M1-12178)
Anti-ZO-1	Primary	Rabbit	1/500	Santa Cruz Biotechnology (SC-10804)
Anti-E-Cadherin	Primary	Rabbit	1/500	ThermoFisher (PA5-32178)
Anti-glutamylated tubulin (GT335)	Primary	Mouse	1/10000	Gift
Anti-mouse-AF594	Secondary	Donkey	1/1000	Jackson ImmunoResearch (715-585-150)
Anti-rabbit-AF488	Secondary	Goat	1/1000	Jackson ImmunoResearch (111-545-144)
Anti-mouse-AF647	Secondary	Donkey	1/1000	ab150107

2.4-4 Scanning and Transmission Electron microscopy

These experiments were done in collaboration with René Lai-Kuen at the electron microscopy facility of the faculty of pharmacy (Université de Paris). The morphology of Calu-3 and THP-1 cells was observed by transmission and/or scanning electron microscopy. For Calu-3 cells cultured on inserts, all the preparation steps were performed on the insert. For THP-1 cells, all the preparation steps were performed in suspension following trypsinization to detach cells from the plate. Each buffer change was followed by 5 min centrifugation at 3,000*g* at 4°C. Samples were slowly resuspended in new buffer solutions to avoid cell loss.

Cell fixation was done in 2.5% v/v glutaraldehyde and 2% v/v paraformaldehyde in 0.1M sodium cacodylate pH 7.3 with 45 min incubation at room temperature. After washing three times with sodium cacodylate buffer, the samples were treated with 1% v/v osmium tetroxide for 45 min at 4°C and incubated in 1% v/v aqueous uranyl acetate solution for 2 h at room temperature. The samples were dehydrated in ethanol solutions of increasing percentage (30%, 50%, 70%, 95% and 100%, 3 x 10 min each), in ethanol:propylene oxide mix (1:1 v), and finally in propylene oxide (3 x 10 min).

a) TEM

For transmission electron microscopy, each sample was embedded in Epon epoxy resin. Epoxy infiltration was done overnight. Epoxy was replaced by fresh resin twice, and incubated for 3 hours each time at room temperature. Samples were transferred to a mold with fresh resin and the polymerization was done at 60°C for 48 h. Ultra-thin sections of 80 nm thickness were cut with a Leica Ultracut S microtome equipped with a diamond knife (Diatome ultra-45) and transferred on Cu grids. Only control cultures (not exposed to nanoparticles) were stained with lead citrate to enhance the image contrast. Unstained control and treated cells were observed for the analysis of NP uptake. Samples were imaged with a JEM-100S microscope (Jeol Ltd Tokyo, Japan) operating at 80 kV. Images were acquired with an Orius 200 digital camera (Gatan-Roper Scientific, Evry, France) using Gatan software and treated using ImageJ software.

b) SEM

For scanning electron microscopy, after serial dehydration in alcohol, cells were treated with hexamethyldisilazane (HMDS) to finish dehydration. Samples were mounted in an SEM holder and the surface was sputter-coated with a 5 nm thick layer of palladium under vacuum using a Jeol JFC-1300 Autofine Coater. Images were acquired with a Joel 100S SEM microscope (Jeol, France) and analyzed using ImageJ.

2.5- Methods to evaluate the cellular responses to AgNPs

In addition to the assays described below, the TEER and LY permeability were again measured following exposure to AgNPs to determine whether the treatment could affect the epithelial barrier integrity (see 2.4-1 and 2.4-2). Besides, TEM was used for a first evaluation of AgNP uptake (see 2.4-4) before quantification by ICPMS.

2.5-1 Cell viability assays

Cell viability is classically estimated by measuring the metabolic activity of living cells. The metabolic activity can be measured based on the colorimetric or fluorometric changes of chemical species within living cells.

AlamarBlue (AB) cell viability reagent is a commercially available assay that gives a quantitative indication of metabolic activity in the form of a fluorometric change. Resazurin, the active compound of the Alamar blue assay, is a cell-permeable and non-toxic molecule, allowing for a non-invasive method to estimate cell viability. Following its uptake by living cells, the blue and non-fluorescent resazurin is reduced to resorufin, a red and highly fluorescent compound. AB is reduced by mitochondrial enzymatic activity (Al-Nasiry et al. 2007). Fluorescent resorufin can be detected in fluorescence plate readers.

For cells grown at ALI in inserts, the basal medium was replaced by fresh medium containing 10% v/v AB solution. Cells were incubated at 37°C, 5% CO_2 for 1h. Then, 100 µL medium were transferred to a 96-well plate. The measurements were carried out on a FlexStation 3 microplate reader, in bottom-read mode, with λ_{exc} = 545 nm and λ_{em} = 590 nm.

WST-1 is a viability assay based on the measurement of the mitochondrial activity. WST-1 is a tetrazolium salt (slightly red) that is cleaved into formazan (dark yellow) by mitochondrial dehydrogenase enzymes in living cells. Compared to AB assay, WST-1 assay is invasive. This assay was used on THP-1 derived cells only.

THP-1 derived macrophages were cultured as described in section 2.2-3 in duplicate in 96-well plates. After NP treatment, cells were rinsed with PBS. Then, one plate was incubated for 15 min at 37°C, 5% CO_2 with 100 µL/well serum-free fresh medium without phenol red, and the second plate with 0.2% Triton X-100 in serum-free medium without phenol red. 50 µL WST-1 (1/5) was added to each well and incubated for 30 min at 37°C with 5% CO_2. Triton X-100 treated plate was used as a control to evaluate and subtract AgNP interference with WST-1. Absorbance was measured at 450 nm on a FlexStation 3 microplate reader. Results were expressed relatively to the control following the equation:

$$Cell\ viability\ (\%) = \frac{(Sample_{A450} - Blk_{A450}) - (Tsample_{A450} - Tblk_{A450})}{(Contol_{A450} - Blk_{A450}) - (Tcontrol_{A450} - Tblk_{A450})}\ x\ 100$$

where Sample_{A450} correspond to NP treated cells, control_{A450} to non- exposed cells, Blk_{A450} to a cell-free well. T indicates cells treated with Triton X-100.

2.5-2 Assessment of the pro-inflammatory response by ELISA

The release of cytokines was measured in the basal culture medium of Calu-3 cells and in the culture medium of THP-1 cells. Following NP exposure, the media were collected and stored at -80°C before analysis. Cytokine quantification was performed using ELISA kits (DuoSet ELISA kit, R&D Systems) according to the manufacturer's instructions. Briefly, ELISA plates (9018, Corning) were coated with a specific capture antibody overnight at room temperature. After washing, standard and samples were applied to coated ELISA plates allowing cytokine-antibody binding. The bound cytokine was recognized by a secondary antibody coupled to horseradish peroxidase (HRP) enzyme permitting the quantification of bound proteins by enzymatic conversion of tetramethylbenzidine (TMB) (OptEIA^{TM}, BD Bioscience) colorimetric reagent. The enzymatic reaction was stopped with 2N H_2SO_4 and the absorbance was measured at 490 nm on a FlexStation 3 microplate reader.

2.5-3 Glycoprotein quantification by ELLA assay

The glycoprotein concentration in the apical secretome of Calu-3 and NHBE cells was measured by the enzyme-linked lectin assay (ELLA). ELISA 96-well plates (9018, Corning) were coated with lectin from *Triticum vulgaris* (L0636, Sigma-Aldrich) at 37°C for 1h. Then, the plates were washed three times with a washing solution (0.5M NaCl — 0.1% Tween 20 — PBS buffer). For sample incubation, 50 µL of standard and samples were added in duplicates for 1h at 37°C. Standard calibration curves were done with a serial dilution of known concentration of Porcine stomach mucin (2378, Sigma-Aldrich). After washing, 50 µL of Lectin Glycine max peroxidase conjugate (L2650, Sigma-Aldrich) detection solution was added to the sample and standard wells for 1h at 37°C. After washing, the substrate reagent TMB (OptEIA^{TM}, BD Bioscience) was added to each well and incubated for 20 min at room temperature in the dark. The enzymatic reaction was stopped with 2N H_2SO_4 and the absorbance was measured at 490 nm on a FlexStation 3 microplate reader.

2.5-4 Gene expression analyzed by RT-qPCR

The gene expression of Calu-3 cells after exposure to AgNPs was measured by Real-time quantitative PCR (RT-qPCR) using primers for mucins, pro-inflammatory cytokines, as well as for other genes involved in the metallic detoxification and anti-oxidant responses, such as metallothionein and heme oxygenase-1 respectively.

RNA was extracted using the NucleoSpin® kit (Macherey-Nagel, France) following the manufacturer's recommendations. Briefly, lysis buffer was used to extract total RNA and each sample was deposited in a column with a silica membrane for RNA binding. Samples were desalted and DNA was removed using DNase. Pure RNA was eluted in ultrapure water and stored at -80°C. RNA concentration, purity and integrity were checked by measuring the absorbance at 230 nm, 260 nm and 280 nm on a Nanodrop (Nanodrop 2000, ThermoFisher Scientific). Only samples with A(260nm)/A(280nm) ratio of 1.8-2.0 and A(260nm)/A(230nm) ratio > 1.5 were kept for analysis. Reverse transcription PCR (RT-PCR) was performed using the High-capacity cDNA Reverse Transcription kit (ThermoFisher, France) following the manufacturer's instructions. 2 µg of total RNA with dNTP mix, random primers and 50U MultiScribe^{TM} reverse transcriptase were used for RT-PCR in a final volume of 20 µL. A thermal cycler (BioRad) was used for the amplification steps. The cycles were divided into 4 steps (Table 8):

Table 8: Reverse transcriptase thermal cycler cycles

	Step 1	**Step 2**	**Step 3**	**Step 4**
Temperature (°C)	25	37	85	4
Time (min)	10	120	5	∞

RT-qPCR was used to determine the relative expression of genes listed in Table 9 using *rpl19* as the housekeeping gene. The genes were amplified and quantified using a thermocycler Lightcycler 480 (Roche). Samples were transferred to a 384-well plate with a 10 µL final volume. Solutions were prepared as follow:

- 2.5 µL of cDNA 1/10 diluted
- 7.5 µL of PCR mix:
    - ⇒ 1 µL of mix primers (forward and reversed primers 1/10)
    - ⇒ 5 µL of SYBR green PCR master mix
    - ⇒ 1.5 µL nuclease-free water

The thermocycler was set to 45 amplification cycles in quantification analysis mode. The melting curves were measured for primers quality control to check that unique fragments were amplified. The gene expression was calculated using the $2^{-\Delta\Delta Ct}$ method and normalized to *rpl19* housekeeping gene. The log 2-fold change was expressed relatively to the control.

Table 9: Sequences of the primers used for RT-qPCR

	Gene name	**Forward (5'- 3')**	**Reversed (5'- 3')**
Housekeeping	*rpl19*	GGCTCGCCTCTAGTGTCCTC	GGCTCGCCTCTAGTGTCCTC
Mucins	*muc5ac*	AACTACTCCCAGCCCTGTTC	GTAGAGGCAGGGGTTGTTCT
	muc5b	GGGATCTTCCTGGTCATCGA	GCTACGCGTGGCAAAGTCAT
Pro-inflammatory cytokines	*il-1α*	CTCACGGCTGCTGCATTACA	CTTCAGCAGCACTGGTTGGT
	il-1β	GGACAAGCTGAGGAAGATGC	CGTGCACATAAGCCTCGTTA
	il-6	TGGTCTTTTGGAGTTTGAGG	CGCAGAATGAGATGAGTTGTC
	il-8	AGACAGCAGAGCACACAAGC	ATGGTTCCTTCCGGTGGT
	tnf-α	GCTCCCCAAGAAGACAGG	GCCAGAGGGCTGATTAGA
Tight junctions	*zo-1*	TGCAGCCAAGGAAGGCTTAGA	GGTCAAGCAGGAAAAGGACGG
	cdh-1	GGACAGGGACTGATTTTGAGC	GTGAAGGGAGATGTATTGGG
Metallic detoxification	*mt1x*	ACTCCTGCTTCTCCTTGCCTC	TGCACTTGTCTGACGTCCCTT
	mt2a	TCCTGCAAATGCAAAGAGTGC	AAAATCCAGGTTTGTGGAAGTCG
Oxidative stress	*hmox-1*	CGTTCCTGGTCAACATCC	CTGTCGCCACCAGAAAG
Osmotic pressure	*alb*	TAGAGAAGTGCTGTGCCGCT	AGTTGGAGTTGACACTTGGGGT

2.6 Methods for protein analysis

2.6-1 Total protein quantification: BCA assay

The protein concentration in the apical secretome was measured using the bicinchoninic acid (BCA) protein assay (PierceTM BCA protein assay kit, ThermoFisher Scientific) following the manufacturer's protocol. Briefly, 25 µL of sample previously diluted in HBSS$^{Ca2+/Mg2+}$ and the standard (working range 20-2000 µg/mL) were deposited in a 96-well plate in duplicate. 200 µL working reagent solution (reagent A and reagent B, 50:1 v/v) was added to each well and incubated for 30 min at 37°C. The absorbance was measured at 562 nm on the FlexStation 3 microplate reader (Molecular Devices). The protein concentration was estimated by interpolation of the standard curve.

2.6-2 Gel electrophoresis for protein characterization and protein corona extraction

The SDS-PAGE was used (1) to characterize the protein profile of the apical secretome and the protein corona, and (2) to isolate the protein corona from AgNPs before complete proteomic analysis by mass spectrometry.

a) The characterization of the apical secretome and the protein corona was performed by gel electrophoresis first. 10 µg proteins (secretome) or adsorbed proteins (AgNP corona) (see 2.3-5) was resuspended in 20 µL of lithium dodecyl sulfate (LDS) (1x) loading buffer (NP0007, Invitrogen) with 50 mM DTT and heated at 100°C for 5 min. All samples were loaded in 10% SDS-PAGE gel and run at 100-120 V for 1-1h30 until the migration front reached the bottom of the gel.
    1. Gel staining: Proteins were fixed with 50% methanol, 7% acetic acid, in milli-Q water for 30 min. The proteins were stained with SYPRO® Ruby (S12000, Molecular Probes) overnight with gentle shaking. Then, the gel was washed three time with 10% methanol, 7% acetic acid, in milli-Q water. Before imaging, the gel was rinsed with tap water twice for 5 minutes. Images were taken using a UV transilluminator and a CCD camera.
    2. Immunoblotting: Proteins were transferred from the gel to a nitrocellulose blotting membrane (0.45 µm, 10600002, GE Heathcare) in a cassette by applying a 100mA current for 1h. The membrane was blocked with 2% BSA in Tris-Buffer Saline (TBS) buffer for 30 min. The primary antibody was incubated overnight at 4°C in diluted TBS. After washing, the secondary antibody coupled to HRP was incubated for 45 min at room temperature. The antibodies were visualized by chemiluminescence using

enhanced chemiluminescence (ECL) (28980926, GE Healthcare) as the HRP substrate. Images were acquired with an Imager 600 system (Amersham).

b) Before the analysis of the protein corona by LC-MS/MS, the same protocol was applied to the samples containing AgNPs with their protein corona. The electrophoresis ran for 10-15 min only in order to separate the proteins, which migrate through the gel, from the AgNPs, which cannot migrate in the gel and remained in the wells. This short electrophoresis also allows stacking proteins in a single band on the gel, which can be easily cut and digested ahead of mass spectrometry analysis.

Table 10: List of primary and secondary antibodies used for western blots. MUC5AC: mucin 5AC. MUC5B: mucin 5B.

Antibody	Type	Specie	Dilution	Reference
Anti-MUC5AC	Primary	Mouse	1/500	ThermoFisher, 45M1-12178
Anti-MUC5B	Primary	Rabbit	1/500	Sigma, HPA008246
Anti-mouse-HRP	Secondary	Goat	1/3000	Jackson ImmunoResearch 115-035-003
Anti-rabbit-HRP	Secondary	Goat	1/3000	Jackson ImmunoResearch 111-035-003

2.6-3 Proteomic analysis by LC-MS/MS

a) Analysis of the apical secretome of Calu-3 and NHBE cells

Quantitative proteomic analysis was performed on the apical secretome of the Calu-3 and NHBE cells collected at day 4, 11-12 and 18 after ALI. For each cell type, three biological replicates were analyzed at day 4 and day 11-12, and 2 biological replicates were analyzed at day 18. Each biological replicate corresponded to the apical secretome collected from:

- a pool of 3 different Transwell® from the same donor for NHBE cells,
- a pool of 3 different Transwell® from 2 different culture batches for Calu-3 cells.

A label-free quantitative proteomic analysis using LC-MS/MS was performed after protein digestion with trypsin. The analysis was run at the Proteomic platform (Université de Paris, CNRS, Institut Jacques Monod).

Briefly, 16 µg of proteins were precipitated in cold acetone, then resuspended in 25 mM NH_4HCO_3 buffer before trypsin digestion overnight (V5111, sequencing-grade Trypsin, Promega). Peptides were desalted and concentrated using 10µL ZipTip µ-C18 Pipette Tips (Millipore). The peptides were analyzed on a Q-Exactive Plus mass spectrometer coupled to a

Proxeon 1000 Nano-LC (ThermoFisher). Peptides were separated by liquid chromatography using the following specifications: Acclaim PepMap100 C18 pre-column (2 cm, 75 µm i.d., 3 µm, 100 Å); Pepmap-RSLC Proxeon C18 column (50 cm, 75 µm i.d., 2 µm, 100 Å); 300 nL/min flow rate, 98 min gradient going from 95% solvent A (water, 0.1% formic acid) to 35% solvent B (100% acetonitrile, 0.1% formic acid) followed by column regeneration (total time 120 min). Peptides were first analyzed in positive mode in the Orbitrap cell at high resolution, with an m/z range of 375-1500. MS/MS data were acquired in the Orbitrap cell in a Top20 mode with an AGC target of 3.10^6 for full MS. Fragments were obtained by Higher-energy C-trap Dissociation (HCD) activation with a collisional energy of 27%, a quadrupole isolation window of 1.4 Da, and an AGC target of 2.10^5. MS/MS data were acquired in a data-dependent mode with a dynamic exclusion of 30 s. Monocharged peptides or peptides with unassigned charge states were excluded from the analysis. The maximum ion accumulation times were set to 50 ms and 45 ms for MS and MS/MS acquisition respectively.

Label-Free quantitation was performed with Progenesis QI software (Waters) using the HI-3 method for protein quantification. Data were processed with Proteome Discoverer 2.2 software (ThermoFisher Scientific). The mass tolerance was set to 6 ppm for precursor ions and 0.02 Da for fragments. The MASCOT software (Matrix Science, v. 2.4) was used for protein identification on the Homo sapiens and Bos Taurus Swissprot databases (2019).

The following post-translational modifications were searched in dynamics parameters: oxidation (M), phosphorylation (S/T/Y), acetylation (Protein N-terminal). The maximum number of missed cleavages was limited to 2 for trypsin digestion. P-values of peptides were calculated using the percolator algorithm, and a 5% threshold was applied. Filters used in the MASCOT software correspond to proteins identified with a minimum of 2 peptides, a MASCOT score > 40, and a p-value < 0.05. Extracellular proteins were identified using the extracellular compartment database of the Progenesis software.

b) Analysis of the acellular and cellular protein corona

AgNPs with their protein corona were isolated from the secretome by centrifugation (see 2.3-5) and proteins were separated from the nanoparticles by SDS-PAGE as described before (see 2.6-2 b). Label-free quantitative proteomic analysis of acellular and cellular protein corona was performed by LC-MS/MS following protein digestion with trypsin on the Orbitrap Fusion Tribrid MS at the National Institute for Cellular Biotechnology (NICB)-Dublin City University. Each analysis was performed in triplicates. Peptides were separated by liquid chromatography for 60 min in high-resolution mode. Before LC-MS/MS, proteins were digested. Briefly, using a clean razor blade, the protein band was cut from the gel and kept in microcentrifugation tube prewashed with acetonitrile (ACN). The gel was distained using 40% methanol and 10% acetic acid in water for 10 min, and dehydrated with 2 serial incubations of 200 mM ammonium bicarbonate/ACN (2:3 V/V) and 100% ACN for 10 min at 37°C. Then, the proteins were denatured with 10 mM DTT in 100 mM ammonium bicarbonate for 1 h at 56°C followed by reduction and alkylation step with iodoacetamide (144-48-9, Sigma-Aldrich) for 30 min in the dark. After the gel was rinsed with ammonium bicarbonate and ACN at 37°C, 20 µg/mL Trypsin Gold (V5280, Promega) diluted in 50 mM ammonium bicarbonate was added, and the samples were incubated overnight at 37°C with gentle mixing. Peptides were extracted and recovered from the gel by 2 incubations with 30% ACN/0.2% trifluoroacetic acid. All the extracted peptides were pooled in a new tube. Purification and concentration of extracted peptides were done using Pierce® C18 tips (87783, Thermo Scientific).

Protein and peptide identification for all MS raw files were performed with MaxQuant software using the search engine Andromeda (J. Cox et al. 2011). Enzymatic digestion with trypsin was selected, together with a precursor mass tolerance of 10 ppm and a fragment tolerance of 0.5 Da. The search database used FASTA file on the *Homo sapiens* and *Bos taurus* from RefSeq NCBI database (2021).

The following post-translational modifications were searched in dynamics parameters: oxidation (M), phosphorylation (S/T/Y), acetylation (Protein N-terminal). The maximum number of missed cleavages was limited to two for trypsin digestion. The false discovery rate (FDR) was set to 0.01 for both peptide and protein identifications. Normalized label-free quantification was done by applying the MaxLFQ algorithm set up in MaxQuant software.

The identified proteins were further analyzed using Perseus software (Tyanova et al. 2016). Potential contaminants and false positive proteins were excluded from the analyzes.

2.6-4 Bioinformatic analysis of the proteomic data

The bioinformatic analysis and the corresponding figures were developed using R software (v. 3.6.2). Heatmaps were represented using the ‘pheatmap’ package (Kolde 2019), where correlation clustering distance row was applied. PCA was calculated from the abundance of the extracellular proteins identified in each replicate and the results were presented using the ‘ggbiplot’ package (Vu 2011). The ‘packcircles’ package (Bedward, Eppstein, and Menzel Peter 2018) was used to represent protein abundance, where the circle area is proportional to each protein abundance.

2.7 Biological pathways and gene ontology terms enrichment analysis

We used a web-based implementation of g:Profiler (https://biit.cs.ut.ee/gprofiler/gost) to perform functional enrichment analysis based on the biological pathways and gene ontology terms associated with each protein. Functional enrichment was done with g:GOSt, which provides functional information for each gene and detects statistically significantly enriched terms. The analysis was performed using g:SCS algorithm with a threshold of 0.05.

2.8 Statistical analysis

The statistical analysis was performed with Prism GraphPad Software (v. 7.0). Data were expressed as mean ± standard error of the mean. All data passed the D'Agostino and Pearson or the Shapiro-Wilk normality test ($\alpha = 0.05$). When comparing groups, multiple comparison two-way ANOVA corrected with Benjamini, Krieger and Yekutieli test was used. For comparing time variability within the group, three-way ANOVA corrected with Benjamini, Krieger and Yekutieli test was used. For Lucifer yellow permeability, the Bonferroni-Dunn t-test method was applied. P-values < 0.05 were considered as statistically significant.

Chapter 3: Using Calu-3 cell line to establish a long-term bronchial epithelium model at the air-liquid interface

The respiratory tract is the main route of exposure to airborne particles. Among them, nanomaterials (NMs) have become a potential hazard for human health due to the increase in their production and use. The lung toxicity can be studied on animals following NM instillation or inhalation. However, the cost of such studies and their inability to cope with a large number of NMs, led to the exploration of new approaches for rapid toxicity screening. Moreover, the uncertainties on the data extrapolation from animal models to humans, as well as ethical issues, have favored the development of *in vitro* models of the human respiratory epithelium. The availability of human cells combined with progress in culture conditions to promote *in vitro* differentiation has opened the way to new human models to better assess NM toxicity (Fang and Eglen 2017).

Human primary airway cells are commercially available and represent a gold standard to evaluate the chronic toxicity of xenobiotics, including NMs, *in vitro* (García-Salvador et al. 2021). Indeed, they can be maintained in culture for several weeks when grown on inserts at the air liquid interface (ALI). They also form a tight bronchial epithelium similar to what is observed *in vivo*, which is composed of different cell types. Unfortunately, they present some limitations due to their cost and limited availability, the low rate of cell expansion, and donor variability (Rayner et al. 2019). Besides, in the context of nanotoxicology, nanoparticle (NP) translocation studies are limited by the pore diameter of the insert, which is 0.4 µm in diameter for normal human bronchial epithelial (NHBE) cells.

Alternatively, human lung cell lines derived from tracheobronchial cells, such as BEAS-2B (Feng et al. 2019; Vranic et al. 2018) and Calu-3 (Jeong et al. 2019; Cingolani et al. 2019; Forti et al. 2011), from bronchoalveolar cells, such as NCI-H92 and 16HBE, or from alveolar cells, such as A549 (George et al. 2015), have been largely used in the toxicological studies of xenobiotics. However, most of the studies were limited to the study of the acute toxicity (Jeong et al. 2019; Vranic et al. 2017), because the cells need regular passages when classically grown in plastic flask. Among these cell lines, Calu-3 has the advantage of being able to differentiate and form a tight epithelium that secretes mucus when grown at the air-liquid interface (Figure 33) (Madlova et al. 2009; Braakhuis et al. 2015). This makes Calu-3 cells a suitable model of the human bronchial epithelium for chronic toxicity studies of NMs. It also allows exposing cells on their apical side at ALI, directly on the mucus layer.

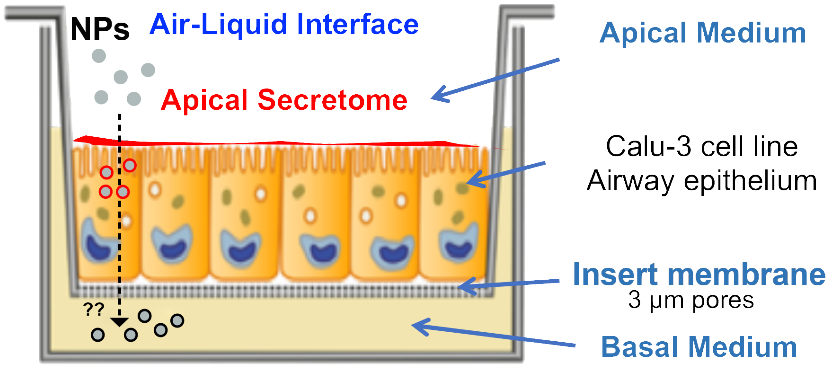

Figure 33: Schematic of Calu-3 cultures at the air-liquid interface for the study of NP toxicity and translocation through the bronchial epithelium.

Calu-3 cells were seeded on inserts having a membrane with a 3-µm porosity in diameter, with culture medium added both in the apical and basal compartment. When the culture reached confluence, the apical medium was removed, and cells were kept at ALI, letting cell to differentiate, formation of a tight epithelium a and mucus secretion (here denoted as the apical secretome).

Our aim in this study is to improve the culture conditions of Calu-3 cells to design a 3D bronchial epithelium model for chronic exposure to nanoparticles. This model will be used to investigate the biological responses of the epithelium, the NP translocation, and the formation of the biomolecular corona on NPs in the secretome in the presence of cells. These improvements include the reduction of Foetal Bovine Serum (FBS) supplementation in the culture medium – to reduce the amount of exogenous proteins, and the use of inserts with a large porosity – to follow NP translocation through the epithelium and the insert (Figure 33). At the same time, we would like to obtain a culture that differentiates into a functional epithelium, and which can be kept at ALI for several weeks.

FBS is necessary for cell culture, but minimizing the intake of exogenous proteins is important for drug and particle toxicological studies. FBS proteins can form complexes with some drugs, changing their bioavailability. Moreover, NPs are known to adsorb proteins on their surface, forming a so-called protein or biomolecular corona that drives nanoparticle-cell interactions and can profoundly change their biological fate and effects (Shaw et al. 2016; Konduru et al. 2017). Although in cultures at ALI, NPs were deposited on the apical side and the culture medium containing serum was added to the basal compartment only, it cannot be excluded that some serum proteins could diffuse from the basal to the apical compartment. This is why we explored the possibility to reduce the FBS concentration in the basal medium without affecting the epithelial barrier properties. Another change we made compared to the classical Calu-3 cultures was to grow cells on inserts having a membrane of large porosity (3 µm in pore diameter instead of the standard 0.4 µm) in order to have a model suitable for NP translocation studies.

To achieve our objectives, the study was organised in 3 tasks:

- Establishment of long-term Calu-3 cultures using inserts with a porosity of 3 µm to perform chronic toxicological studies of NMs in the future;
- Reduction of FBS supplementation in the basal medium and analysis of its impact on the epithelial barrier integrity and on the protein secretion in the apical secretome;
- Morphological and functional comparison of Calu-3 and NHBE epithelial models.

The results presented in this chapter were part of the results published in Scientific Reports (Sanchez-Guzman et al. 2021).

3.1 - Establishment of Calu-3 epithelial barrier on 3-µm pore inserts at the air-liquid interface

The 0.4-µm pore inserts are the most commonly used to grow Calu-3 cells, but it may impair the translocation of NPs from the apical to the basal compartment. NPs could accumulate in the pores or between the epithelial barrier and the membrane, preventing their crossing to the basal compartment and the accurate quantification of NP translocation. To have a model suitable for future NP translocation studies, it was necessary to establish the Calu-3 culture using larger pores (d = 3 µm). However, the large porosity of the insert membrane may prevent the establishment of an efficient tight epithelium. This effect was evaluated by measuring the trans-epithelial electrical resistance (TEER) and the permeability of Lucifer Yellow (LY), both in submerged conditions and at ALI. Because of the development of tight junctions, the TEER increased and contrary, the paracellular transport of LY through the epithelium decreased. Indeed, following a short incubation time (60 min), LY can cross the epithelial barrier via the paracellular route only, which occurs in case of leakiness of the epithelium induced by dysfunction of tight junctions (Lemmer and Hamman 2013; Cornu et al. 2020).

In this study, Calu-3 cells were seeded at a density of 5×10^5 cells per insert and grown in submerged condition with minimum essential medium (MEM) supplemented with 10% FBS. The ALI was established by removing the apical medium after the cultures were considered confluent (TEER ≥ 700 Ω.cm^2). One day later, the basal medium was replaced by MEM with 0, 2, 4 or 8% FBS supplementation, corresponding to the different experimental conditions tested (Figure 34). The basal medium was changed every 2-3 days. TEER and LY values were measured in submerged and ALI cultures and the minimum TEER value and maximum LY permeability for a tight epithelium defined (Figure 35).

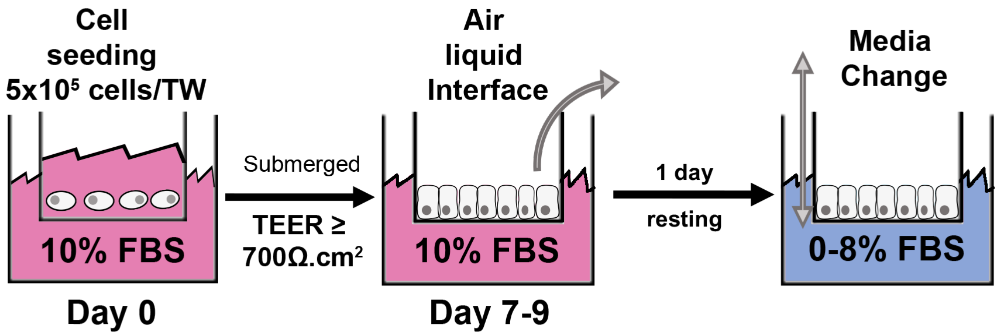

Figure 34: Scheme of the protocol for Calu-3 culture on inserts.

Culture established on a 3-µm porosity, from the seeding of the cells to the culture at ALI with different FBS supplementation in the basal culture medium.

When cultures are submerged, the TEER values increased and LY permeability decreased with time, rising to around 600 Ω.cm^2, and less than 2% permeability 6 days after seeding, respectively (Figure 35a). However, after the ALI was induced, the TEER dropped transiently to a minimum value of 300 Ω.cm^2, while a LY permeability smaller than 2% was preserved (Figure 35b). Similar results were reported by others (Grainger et al. 2006; Stentebjerg-Andersen et al. 2011) with lower TEER values at ALI compared with submerged cultures. These results were used to establish the TEER baseline in submerged and ALI conditions: a minimum of 700 Ω.cm^2 was needed before inducing ALI, reflecting the confluence of the culture; a minimum of 300 Ω.cm^2 was associated with a tight epithelium at ALI (Mura et al. 2011).

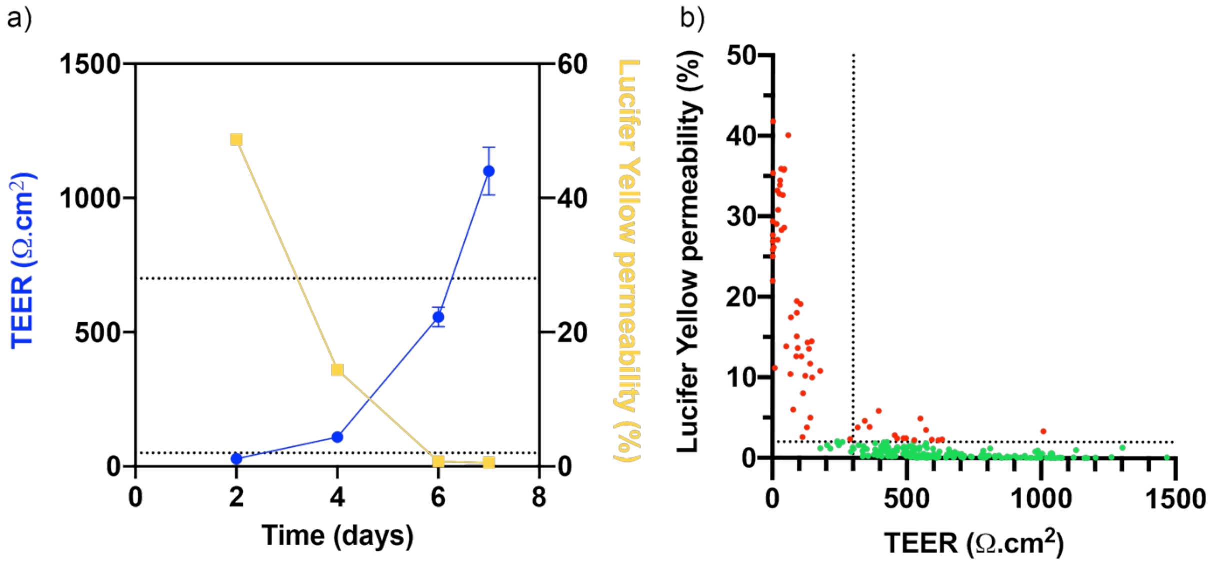

Figure 35 Determination of TEER and Lucifer Yellow permeability baselines

(a) TEER and LY permeability in submerged cultures 2, 4 ,6, and 7 days after seeding. (b) The TEER and LY permeability were measured on 236 different samples in ALI culture with tight or leaky epithelial barriers. The vertical dotted line corresponds to the maximum LY permeability defined by the manufacturer for a tight epithelium (LY permeability < 2%). The horizontal dotted line corresponds to the minimum TEER value we defined for a tight epithelium with Calu-3 cells in our experimental conditions based on our data (TEER > 300 Ω.cm²). Red dots correspond to samples with LY permeability > 2% and green dots correspond to samples with LY permeability < 2%.

The epithelium integrity, which was monitored with TEER and LY permeability, was completed by morphological and ultrastructural observations. Transmission electron microcopy (TEM) images showed a polarized epithelium (Figure 36a), where the apical part can be distinguished from the basal side by the presence of microvilli in the plasma membrane, tight junctions and desmosomes (Figure 36b and c). In addition, the intracellular apical part was richer in ribosomes and vesicles. The basal part of the cell attached to the insert membrane and harbored the nucleus. The tight junctions, an essential component of differentiated epithelial cells, are required for the polarized transport, the intercellular integrity, and for signaling (Eckert and Fleming 2008).

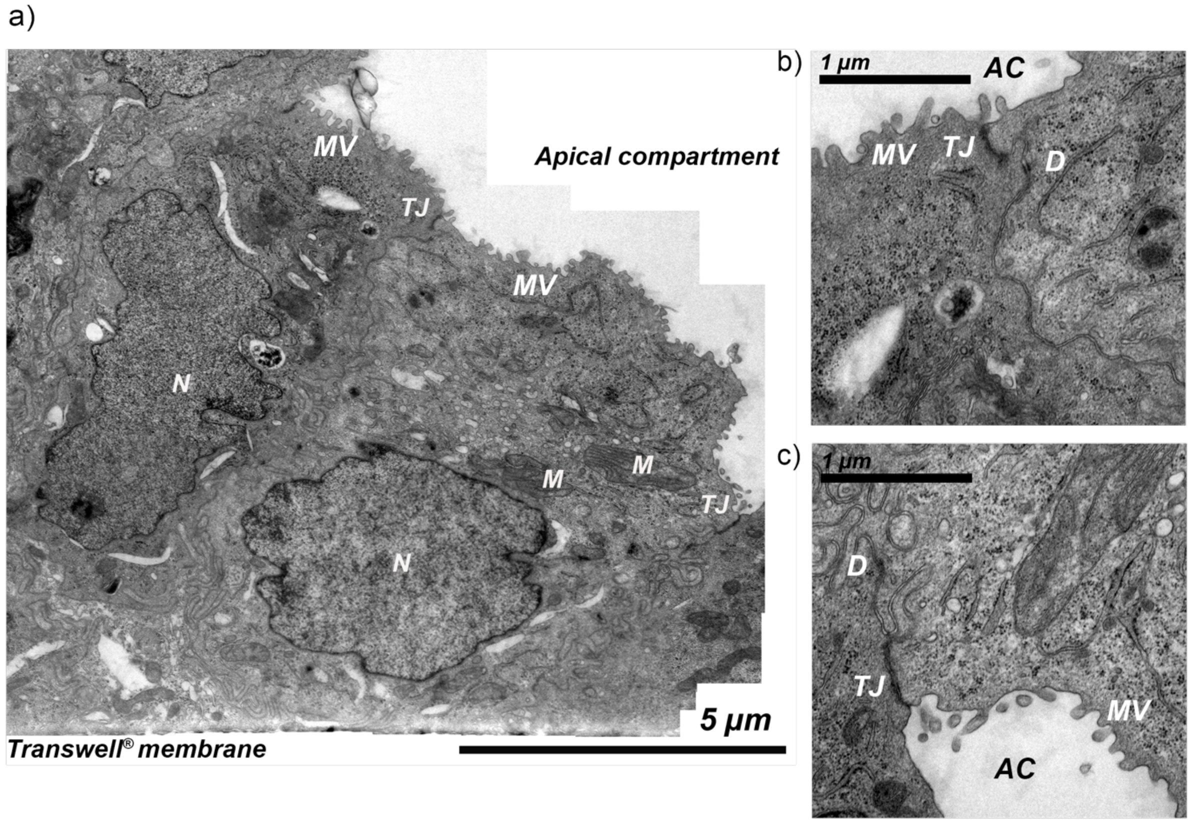

Figure 36: Morphological analysis of the Calu-3 epithelium by TEM.

TEM images of Calu-3 cells grown with 4% FBS in the basal medium and fixed 8 days after ALI. (a) Overview of the bronchial epithelium with the insert membrane at the bottom and the apical surface at the top right. (b-c) Tight junctions and desmosomes. N nucleus, TJ tight junctions, D desmosomes, M mitochondria, AC apical compartment, MV microvilli.

3.2 - Effect of reduced serum supplementation on Calu-3 epithelium

The protocol used for these experiments is described in Figure 34.

3.2-1 Integrity of the epithelial barrier

The *in vitro* study of the protein corona that forms on NPs may become less relevant due to the presence of serum proteins, which composition differs from the epithelial lung lining fluid. To solve this issue, we investigated the possibility to modulate the FBS concentration. However, it is known that the reduction of serum concentration in the culture medium could impair cell viability, and here the epithelial barrier integrity. We compared the effect of 0, 2, 4 and 8% FBS supplementation in the basal medium after ALI. We monitored the epithelial integrity to determine which conditions could sustain a tight epithelium over a long period (up to 4 weeks).

The integrity of the epithelium was monitored in 3 independent experiments (Figure 37a-c) with 3 technical replicates per experiment. The measurements of the TEER were performed every 2-3 days in replicates 1 and 2 (Figure 37a and b). In replicate 3, the TEER was measured every 4 to 7 days to reduce the manipulation of the culture (Figure 37c). No significant barrier alteration was observed in comparison with the other 2 replicates.

During submerged periods, we observed an increase of the TEER with time, reaching maximum values of 738 ± 98 $\Omega.cm^2$, 940 ± 52 $\Omega.cm^2$ and 1068 ± 72 $\Omega.cm^2$ in replica 1, 2 and 3 respectively. These maximum values were observed at different times before ALI induction. After 1-2 days at ALI, the TEER values dropped to 682 ± 49 $\Omega.cm^2$ and 607 ± 58 $\Omega.cm^2$ in replicates 2 and 3 respectively. By contrast, in replicate 1, 3 days after ALI, the TEER values were maintained at 794 ± 127 $\Omega.cm^2$. Following the change of the basolateral medium to match the experimental conditions (0 to 8% of FBS), the TEER values were always >300 $\Omega.cm^2$ during the 25 days of culture, whatever the serum concentration, with only minor differences between conditions. The 3 replicates followed the same trend over time. At the beginning, there were no significant change in TEER independently of the serum concentration, with the exception of replicate 1. In this case, we observed significantly lower values for 8% FBS at day 16, 17 and 18, and restoration of normal values at day 21. The highest TEER values were observed when cells were grown with 2% FBS in the 3 biological replicates. These values were significantly different to the other conditions in replicates 1 (day 21) and 2 (day 14). Surprisingly, the lowest values were observed with 0 and 8% FBS culture conditions.

The epithelial barrier integrity evidenced by the TEER measurements was confirmed by the measurement of the LY permeability. After ALI, LY permeability always remained below the maximum value (2%) recommended by the manufacturer (Figure 37d). These values were compared to the permeability of an empty insert, which confirmed the passage of LY through the inserts (30-40 % corresponding to the maximum permeability).

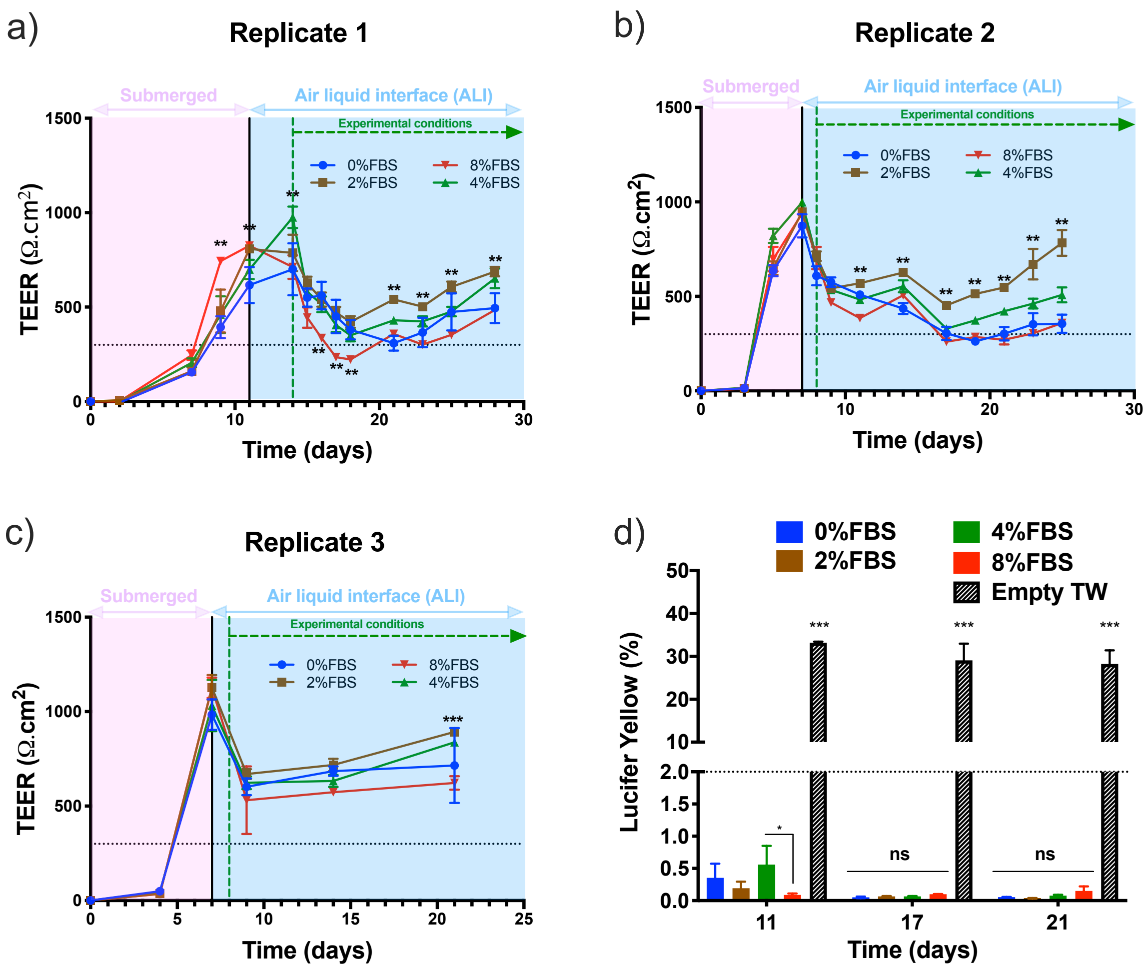

Figure 37: Time course study of the epithelial barrier integrity as a function of FBS supplementation (0, 2, 4, 8%) in the basal medium after ALI

*(a-c) TEER measurement of 3 independent experiments. Error bars represent the variability of the 3 technical replicates expressed as mean ± SEM. (d) Lucifer Yellow (LY) permeability assay at 11, 17 and 21 days after seeding of replicate 2. Empty insert was used as a negative control for LY measurement. n= 3. * p-value < 0.05, *** p-value < 0.001.*

3.2-2 Mucus secretion

The effect of FBS reduced supplementation on the apical protein secretion by Calu-3 cells was monitored for 17 days at ALI. The total protein concentration significantly increased with time and with FBS percentage (Figure 38a). Because of different starting points at ALI between the biological replicates, we did not collect the apical secretome at exactly the same time points. In Figure 38, the orange squares represent the mean values of 2 independent biological replicates. The red and blue squares represent the mean values of 3 technical replicates in replicate 1 and 2, respectively. Nonetheless, the same trends in protein production were always observed whatever the replicates, with an increase of protein secretion over time and with FBS %. The results reflected the increase in the metabolic activity, which could be due to a more advanced stage in the differentiation of the epithelium.

A representative protein profile of the apical secretome of Calu-3 cells at ALI obtained by SDS-PAGE is shown in Figure 38b.The same amount of proteins was loaded in each well. 3 technical replicates per conditions are shown. The proteins were detected by SYPRO ruby staining. No difference in the protein profile was observed between the different experimental conditions. The mucins were unable to enter the gel and to migrate during electrophoresis, due to their larger size and high glycosylation. We suppose that they remained at the bottom of the well. The presence of MUC5AC (Figure 38c) and MUC5B (Figure 38d) in each well was confirmed by immunodetection on Western blots (WB). Variability in the detection of the mucins on the WB membranes was observed between conditions, possibly due to the difficult transfer of highly glycosylated proteins to the nitrocellulose membrane or sample variability. Interestingly, some MUC5AC and MUC5B fragments could migrate into the gel and could be detected by WB. One MUC5B fragment with a molecular weight of 97.6 kDa was observed.

To evaluate mucin secretion, we used the ELLA assay (Figure 38e-f). This assay is not specific to mucins, but to glycoproteins. Here, we used it first as a surrogate to evaluate mucin concentrations in the apical secretome. Indeed, mucins are essential components of the mucus layer forming the epithelial lining fluid. Surprisingly, the glycoprotein concentration followed a different trend compared to the total secreted protein concentrations, in the different culture conditions. In particular, at 0% FBS, the glycoprotein concentration in the apical secretome was significantly higher than for the other FBS concentrations after 10 days at ALI (Figure 38e). We normalized the glycoprotein concentration to the total protein concentration at each day (Figure 38f). The comparison of normalized glycoprotein values showed statistically significant differences between 0 and 2% FBS from day 3 after ALI, and between 0 and 4-8% FBS from day 4 after ALI. In addition, we observed that the production of glycoproteins was stable once the epithelial barrier was well established for all cells cultured with reduced FBS supplementation. By contrast, a complete lack of FBS induced the hypersecretion of glycoproteins by Calu-3 cells at ALI.

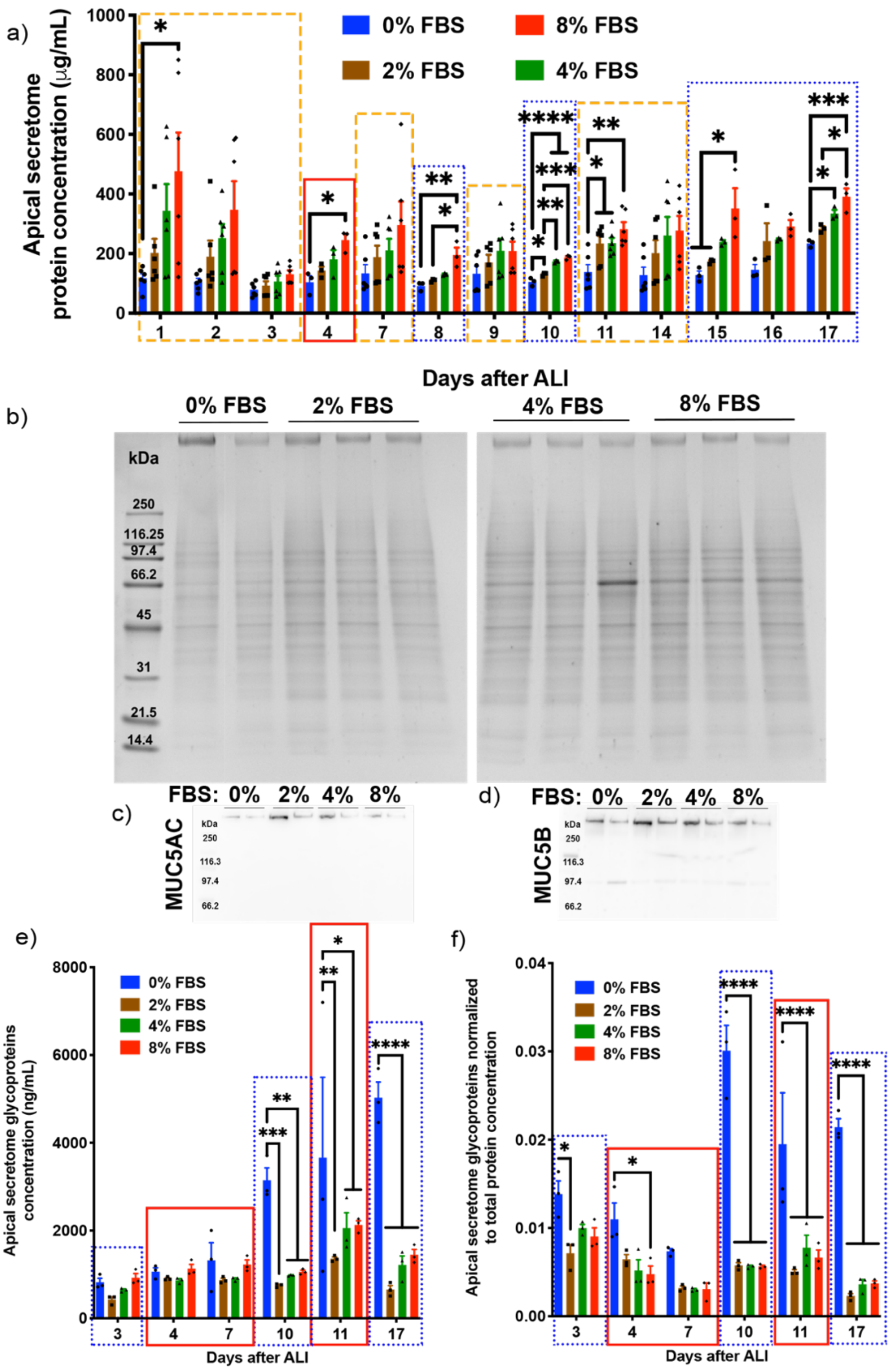

Figure 38: Effect of reduced FBS supplementation (0, 2, 4, 8%) on the protein content of the apical secretome of Calu-3 cultures from day 1 to day 17 after ALI.

(a) Concentration of total proteins in the apical secretome at different time points after ALI. (b) SDS-PAGE protein profile of the apical secretome at day 14 after ALI: 10 µg of protein were loaded in each well. Proteins were detected with SYPRO® ruby. 2 to 3 technical replicates were loaded in each well for each serum condition (c-d) Western blots using (c) anti-MUC5AC and (d) anti-MUC5B primary antibodies. (e) Glycoprotein concentration of the apical secretome at different time points after ALI. (f) Glycoprotein concentration normalized by the total protein concentration in the apical secretome. Orange squares are the means of two biological replicates. Red and blue squares are the means of 3 technical replicates for replicate 1 and replicate 2, respectively. One-way ANOVA statistical analysis was used for each time point.

The presence of tight junctions and mucins was confirmed by fluorescence confocal microscopy in Calu-3 cultures supplemented with different percentages of FBS. The immunolabelling of the tight junction associated protein, zonula occludens-1 (ZO-1), and the gel-forming mucin MUC5AC (Figure 39a-d) showed that both proteins were expressed in the cultures independently of FBS supplementation. ZO-1 staining confirmed the formation and preservation of tight junctions in long-term Calu-3 cultures. MUC5AC staining confirmed the secretion of mucins in the apical part of Calu-3 cultures. However, the intensity and distribution of MUC5AC labelling differed depending on FBS supplementation in the basal medium. MUC5AC labelling appeared as small dots distributed in the apical region of the cell for 2, 4 and 8% FBS conditions, whereas it formed large patches that appeared as thick mucus filaments for the condition without FBS. These results are in agreement with the glycoprotein quantification by the ELLA assay.

The presence of mucus vesicles inside Calu-3 cells was confirmed by TEM observations (Figure 39e-f). In Figure 39e, one Calu-3 cell full of mucus vesicles is shown. We can see that mucus vesicles accumulated mainly in the apical region of the cell. This observation can explain the dot labelling seen after MUC5AC immunolabelling in 2, 4 and 8% FBS cultures. Without FBS, we observed filament-like MUC5AC staining, which could be due to an exacerbated secretion of the gel-forming mucins to the apical compartment, following the fusion of the mucus vesicles with the apical membrane (Figure 39f). The presence of a mucus layer outside Calu-3 cells was confirmed by scanning electron microscopy (SEM) 21 days after ALI (Figure 39g). Calu-3 cultures were fixed with a modified protocol to preserve the mucus layer for this experiment, with a first fixation step with osmium oxide (OsO_4). The mucus network is highlighted in green at a higher magnification in Figure 39h.

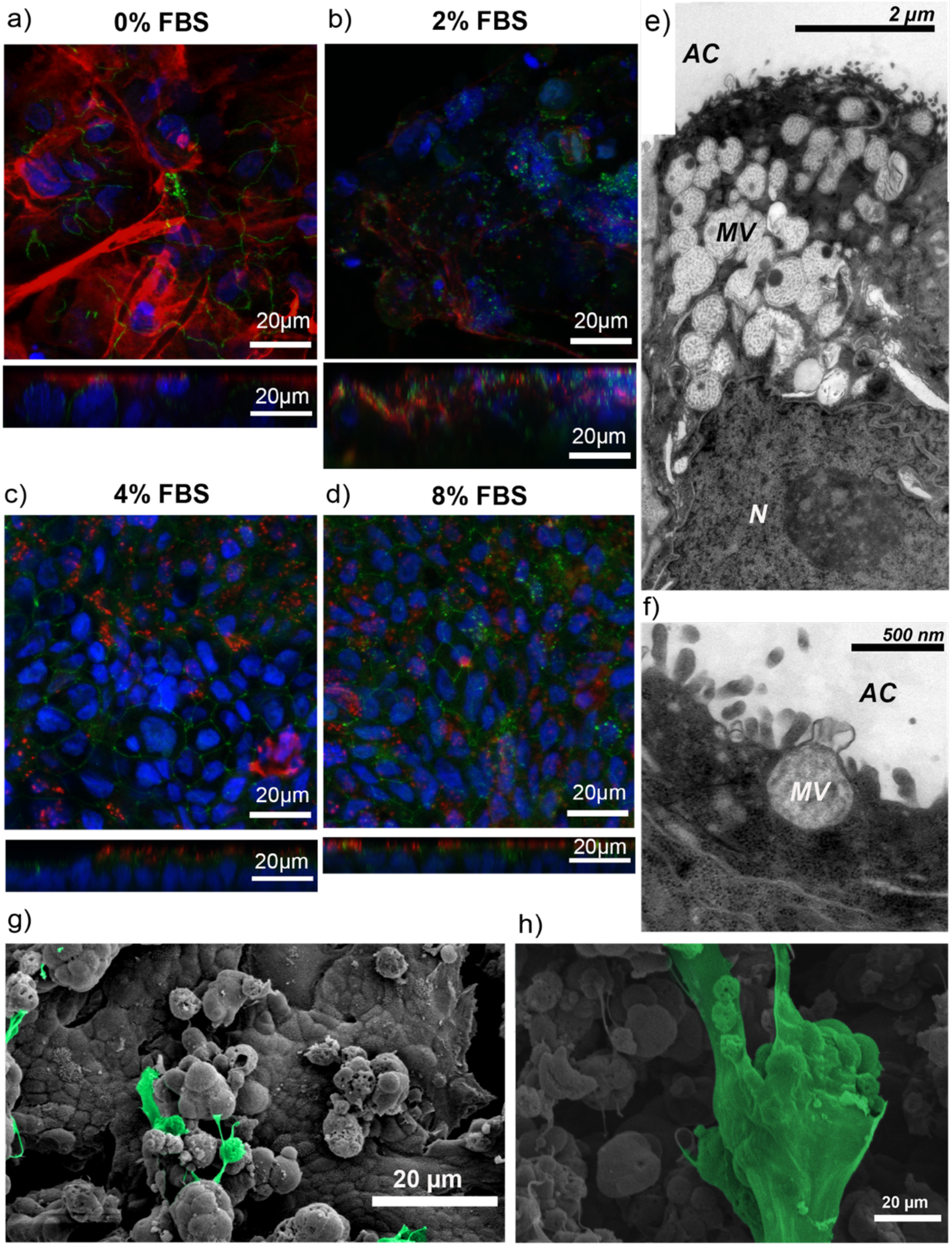

Figure 39: Characterization of mucus secretion by Calu-3 cells as a function of FBS percentage by fluorescence confocal microscopy, TEM and SEM.

(a-d) Immunolabelling of ZO-1 tight junction associated protein (green) and MUC5AC gel-forming mucin (red). Cells were fixed 17 days after ALI. (a) 0% FBS, (b) 2% FBS, (c) 4% FBS and (d) 8% FBS. All the cultures were co-stained with DAPI (blue). (e) TEM image of one Calu-3 cell containing mucus vesicles. (f) Detail of a mucus vesicle fusing with the plasma membrane at the apical surface. (g-h) SEM images of Calu 3 cells cultured with 4% FBS and fixed 21 days after ALI with OsO_4 to preserve the mucus layer. (g) Overview of the culture, (h) detail of the mucus layer. Mucus is highlighted in green. AC: apical compartment, MV: mucus vesicles, N: nucleus.

3.3 - Morphological characterization of the Calu-3 epithelium with 4% FBS supplementation

We selected a 4% FBS supplementation and performed further characterization of the Calu-3 culture at ALI by optical, confocal, and scanning electron microscopy. Optical images of Calu-3 cells on inserts (3-µm porosity) are shown in Figure 40. Two days after seeding, the cultures were not confluent, hence we can see the porous membrane of the insert and some areas covered by cells (Figure 40a). Following ALI induction, we obtained a fully differentiated epithelium, which evolved with time. 5 days after ALI (Figure 40b), the culture presented a flat surface. 7 days after ALI, the surface became rougher, suggesting the formation of polyp-like structures (Figure 40c). The formation of polyps might be a consequence of the loss of contact cell proliferation inhibition observed in tumor cells.

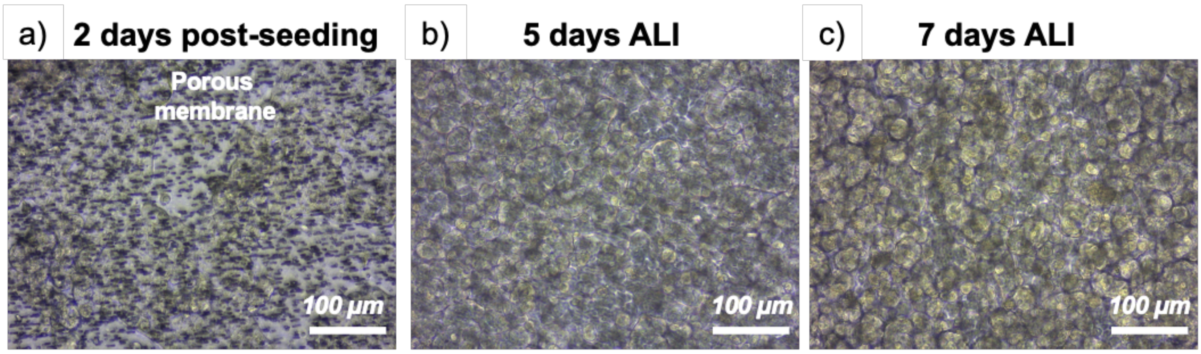

Figure 40: Optical microscopy images of Calu-3 cells on inserts with a 3µm-pore polyester membrane.

(a*) 2 days after seeding, (b) 5 days after ALI, (c) 7 days after ALI. Scale bar 100 µm.*

In order to evaluate the cell viability at ALI, we used the live/dead fixable green dead cell stain kit. The green fluorescence dye only penetrates the permeable membranes of dead cells and accumulates in the intracellular region. The nuclei were stained with DAPI in blue. The green/blue co-staining allows distinguishing dead cells from live cells (Figure 41). A heterogeneous distribution was observed, with some regions showing a higher number of dead cells compared to others. Although a quantitative analysis was not performed, the number of dead cells seemed relatively low in most regions.

The transversal view of the Calu-3 culture at ALI revealed differences in the thickness of the epithelial barrier. Some areas exhibited several layers of nuclei/cells, likely corresponding to the polyp-like structures (Figure 41b) seen by optical microscopy (Figure 40c). The thinner parts of the culture, where no stratification occurred, did not exhibit green labeling, suggesting that they were predominately formed by living cells (Figure 41a). By contrast, dead cells were found mainly in the thickest parts of the epithelial culture, especially in the upper part of these multilayered zones as shown by the transversal view in Figure 41b. A 3D confocal image reconstruction (Figure 41c) better showed these multilayer cell structures with the enrichment in dead cells in the top part. Altogether, these observations suggest that a cell removal process occurred in the culture, concentrated in the multilayered part of the epithelial barrier.

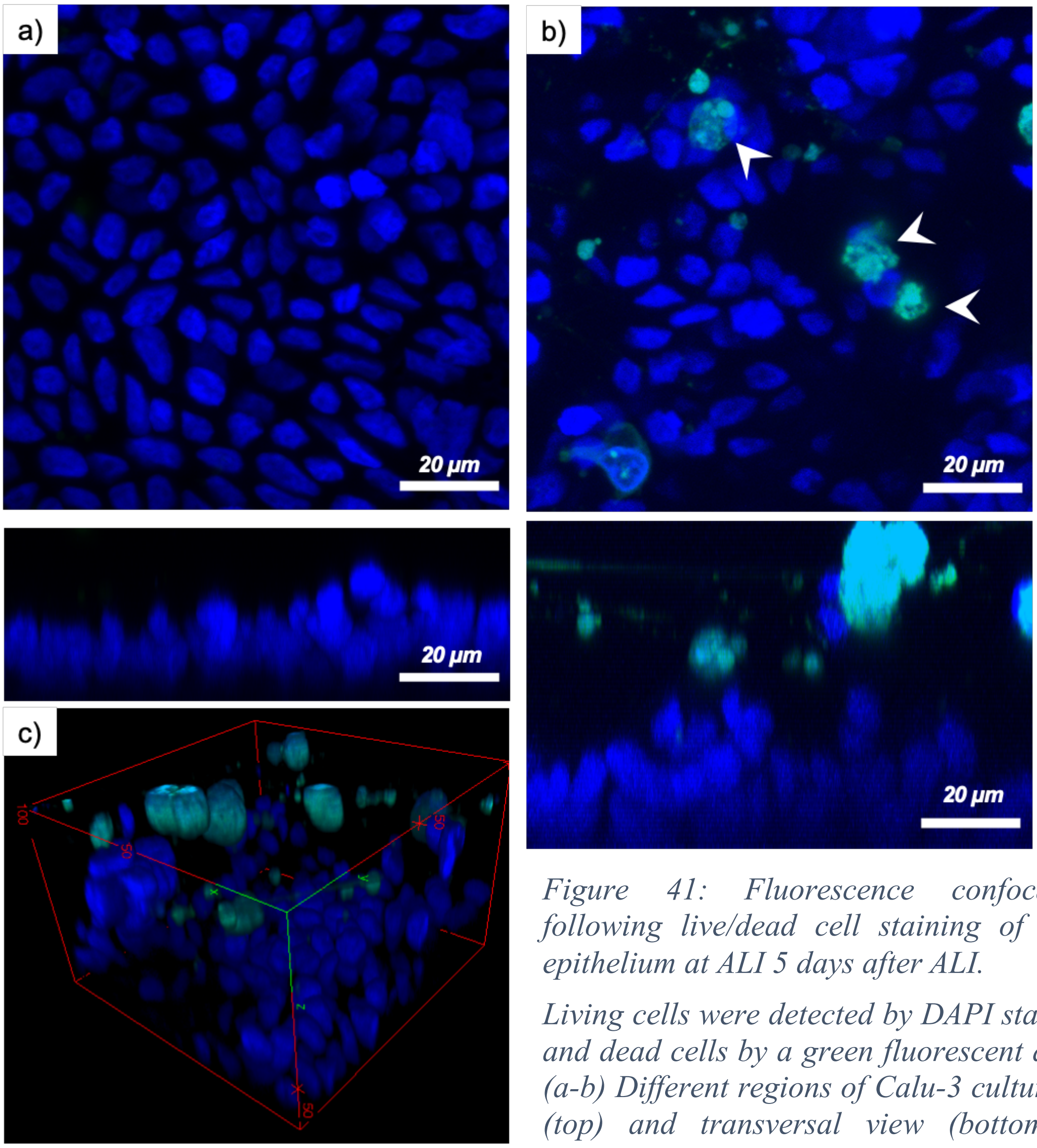

Figure 41: Fluorescence confocal images following live/dead cell staining of the Calu-3 epithelium at ALI 5 days after ALI.

Living cells were detected by DAPI staining (blue) and dead cells by a green fluorescent dye (green). (a-b) Different regions of Calu-3 culture: top view (top) and transversal view (bottom). (c) 3D reconstruction of image b.

SEM images confirmed the presence of multilayered regions especially after several days at ALI. SEM images provided a more detailed analysis of Calu-3 morphology (Figure 42). At 8 days after ALI, the culture mainly formed a monolayered epithelium with characteristic microvilli (Figure 42a and b). After 21 days at ALI, multilayered structures were observed corresponding to the polyp-like structures (Figure 42c). Additionally, the microvilli were preserved and better distributed in the long-term culture (Figure 42d). Those structures were also described in Calu-3 cultures grown at ALI with 2.5% FBS, where similar structures were more abundant after 3 week in cultures (Kreft et al. 2015).

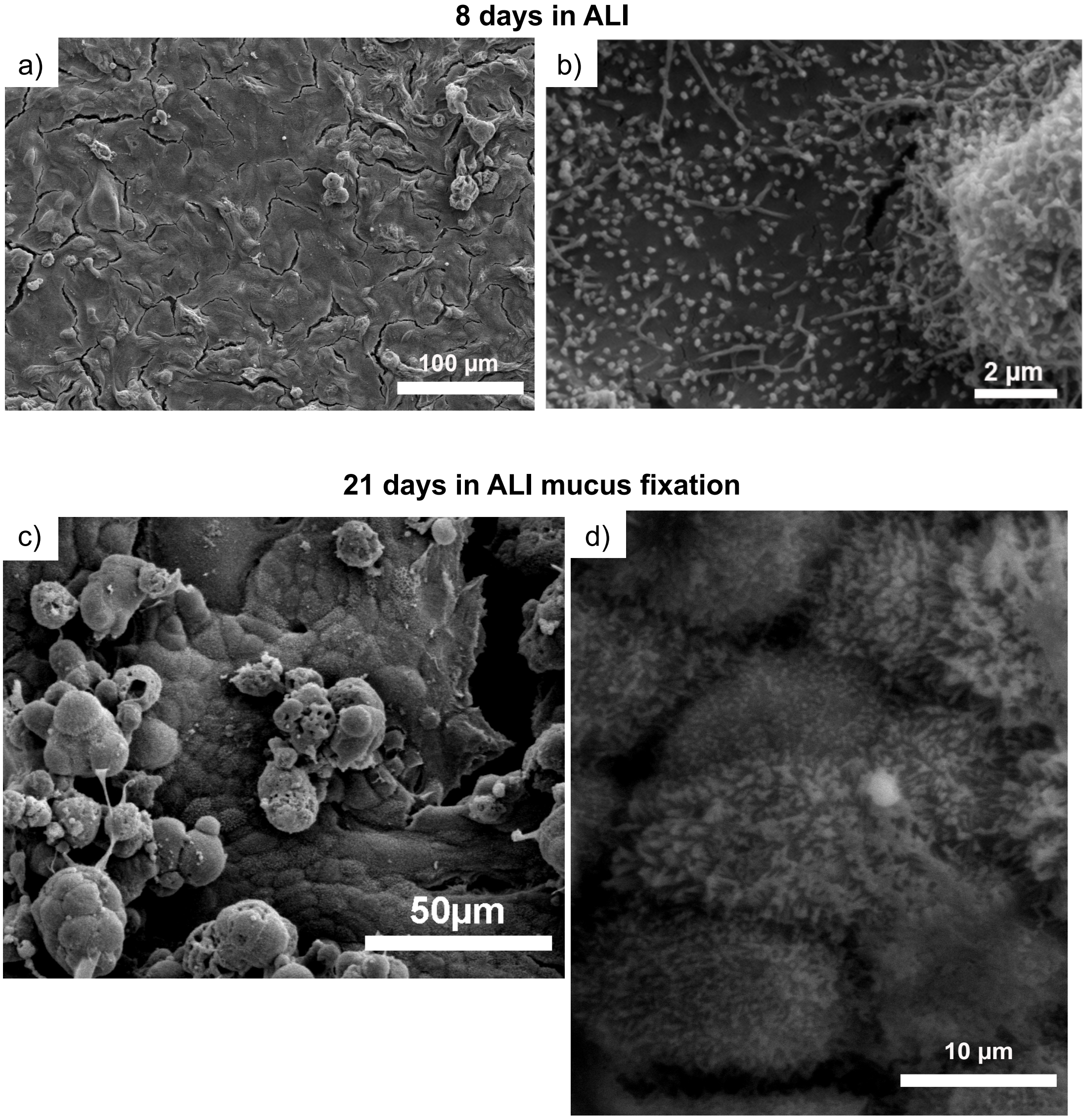

Figure 42: Scanning electron microscopy images of Calu-3 cultures at ALI (SEM).

(a) Panoramic view of Calu-3 cultures 8 days after ALI (b) detailed view of microvilli. (c-d) Calu-3 cultures observation 21 days after ALI using a specific protocol for mucus fixation. (c) General view and (d) microvilli details.

3.4- Characterization of Normal Human Bronchial Epithelial (NHBE) cells

As NHBE cells came from different donors and were kept for several days or weeks in culture, it was important to characterize these cultures in order to determine whether the barrier integrity and morphology were maintained, and that they presented similar features between different donors.

3.4-1 Epithelial barrier integrity

The primary normal human bronchial epithelial (NHBE) cultures were obtained from Epithelix and received already fully differentiated. They came from 3 healthy donors of different age and sex (Figure 43a). 3 inserts were available for each donor. At reception, the cultures had been at ALI for 12 days for donors 1 and 3, and for 26 days for donor 2. The NHBE epithelia rested for one day following reception. The epithelium integrity was checked every week by TEER measurement (Figure 43b). The epithelial barrier was considered tight for TEER values > 200 $\Omega.cm^2$ as recommended by the manufacturer. All the inserts presented TEER values > 200 $\Omega.cm^2$ except for donor 2, which exhibited a TEER of 117 ± 20 $\Omega.cm^2$ one week after reception. However, the culture recovered and exhibited good TEER values > 200 $\Omega.cm^2$ from day 14 at ALI. The NHBE cells from donor 2 had been at ALI longer than cells from donors 1 and 3 before reception (+ 14 days), which could explain this difference. The bright field images acquired to monitor the state of the cultures from the 3 donors (Figure 43c-e) showed that 4 days after reception, no visible differences were observed between donors 1 and 3, whereas black dots and vesicles were visible in NHBE cells from donor 2 (Figure 43d, lower image). The vesicles were mainly formed by ciliated cells, and high cilia beating was observed. Epithelix had already reported the appearance of black dots following culture stress, which may have been induced by the shipment. These stress signals could explain the lower TEER values observed in the epithelium from donor 2 compared to donors 1 and 3 after reception.

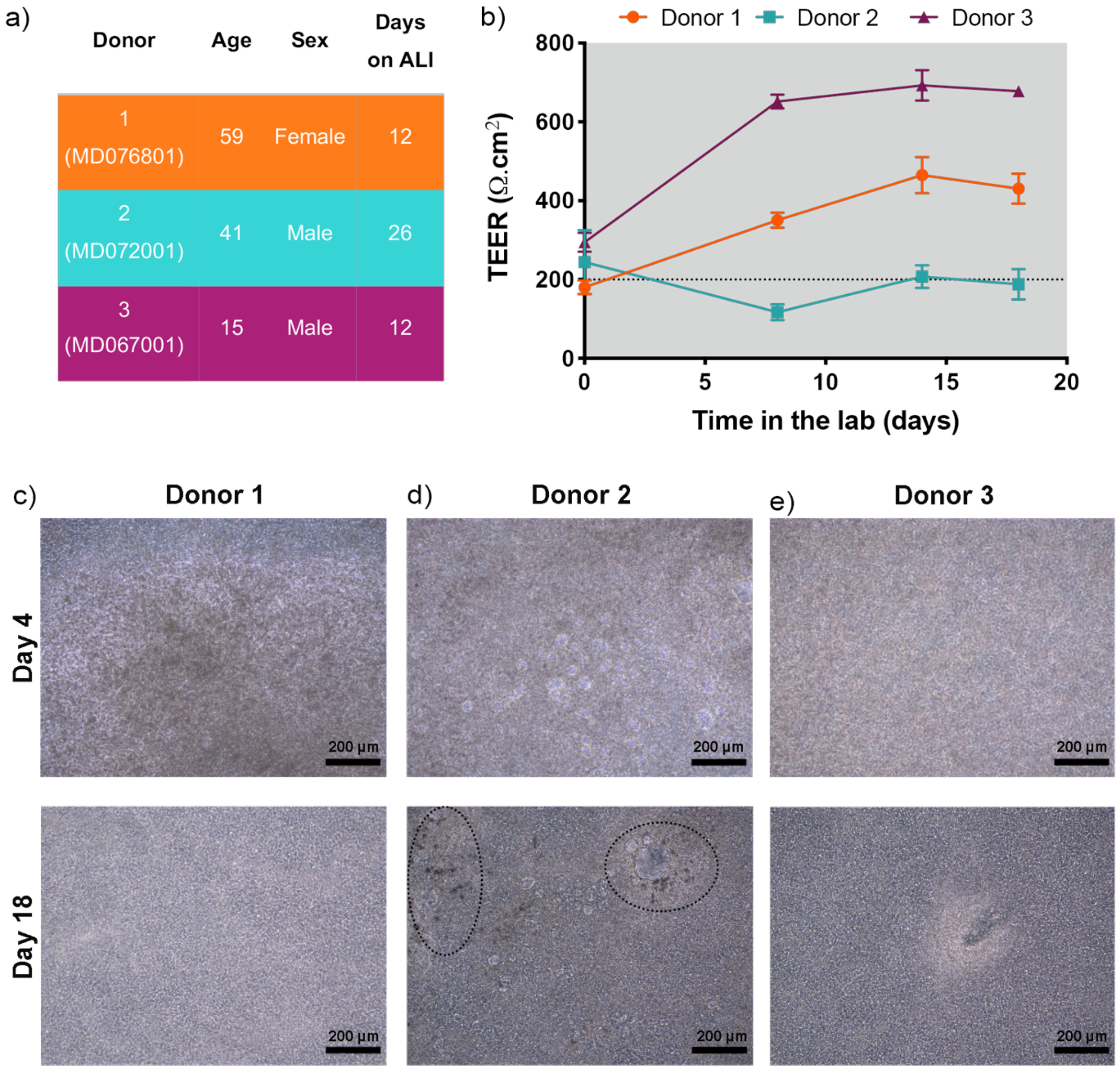

a)

Donor	Age	Sex	Days on ALI
1 (MD076801)	59	Female	12
2 (MD072001)	41	Male	26
3 (MD067001)	15	Male	12

Figure 43:TEER measurement and optical microscopy imaging characterization of the NHBE epithelia from 3 different donors provided by Epithelix.

(a) Table with the age and sex of the donors. (b) TEER measurements during the culture time in our laboratory. (c-e) Optical microscopy images from (c) donor 1, (d) donor 2 and (e) donor 3, 4 days after reception (top) and 18 days after reception (bottom). Black dots and vesicles are highlighted in the image of the cells from donor 2 (d).

3.4-2 Morphological and functional characterization of the epithelial barrier (Day 18)

The immunohistochemistry analysis showed a tight and functional secretory epithelium for the 3 donors at day 18 after reception (Figure 44). The tight junctions were visualized by immunolabelling of ZO-1 (Figure 44a-b), which was mainly detected closer to the apical part of the cells. The gel-forming mucin, MUC5AC, was localized inside specific cells only, corresponding to the goblet cells (Figure 44a). We did not detect any MUC5AC labelling outside the cells, likely due to the collection of the secretome and washing performed before cell fixation. Interestingly, the relative number of goblet cells was low compared to ciliated cells, in line with the expected cellular composition of the human bronchial epithelium (Knight and Holgate 2003). Although NHBE cells formed a flat epithelium, we found some regions with a larger thickness, populated mainly by ciliated cells (Figure 44b). These regions correspond to the vesicles, observed by optical microscopy (Figure 43d-e, bottom images), exhibiting high cilia beating. The paraffin sections showed a well-developed pseudostratified columnar epithelium, that is a single cell layer with irregular shape and columnar cells of different sizes, composed of goblet cells containing mucins (Figure 44c, red), ciliated cells stained evidenced by the GT335 cilia marker (Figure 44d, magenta), and flat basal cells on the insert membrane.

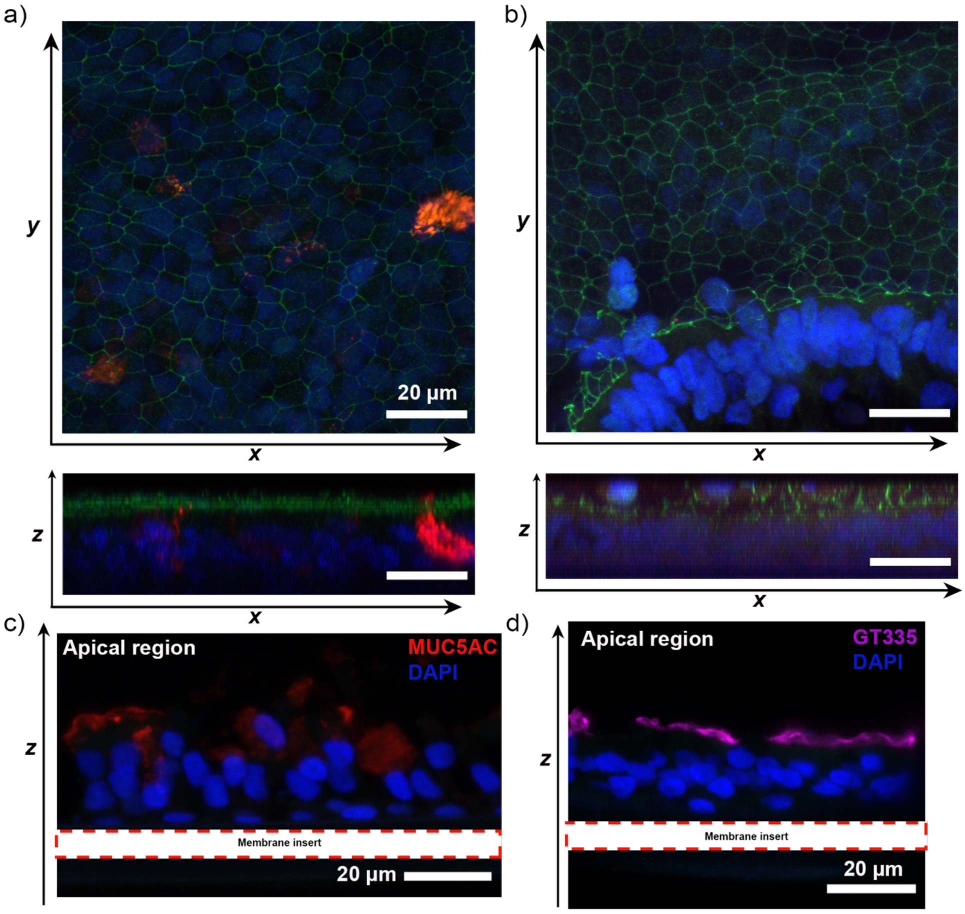

Figure 44: Characterization of the NHBE epithelium and paraffin-embedded z sections by immunolabelling 18 days after reception.

Images form donor 1 and 2. (a-b) Top view of two cultures immunolabelled for ZO-1 tight junctions associated proteins (green) and MUC5AC gel-forming mucin (red). The bottom image corresponds to the z-stack. (c-d) Inserts were embedded in paraffin and cut in 7-µm sections. Immunolabelling of (c) MUC5AC and (d) GT335 ciliated marker. All cultures were co-stained with DAPI (blue).

3.5 - Discussion

Our objective was to establish a functional 3D model of the bronchial epithelium at the air liquid interface, with a reduced FBS supplementation and insert of a large pore size, using the Calu-3 cell line. We provided evidence that the use of inserts with a large porosity, necessary for the analysis of NP translocation (F. Zhang et al. 2019), was compatible with the establishment and functionality of the epithelium at ALI for 18 days. This was demonstrated in particular in terms of barrier integrity.

The trans-epithelial electrical resistance has been commonly used to monitor the epithelium functionality and integrity. During the first stage of the epithelium development, the TEER values increased following cell growth and the establishment of the barrier. Immediately after ALI induction, the TEER values dropped, as reported by others (Grainger et al. 2006; Stentebjerg-Andersen et al. 2011; He et al. 2021), with higher TEER values measured in submerged compared to ALI conditions. The TEER values reported in the literature for Calu-3 cells vary depending on the culture conditions. In submerged cultures, the TEER ranged from 900 to 2500 Ω.cm^2 (Loman et al. 1997; Patel et al. 2002), whereas values at ALI were reported between 300 and 1000 Ω.cm^2 (Grainger et al. 2006; Mathias et al. 2002). The TEER variability may be related to differences in the experimental setup used.

Here, we used inserts with a large porosity to later use this model for nanoparticle translocation studies. This was not the case in most published studies. The high cell seeding density favored cell contacts, avoiding translocation of the cells to the basal compartment. In submerged condition, high TEER values ≥ 700 Ω.cm^2 reflected the epithelium confluence, which was necessary to avoid culture medium leakage to the apical compartment once ALI was induced. At ALI, the TEER values decreased to a minimum of 300 Ω.cm^2. LY permeability was measured, showing that the barrier integrity was preserved. Therefore, the maximum and minimum values of TEER were selected based on the epithelial LY permeability in our culture conditions. The formation of a tight epithelium blocked the paracellular transport of LY, and provided a more accurate and stable measurement of the epithelium tightness. We can notice that the minimum value of 300 Ω.cm^2 determined at ALI in our conditions was also used by others (Mura et al. 2011; Madlova et al. 2009).

Compared to standard culture conditions of Calu-3 cells, we also decreased FBS supplementation for the study of the protein corona of nanoparticles. The FBS concentration was reduced from the usual 10% (Grainger et al. 2006; Stentebjerg-Andersen et al. 2011; Babu, Chidekel, and Shaffer 2004) to 0-8% in this study. The FBS supplementation is essential for *in vitro* cell cultures. FBS consists of a cocktail of factors needed for cell attachment, growth and proliferation (Brunner et al. 2010). However, the use of serum presents drawbacks, especially in toxicology studies. FBS is composed of more than 1800 proteins and 4000 metabolites. It displays quantitative and qualitative variations between batches (Gstraunthaler, Lindl, and Van Der Valk 2013). Thus, FBS introduces unknown variables in the culture system. From a toxicology point of view, it is also known that serum proteins can form complexes with different drugs and pollutants, changing their bioavailability. For example, the toxicity of the organic pollutant, perfluorooctanoic acid (PFOA), on the human DLD-1 and A549 cell lines was attenuated by the binding of serum albumin to PFOA, which reduced PFOA uptake (R. Zhang et al. 2020). Moreover, in the context of nanotoxicology, NPs are prone to adsorb proteins on their surface, forming a protein corona that drives nanoparticle-cell interactions (Konduru et al. 2017; Shaw et al. 2016). Therefore, it is important to avoid the formation of a non-representative protein corona in *in vitro* models for nanotoxicology studies.

Alternatives to FBS also exist, such as a vegetal serum (Pazos et al. 2004) and human platelet lysates (Rauch et al. 2011), which were successfully used to grow and maintain epithelial cells. Unfortunately, these products are not commercially available. Moreover, the human platelet lysates cannot be used on all cell types due to incompatibility issues. Commercial serum substitutes exist, but their composition remains confidential. Whatever the alternatives, they all contain proteins that are different from the one present in the epithelial lining fluid produced by epithelial cells, and could compete with them when the protein corona forms on NPs if they are present in the apical and/or basal compartments.

The strategy we chose to reduce FBS interferences was to optimize and reduce FBS supplementation in the culture. We provided evidence that the integrity of the epithelium barrier was maintained with lower FBS concentration in the basal culture medium. The TEER measurements did not show any significant differences between cultures grown with 0 or 8% FBS. However, the higher TEER values were obtained in cultures supplemented with 2% FBS, followed by cultures with 4% FBS. No significant differences were observed in terms of LY permeability when comparing the different FBS concentrations. The TEER differences could be explained by differences in the epithelial thickness or ion transport between cultures (Ferruzza et al. 2013). The possibility to grow Calu-3 cells with lower FBS concentration was also demonstrated by Kreft *et al.* The authors developed Calu-3 cultures at ALI using advanced minimum essential media supplemented with 2.5% FBS (Kreft et al. 2015). In this condition, a well-established epithelium with microvilli and secretory vesicles was formed. This result is in agreement with our observations showing secretory vesicles (Figure 39e-f), microvilli (Figure 42b and d) and a well-structured network of tight junctions (Figure 38c-e) (Figure 39a-d).

The effect of FBS concentration on protein secretion was investigated in the apical compartment only. The concentrations of secreted proteins increased with FBS concentration in the basal compartment, which may be linked to a higher metabolic activity of the cells. A limited passage of proteins through a monolayer culture (hCMEC/D3 model for brain-blood barrier) was reported by Cox *et al.* with only a 4.7% of protein migration (A. Cox et al. 2018). The possible diffusion or transport of FBS proteins from the basal to the apical compartment was investigated by western blot and proteomic analysis of the secretome. The lack of antibodies specific for human vs bovine albumin did not allow to distinguish between BSA and HSA by western blot. However, the analysis of the peptide sequences by LC-MS/SM confirmed that HSA only was detected in the apical secretome of the Calu-3 cells. By comparing human vs bovine proteins in the secretome, we concluded that the contamination of the secretome by FBS was unlikely in our conditions. Finally, the amount of protein secreted increased with time (days at ALI) in all the conditions tested.

Among these proteins, the highly glycosylated mucins are involved in the formation of the mucosal gel (Rose, Lynn, and Kaufman 1979). Mucus contributes to the protection and clearance of both pathogens and inhaled particles in the upper airways. It is secreted both by the goblet cells in the airway epithelium and the mucous glands (Bals, Weiner, and Wilson 1999). A striking finding was the observation of the hypersecretion of glycoproteins in Calu-3 cell cultures grown without FBS. This result suggests that an exacerbated mucus production and release was driven by the extreme culture conditions. This feature is reminiscent of mucus hypersecretion involved in several airway diseases such as asthma, chronic obstructive pulmonary diseases (COPD) and lung cancer (Ridley and Thornton 2018; Rogers 2003; Turner and Jones 2009). The immunolabelling of MUC5AC revealed its presence in all the cultures, albeit with a higher amount in 0% FBS cultures. For the other FBS concentrations tested, the glycoprotein concentration in the apical secretome did not show any significant difference between 2, 4 and 8% FBS at day 3 and day 10 after ALI. However, at day 17, the cells supplemented with only 2% FBS showed a slightly lower glycoprotein concentration compared to 4 and 8% FBS. By contrast, 4 and 8% FBS did not show difference in time. Therefore, the 4% FBS condition was selected for the next experiments.

We have contributed to the development of the Calu-3 model to use it as an alternative to the NHBE cell model. The low cost, easy handling and the absence of donor variability of the Calu-3 model, make it interesting for screening the long-term toxicity of xenobiotics. However, the Calu-3 epithelium consists of only one cell type, goblet cells, contrarily to the NHBE epithelium, which is composed of goblet, ciliated and basal cells. The goblet cells are the main mucus producing cells in the airways contributing to the formation of the protective mucus layer. In this prospect, they are an appropriated model to understand the pathological consequences of nanoparticle inhalation. Although the cell composition is different between the Calu-3 and NHBE epithelia, we provided evidence that several functional features were shared, such as the barrier tightness and the mucus secretion, which are both maintained for several weeks, here up to 3 weeks at ALI. In agreement with Bovard *et al.* (Bovard et al. 2020) we reported morphological variabilities in the primary epithelial cultures prepared from different donors, though similar functionality and metabolic activity were observed after a week.

3.6 - Conclusion

To summarize, we improved the 3D model of the human bronchial epithelium using Calu-3 cell to deal with nanotoxicology endpoints such as NP translocation, chronic toxicity studies and protein corona analysis. We implemented 2 new adaptations in the culture - the large porosity of the insert membrane and the reduction of FBS concentration - that proved to be suitable for long term cultures at ALI. Our conclusions were drawn from a thorough characterization of the Calu-3 epithelial tissue through its basic functions of protection such as its barrier properties, mucus production and apical surface fluid composition.

This characterization was continued by the quantitative proteomic analysis of the apical secretome of Calu-3 cells with 4 % FBS supplementation and its comparison with the apical secretome of NHBE cells. These data will be presented in the next chapter.

Finally, the establishment of a long-term culture using Calu-3 cells allows repeated exposure to NMs and chronic toxicity studies. This was tested in the framework of the Biorima project with silver and iron oxide NPs, with up to 12 repeated exposures over a period of 12 to 28 days (data not shown). It highlights the advantage of using the Calu-3 model to mimic the 28-day sub-acute regulatory toxicity studies performed in animal toxicity assays.

Chapter 4: Characterization of the secretome of the Calu-3 and NHBE bronchial epithelia

The lung is one of the most exposed organs to hazardous compounds in humans. For its protection, the respiratory tract has developed different mechanisms of defense that contribute to the sterilization and detoxification of the air contaminants. Before reaching the bronchioles, the inhaled particles and molecules encounter the airway surface liquid (ASL), which is the first line of defense against inhaled pathogens and pollutants. The ASL is an aqueous solution composed of ions (Cl^-, Na^+, K^+, HCO_3^-) and proteins, which include mucins, antimicrobial peptides, and various enzymes (Webster and Tarran 2018). These molecules maintain the lung homeostasis and contribute to the mucociliary clearance that allows the entrapment and removal of inhaled pollutants (Progress, Fahy, and Dickey 2010). In the ASL, we can distinguish between the mucous layer and the periciliary layer, which are both necessary for proper mucociliary clearance. The mucus layer traps inhaled particles and pathogens, while the periciliary layer lubricates the airway surfaces, facilitating ciliary beating for an efficient mucus clearance (Bustamante-Marin and Ostrowski 2017).

3D *in vitro* cultures of the bronchial epithelium have been developed so that a bronchial barrier can be formed at the air-liquid interface, constituting a biological environment close to *in vivo* conditions. Primary cultures, which have the capacity to differentiate *in vitro*, can secrete mucus in the apical region. They also exhibit functional cilia to achieve ciliary beating needed in the mucociliary clearance (Rayner et al. 2019). Cell lines such as Calu-3, which also differentiates at the ALI, can form a tight bronchial epithelium. These cell lines develop an epithelial barrier composed of a unique cell type (absence of ciliated cells), where no ciliary beating occurs, but they retain the capacity to form a mucus layer.

In this chapter, the composition of the apical secretomes of Calu-3 and NHBE cells grown at ALI was compared by mass spectrometry (LC-MS/MS). For Calu-3, cultures supplemented with 4% FBS were selected based on the results presented in chapter 3. The apical secretome was analyzed after 4, 11 and 18 days at ALI for Calu-3 cells. For NHBE cultures, the apical secretomes of cells from 3 different donors (2 males, 1 female) were analyzed after 4, 12 and 18 days of culture at ALI following their reception at the laboratory.

Most of the results shown in this chapter were published in Scientific reports (Sanchez-Guzman et al. 2021).

Aims:

- Characterization of the secretome of the Calu-3 model of the human bronchial epithelium;
- Comparison of the secretomes of Calu-3 and NHBE epithelia;
- Analysis of the long-term evolution of the secretome in 3D models;
- Analysis of the functional enrichment of the biological and gene ontology terms to study the role of the most abundant proteins in Calu-3 and NHBE mature secretomes.

4.1 Analysis of the secretome of Calu-3 and NHBE models

The apical secretomes were systematically collected every 48 h in 200 µL HBSS$^{Ca2+/Mg2+}$ during a washing step described in section 2.2-1. The secretomes of NHBE cells (from 3 donors) and Calu-3 cells (from 3 independent cultures) collected at day 4, 11/12 and 18 were selected for mass spectrometry analysis. Three replicates were used for quantitative proteomic analysis that was performed at the Proteomic platform, Université de Paris, CNRS (Institut Jacques Monod).

4.1-1 Protein and glycoprotein concentrations

The Figure 45a shows the total protein concentration in the apical secretomes collected every 48 h. Days 4, 12 and 18 only are represented. The total protein concentration did not significantly change over time, or between the Calu-3 and NHBE models. The two models presented a stable protein production in the apical secretome during this period.

The glycoprotein content was measured using the ELLA assay (Figure 45b). The glycoprotein concentrations oscillated between 4-5 µg/mL, representing roughly 1% of the total proteins secreted (350-400 µg/mL). For NHBE cultures, the glycoprotein concentrations were not significantly different over time and remained at the same level from day 4 to day 18. In contrast, the glycoproteins released by Calu-3 culture exhibited a significant increase from day 4 to day 9 at ALI. No significant difference was observed between day 9 and 18, indicating a stable glycoprotein secretion.

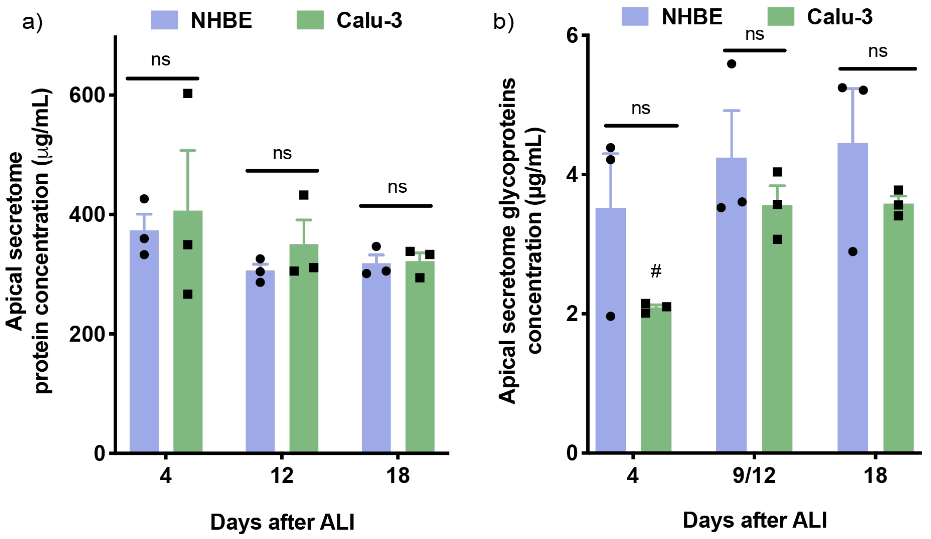

Figure 45: Total protein and glycoprotein concentrations in the apical secretome of NHBE and Calu-3 cells measured using BCA and ELLA assays respectively from day 4 to day 18 after ALI.

(a) Total protein concentration in the apical secretome of NHBE and Calu-3 cells after 4, 12 and 18 days at ALI. (b) Glycoprotein concentration in the apical secretome of Calu-3 and NHBE cells after 4, 9 or 12, and 18 days at ALI. (n=3) # statistically different between days, P < 0.05. ns not significant between the 2 models.

4.1-2 Quantitative proteomic analysis

Quantitative proteomic analyses of Calu-3 and NHBE secretomes were performed after 4, 11/12 and 18 days at ALI. A total number of 1684 and 1683 proteins were identified in the apical secretome of Calu-3 and NHBE cells, respectively. These proteins included intracellular proteins that may originate from dead cells and cell debris. Cell debris were not removed from the collected secretomes before analysis, because it would require centrifugation, which induces the sedimentation of high molecular weight proteins such as mucins, producing a truncated sample of the proteins of interest. Therefore, the data analysis was first performed on all the proteins identified (both intracellular and extracellular), then on extracellular proteins only using a reference database (Proteome discoverer software) to select them in our dataset.

Using the total number of proteins identified, we represented the composition of the secretome in a Venn diagram for each cell model over time, which corresponds to the qualitative analysis of the secretomes (Figure 46). Here, we considered only proteins that were identified in at least 2 biological replicates for each condition. For Calu-3, we observed 99.3% similarities of the secretomes collected at day 4, 11 and 18. For NHBE, there was 99.5% similarity (Figure 46b) between secretomes at day 4, 12 and 18. The common proteins to all time points in the secretomes of Calu-3 (1673) and NHBE (1674) cells were compared. 1663 common proteins were identified, corresponding to 99.3% similarity between the two cell models (Figure 46c). This first comparison was done based on the protein identity only.

A principal component analysis (PCA) of the quantitative MS data corresponding to the relative abundance of each protein identified is represented in Figure 46d. It shows 3 distinct clusters when comparing the first two components, PC1 (48%) and PC2 (18%): one cluster for NHBE secretomes, which includes the secretomes of the 3 donors collected at day 4, 12 and 18 (corresponding to the 2 blue circles on the figure); and 2 clusters for Calu-3 secretomes, one for the secretome collected at day 4 and a second one for the secretome collected at day 11 and 18. These results revealed a time evolution of the secretome in the Calu-3 model, with cells producing an immature secretome 4 days after ALI and a stable and mature secretome from day 11 at ALI.

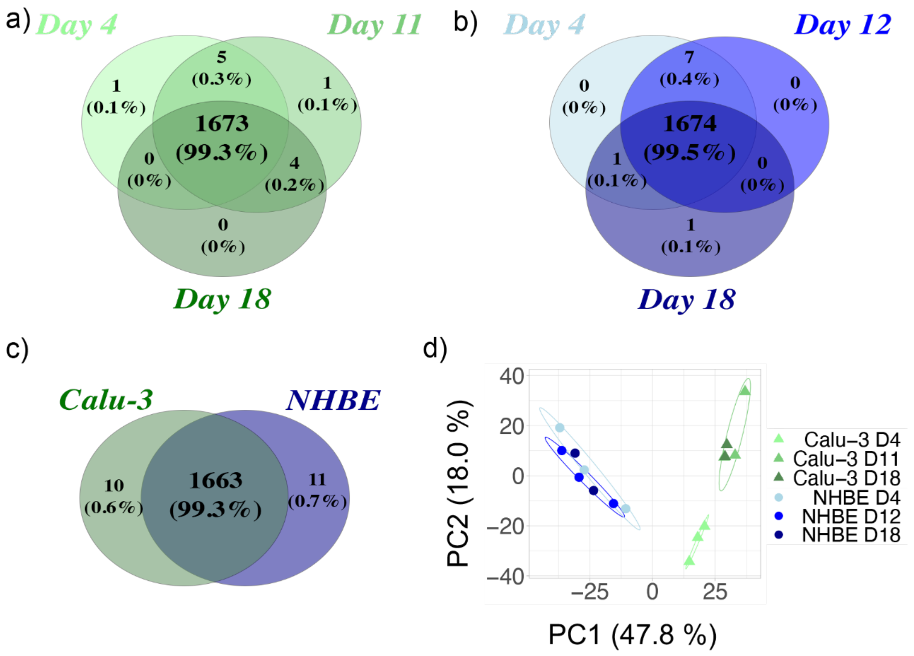

Figure 46: Proteomic analysis by LC-MS/MS of the apical secretome of the human bronchial epithelium in Calu-3 (green) and NHBE (blue) models.

Both extracellular and intracellular proteins were considered in this analysis. (a) Venn diagram showing the total number of proteins identified in at least 2 biological replicates of Calu-3 secretome at day 4, day 11 and day 18 after ALI. (b) Venn diagram showing the total number of proteins identified in at least 2 donors of NHBE secretome at day 4, day 12 and day 18 after ALI. (c) Common proteins identified at all time points both in Calu-3 and NHBE secretomes. (d) Principal Component Analysis (PCA) of the quantitative MS data. The secretomes of the 3 donors (NHBE cells) and of the 3 biological replicates (Calu-3 cells) are represented for each condition. Circles correspond to different time points. The first two principal components (PC) are shown, representing 47.8% and 18%, respectively.

Whatever the cell models, the secretomes included intracellular proteins likely derived from injured cell. For further analysis, we only considered the extracellular proteins that represented 22% of the total proteins in number. The extracellular proteins were selected using the Proteome Discoverer database, selecting the extracellular proteins from the gene ontology (GO) cellular component. Using this filter, we selected 408 extracellular proteins in the Calu-3 secretome and in the NHBE secretome, which were identified in at least two biological replicates for each model. Surprisingly, the qualitative analysis represented in the Venn diagram (Figure *47*a) shows 100% similarity between the extracellular proteins identified in the secretome of Calu-3 and NHBE cells, without any change over time. However, differences in protein abundance were observed between the Calu-3 and NHBE secretomes.

The relative protein abundance was used to compare the level of secretion of each protein in Calu-3 and NHBE models over time. A first approach using a PCA (Figure *47*b) showed a single cluster for NHBE secretomes over time. The NHBE secretome did not present any large variation in its composition over time, and only a slight variability between donors. On the contrary, the Calu-3 secretomes formed 2 separate clusters, one corresponding to samples collected at day 4 and another one that grouped secretomes collected at day 11 and 18 after ALI. These results suggest that the protein abundance, hence the composition of the apical secretomes of Calu-3 cells, evolved during the first days at ALI. This is possibly due to ongoing cell differentiation. Then, the secretome composition stabilized when complete epithelial differentiation was reached, forming a mature secretome from day 11 at ALI. Similar observations were made when considering the relative abundance of both intracellular and extracellular proteins (Figure 46d) as well as when considering the glycoprotein concentration (Figure 45b), which tended to stabilize after a delay of 4-10 days.

The relative abundance of the extracellular proteins was represented in a heat map (Figure *47*c). This representation highlights the high level of similarity of the NHBE apical secretome over time. For Calu-3 cultures, the largest variations in protein abundances were observed at day 4 compared to day 11 and 18 after ALI. Interestingly, while Calu-3 and NHBE shared the same proteins in their apical secretome, the abundance of each protein shifted as function of time and between the models.

Larger differences were observed in the Calu-3 model, confirming the evolution over time in terms of protein abundance. This evolution was not observed in the NHBE model. This could be expected because NHBE were already fully differentiated when the cultures were delivered by Epithelix. The Calu-3 secretome exhibited a more stable composition at day 11, with protein abundances similar to the ones measured at day 18. These results suggest an evolution in the secretome of Calu-3 due to ongoing epithelial differentiation. For Calu-3, we defined two stages in secretome evolution: the first one corresponds to an immature secretome, which changed in terms of protein abundance due to the ongoing epithelial differentiation, and the second one corresponds to a mature secretome, which presented only slight changes between days 11 and 18.

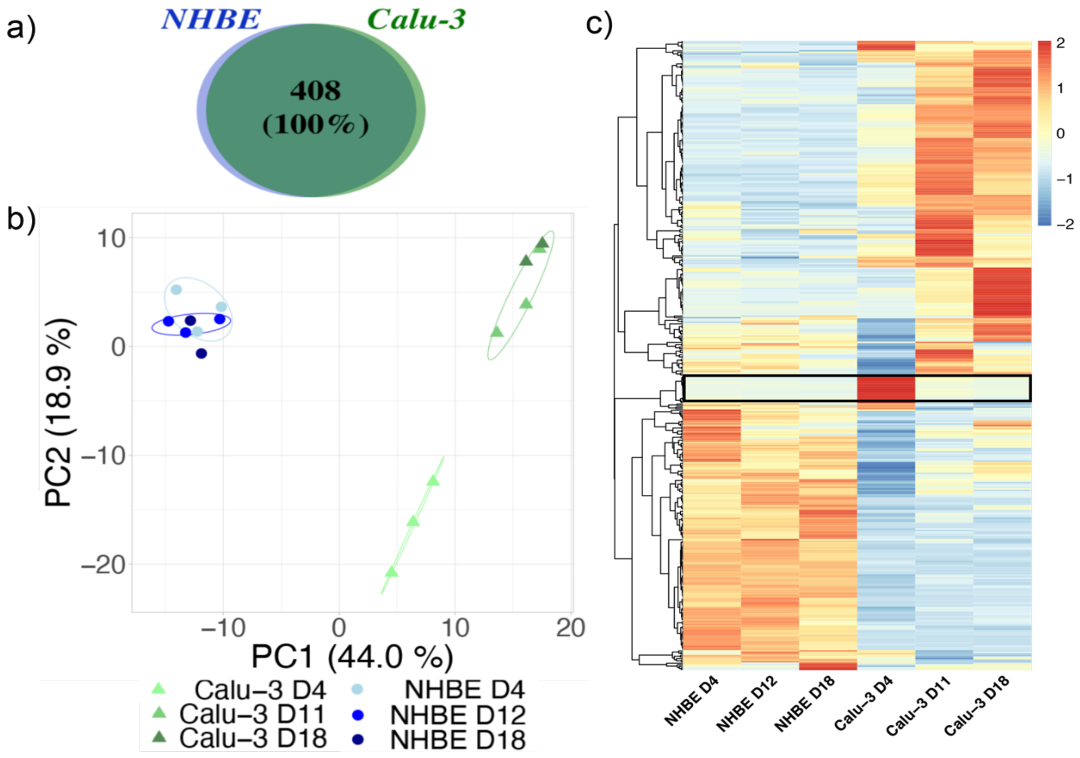

Figure 47: *Proteomic analysis of the extracellular proteins of the apical secretome of the human bronchial epithelium in Calu-3 and NHBE models by LC-MS/MS.*

(a) Qualitative analysis of the extracellular proteins of Calu-3 and NHBE cells at day 4, day 11 (Calu-3) or 12 (NHBE), and day 18 after ALI. The total number of proteins and the percentage of common proteins are shown in a Venn diagram. (b) PCA analysis of the quantitative MS data for the extracellular proteins only. The analysis was performed at day 4, day 11 (Calu-3) or 12 (NHBE), and day 18. The different donors (NHBE cells) and biological replicates (Calu-3 cells) are represented for each condition. Circles correspond to different time points. The percentage associated with each PC is indicated in the axis legend. (c) Heat map of the extracellular proteins identified in the apical secretome of Calu-3 cells and NHBE cells at day 4, 11-12, and 18 after ALI. Colours correspond to low (blue) or high (red) relative protein abundance. A protein set showing larger differences at day 4 compared to day 11 and 18 in the secretome of Calu-3 cells is surrounded by a black rectangle.

A sphere diagram was used to represent each extracellular protein as a sphere, whose size depended on their relative protein abundance in the secretome (Figure 48). Human albumin

(ALB) was overrepresented in the secretome of Calu-3 at day 4 (Figure 48a) followed by proteins involved in formation of the mucus layer and in the immune defense. With time in culture, the proteins involved in mucus layer formation (MUC5AC), in cell-to-cell communication and in defence, such as neutrophil gelatinase-associated lipocalin 2 (LCN2), polymeric immunoglobulin receptor (PIGR), alpha-1-antitrypsin (SERPINA1), alpha-1-antichymotrypsin (SERPINA3), became more abundant in the secretome of Calu-3 cells. The relative abundance of proteins was stable from day 11 ((Figure 48b) to day 18 (Figure 48c), where only slight changes were observed (when considering the most abundant ones).

Contrarily to the secretome of Calu-3 cells, the relative abundance of proteins in the secretome of NHBE (Figure 48d-f) was stable during the culture time. In NHBE, proteins such as LCN2, PIGR, Bactericidal Permeability Increasing (BPI) fold containing family A and B member 1 (BPIFA1, BPIFB1) and uteroglobin (SCGB1A1), were the main proteins contributing to the apical secretome. They are all involved in the epithelium innate immune responses.

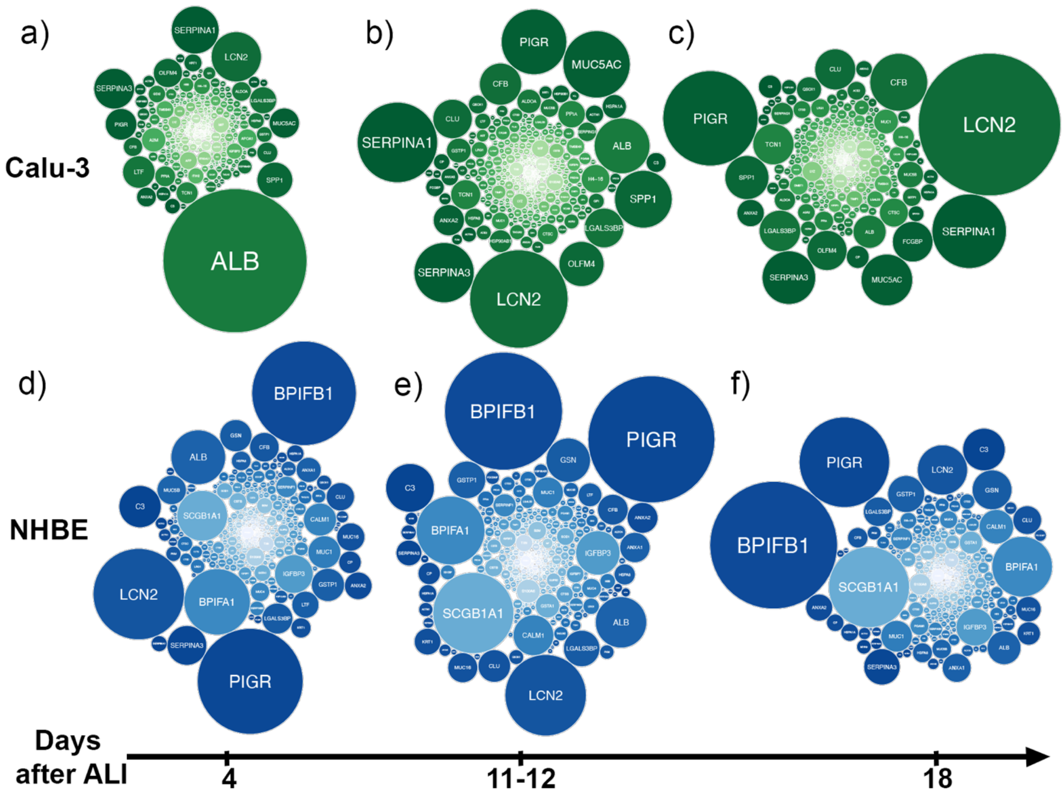

Figure 48: Time evolution of the secretome of Calu-3 and NHBE cells.

Sphere diagram representing the relative abundance of proteins secreted by Calu-3 (green) and NHBE (blue) cells at day 4 (a-b), 11-12 (c-d), and 18 (e-f) after ALI. A larger sphere denotes a higher protein abundance. Proteins are referred to by the gene name.

Interestingly, among the 20 most abundant proteins in Calu-3 and NHBE secretomes (Table 11), we identified proteins common to all time-points such as LCN2, PIGR, SERPINA3, ALB, clusterin (CLU), galectin 3 binding (LGALS3BP) and annexin A2 (ANXA2) for both models. The 20 most abundant proteins for each condition are represented in a Heatmap (Figure 49a) to highlight the different trends in the evolution of Calu-3 and NHBE secretomes. The NHBE secretome composition was relatively stable during the experimental period with only slight decreases for some proteins, such as mucins (*muc1*and *muc5b*), ceruloplasmin (*cp*), lactotransferrin *(ltf)* and *serpina3.* Some of the proteins highly abundant in NHBE were secreted at a lower level by Calu-3, such as uteroglobin (*scgb1a1),* gelsolin *(gsn),* glutathione S-transferase *(gsta1, gstp1), bpifa1 and bpifb1, muc16,* insulin-like growth factor-binding protein 3 *(igfbp3),* complement C3 *(c3) and* calmodulin-1 (*calm1)* (corresponding gene names in bracket).

By contrast, some proteins, which were highly abundant in the Calu-3 secretome, such as fructose-bisphosphate (*aldoa*), *serpina1*, *serpina3*, *muc5ac*, olfactomedin-4 (*olfm4*) and sphingosine-1-phosphate phosphatase-1 (*spp1*), were secreted in lower amounts by NHBE cells. Additionally, some proteins were found in similar relative abundance in NHBE and Calu-3 secretomes at days 11 and 18, such as *muc5b*, *anxa2, pigr* and ceruloplasmin (*cp*). Some proteins, such as *lgals3bp*, *clu*, *lcn2*, sulfhydryl oxidase-1 (*qsox-1*), complement factor B (*cfb*), dipeptidyl peptidase-1 (*ctsc*), were underrepresented in Calu-3 secretome at day 4 compared to NHBE secretome, but they reached similar values at day 11, and became more abundant at day 18.

Several antimicrobial peptides (AMPs) were identified in the secretomes of Calu-3 and NHBE cells (Figure 49b). Some proteins exhibited a similar abundance between NHBE and Calu-3 cells at days 11 and 18, such as lysozyme C (*lyz*), LCN2 and CLU proteins. However, NHBE secretome had a higher concentration of some antimicrobial peptides compared to Calu-3 secretome, such as BPI fold containing family A and B, and the S100A8 and A9 proteins.

The contribution of mucins to the secretome of Calu-3 and NHBE was also studied (Figure 49c). Both Calu-3 and NHBE cells secreted the gel-forming mucins (MUC5AC, MUC5B) and the membrane-tethered mucins (MUC1, MUC4, MUC16 and MUC20), which compose the mucus of the human bronchial epithelium (Bansil and Turner 2018). However, the gel-forming ones were more abundant in the Calu-3 secretome, while the membrane-tethered ones were more abundant in the NHBE secretome. MUC4 is produced by ciliated cells, and MUC1 and MUC16 are produced both by ciliated and secretory cells, which could explain their higher abundance in the NHBE secretome. MUC16 can also be secreted to the ASL (Hattrup and Gendler 2008).

These results show the evolution of the protein secretion by Calu-3 cells over time, with a distinct composition at day 4 compared to day 11 and 18, as observed in PCA (Figure *47*b).

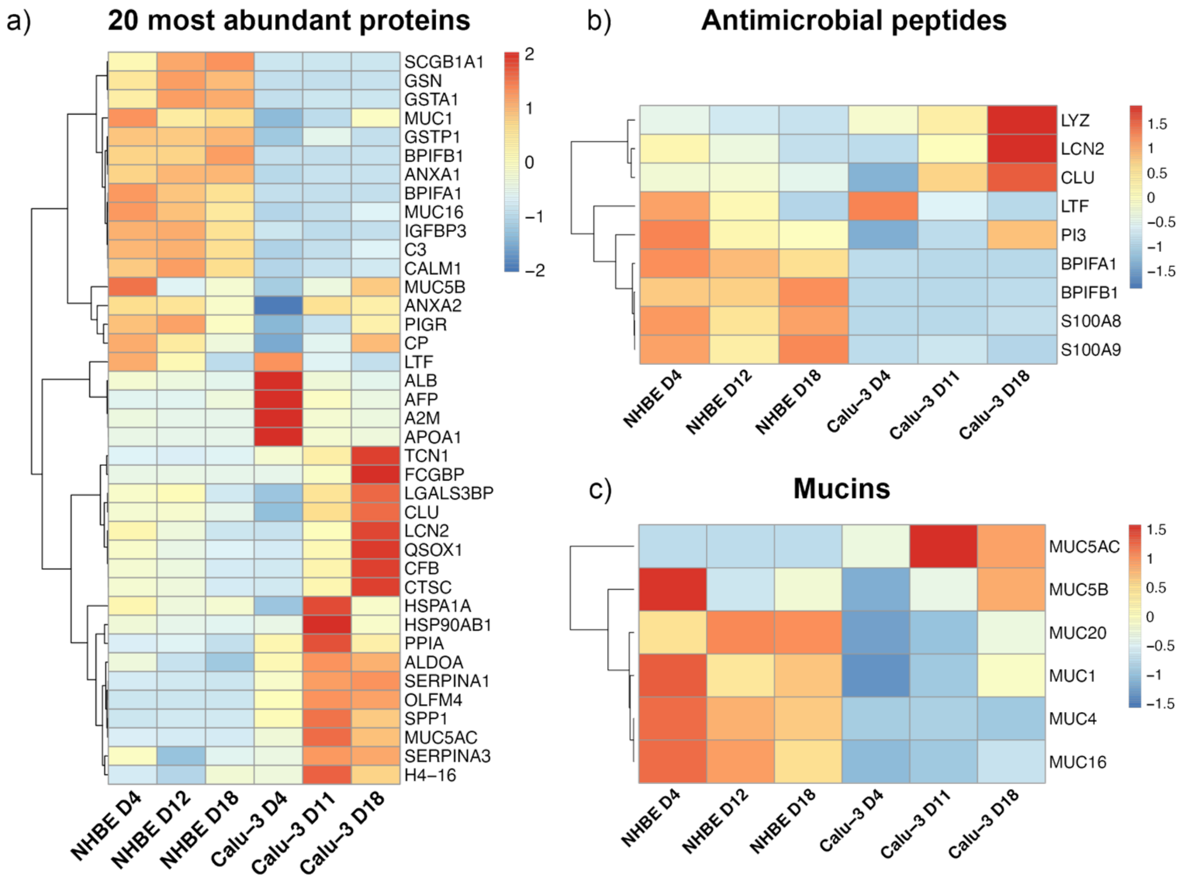

Figure 49: Heatmaps of the 20 most abundant extracellular proteins.

(a) antimicrobial peptides (b) and mucins (c) identified in Calu-3 and NHBE secretomes at day 4, 11-12 and 18 after ALI.

Some proteins highly secreted at day 4, such as albumin, alpha-fetoprotein (*afp*), alpha-2-macroglobulin (*a*2*m*) and apolipoprotein A1 (*apoa*1), are also present in fetal bovine serum, which was used to supplement the culture medium in the basal compartment. We investigated whether these proteins were human proteins secreted by Calu-3 cells, or whether they could originate from contamination of the apical compartment by FBS. The sequence of HSA and BSA is represented in Figure 50 a and b, respectively. We selected unique peptides in the protein quantification to analyse only human proteins. The peptides chosen for protein quantifications (selected by Progenesis software) are highlighted. In total, 3 peptides were used for protein quantification. After verification, only one peptide (KVPQVSTPTLVEVSR) was identified in both protein sequences. To confirm the choice of unique peptides for protein identification, an additional analysis was performed using the Uniprot website REST API tool. The API tool is employed to identify peptides and can be used to select unique protein peptides. This analysis identified the peptide (KVPQVSTPTLVEVSR) only in HSA, classifying the peptide as unique for the human protein (Figure 50c, red square). This unique peptide was used for MS analysis, which confirmed the identification and quantification of HSA only in the secretome of Calu-3 cells.

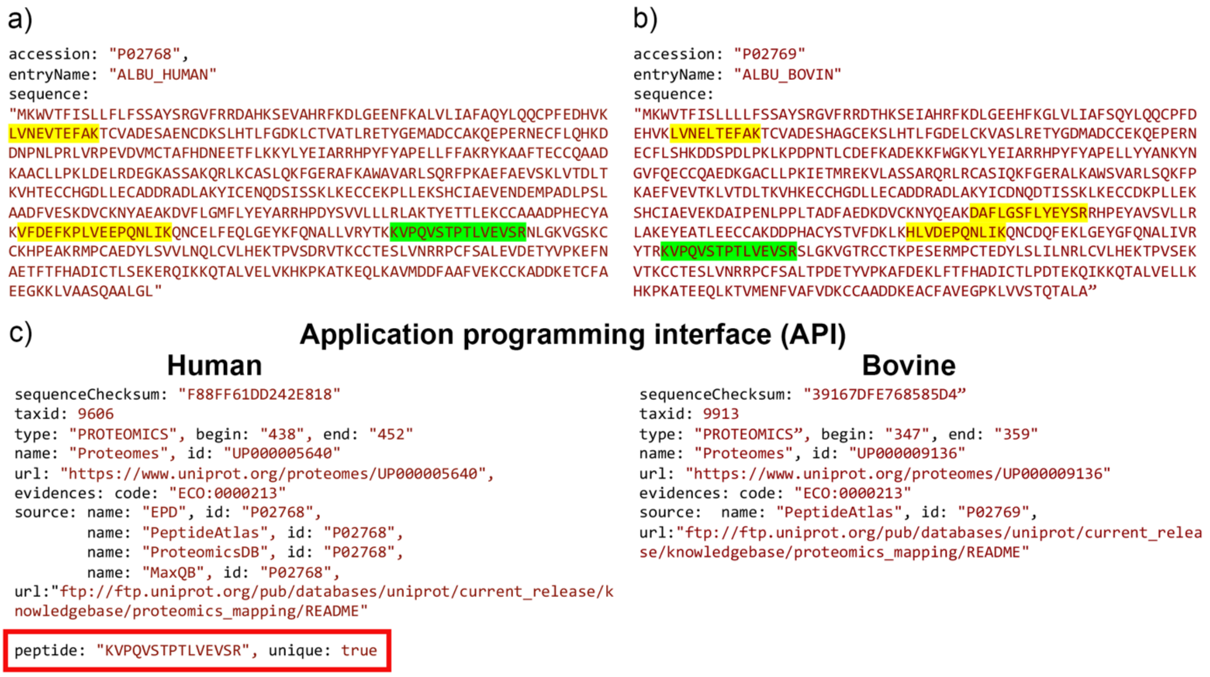

```
accession: "P02768",
entryName: "ALBU_HUMAN"
sequence:
"MKWVTFISLLFLFSSAYSRGVFRRDAHKSEVAHRFKDLGEENFKALVLIAFAQYLQQCPFEDHVK
LVNEVTEFAKTCVADESAENCDKSLHTLFGDKLCTVATLRETYGEMADCCAKQEPERNECFLQHKD
DNPNLPRLVRPEVDVMCTAFHDNEETFLKKYLYEIARRHPYFYAPELLFFAKRYKAAFTECCQAAD
KAACLLPKLDELRDEGKASSAKQRLKCASLQKFGERAFKAWAVARLSQRFPKAEFAEVSKLVTDLT
KVHTECCHGDLLECADDRADLAKYICENQDSISSKLKECCEKPLLEKSHCIAEVENDEMPADLPSL
AADFVESKDVCKNYAEAKDVFLGMFLYEYARRHPDYSVVLLLRLAKTYETTLEKCCAAADPHECYA
KVFDEFKPLVEEPQNLIKQNCELFEQLGEYKFQNALLVRYTKKVPQVSTPTLVEVSRNLGKVGSKC
CKHPEAKRMPCAEDYLSVVLNQLCVLHEKTPVSDRVTKCCTESLVNRRPCFSALEVDETYVPKEFN
AETFTFHADICTLSEKERQIKKQTALVELVKHKPKATKEQLKAVMDDFAAFVEKCCKADDKETCFA
EEGKKLVAASQAALGL"
```

```
accession: "P02769"
entryName: "ALBU_BOVIN"
sequence:
"MKWVTFISLLLLFSSAYSRGVFRRDTHKSEIAHRFKDLGEEHFKGLVLIAFSQYLQQCPFD
EHVKLVNELTEFAKTCVADESHAGCEKSLHTLFGDELCKVASLRETYGDMADCCEKQEPERN
ECFLSHKDDSPDLPKLKPDPNTLCDEFKADEKKFWGKYLYEIARRHPYFYAPELLYYANKYN
GVFQECCQAEDKGACLLPKIETMREKVLASSARQRLRCASIQKFGERALKAWSVARLSQKFP
KAEFVEVTKLVTDLTKVHKECCHGDLLECADDRADLAKYICDNQDTISSKLKECCDKPLLEK
SHCIAEVEKDAIPENLPPLTADFAEDKDVCKNYQEAKDAFLGSFLYEYSRRHPEYAVSVLLR
LAKEYEATLEECCAKDDPHACYSTVFDKLKHLVDEPQNLIKQNCDQFEKLGEYGFQNALIVR
YTRKVPQVSTPTLVEVSRSLGKVGTRCCTKPESERMPCTEDYLSLILNRLCVLHEKTPVSEK
VTKCCTESLVNRRPCFSALTPDETYVPKAFDEKLFTFHADICTLPDTEKQIKKQTALVELLK
HKPKATEEQLKTVMENFVAFVDKCCAADDKEACFAVEGPKLVVSTQTALA”
```

```
sequenceChecksum: "F88FF61DD242E818"
taxid: 9606
type: "PROTEOMICS", begin: "438", end: "452"
name: "Proteomes", id: "UP000005640"
url: "https://www.uniprot.org/proteomes/UP000005640",
evidences: code: "ECO:0000213"
source: name: "EPD", id: "P02768",
        name: "PeptideAtlas", id: "P02768",
        name: "ProteomicsDB", id: "P02768",
        name: "MaxQB", id: "P02768",
url:"ftp://ftp.uniprot.org/pub/databases/uniprot/current_release/k
nowledgebase/proteomics_mapping/README"

peptide: "KVPQVSTPTLVEVSR", unique: true
```

```
sequenceChecksum: "39167DFE768585D4”
taxid: 9913
type: "PROTEOMICS”, begin: "347", end: "359"
name: "Proteomes", id: "UP000009136"
url: "https://www.uniprot.org/proteomes/UP000009136"
evidences: code: "ECO:0000213"
source:  name: "PeptideAtlas", id: "P02769",
url:"ftp://ftp.uniprot.org/pub/databases/uniprot/current_relea
se/knowledgebase/proteomics_mapping/README"
```

Figure 50: Proteomics peptides search of human and bovine serum albumin.

Search for protein homologies in peptides used for protein quantification using Uniprot Proteins REST API. (a) HSA and (b) BSA sequences with corresponding MS peptides used for relative abundance quantification. Peptides identified in only one protein are highlighted in yellow. Peptides identified in both HSA and BSA are highlighted in green.

4.1-3 Functional enrichment of Reactome pathways and biological processes associated with mature secretomes

To explore the biological role of the proteins secreted by Calu-3 and NHBE cells and their interactions, first we focused our analysis on the 20 most abundant proteins that constituted the apical secretome of Calu-3 cells and NHBE at day 11/12 and 18. We excluded the secretome at day 4 because of the observed differences in Calu-3 model between the immature and mature secretome. The 20 most abundant proteins were selected to focus our analysis on the most representative proteins. Among the 20 most abundant proteins of each model, 14 proteins (Calu-3) and 18 proteins (NHBE) were common to days 11 and 18, and used for further analysis.

The biological pathway and gene ontology (GO) analyses were performed using g:Profiler (https:/biit.cs.ut.ee/gprofiler), a web tool that performs the analysis of functional categories enrichment based on data from the entire human proteome. The statistically enriched Reactome pathways (Figure 51a) and GO categories of cellular components (Figure 51b), biological processes (Figure 51c) and molecular functions (Figure 51d) are presented for the 14 (Calu-3) and 18 proteins (NHBE) common proteins to days 11 and 18.

The Reactome pathways associated with the secretomes of Calu-3 and NHBE cells were strongly associated with the immune response in both models (Figure 51a). This response involved pathways from the innate immune system, such as neutrophil degranulation and antimicrobial peptides. The antimicrobial peptide pathway was not significantly enriched in Calu-3 secretomes due to the lack of BPI fold containing family A and B in the 20 most abundant proteins. Proteins such as lipocalin 2, clusterin and BPI fold containing family are essential in the mucosal immune defense against pulmonary infections (Guglani et al. 2012; Liu et al. 2013) and are present in the epithelial lining fluid. In addition, biological pathways associated with hemostasis and platelet activation were enriched due to the presence of albumin, calmodulin-1, serpina 3, clusterin and galectin-3 binding proteins in the secretome. These proteins may contribute to the regulation of the osmotic pressure in the epithelium through their ionic interactions with Ca^{2+}, Na^{+} and K^{+} (Yu et al. 2016; Majorek et al. 2012).

The cellular structures associated with the secreted proteins are shown in Figure 51b. As expected, an enrichment in the extracellular location and vesicle-associated proteins was observed. These results confirmed the correct selection of the extracellular proteins based on existing databases.

The GO analysis of the associated biological processes (Figure 51c) highlighted the role of the secretome in the cell activation of granulocyte, neutrophile and myeloid cells, in humoral, antimicrobial and defence responses, in cell secretion and exocytosis, and in response to external and biotic stimuli.

Finally, the analysis of the molecular functions of the secreted proteins (Figure 51d) showed that several processes of binding to enterobactin and macrolide were overrepresented in both secretomes. However, differences were observed between the two cell models. NHBE secretome was more enriched in proteins involved in ion-, metal- and lipid-binding. Proteins with high binding affinity to ions as Ca^{2+} (e.g. annexin-1(Mailliard, Haigler, and Schlaepfer 1996), calmodulin (Sachyani et al. 2014) and gelsolin (Huff et al. 2003)) were present in higher abundance in NHBE compared to Calu-3. By contrast, Calu-3 secretomes were enriched in peptidase regulator and inhibitor activities, which were not enriched in NHBE analysis due to the lack of serpina-1 in the 20 most abundant proteins.

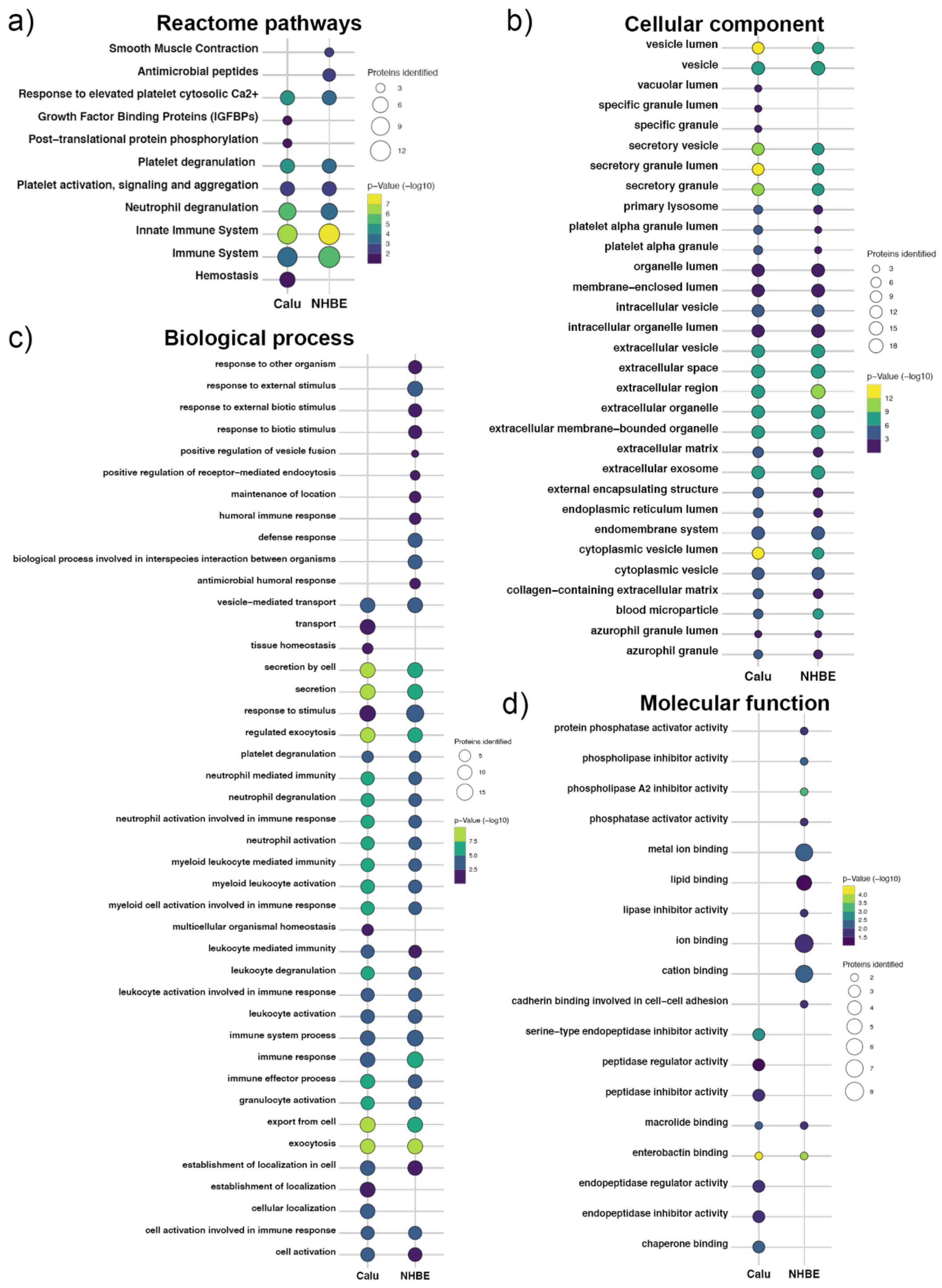

Figure 51: Functional enrichment analysis of gene ontology and Reactome pathways of the cell secretomes using g:GOST.

(a) Statistically significant enrichment of reactome pathways, (b) cellular components, (c) biological processes and (d) molecular functions of the 20 most abundant proteins identified at day 11/12 and 18 in the Calu-3 and NHBE secretomes. g:SCS threshold was set to 0.05. The circle size reflects the number of identified proteins in each pathway. The color scale corresponds to the adjusted p-value (expressed as -log$_{10}$*).*

4.2 Comparison of the secretomes from *in vitro* models with human bronchoalveolar lavage (hBAL)

To evaluate the biological relevance of the *in vitro* models of the human bronchial epithelium in the production of lung lining fluid (here at the bronchial level), we compared the composition of the secretome of Calu-3 and NHBE cells to one clinical sample of broncho-alveolar lavage (hBAL) from a healthy donor. Extracellular proteins (413 proteins) only were considered in this analysis, though intracellular proteins (1237 proteins) were also identified in the hBAL (representing 34% of the total proteins in protein number).

This preliminary analysis was performed on one clinical sample only, due to limited access to hBAL samples from healthy donors. Therefore, only qualitative MS analysis of hBAL could be performed (3 biological replicates are needed for quantitative MS analysis). We identified 413 extracellular proteins in the hBAL, compared to 408 in the apical secretome of Calu-3 and NHBE cells. The Venn diagram (Figure 52) shows that 231 extracellular proteins were common to hBAL and secretomes from cell models, corresponding to 39.2% similarity. 177 proteins (30%) and 182 proteins (30.8%) were specific to the cell culture secretome and to hBAL, respectively.

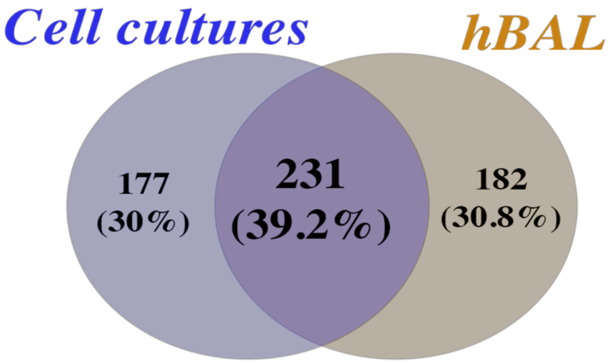

Figure 52: Qualitative proteomic analysis of one sample of human bronchoalveolar lavage from a healthy donor compared to the secretomes collected in cell cultures.

The total number of proteins and the percentage of common proteins are shown in a Venn diagram. 231 protein (39.2%) were common to hBAL and the cell secretomes. 177 proteins (30%) and 182 (30.8%) were specific to the cell culture secretomes and hBAL, respectively. Only extracellular proteins were used in the analysis.

The biological roles of the common and unique proteins identified in the cell secretome and the human BAL were analysed using the Reactome pathway functional enrichment (Figure 53).

Enrichments in pathways involved mainly in the innate immune responses, vesicle secretions, homeostasis, post-translational protein modifications, protein metabolism were observed for the 232 common proteins. The common proteins included gel-forming mucins (MUC5AC and MUC5B), antimicrobial peptides (*lcn2*, *lyz*, *clu*, *s100a8, s100a9, bpifa1, and bpifb1*) and antioxidant proteins (glutathione S-transferase A1 (*gsta1), alb,* apolipoprotein E *(apoe)*). The proteins exclusively present in the hBAL were implicated in pathways restricted to the alveolar region, such as surfactant metabolism. Indeed, the cell types responsible for their production are absent from our bronchial epithelium models. The surfactant-associated proteins A1, A2, B and D were identified in the hBAL sample. Pathways involved in parasite infections, infectious diseases and the adaptive immune response were also enriched. These results suggest a possible infection of this donor. Samples from other donors would be necessary to give conclusive results on this point.

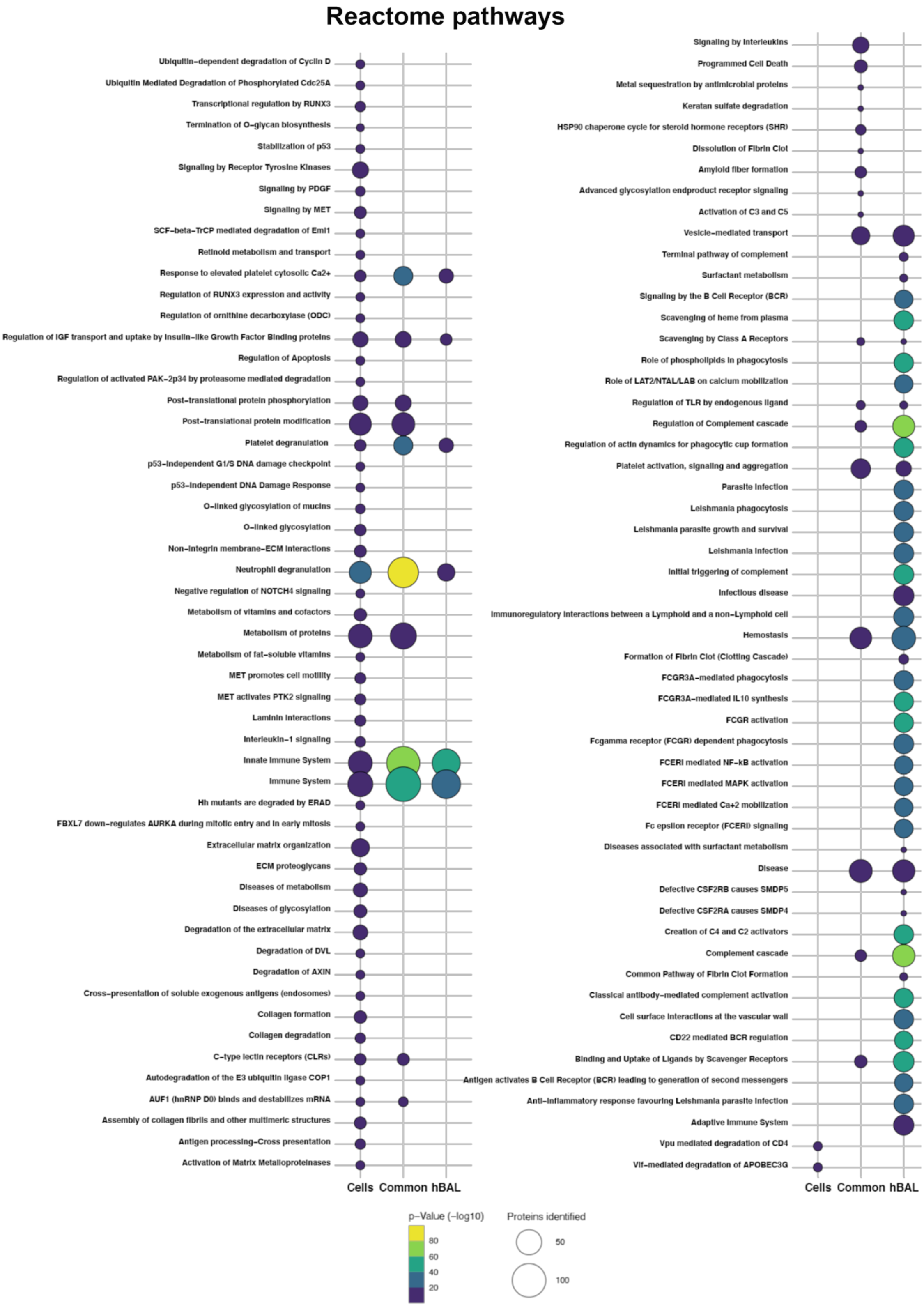

Figure 53: Functional enrichment analysis of Reactome pathways of hBAL and in vitro secretomes using g:GOST.

Statistically significant reactome pathways enrichment of the common and unique proteins identified in the cell culture secretomes and in the hBAL. g:SCS threshold was set to 0.05. The circle size represents the number of identified proteins involved in each reactome pathway. The color scale represents the adjusted p-value (expressed as -log$_{10}$).

4.3 Discussion

The aim of this part was to characterize and compare the apical secretomes of the Calu-3 and NHBE human bronchial epithelium models and to validate the use of Calu-3 cells as a relevant model for nanotoxicology studies.

The apical secretome of Calu-3 cell cultures supplemented with 4% FBS was compared to the apical secretome of NHBE cells. The total protein and glycoprotein concentrations of the two models were quantified up to 18 days at ALI. No statistically significant difference in total protein concentration in the secretome was observed during the experimental time. We also measured the concentration of glycoproteins, which include the mucin family. Mucins are a key component of the epithelial lining fluid at the bronchial level that ensures the protection against and clearance of pathogens and inhaled particles (Bals, Weiner, and Wilson 1999). The glycoprotein quantified in Calu-3 and NHBE apical secretome presented no significant differences between the two models. Statistically significant differences in glycoprotein concentrations were observed in Calu-3 cultures at day 4 only, compared to cells that stayed longer at ALI, a difference that we attributed to the ongoing epithelial differentiation of Calu-3 cells up to 11 days at ALI.

Mass spectrometry analysis identified 1685 different proteins in the apical secretomes of Calu-3 and NHBE cells, a large part of which are intracellular proteins (1277 proteins). We chose to analyse the total secretome collected in HBSS at the cell surface by gentle washing, without a centrifugation step to remove cells debris, in order to retain all of its components. The presence of mucus in the samples makes their manipulation more difficult. The centrifugation favours the sedimentation of high molecular weight proteins such as mucins, which can trap others proteins leading to their removal from the analysed sample. When considering the total proteins (both intracellular and extracellular), the secretomes of the two models shared more than 99% of the proteins identified (qualitatively), but showed significant differences in relative protein abundances. When considering extracellular proteins only, selected after the data analysis using the proteome discoverer database, the qualitative proteome analysis showed 100% similarity between the apical secretome of Calu-3 and NHBE cells from day 4 to day 18. These results were surprising, considering the different cellular composition of Calu-3 and NHBE epithelium. However, the secretion of the proteins that form the ASL are mainly produced by secretory cells, corresponding to the Calu-3-derived cell type.

Gupta *et al.* analyzed the exosomes collected in the apical secretions of Calu-3 and primary human tracheobronchial (HTBE) cells following sample centrifugation. Approximately 50% similarity in terms of proteins identified was reported for the exosomes isolated from the two cultures (Gupta et al. 2019). We compared the proteins identified by Gupta *et al.* with our results. Common proteins were identified in both studies, especially proteins involved in the innate defense, such as polymeric immunoglobulin receptor (*pigr*), alpha-1-antichymotrypsin (*serpina3*), complement 3 (*c3*), MUC5AC, MUC5B, and albumin. However, Gupta *et al.* observed larger differences in the exosomal composition of the Calu-3 compared to the HTBE cells, compared to our analysis of the full apical secretome of Calu-3 and NHBE cells. This difference could be explained by several factors: i) the authors used primary human tracheobronchial (HTBE) cells while we used NHBE cells in our model, ii) cell differentiation was performed in their lab, which could lead to differences in culture differentiation (Rayner et al. 2019) and iii) the analysis of a specific secretome fraction (exosomes). Gupta *et al.* specifically analysed the proteins forming exosomes isolated from the total secretome, whereas we considered the whole secretome. In addition, different software and databases were employed for MS data analysis. Using different software can lead to slight differences at the protein identification step, due to different peptide analysis methods (Gonzalez-Galarza et al. 2012; Al Shweiki et al. 2017).

Furthermore, our quantitative proteomic analysis revealed differences in protein abundances in the apical secretomes of Calu-3 and NHBE cells. In the case of NHBE cells, the protein composition and abundance were very similar between donors and over time. By contrast, for Calu-3 secretome, the relative abundance of the secreted proteins changed with the time of culture. An immature secretome was produced during the first days at ALI, while a mature secretome was reported in our experiment from day 11 following full epithelial differentiation. These results support the hypothesis that the secretome changed in terms of protein abundance during the epithelial differentiation, even if a tight barrier had already been formed. The mature secretome of Calu-3 was closer to the NHBE secretome than the immature secretome. In addition, the NHBE secretome was stable for the duration of the experiment (here 18 days).

Proteins such as neutrophil gelatinase-associated lipocalin (*lcn2*), polymeric immunoglobulin receptor (*pigr*), serum albumin (*alb*), alpha-1-antichymotrypsin (*serpina3*), galectin-3-binding protein (*lgals3bp*), clusterin (*clu*) and annexin A2 (*anxa2*) were present in the apical secretome of both Calu-3 and NHBE cultures. These proteins are involved in the innate immune response against bacterial infection (LCN2 (Chan et al. 2009), PIGR (Borrok et al. 2018)), and against viruses (LGALS3BP (Xu et al. 2019), ANXA2, CLU (Tripathi et al. 2013)).

The fold-enrichment Reactome pathway analysis showed a high representation of the immune system pathways in the mature apical secretomes of both Calu-3 and NHBE cells. In particular, several proteins identified in the secretome could be involved in the innate immune response. In the case of NHBE, among the innate defence protein, we identified the BPI fold containing family A and B member 1, which are anti-microbial peptides (Liu 2013).

Surprisingly, the Reactome pathways involved in hemostasis, platelet activation, signaling and aggregation were also enriched in the secretomes of Calu-3 and NHBE cells, as well as in the hBAL. Proteins involved in these pathways, such as CALM1 (Yu et al. 2016) and ALB (Majorek et al. 2012), present a high capacity in modulating ion channels, which may contribute to the regulation of the osmotic pressure in the cell culture.

The analysis of one human BAL that we were able to carry out revealed that 232 extracellular proteins were common to the hBAL sample and the secretomes of the *in vitro* models of the bronchial epithelium, including gel-forming mucins (MUC5AC and MUC5B), antimicrobial peptides (*lcn2*, *lyz*, *clu*, *s100a8, s100a9, bpifa1 and bpifb1*) and antioxidant proteins (*gsta1, alb and apoe)*. Moreover, the analysis of this hBAL revealed that it was in line with the composition of human bronchoalveolar lavages from healthy donors reported in the literature (Jinzhi Chen et al. 2008). hBAL is composed of proteins such as albumin, complement C3, polymeric immunoglobulin receptor, galectin-3-binding protein between others (Foster et al. 2013).

The gene ontology analysis confirmed the role of the secreted proteins in the epithelium defence. The GO biological processes were enriched in innate defence response and in immune cell activations. Other glycoproteins, such as olfactomedin-4, can be involved in the recruitment of neutrophils (Xiao et al. 2021). The molecular functions enriched in the secretome were related to the binding of ions, lipids, and metals, which are important processes for cell recognition. In addition, peptidase regulator and inhibitor activity were also enriched. The balance of proteases and antiproteases is essential in the respiratory inflammation homeostasis following viral infections (Meyer and Jaspers 2015).

Finally, the extracellular localization of the proteins was confirmed by GO cellular compartment analysis, with an enrichment for vesicles and extracellular proteins, suggesting that part of the identified proteins can be involved in exosomes.

The high relative abundance of serum albumin in the secretome of Calu-3 cells at day 4 raised the question of a potential contamination by FBS proteins from the culture medium, for example in case of an immature barrier or through protein exchange (A. Cox et al. 2018). The quantification of HSA in Calu-3 secretome was performed using Progenesis QI software. This software allows for the discrimination of unique peptides for proteins of human vs bovine origin, reducing protein quantification mismatch. This analysis confirmed that HSA was secreted by Calu-3 cells *in vitro*. This result is consistent with the study of Chen et al, which identified HSA in the hBAL of 6 healthy donors (Chen *et al.*, 2008). Finally, the identification of common proteins in Calu-3 secretome, NHBE secretome, and hBAL emphasized the high similarity of the Calu-3 secretome with the epithelial lining fluid at the bronchial level (Jinzhi Chen et al. 2008).

4.4 Conclusion

In this part of the work, we used the 3D bronchial epithelium model previously developed using Calu-3 cells (Chapter 3) to analyze the composition of the apical secretome and to compare its composition and evolution with the secretome of normal human bronchial epithelium (NHBE).

We characterized the protein secretion of Calu-3 and NHBE cultures. We observed high similarities in the protein composition of both cultures, but differences in relative protein abundances. We have identified two stages in the evolution of the apical secretome of Calu-3, corresponding to the ongoing differentiation of the epithelium after ALI. After full epithelial differentiation was established, a mature secretome could be maintained for at least 18 days. The Calu-3 model was also able to produce a functional secretome with protective functions highly similar to the ones associated with the secretome of NHBE *in vitro* models and one human bronchoalveolar lavage.

Because the secretome may have an impact on the NP-cell interaction and NP toxicity following protein-NP interaction, the formation of the protein corona on silver nanoparticles in the mature Calu-3 secretome was investigated in the last part of this thesis.

Table 11:List of the 20 most abundant proteins identified in Calu-3 and NHBE secretome at the different time points (22 total number, 14 common).

In green and blue are highlighting the protein exclusively found in the most abundant for Calu-3 and NHBE, respectively.

Accessio	**Description**	**Biological Process**	**Cellular Component**	**Molecular Function**	**Gene Symbol**	**NHBE**			**Calu-3**		
						4	12	18	4	11	18
P01024	Complement C3 OS=Homo sapiens OX=9606 GN=C3 PE=1 SV=2	Cell organization and biogenesis Defense response Metabolic process Regulation of biological process Response to stimulus Transport	Extracellular Membrane Organelle lumen	Catalytic activity Enzyme regulator activity Protein binding	C3	X	X	X			X
P01009	Alpha1antitrypsin OS=Homo sapiens OX=9606 GN=SERPINA1 PE=1 SV=3	Cell organization and biogenesis Coagulation Defense response Metabolic process Regulation of biological process Response to stimulus Transport	Endoplasmic reticulum Extracellular Golgi membrane Organelle lumen	Enzyme regulator activity Protein binding	SERPINA1				X	X	X
P01011	Alpha1antichymotrypsin OS=Homo sapiens OX=9606 GN=SERPINA3 PE=1 SV=2	Defense response Regulation of biological process Response to stimulus Transport	Extracellular Nucleus Organelle lumen	DNA binding enzyme Regulator activity Protein binding	SERPINA3	X	X	X	X	X	X
P98088	Mucin5AC OS=Homo sapiens OX=9606 GN=MUC5AC PE=1 SV=4	Metabolic process Regulation of biological process Response to stimulus	Cytoplasm Extracellular Membrane Organelle lumen	Protein binding Structural molecule activity	MUC5AC				X	X	X
P08238	Heat shock protein HSP 90beta OS=Homo sapiens OX=9606 GN=HSP90AB1 PE=1 SV=4	Cell organization and biogenesis Metabolic process Regulation of biological process Response to stimulus Transport	Cell surface Cytoplasm Cytosol Extracellular Membrane Mitochondrion Nucleus Organelle lumen	Enzyme regulator activity Nucleotide binding Protein binding RNA binding	HSP90AB1					X	
P01833	Polymeric immunoglobulin receptor OS=Homo sapiens OX=9606 GN=PIGR PE=1 SV=4	Cell organization and biogenesis Regulation of biological process Response to stimulus Transport	Extracellular Membrane	Receptor activity Signal transducer activity	PIGR	X	X	X	X	X	X

Q8TDL5	BPI fold containing family B member 1 OS=Homo sapiens OX=9606 GN=BPIFB1 PE=1 SV=1	Defense response Regulation of biological process Response to stimulus	Extracellular		BPIFB1	X	X		X				
P0DMV8	Heat shock 70 kDa protein 1A OS=Homo sapiens OX=9606 GN=HSPA1A PE=1 SV=1	Cell organization and biogenesis Metabolic process Regulation of biological process Response to stimulus Transport	Cytoplasm Cytoskeleton Cytosol Endoplasmic reticulum Extracellular Mitochondrion Nucleus	Catalytic activity Nucleotide binding Protein binding Receptor activity RNA binding	HSPA1A						X		
P07355	Annexin A2 OS=Homo sapiens OX=9606 GN=ANXA2 PE=1 SV=2	Cell organization and biogenesis Metabolic process Regulation of biological process Response to stimulus Transport	Cell surface Cytoplasm Cytosol Endoplasmic reticulum Endosome Extracellular Membrane Nucleus Organelle lumen	Enzyme regulator activity Metal ion binding Protein binding RNA binding	ANXA2	X	X		X	X	X		X
P10451	Osteopontin OS=Homo sapiens OX=9606 GN=SPP1 PE=1 SV=1	Cell differentiation Cell organization and biogenesis Defense response Metabolic process Regulation of biological process Response to stimulus	Extracellular Golgi Organelle lumen	Protein binding	SPP1					X	X		X
Q8WXI7	Mucin16 OS=Homo sapiens OX=9606 GN=MUC16 PE=1 SV=3	Metabolic process Regulation of biological process Response to stimulus	Extracellular Membrane Organelle lumen	Protein binding	MUC16	X	X		X				
P00751	Complement factor B OS=Homo sapiens OX=9606 GN=CFB PE=1 SV=2	Defense response Metabolic process Regulation of biological process Response to stimulus	Extracellular Membrane	Catalytic activity Protein binding	CFB	X	X			X	X		X

P10909	Clusterin OS=Homo sapiens OX=9606 GN=CLU PE=1 SV=1	Cell death Cell organization and biogenesis Cell proliferation Defense response Metabolic process Regulation of biological process Response to stimulus Transport	Cell surface Cytoplasm Cytosol Endoplasmic reticulum Extracellular Golgi Membrane Mitochondrion Nucleus Organelle lumen	Catalytic activity Protein binding	CLU	X	X		X	X	X		X
P06396	Gelsolin OS=Homo sapiens OX=9606 GN=GSN PE=1 SV=1	Cell death Cell organization and biogenesis Metabolic process Regulation of biological process Response to stimulus Transport	Cytoplasm Cytoskeleton Cytosol Extracellular Membrane Nucleus Organelle lumen	Metal ion binding Protein binding	GSN	X	X		X				
Q08380	Galectin3binding protein OS=Homo sapiens OX=9606 GN=LGALS3BP PE=1 SV=1	Defense response Regulation of biological process Response to stimulus Transport	Extracellular Membrane Organelle lumen	Protein binding Receptor activity	LGALS 3BP	X	X		X	X	X		X
Q6UX06	Olfactomedin4 OS=Homo sapiens OX=9606 GN=OLFM4 PE=1 SV=1	Cell organization and biogenesis Regulation of biological process Transport	Extracellular Membrane Mitochondrion Organelle lumen Vacuole	Catalytic activity Protein binding	OLFM4					X	X		X
P80188	Neutrophil gelatinaseassociated lipocalin OS=Homo sapiens OX=9606 GN=LCN2 PE=1 SV=2	Cell communication Cell death Cell organization and biogenesis Cellular homeostasis Defense response Regulation of biological process Response to stimulus Transport	Cytosol Extracellular Organelle lumen	Metal ion binding Protein binding Transporter activity	LCN2	X	X		X	X	X		X
P04075	Fructosebisphosphate aldolase A OS=Homo sapiens OX=9606 GN=ALDOA PE=1 SV=2	Cell organization and biogenesis cellular Homeostasis Metabolic process Regulation of biological process Transport	Cytoplasm Cytoskeleton Cytosol Extracellular Membrane Nucleus Organelle lumen	Catalytic activity Protein binding RNA binding	ALDOA					X	X		
P02768	Serum albumin OS=Homo sapiens OX=9606 GN=ALB PE=1 SV=2	Cell communication Cell organization and biogenesis Metabolic process Regulation of biological process Response to stimulus Transport	Cytoplasm Endoplasmic reticulum Extracellular Golgi Nucleus Organelle lumen	Antioxidant activity Catalytic activity DNA binding Metal ion binding Protein binding	ALB	X	X		X	X	X		X

P02788	Lactotransferrin OS=Homo sapiens OX=9606 GN=LTF PE=1 SV=6	Cellular homeostasis Defense response Metabolic process Regulation of biological process Response to stimulus Transport	Cell surface Cytoplasm Extracellular Nucleus Organelle lumen	Catalytic activity DNA binding Enzyme regulator activity Metal ion binding Protein binding	LTF	X				X			
P09211	Glutathione Stransferase P OS=Homo sapiens OX=9606 GN=GSTP1 PE=1 SV=2	Cell communication Cell proliferation Metabolic process Regulation of biological process Response to stimulus Transport	Cytoplasm Cytosol Extracellular Membrane Mitochondrion Nucleus Organelle lumen	Antioxidant activity Catalytic activity Enzyme regulator activity Protein binding	GSTP1	X	X		X		X		
P04083	Annexin A1 OS=Homo sapiens OX=9606 GN=ANXA1 PE=1 SV=2	Cell differentiation Cell organization and biogenesis cellular Component Movement Defense response Metabolic process Regulation of biological process Response to stimulus Transport	Cell surface Cytoplasm Cytoskeleton Cytosol Endosome Extracellular Membrane Nucleus Vacuole	Catalytic activity DNA binding Enzyme regulator activity Metal ion binding Protein binding RNA binding Structural molecule activity	ANXA1		X		X				
P62937	Peptidylprolyl cistrans isomerase A OS=Homo sapiens OX=9606 GN=PPIA PE=1 SV=2	Cell organization and biogenesis cellular Component Movement Metabolic process Regulation of biological process Response to stimulus Transport	Cytoplasm Cytosol Extracellular Membrane Nucleus Organelle lumen	Catalytic activity Protein binding RNA binding	PPIA					X	X		
P20061	Transcobalamin1 OS=Homo sapiens OX=9606 GN=TCN1 PE=1 SV=2	Metabolic process Transport	Extracellular Organelle lumen		TCN1					X	X		X
P15941	Mucin1 OS=Homo sapiens OX=9606 GN=MUC1 PE=1 SV=3	Metabolic process Regulation of biological process Response to stimulus	Cytoplasm Extracellular Membrane Nucleus Organelle lumen	DNA binding Protein binding	MUC1	X	X		X				X
P62805	Histone H4 OS=Homo sapiens OX=9606 GN=HIST1H4A PE=1 SV=2	Cell organization and biogenesis Metabolic process Regulation of biological process Response to stimulus	Chromosome Extracellular Membrane Nucleus	DNA binding Protein binding RNA binding	H4-16						X		

P0DP23	Calmodulin1 OS=Homo sapiens OX=9606 GN=CALM1 PE=1 SV=1	Metabolic process Regulation of biological process Response to stimulus Transport	Cytoplasm Cytoskeleton Cytosol Extracellular Membrane	Catalytic activity Enzyme regulator activity Metal ion binding Protein binding Transporter activity	CALM3 CALM2 CALM1	X	X		X	
Q9NP55	BPI foldcontaining family A member 1 OS=Homo sapiens OX=9606 GN=BPIFA1 PE=1 SV=1	Cellular component Movement Defense response Regulation of biological process Response to stimulus Transport	Extracellular	Protein binding Transporter activity	BPIFA1	X	X		X	
P17936	Insulinlike growth factorbinding protein 3 OS=Homo sapiens OX=9606 GN=IGFBP3 PE=1 SV=2	Cell death Cell differentiation Cell proliferation Metabolic process Regulation of biological process	Extracellular Nucleus Organelle lumen	Enzyme regulator activity Metal ion binding Protein binding	IGFBP3	X	X		X	
P02647	Apolipoprotein AI OS=Homo sapiens OX=9606 GN=APOA1 PE=1 SV=1	Cell organization and biogenesis Cell proliferation Cellular component Movement Metabolic process Regulation of biological process Response to stimulus Transport	Cell surface Cytosol Endosome Extracellular Membrane Nucleus Organelle lumen	Enzyme regulator activity Protein binding Transporter activity	APOA1					X
P01023	Alpha2macroglobulin OS=Homo sapiens OX=9606 GN=A2M PE=1 SV=3	Cell differentiation Cell organization and biogenesis Metabolic process Regulation of biological process Response to stimulus Transport	Cytosol Extracellular Organelle lumen	Enzyme regulator activity Protein binding	A2M					X
P08263	Glutathione Stransferase A1 OS=Homo sapiens OX=9606 GN=GSTA1 PE=1 SV=3	Cell communication Cell differentiation Cell proliferation Metabolic process Regulation of biological process Response to stimulus Transport	Cytoplasm Cytosol Extracellular Membrane Mitochondrion Nucleus Organelle lumen	Antioxidant activity Catalytic activity Enzyme regulator activity Protein binding	GSTA1				X	
P11684	Uteroglobin OS=Homo sapiens OX=9606 GN=SCGB1A1 PE=1 SV=1	Regulation of biological process Response to stimulus	Cytoplasm Endoplasmic reticulum Extracellular	Enzyme regulator activity Protein binding	SCGB1 A1	X	X		X	

P02771	Alphafetoprotein OS=Homo sapiens OX=9606 GN=AFP PE=1 SV=1	Metabolic process Regulation of biological process Reproduction Response to stimulus Transport	Cytoplasm Cytosol Extracellular Organelle lumen	Metal ion binding Protein binding	AFP		X	
Q9HC84	Mucin-5B OS=Homo sapiens OX=9606 GN=MUC5B PE=1 SV=3	Metabolic process Regulation of biological process Response to stimulus	Extracellular Membrane Organelle lumen	Protein binding	MUC5B	X		X
Q9Y6R7	IgGFc-binding protein OS=Homo sapiens OX=9606 GN=FCGBP PE=1 SV=3		Extracellular	Protein binding	FCGBP			X
P00450	Ceruloplasmin OS=Homo sapiens OX=9606 GN=CP PE=1 SV=1	Cellular homeostasis Metabolic process Transport	Extracellular Membrane Organelle lumen	Catalytic activity Metal ion binding Protein binding	CP			X
O00391	Sulfhydryl oxidase 1 OS=Homo sapiens OX=9606 GN=QSOX1 PE=1 SV=3	Cellular homeostasis Metabolic process Regulation of biological process Transport	Extracellular Golgi Membrane Organelle lumen	Catalytic activity	QSOX1			X
P53634	Dipeptidyl peptidase 1 OS=Homo sapiens OX=9606 GN=CTSC PE=1 SV=2	Cell death Cell organization and biogenesis Metabolic process Regulation of biological process Response to stimulus Transport	Endoplasmic reticulum Extracellular Golgi Membrane Organelle lumen Vacuole	Catalytic activity Enzyme regulator activity Protein binding	CTSC			X

Chapter 5: Formation of the protein corona on silver nanoparticles in the Calu-3 secretome and its biological implications

As soon as nanomaterials (NMs) enter the body, they are coated by biomolecules, particularly proteins, forming a so-called protein (or biomolecular) corona, which modulates their fate and biological effects. The protein corona formation is influenced by the surface chemistry of the NM, its shape and size, and by the composition of the surrounding physiological media (Walkey and Chan 2012). The protein corona can affect processes such as NM-cell interaction and NM uptake, depending on the adsorbed proteins (Park 2020). For example, it was shown that the presence of clusterin in the protein corona of silver and silica nanoparticles (NPs) inhibited their cellular uptake by human macrophage-like cells (THP-1 cells) (Aoyama et al. 2016). Because of the protein corona influence on the biological effects and toxicity of NMs, the study of the protein corona formation on NPs in relevant biological media has become necessary.

Until now, the formation of the protein corona has mainly been investigated in the presence of serum and plasma proteins, either in cell culture media supplemented with FBS or directly in human serum or plasma (Lundqvist and Cedervall 2020; Böhmert et al. 2020). These studies have allowed the identification of the adsorbed proteins following NP separation with their protein corona from the free proteins in the medium by centrifugation (in most cases). The analysis of the protein corona by proteomics compared to the composition of the biological medium, that is identifying the adsorbed versus non-adsorbed proteins, led to the identification of the physical, chemical and biochemical determinants associated with protein adsorption and the formation of the protein corona in biological media (Mathé et al. 2013). They include parameters related to the properties of the NMs (size, chemistry, shape, charge, crystallinity...) and parameters related to the proteins present in these fluids (sequence, structure, flexibility…) (see chapter 1.4-1).

The main routes of exposure to NMs are ingestion, inhalation and direct contact with the skin. In all of these scenarios, the composition of the biological medium in which the biomolecular corona will first form differs from human plasma. Regarding the inhalation route, the airway epithelial secretions are mainly composed of mucins, antimicrobial peptides, proteases and antiproteases, while the most abundant plasma proteins are albumin, globulin, fibrinogen and regulatory proteins. Until now, little is known about the protein corona formed on inhaled NMs.

The aim of our study was to characterize the protein corona that forms on AgNPs when they encounter the airway fluid, and to determine how it would influence the effects of AgNPs on macrophages. For this purpose, we used the apical secretome of the Calu-3 epithelial barrier, described in chapter 4, as the airway biological fluid. Moreover, the interaction of AgNPs with the apical secretome was studied in two different conditions called "acellular" and "cellular" conditions. For the "acellular protein corona", AgNPs were incubated in the apical secretome of Calu-3 cells (previously collected) in Eppendorf tubes for 10 min to 1h (Figure 54a), whereas for the "cellular protein corona", the Calu-3 cells were exposed at ALI to AgNPs for 1 to 48h and AgNPs were recovered with their protein corona by washing the apical compartment (Figure 54b). In the first case, the NPs were exposed to a secretome which composition remained constant with time, whereas in the second case, NPs were exposed to a dynamic airway fluid, which composition can be modified by living cells' response to AgNP exposure.

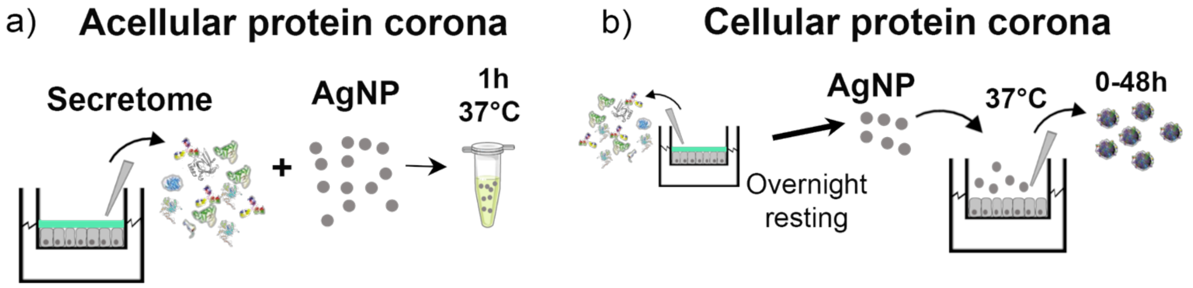

Figure 54: Schematic representation of the protocol we used for the acellular and cellular protein corona formation on AgNPs in the secretome of Calu-3 cells.

(a) For the acellular corona, the secretome was collected from Calu-3 cultures at ALI in 200µL HBSS$^{Ca2+/Mg2+}$ *before AgNPs were incubated in the secretome in Eppendorf tubes at 37°C for 10 min or 1h. (b) For the cellular corona, the Calu-3 cells were directly exposed to AgNPs. After 1 to 48h exposure, AgNPs with their protein corona were recovered by washing the apical compartment with 200 µL HBSS*$^{Ca2+/Mg2+}$.

The particularity of the airway fluid is the presence of mucus, which contributes to trapping and eliminating the inhaled particles by mucociliary clearance. From a methodological point of view, the presence of mucus has complicated the separation of NPs from the airway secretions for protein corona studies. Until now, the methods used to separate NPs (with their adsorbed protein corona) from the surrounding biological fluid (containing free proteins only) have not been standardized. The most commonly used methods for NP isolation are centrifugation and magnetic separation (for magnetic NPs only), and less frequently, size exclusion chromatography (SEC). These methods and others were recently reviewed by different authors (Weber, Morsbach, and Landfester 2019; Böhmert et al. 2020). The selection of the most appropriate separation method depends on the type of NPs and the biological fluid studied. Selecting the appropriate method will reduce artefacts that may occur following the precipitation of free proteins (false positives) or the loss of adsorbed proteins during the separation step (false negative). The separation methods we considered for this study of protein corona formation in mucus were centrifugation, magnetic separation and size exclusion chromatography.

In this chapter, first we describe the different methodologies we tested in order to improve the recovery of NPs from the mucus produced by the Calu-3 epithelial barrier. Then, we analyzed the composition of the acellular and cellular protein corona formed on AgNPs using proteomics and we investigated the cellular effects of AgNPs on Calu-3 cells at ALI. Finally, we studied the role of the protein corona in the cellular effects of AgNPs on macrophages.

Aims:

- To determine the appropriate NP separation method in airway epithelial mucus for protein corona study
- To analyse the protein corona composition following incubation of AgNPs in the secretome with (“cellular”) and without (“acellular”) Calu-3 cells
- To monitor the cellular responses of Calu-3 cells to AgNP exposure at ALI
- To study the role of the protein corona in the cellular effects of AgNPs on THP-1 macrophages

5.1 Strategies to separate AgNPs from the secretome to analyse the protein corona

The most widely used method for NP separation for protein corona analysis is centrifugation. It is easy to implement with standard equipment and it can be applied to most nanomaterials. The main limitation of this method is the modification of the protein corona during the separation step: the “hard corona” composed of tightly bound proteins is preserved, whereas the “soft corona” that contains loosely bound proteins may be lost (Winzen et al. 2015). In the Calu-3 secretome, the formation of a mucus layer in the secretome and the presence of highly glycosylated proteins make NP separation by centrifugation more difficult. Indeed, free proteins tend to precipitate during centrifugation, impairing the separation between NPs and free proteins from the medium. The drawbacks of the centrifugation method can be solved by using the magnetic separation instead. However, the latter is restricted to magnetic NPs and therefore it cannot be applied to bare AgNPs. Another alternative is the size exclusion chromatography, which is less frequently used due to higher cost and lower throughput (Böhmert et al. 2020). The application of these 3 methods to NP separation in the secretome, for either the acellular or the cellular protein corona analysis, is presented below.

5.1-1 Standard centrifugation protocol for NP separation

First, we used a standard centrifugation protocol to isolate AgNPs with their adsorbed protein corona from the free proteins in the Calu-3 secretome. Briefly, the samples were centrifuged at 4°C for 20 min at 14,000g following AgNP incubation in the secretome (acellular protein corona), or their recovery from the apical compartment of the Calu-3 culture (cellular protein corona) (Figure 55a). The pellet, containing AgNPs with their protein corona, was resuspended in 500 µL HBSS and centrifuged for 20 min at 14,000g (washing step). Three washing steps were done in order to remove all the free proteins. This step also likely removed the proteins weakly bound to AgNPs. The free proteins (from the first supernatant) and the adsorbed proteins (AgNP-protein corona) were mixed with NuPAGE^{TM}-LDS buffer with 0.05M of DTT, heated 10 min at 95°C, and loaded in the SDS-PAGE electrophoresis gel. This treatment induced both protein denaturation and desorption from AgNPs. The nanoparticles were subsequently trapped in the well and they did not migrate into the gel. Sypro® Ruby was used for protein staining as it can achieve high sensitivities in the 0.25-1 ng range for most of the proteins (Figure 55b and c).

For the analysis of the acellular protein corona formation, we selected two different incubation times in the Calu-3 secretome: 10 min and 1 h (Figure 55b). All the samples were incubated at 37°C with gentle shaking. In addition, we also analysed a sample containing the secretome only as a control, using the same centrifugation and washing protocol before running the gel electrophoresis (Figure 55a). One control was always analysed for each condition (acellular and cellular corona). The control showed the presence of free proteins that precipitated by centrifugation. These proteins correspond to false positives that will be excluded from the protein corona analysis.

The acellular protein corona formed after 10 min or 1 h exhibited a similar profile. The same protein profile was also observed in the supernatant corresponding to non-adsorbed proteins for the two time points. We identified an enrichment of proteins in the protein corona which was composed of proteins with different sizes (ranging from 31 to 97 kDa). However, small proteins (<50 kDa) were highly enriched in the corona, and were absent in the supernatant protein profile. The effect of a longer incubation time (e.g., 24 or 48h) on the composition of the acellular protein corona could not be analysed due to the higher protease activity in the samples at 37°C.

In the case of the cellular protein corona, a first striking observation was the high protein content in the pellet of the secretome control. This result shows that the centrifugation favored the protein sedimentation, likely due to the presence of highly glycosylated proteins. However, we observed that the pellets of freshly collected secretomes differed from the pellets of secretomes frozen at -80°C for storage before the analysis (Figure 55b and c). Fewer proteins precipitated in the latter condition. It suggests that freezing could alter the structure of the mucus network. The modification or disruption of the mucus network may prevent a high protein loss during secretome centrifugation. We further tested this hypothesis by implementing an advanced centrifugation protocol.

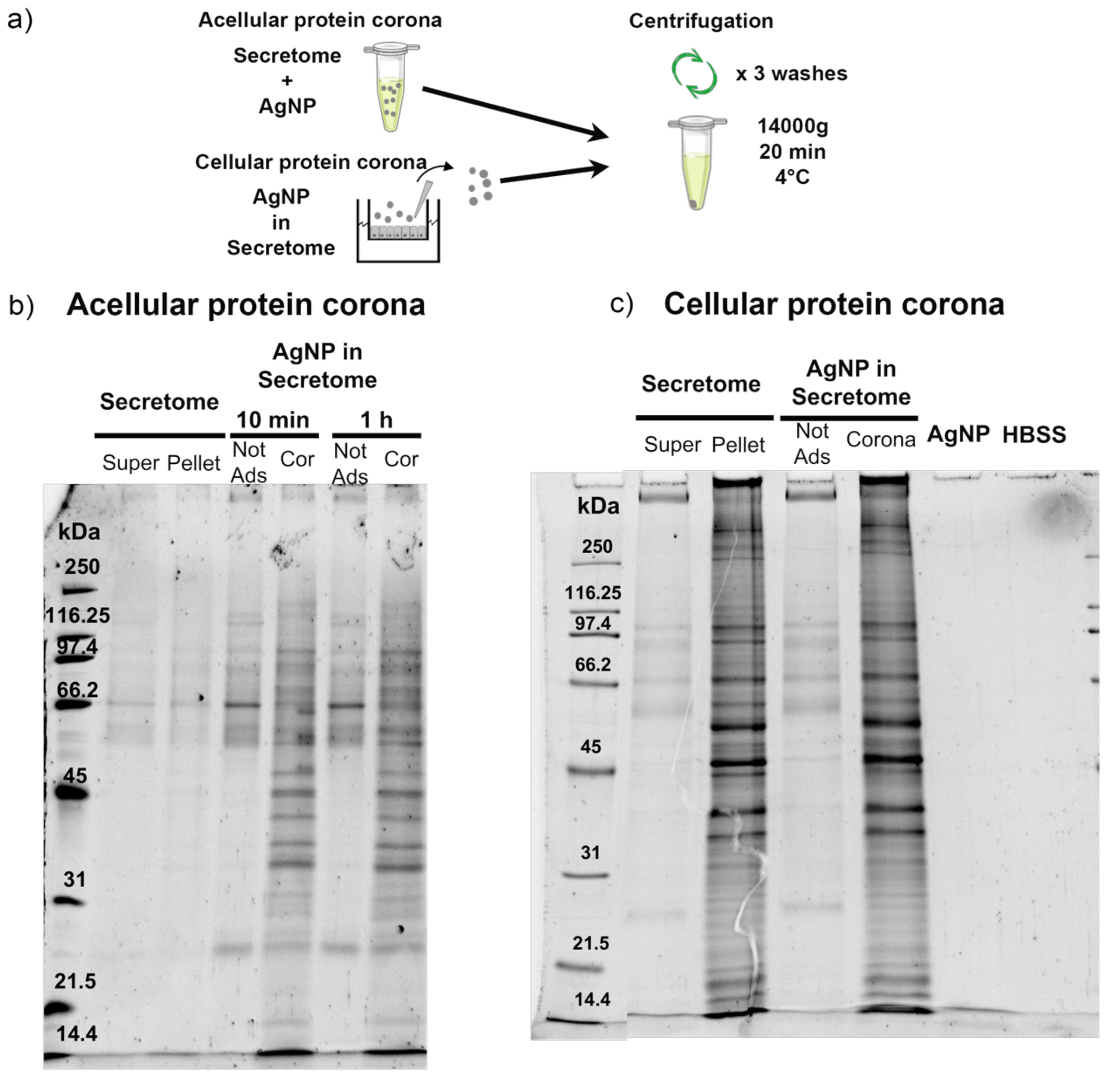

Figure 55: Centrifugation protocol for the separation of AgNPs from the Calu-3 secretome.

(a) Schematic of the centrifugation protocol used for the study of the acellular and cellular protein corona. For the acellular corona, the frozen secretome was thawed and mixed with 10 µg AgNPs for 10 min or 1 h at 37°C. For the cellular corona, Calu-3 cells were exposed to 10 µg AgNPs for 24 h. At the end of the incubation period, the samples were centrifuged to separate AgNPs with their protein corona. The remaining free proteins were removed by 3 washes. (b) SDS-PAGE analysis in the acellular condition. A secretome sample was used as a control. (c) SDS-PAGE analysis in the cellular condition. A culture treated with HBSS was used as a control. Proteins were stained with SYPRO® Ruby. Super: supernatant, Not Ads: free proteins. Cor: Protein corona.

5.1-2 Advanced centrifugation protocol for the separation of AgNPs in mucus samples

We modified the centrifugation protocol to reduce protein sedimentation in the absence of NPs. As we did not observe a large sedimentation of free proteins from the secretomes that were frozen at -80°C (Figure 55b) compared to fresh secretomes (Figure 55c), an additional freezing/thawing step was included before NP isolation by centrifugation for the analysis of the cellular protein corona. First, the secretome collected on Calu-3 cells following AgNP exposure (cellular conditions) was frozen at -80°C. Then, two centrifugation steps were used to separate AgNPs from the free proteins in the secretome (Figure 56a). First, centrifugation was performed at low speed (3,000*g*) to separate AgNPs while reducing the sedimentation of free proteins (Figure 56b). The supernatants of the first centrifugation step (Ctl and AgNP) were analysed by SDS-PAGE (Figure 56b, red square). A low amount of protein was detected due to large samples volumes, which diluted the protein content. Then, the supernatant was removed and 3 washing steps of the AgNPs at high centrifugation speed was performed as before. The following supernatants obtained during the washing steps were also analysed by SDS-PAGE. No proteins were detected (large volumes of buffer were also used for the washing step). Finally, the secretome alone and AgNP pellets were analysed by SDS-PAGE gel (Figure 56b, blue dotted square). Proteins were only detected in the pellet of AgNP samples and none were detected in the pellet of the secretome alone. We selected this protocol for the study of the acellular and cellular protein corona analysis.

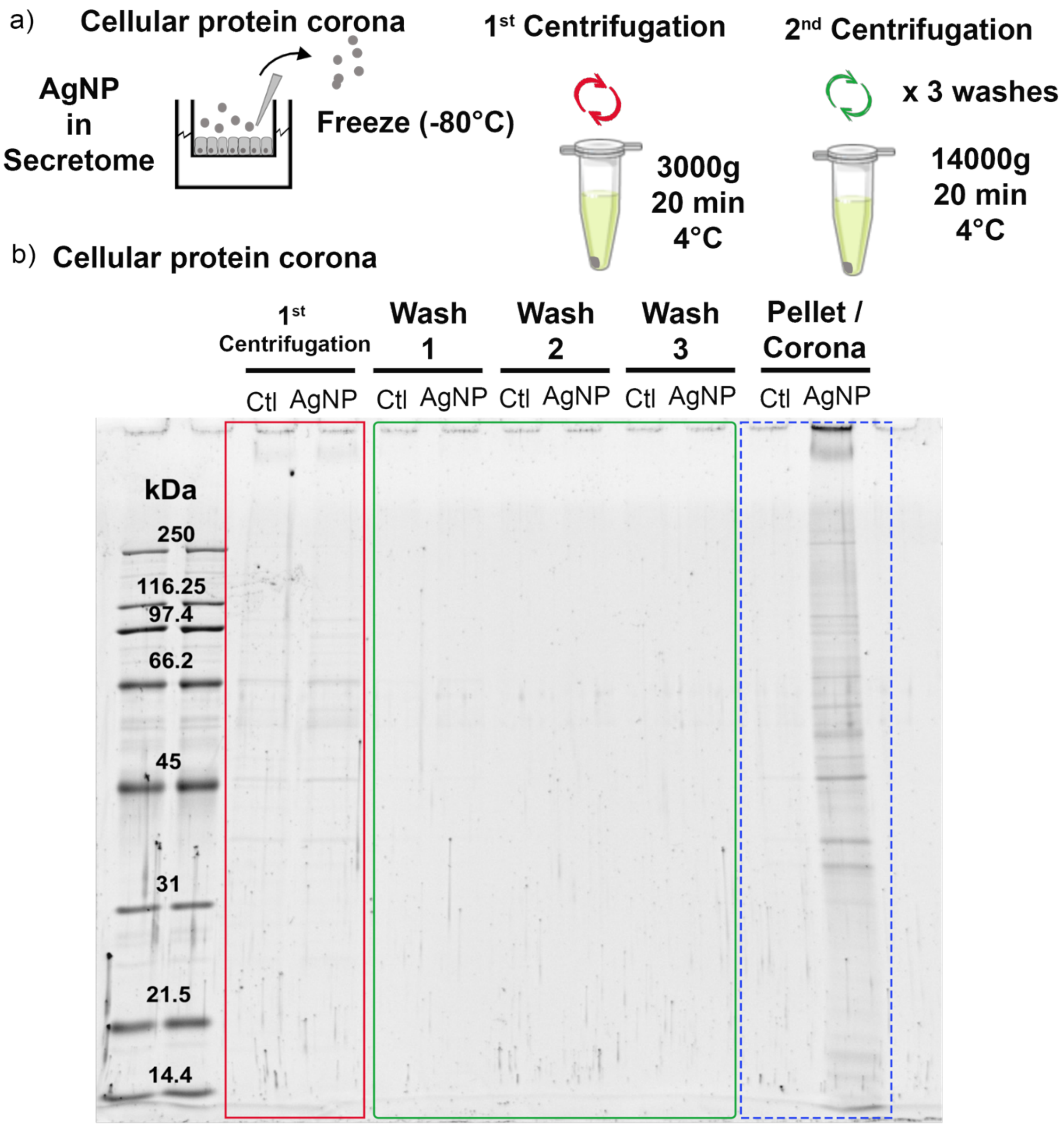

Figure 56: Modified centrifugation protocol for the separation of AgNPs in the secretome.

(a) Schematic of the centrifugation protocol used for the analysis of the cellular protein corona on AgNPs. AgNPs were collected in 200µL HBSS in the apical compartment of Calu-3 cells. The samples were frozen at -80°C. Thawed samples were centrifuged in two steps, at 3,000g for 20 min at 4°C, then at 14,000g for 20 min at 4°C, followed by 3 washes in HBSS. (b) SDS-PAGE analysis of the cellular protein corona on AgNPs. NP-free sample (Ctl) and exposure to 10µg AgNPs (AgNP). Proteins were stained with SYPRO® Ruby. Red square shows supernatants of the first separation step (samples highly diluted). Green square shows supernatants for each wash (samples highly diluted). Blue square with a dotted line shows the pellet from a NP-free secretome (Ctl) and AgNP-protein corona (AgNP).

5.1-3 Comparison of methods for the NP separation from the mucus

In parallel to our work on the improvement of the centrifugation method, we explored other methods to isolate NPs with their protein corona from the mucus. A collaboration has been set up in this perspective with Dr. Marco Monopoli and his team at RCSI, Dublin, where I moved for a 3-week secondment.

As the centrifugation step may induce modifications of the protein corona (loss of weakly bound proteins and reshuffling of the corona during the manipulation), I compared the protein corona formed in the mucus following NP separation by centrifugation or magnetic separation. For this experiment, I used magnetic iron oxide NPs in addition to AgNPs. The iron oxide NPs were Fe_3O_4-PEG-PLGA NPs from Colorobbia, which are also studied in the framework of the EU BIORIMA project. The biological medium was the Calu-3 secretome collected and frozen at -80°C before use.

The acellular protein corona was formed by mixing 10 µg Fe_3O_4 NPs with 200 µL of Calu-3 secretome. The centrifugation protocol was done as described before, except that the centrifugation speed for the second step was set to 18,000g, which is required for Fe_3O_4 NPs. For magnetic separation, the Fe_3O_4 NPs were mixed with metallic beads (extracted from chromatography columns) following incubation with the secretome, and separated using a strong magnet through the Eppendorf tube (F329, Magnet expert LTD, 14kg pull) (Figure 57a). 3 washes were performed in HBSS using the magnet. Finally, the Fe_3O_4NPs were resuspended in 20 µL HBSS and 3-4 back and forth movements were done with the pipet to detach NPs from the metallic beads. Then, the protein corona was analysed by SDS-PAGE following the same protocol as before (Figure 57b). As observed with AgNPs, the Fe_3O_4NPs were trapped in the well during the electrophoresis.

The SDS-PAGE profiles of the protein corona formed on Fe_3O_4NPs in the secretome and analysed following either magnetic or centrifugation separation were very similar (Figure 57b). The profiles of the controls (secretome without NPs) revealed the presence of free proteins in the pellet for the centrifugation method, whereas no proteins were detected in the control for the magnetic separation method.

Interestingly, the protein profiles of the corona formed on Fe_3O_4 and AgNPs in the secretome were very similar. Further analysis by mass spectrometry would be needed to investigate the effect of surface chemistry on the protein corona composition in the mucus.

Although these experiments were performed with Fe_3O_4NPs, which behaviour can be different from AgNPs, the results suggest that the centrifugation method we set up provides relatively comparable results with the magnetic separation method. The most visible difference was the precipitation of some free proteins in the pellet during NP isolation by centrifugation.

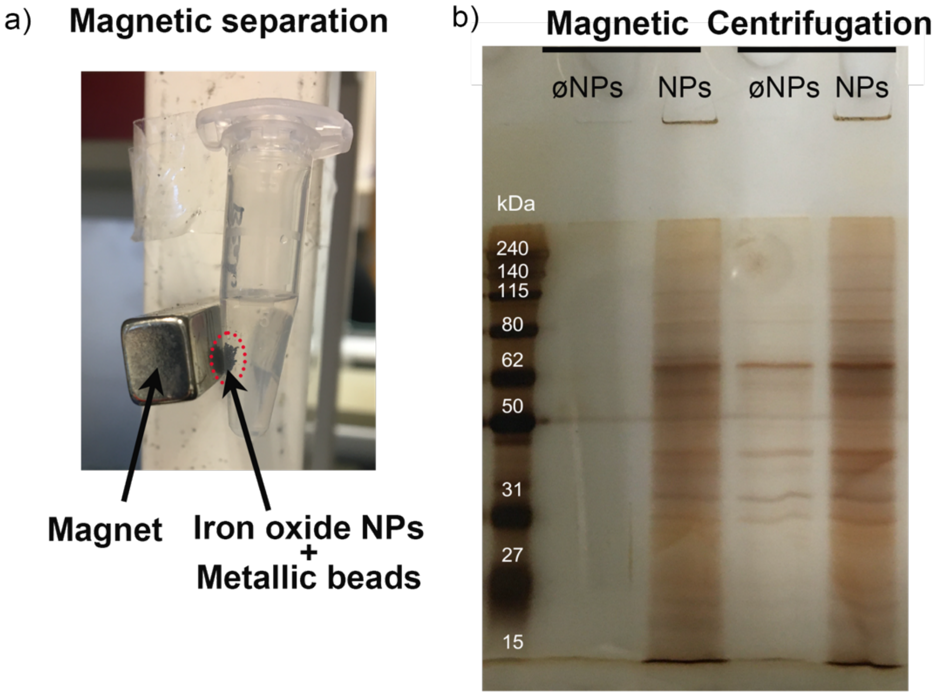

Figure 57: *Magnetic versus centrifugation separation of Fe_3O_4 NPs in the secretome.*

(a) Picture of the sample attached to the magnet. The Fe_3O_4NPs were mixed with metallic beads to enhance Fe_3O_4NP separation (red dotted circle). (b) SDS-PAGE analysis of the protein corona on Fe_3O_4NP following magnetic and centrifugation separation. 10µg Fe_3O_4 NPs were used for the acellular protein corona analysis. A sample without NPs was used as a control (∅ NPs). Proteins were detected with silver stain (Insight, 2D-silver Stain kit II, 167997). ∅NPs: control, NPs: protein corona.

A second secondment was planned at Dr. Monopoli's laboratory to develop the size exclusion chromatography method, which is a promising technique for NP separation in different samples (MONOPOLI et al. 2013). However, due to the Covid-19 travel restrictions, it was canceled. Instead, I developed a preliminary study on AgNP separation by SEC in our laboratory in Paris. A XK16-40 column (GE28-9889-38) was packed with the gel filtration Superdex 200 prep grade (GE-17-1043-01, Ge Healthcare) following manufacture's instruction and connected to a FPLC AKTA (Ge Heathcare). The column was equilibrated with PBS 1mM EDTA (the elution buffer) before used.

First, 200 µL of secretome (without NPs) were loaded in the column at a constant flow rate of 1mL/min. Proteins were monitored by measuring the absorbance at 280 nm with a detector coupled to the column. Unfortunately, no proteins were detected due to low protein concentration in the sample and the dilution associated with the elution. Using the same settings, a secretome sample incubated with 10 µg of AgNPs was loaded in the column. The column was disconnected from the UV detector (to avoid blocking the system with aggregates). The eluted volumes were collected in 1 mL fractions. The passage of AgNPs through the column was confirmed by absorbance measurement at 400 nm, corresponding to the characteristic plasmon band of AgNPs. The collected NPs were concentrated, but we could not recover enough proteins for analysis by SDS-PAGE. We concluded that the sample size (volumes of secretome, NP mass) was too small to apply SEC. SEC requires large volumes of buffer to perform the separation, resulting in a highly diluted sample. Hence, the large volume used to elute the protein corona was not compatible with further proteomic analysis in which concentrated proteins are needed. Further protocol optimization is required before applying this technique.

5.2 Characterization of the acellular protein corona on AgNPs

The formation of the acellular protein corona on AgNPs in the Calu-3 secretome was analyzed by LC-MS/MS. Two AgNP concentrations, corresponding to two protein/NP ratio were used. 10 and 50 µg AgNPs were mixed with 200 µL of the secretome. The AgNP concentrations were chosen to reproduce the conditions of AgNP toxicity testing on Calu-3 cells (10 µg AgNPs) and to maximize the amount of proteins collected from the corona (50 µg AgNPs).

The total protein concentration of the secretome was 250 µg/mL in average, corresponding to a protein/NP ratio of 5 and 1 mg (protein)/mg (NP) for 10 and 50 µg AgNPs respectively. The specific surface area of NM300K AgNP was estimated to 38 m^2/g, so that the total available surface could be estimated to $3.8\ 10^{-4}\ m^2$ for 10 µg AgNPs and $1.9\ 10^{-3}\ m^2$ for 50 µg AgNPs. The corresponding protein/NP ratio expressed in surface area can be estimated to 132 mg (protein)/m^2 for 10 µg AgNPs and 26 mg (protein)/m^2 for 50 µg AgNPs.

The secretome was collected from 3 independent cultures after 10 days at ALI, and frozen at -80°C before use. Briefly, 200 µL secretome was mixed with 10 or 50µg AgNP for 1 h at 37°C with gentle mixing. The AgNPs were separated using the centrifugation protocol described in section 5.1-2. Then, all the samples, including the secretome control without NPs, were treated as described for SDS-PAGE analysis. This step was performed to desorb the proteins from the

NP surface. Instead of running the electrophoresis until full protein separation was obtained, the electrophoresis was run for a short time (approximately 10 min) at 100 V, allowing proteins to migrate into the gel, while AgNPs remained in the wells. A gel band (approximately 1 cm wide, at the top of the gel) was cut and digested before LC-MS/MS analysis. Loading buffer contained Coomassie G250 and Phenol red dyes, which were used to confirm that no proteins could be detected in the remaining gel.

5.2-1 Mass spectrometry analysis of the protein corona

Only the proteins identified in at least two replicates in each condition were considered. 1,297 proteins were identified in the control including mucins (MUC5AC, MUC5B, MUC13), lipocalin-2, BPI-fold containing family, clusterin, annexins between others. Proteins that were detected in the control (false-positives) were excluded from the analysis of the protein corona. Following subtraction, 73 proteins were identified in the protein corona formed with 10 µg AgNP, and 90 in the protein corona formed with 50 µg AgNP. These included 8 unique proteins in the first condition, and 25 unique proteins in the second condition, plus 65 common proteins (Figure 58). In the common proteins, we found proteins with transporter function, such as the aquaporin-1 (AQP1), the growth factor midkine (MDK); proteins involved in chromatin or cytoskeletal proteins binding; and proteins with different catalytic activities, such as proteases, protease inhibitors, ligases transferase. In the 10 µg AgNP protein corona, we identified 8 exclusive proteins, such as the transporter phosphatidylinositol transfer protein beta isoform (PITPNB), the phospholipase monoglyceride lipase (MGLL), and the glia maturation factor beta (GMFB) that is involved in intracellular signaling. By contrast, in the 50 µg AgNP protein corona, 25 proteins were exclusively present. Among them we found two subunits of the transporter importin (KPNA1 and KPNA4) and different binding proteins, such as TATA-binding protein-associated factor 2N (TAF15).

The uses of two AgNP concentrations allowed following the protein corona formation using 2 different protein/NP ratio. The higher protein/NP ratio (10 µg AgNP condition) led to the formation of a protein corona with a lower protein diversity. By contrast, the lowest protein/NP ratio (50 µg AgNP condition) led to the adsorption of a higher diversity of proteins on the surface, suggesting that the larger available surface allowed binding of a larger number of different proteins, perhaps with a different affinity for the surface. The effect of protein/NP ratio on the protein pattern and protein abundance of the protein corona was also reported for silica NPs incubated in human plasma (Monopoli et al. 2011). These results suggest that competitive protein binding took place during the formation of the protein corona on AgNPs in the secretome, possibly driven by different affinities for the surface.

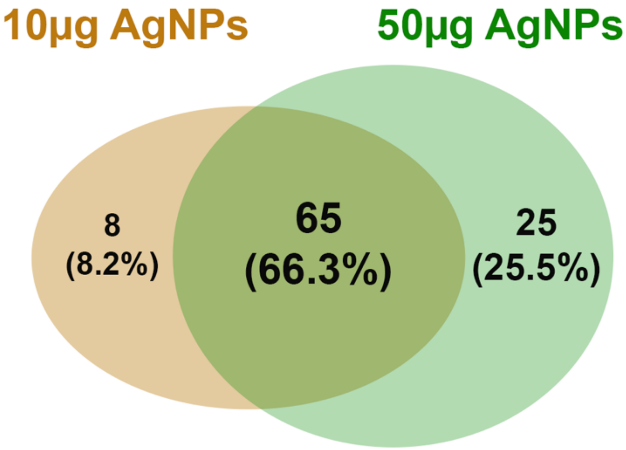

Figure 58: Mass spectrometry analysis of the acellular protein corona formed on AgNPs in the secretome.

LC-MS/MS analysis of the acellular protein corona on 10 µg AgNP and 50 µg AgNP in the secretome. The total number of proteins and the percentage of common proteins are shown in a Venn diagram. False positive proteins identified in the control were excluded from the analysis.

Here, all the proteins identified by mass spectrometry were considered in the analysis, meaning that both intracellular and extracellular proteins were considered. We chose not to exclude the intracellular proteins from this analysis as they could be part of the protein corona, both *in vitro* and *in vivo*, following cell death and the renewal of the epithelial barrier. To determine which proteins in the corona may originate from the intracellular or extracellular compartments, a cellular component enrichment analysis was performed (Figure 59). For the enrichment analysis, 73 proteins and 90 proteins were used for 10 µg and 50 µg AgNP, respectively. Only the first 20 most enriched cellular components are represented. This analysis showed that, in both conditions, the proteins forming the corona come from different intracellular and extracellular compartments. We identified extracellular proteins (released in the extracellular space, or associated to vesicles and exosomes), membrane proteins (from the plasma membrane or organelles), and cytoplasmic proteins. Interestingly, some cellular compartments were only enriched in one of the two conditions. With 10 µg AgNP, we found proteins associated to peptidase and endopeptidase complex, contrarily to the protein corona formed with 50 µg AgNP where we found nuclear, cytosolic, and proteins associated with intracellular anatomical structures.

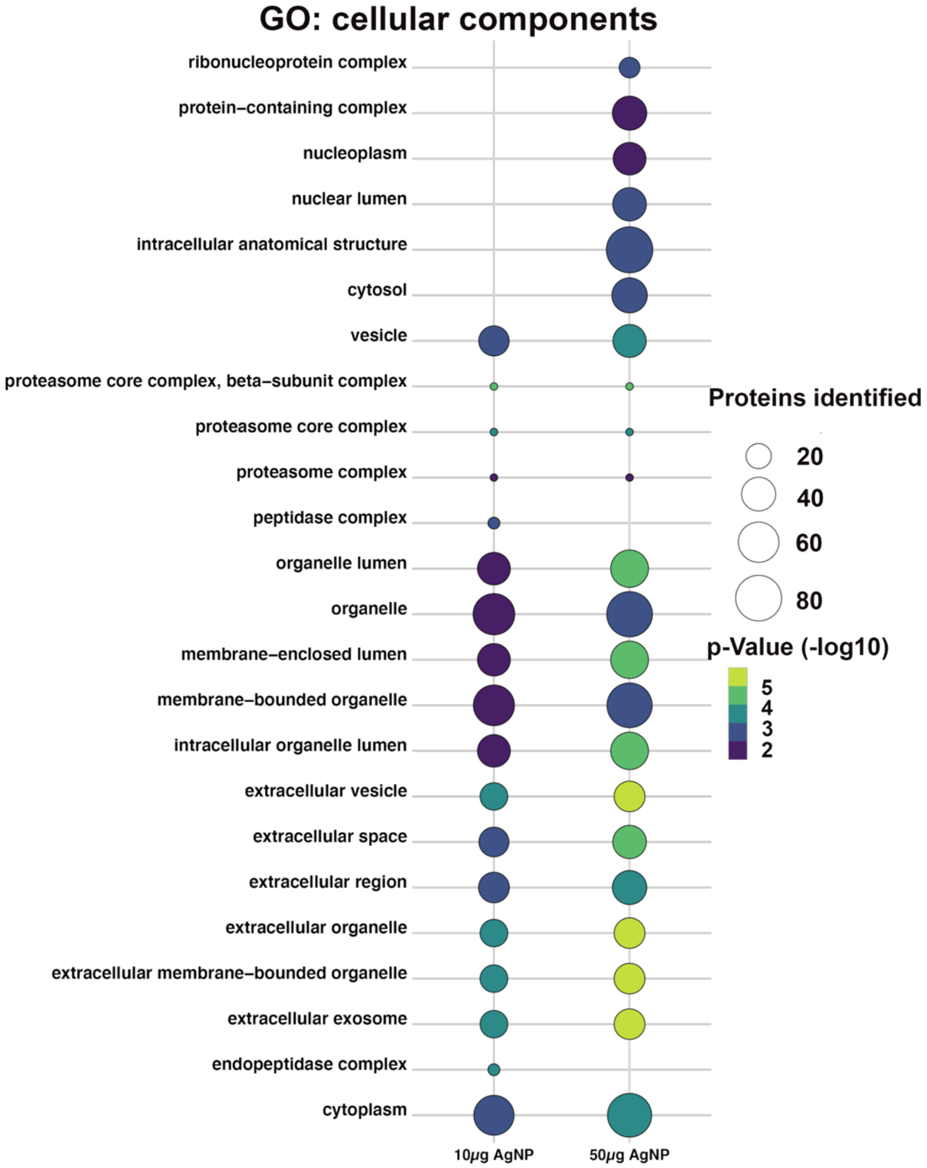

Figure 59: g:GOST functional enrichment analysis of gene ontology cellular components applied to the acellular protein corona.

Statistically significantly enriched gene ontology cellular components are shown for proteins identified in the 10 µg and 50 µg acellular protein corona.

The proteins with their respective relative abundances are represented in a sphere diagram for each acellular protein corona in Figure 60. Each sphere corresponds to one protein whose size reflects their relative abundance in the corona. In the 50 most abundant proteins identified in both protein coronas, we identified proteasome proteins, such as proteasome subunit proteins (PSMB3, PSMB4 and PSM7); cytokines, such as interleukin-18 (IL-18); proteins with enzyme regulator activity, such as activator of 90 kDa heat shock protein (AHSA1) and Rab GDP dissociation inhibitor alpha (GDI1); proteins with receptor regulator activities, such as midkine (MDK) pancreatic prohormone (PNP); proteins with transcription regulation activities, such as RNA-binding protein EWS (EWSR1) and hepatoma-derived growth factor (HDGF); proteins with binding activities, such as tight junction protein ZO-2 (TJP-2), actin-related protein 2/3 (ARPC1B), putative RNA-binding protein (LUC7L2); and proteins with catalytic activities, such as fumarylacetoacetase (FAH), pterin-4-alpha-carbinolamine dehydratase (PCBD1), phosphoserine aminotransferase (PSAT1) and purine nucleoside phosphorylase (PNP). Besides, the protein CDGSH iron-sulfur domain-containing protein 2 (CISD2), which is involved in cellular autophagy regulation at the endoplasmic reticulum (Chang et al. 2009), was also identified in the protein corona in both conditions .

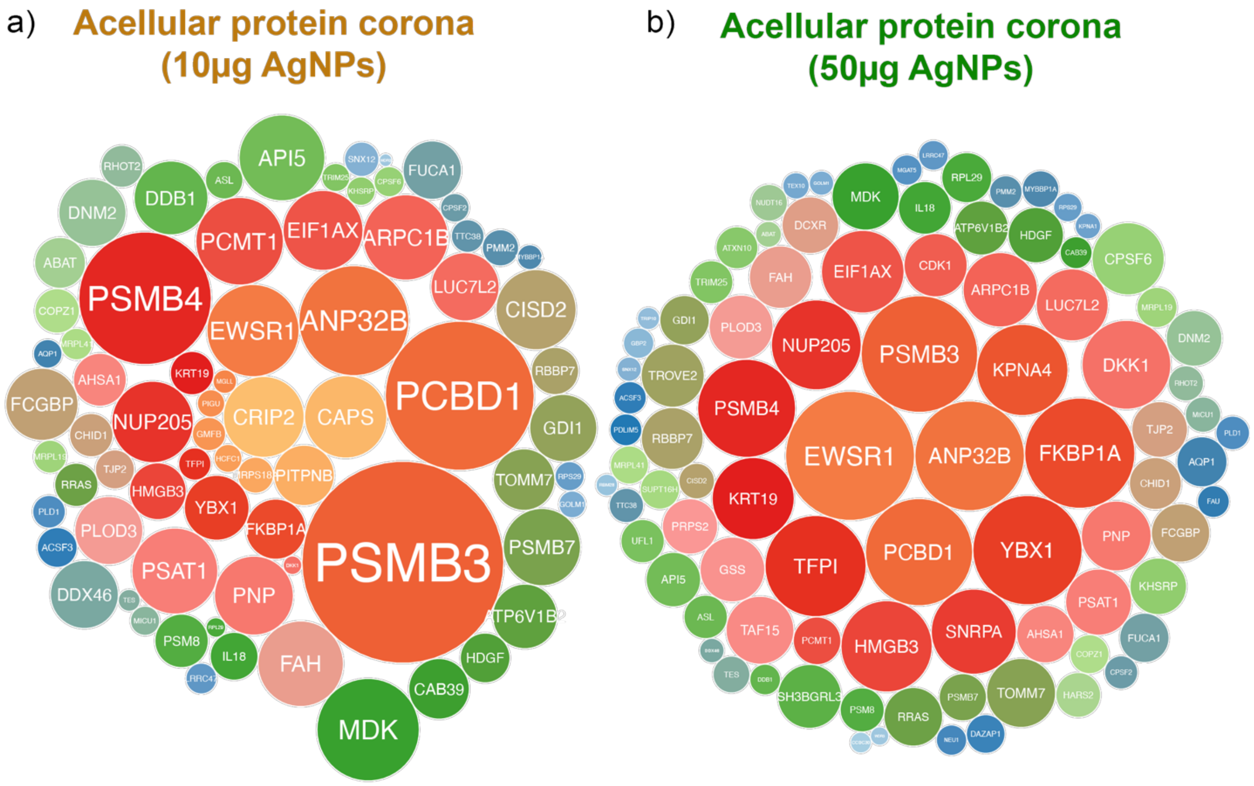

Figure 60: Comparison of the acellular protein corona formed on AgNP in the secretome for 2 protein/NP ratio.

a) 10 µg AgNP and b) 50 µg AgNP. The size of the sphere changes proportionally to the relative protein abundance. Proteins are designated by their corresponding gene names.

The biological role of the adsorbed proteins was further investigated by functional enrichment analysis of the Reactome pathways (Figure 61). Common and unique proteins for each condition were used for the functional enrichment analysis. In both coronas, we found pathways involved in DNA damage and apoptosis regulations, with a low number of proteins identified in each pathway. However, when selecting proteins identified in each condition (but not specific to), we found that pathways involved in the metabolism of RNA and amino acids were significantly enriched with a higher number of proteins identified.

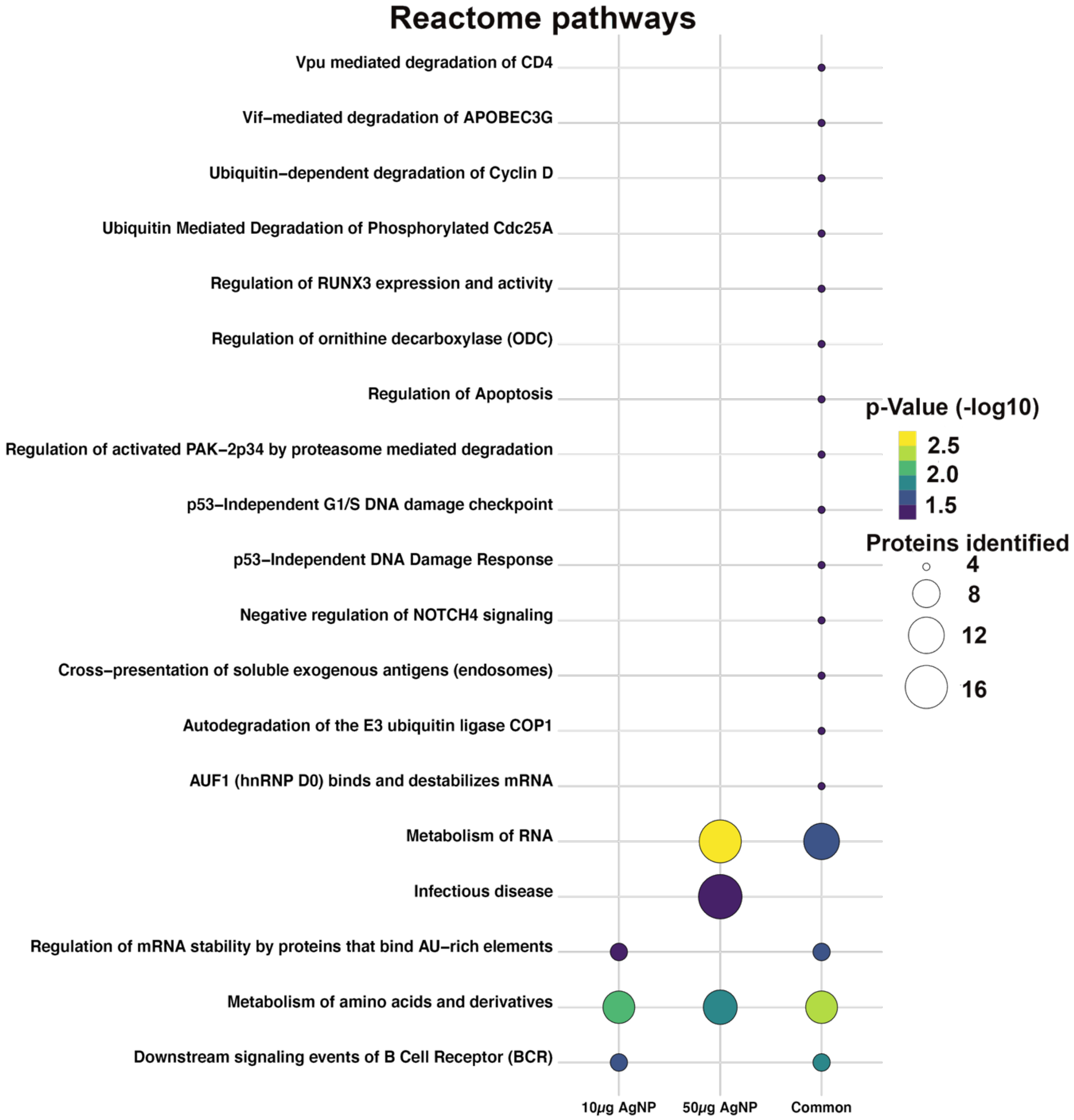

Figure 61: g:GOST functional enrichment analysis of Reactome pathways of the acellular protein corona.

Reactome pathway functional enrichment were analysed for the 73 proteins identified in 10 μg, the 90 proteins identified in 50μg acellular protein corona, and the 65 proteins common to both conditions.

5.3 Characterization of the cellular protein corona following exposure of Calu-3 cells to AgNPs

The formation of the protein corona on AgNPs was also investigated while NPs were in direct contact with Calu-3 cultures ("cellular" protein corona). Calu-3 cells were exposed to HBSS, 10 and 50 µg of AgNPs for 1 h, 24 h and 48 h.

The UV-vis spectra of AgNPs were measured before and after incubation in the secretome. Changes in the optical properties of AgNPs were observed after incubation with Calu-3 cells (Figure 62a). AgNPs present a characteristic absorption peak around 400nm, which corresponds to the surface plasmon band. The surface plasmon depends on the size and the aggregation state of the AgNPs. The intensity of the plasmon band decreased and shifted following incubation of AgNPs in the Calu-3 secretome, possibly due to aggregation in the presence of mucus (Figure 62b-d). One hour after treatment, no changes were observed compared to stock AgNP solutions (Figure 62b). By contrast, after 24 and 48 h of exposure, large changes of the AgNP UV-vis spectra were observed (Figure 62c and d), suggesting an effect of the incubation in the presence of cells on the aggregation state of AgNPs (Figure 62a).

The cellular protein corona was analysed by SDS-PAGE gel (Figure 62e). Curiously, similar protein profiles were observed after 1, 24 and 48 h exposure for both AgNP concentrations (10 and 50 µg). We only observed an increase in protein amount in the corona with time, especially between 1 h and 24-48 h. Some proteins were also identified in the control samples, but at lower concentrations.

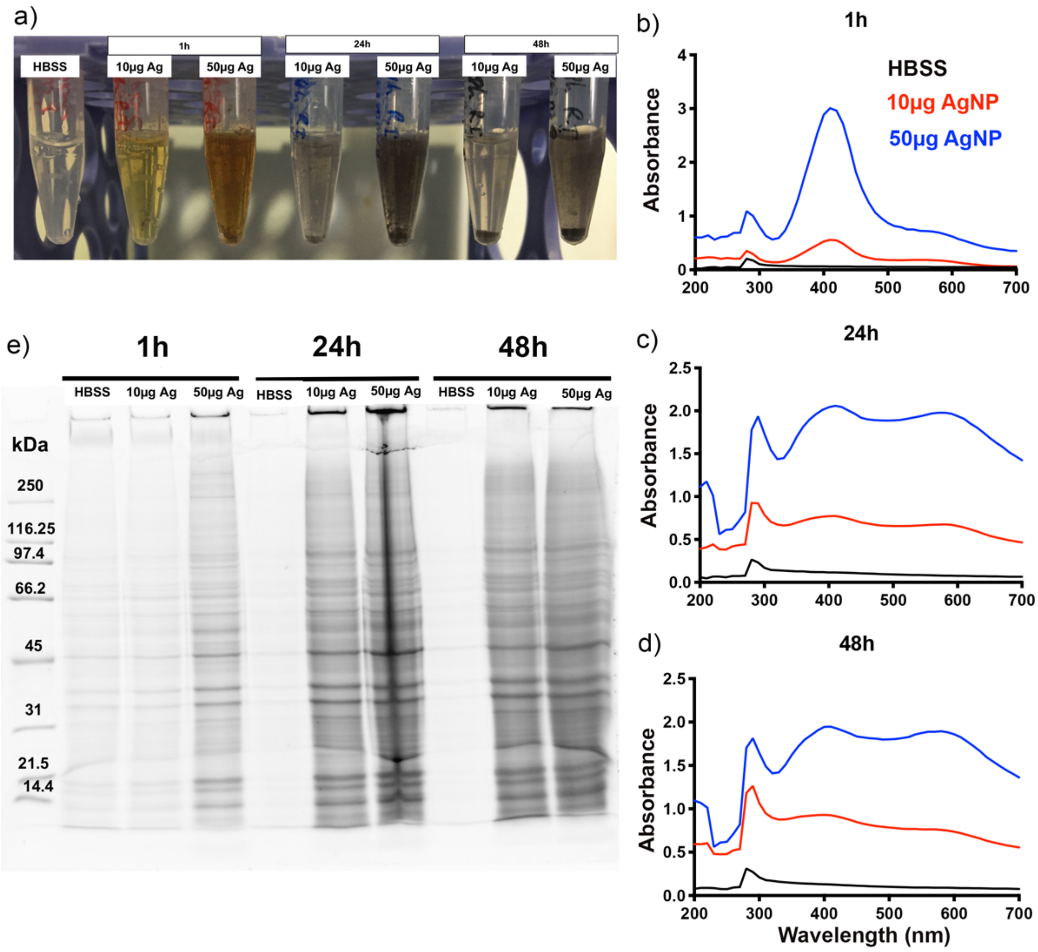

Figure 62: Characterization of AgNPs and the cellular protein corona following exposure to Calu-3 cultures.

(a) Images of the samples after collection. (b, c, d) UV-vis spectra of AgNPs in HBSS and in the secretome following 1, 24, 48 h exposure of Calu-3 cells. (e) SDS-PAGE analysis of the cellular protein corona. AgNPs were isolated from the secretome by centrifugation and the protein corona was analyzed by SDS-PAGE gel using SYPRO® Ruby staining.

5.3-1 Mass spectrometry analysis of the cellular protein corona

The cellular protein corona was characterized by LC-MS/MS. For this analysis, the cellular protein corona formed after 1 h and 24 h exposure of Calu-3 cells to two NPs concentration (10 µg and 50 µg of AgNPs) were selected. Only proteins identified in at least two replicates in each condition were considered. The LC-MS/MS analysis identified 1,266 and 1,001 proteins in the control samples (false-positives) at 1 h and 24 h, respectively. These proteins were excluded from the analysis.

Following subtraction, 100 proteins were identified in the cellular protein corona of 10 µg AgNP and 104 proteins in the cellular protein corona of 50 µg AgNP after 1 h exposure. These included 88 common proteins, and 12 and 16 exclusive proteins for 10 and 50 µg AgNPs, respectively (Figure 63a). After 24 h exposure, 367 proteins were identified in the cellular protein corona of 10 µg AgNP and 377 proteins for 50 µg AgNPs. These included 341 common proteins, and 26 and 36 unique proteins for 10 and 50 µg AgNPs, respectively (Figure 63b). Additionally, common proteins identified for both NP concentrations and exposure time were investigated (Figure 63c). A common protein core of 38 proteins was identified. 1 and 3 proteins were identified exclusively at 10 and 50 µg AgNPs, respectively, independently of the incubation time.

The number of different proteins in the cellular protein corona increased with the exposure time. The maximum protein diversity in the protein corona was observed at 24 h (377 proteins identified for 50 µg AgNPs) compared to 1 h (104 proteins identified for 50 µg AgNPs), suggesting an evolution of the secretome and/or the protein corona during cell exposure.

As observed for the acellular protein corona, both intracellular and extracellular proteins were identified. Especially for the cellular corona, the intracellular proteins could be released following cell injury induced by NPs. To determine which proteins in the corona may originate from the different cellular compartments, a cellular component enrichment analysis was performed (Figure 64). All proteins identified exclusively in the corona by mass spectrometry were considered for this analysis, following removal of the false positives identified in the control. Only the first 20 most enriched cellular components are represented for each condition. This analysis showed that the proteins present in the cellular protein corona come from different intracellular and extracellular compartments. At both time points (1 h and 24 h), we identified adsorbed extracellular proteins (associated to vesicles, organelle or exosomes), membrane proteins (from enclosed lumen or organelles), proteins associated to complexes (such as ribonucleoprotein, protein-containing complexes), intracellular proteins (associated to organelle lumen or anatomical structure), and cytosolic proteins. At 1 h, there was an enrichment in proteins associated to the proteasome complex that was not observed at 24 h. By contrast, at 24 h, there was an enrichment of proteins from ribosomes, mitochondria and the organelle envelopes. In addition, an increase in the number of intracellular proteins was observed in this condition.

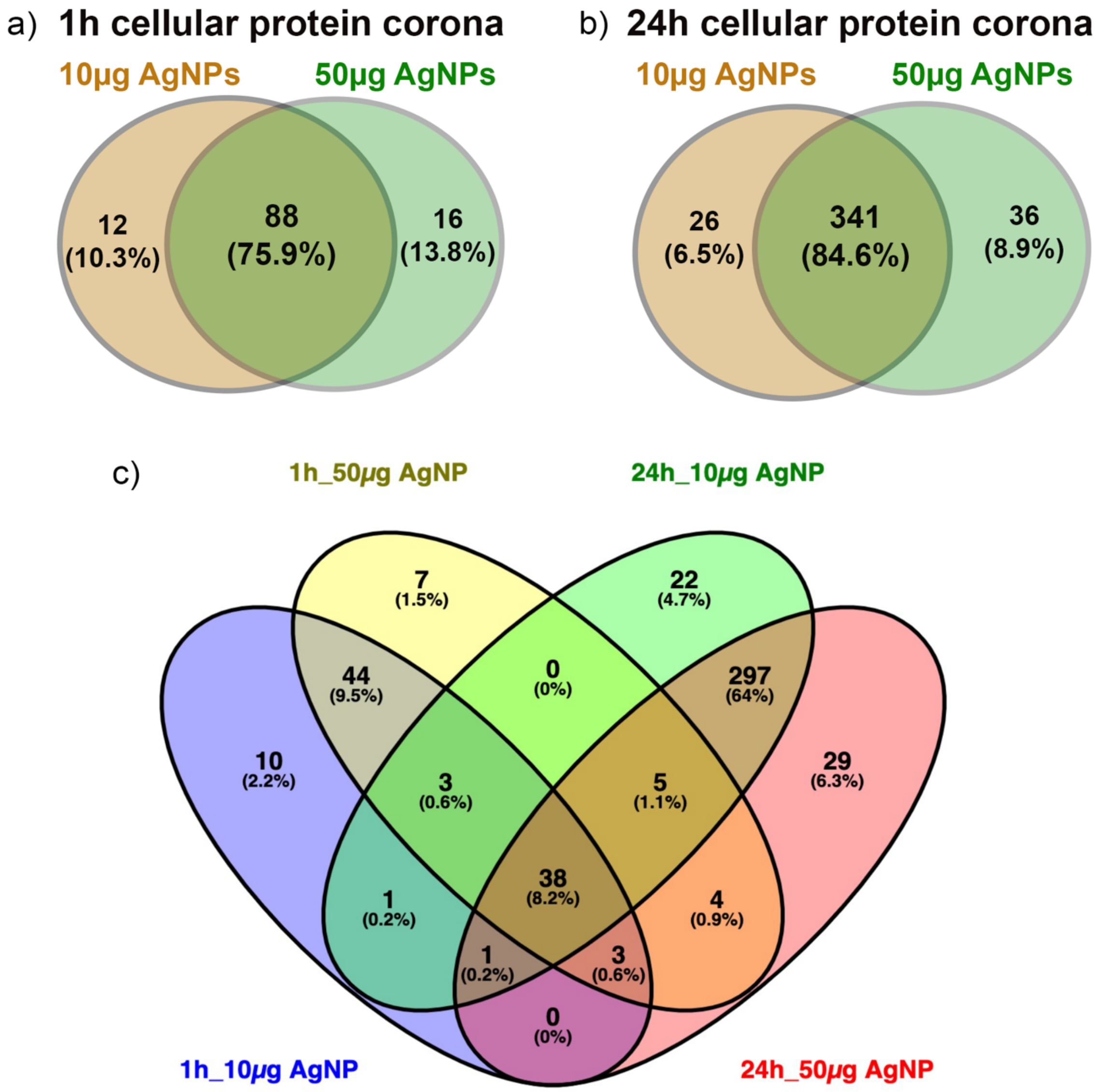

Figure 63: AgNP cellular protein corona analysis after 1 h and 24 h exposure of Calu-3 cells.

The total number of proteins and the percentages of common proteins are shown in a Venn diagram. (a,b) Qualitative analysis of the cellular protein corona identified at 1 h and24 h for 10 µg AgNPs and 50 µg AgNP samples. (c) Qualitative comparison of the cellular protein corona after 1 h and 24 h exposure.

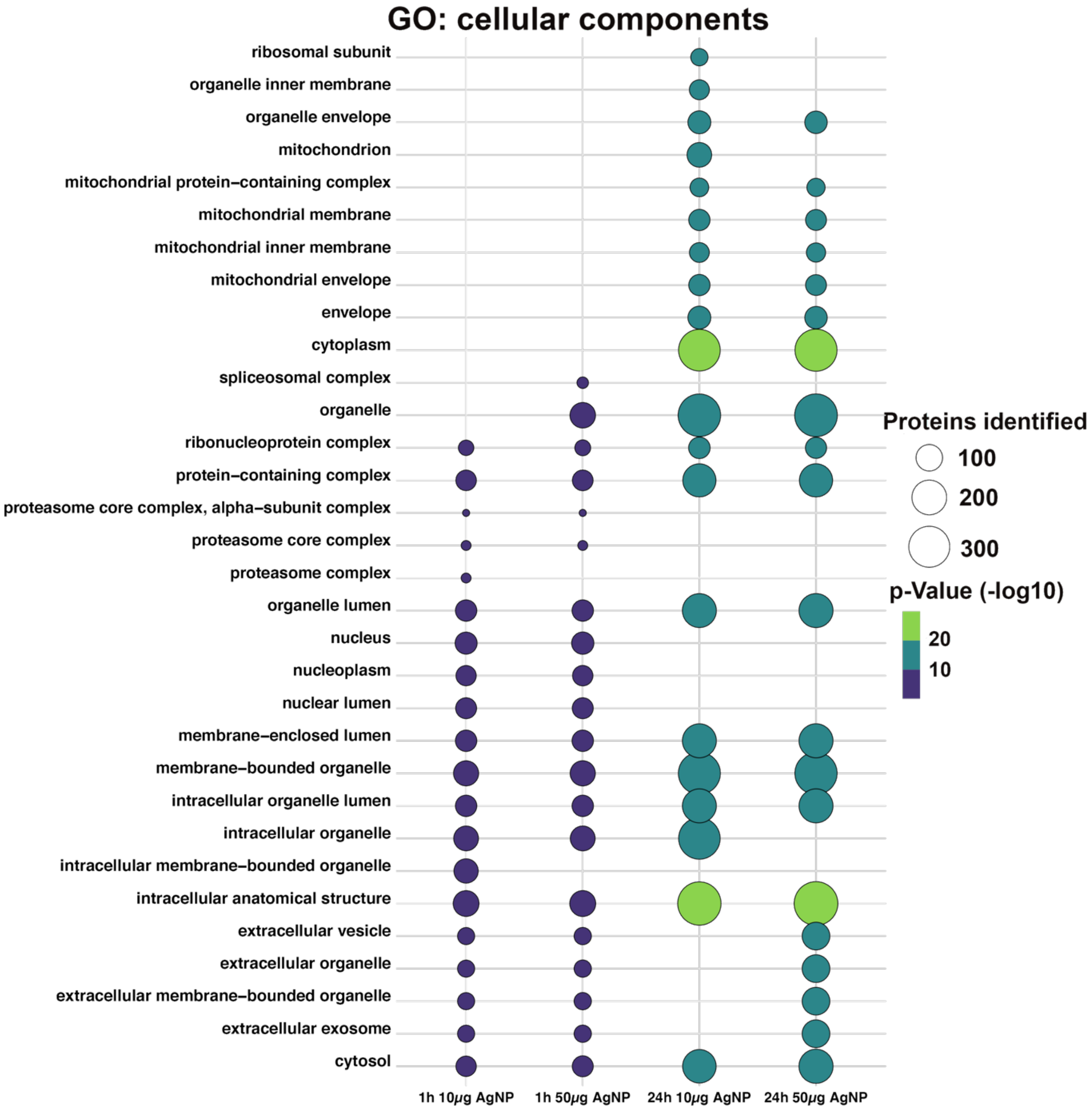

Figure 64: g:GOST functional enrichment analysis of gene ontology cellular components of the cellular protein corona.

Cellular components functional enrichment was performed using the proteins identified in the cellular protein corona: 100 proteins for 1 h 10 µg AgNP, 104 proteins for 1 h 50 µg AgNP, 367 proteins for 24 h 10 µg AgNP and 377 proteins for 24 h 50 µg cellular protein corona.

In addition, a quantitative analysis of the relative protein abundance was performed. It revealed changes in the protein abundance that form the corona after 1 h or 24 h exposure (Figure 65). The sphere graphs show the composition of the cellular protein corona in each condition, with adsorbed proteins after 1 h for 10 µg AgNP (Figure 65a), after 1 h for 50 µg AgNP (Figure 65b), after 24 h for 10 µg AgNP (Figure 65c), and after 24 h for 50 µg AgNP (Figure 65d). The top 10 most abundant proteins within the corona after 1 h and 24 h incubations are also listed in Table 12 and Table 13, respectively. In addition to the changes in protein composition, the exposure time also led to differences in the relative abundance of proteins that composed the protein corona.

The short exposure time (1 h) produced a protein corona mainly formed of binding proteins, such as TATA-binding protein-associated factor 2N (TAF15), Rho-related GTP-binding protein (RHOC), chromatin-binding protein DEK (DEK), intermediate filament binding protein periplakin (PPL), and SAFB-like transcription modulator (SLTM), among others.

The long exposure time (24h) produced a protein corona, is also composed of binding proteins, such as splicing factor 3A (SF3A3) and tubulin (TUBB8), proteins involved in the immune system such as the cytokine C-C motif chemokine 20 (CCL20) and the complement component 1Q (C1QBP), as well as other proteins such as the oxidoreductase cytochrome b5 type B (CYB5B).

We observed differences in the composition of the protein corona after 1 or 24 h exposure of Calu-3 cells to AgNPs. It suggests that an evolution of the secretome composition and/or a reshuffling of the protein corona occurred. We observed an enrichment of TUB8 in the protein corona at 24h, a protein that is normally associated to microtubules in the intracellular regions which could suggest higher cell injury. Protein involved in the metabolism of xenobiotics, such as CYB5B, was also enriched in the cellular protein corona at longer exposure time. To conclude, we demonstrated the evolution of AgNP protein coronas in the secretome and showed that this evolution was highly influenced by the dynamic of the extracellular environment.

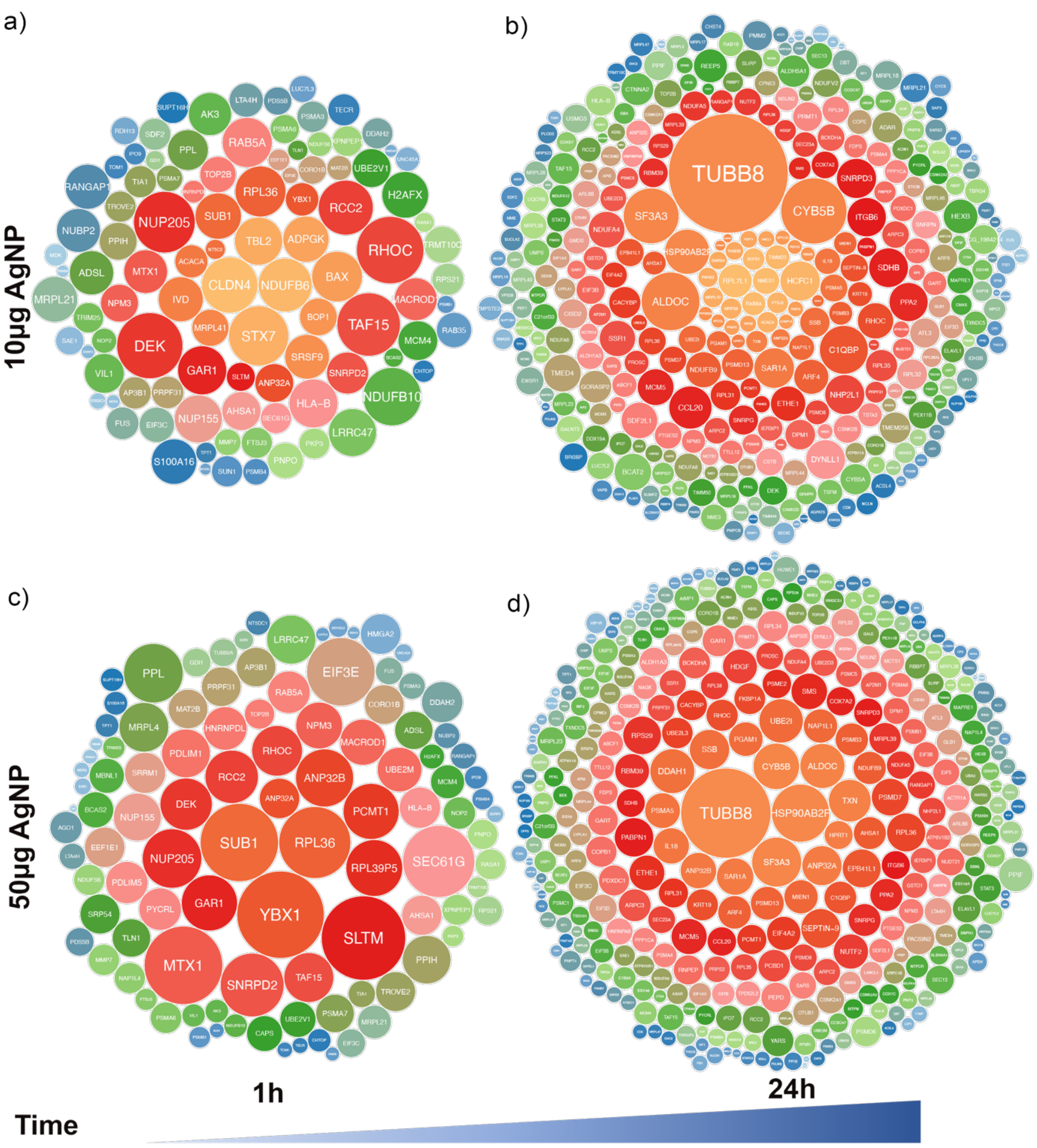

Figure 65: Cellular protein corona formation using 10 and 50 µg of AgNPs during 1 h and 24 h.

Sphere diagram representing adsorbed proteins in the surface of AgNPs using (a-b) 10 µg or (c-d) 50 µg during (a and c) 1 h and (b and d) 24 h. The size of the sphere changes proportionally to the relative abundance. Proteins are designated by their corresponding gene names.

Table 12: Top 10 of the most abundant proteins in the cellular protein corona after 1 h exposure of Calu-3 cells.

Condition	Gene name	Accession	Description
10 µg AgNP	RHOC	P08134	Rho-related GTP-binding protein RhoC
	DEK	P35659	Protein DEK
	TAF15	Q92804	TATA-binding protein-associated factor 2N
	NUP205	Q92621	Nuclear pore complex protein Nup205
	STX7	O15400	Syntaxin-7
	NDUFB10	O96000	NADH dehydrogenase [ubiquinone] 1 beta subcomplex subunit 10
	CLDN4	O14493	Claudin-4
	RCC2	Q9P258	Protein RCC2
	NDUFB6	O95139	NADH dehydrogenase [ubiquinone] 1 beta subcomplex subunit 6
	RPL36	Q9Y3U8	60S ribosomal protein L36
50 µg AgNP	YBX1	P67809	Nuclease-sensitive element-binding protein 1
	SLTM	Q9NWH9	SAFB-like transcription modulator
	MTX1	Q13505	Metaxin-1
	SUB1	P53999	Activated RNA polymerase II transcriptional coactivator p15
	SEC61G	P60059	Protein transport protein Sec61 subunit gamma
	RPL36	Q9Y3U8	60S ribosomal protein L36
	EIF3E	P60228	Eukaryotic translation initiation factor 3 subunit E
	SNRPD2	P62316	Small nuclear ribonucleoprotein Sm D2
	PPL	O60437	PPL

Table 13: Top 10 of the most abundant proteins in the cellular protein corona after 24 h exposure of Calu-3 cells.

Condition	Gene name	Accession	Description
10 µg AgNP	TUBB8	Q3ZCM7	Tubulin beta-8 chain
	CYB5B	H3BUX2	Cytochrome b5 type B
	ALDOC	P09972	Fructose-bisphosphate aldolase C
	SF3A3	Q12874	Splicing factor 3A subunit 3
	C1QBP	Q07021	Complement component 1 Q subcomponent-binding protein
	HSP90AB2P	Q58FF8	Putative heat shock protein HSP 90-beta 2
	CCL20	P78556	C-C motif chemokine 20
	SAR1A	Q9NR31	GTP-binding protein SAR1a
	HCFC1	A6NEM2	Host cell factor 1
	SNRPD3	P62318	Small nuclear ribonucleoprotein Sm D3
50 µg AgNP	TUBB8	Q3ZCM7	Tubulin beta-8 chain
	HSP90AB2P	Q58FF8	Putative heat shock protein HSP 90-beta 2
	SF3A3	Q12874	Splicing factor 3A subunit 3
	CYB5B	H3BUX2	Cytochrome b5 type B
	ALDOC	P09972	Fructose-bisphosphate aldolase C
	DDAH1	O94760	N(G),N(G)-dimethylarginine dimethylaminohydrolase1
	UBE2I	P63279	SUMO-conjugating enzyme UBC9
	TXN	P10599	Thioredoxin
	SSB	P05455	Lupus La protein
	ANP32A	P39687	Acidic leucine-rich nuclear phosphoprotein 32 family member A

To understand the biological implication of the cellular protein corona formed at different concentrations and times, we performed a Reactome pathway functional enrichment analysis (Figure 66). All the proteins identified in each condition were used for the functional enrichment analysis and only the top 20 enriched pathways are presented.

Here, we investigated the effect of protein/NP ratio and the cellular response to AgNPs over time on the evolution of the protein corona. No major differences were observed between the two protein/NP ratio. However, after 1 h exposure, rRNA processing and autodegradation of the E3 ubiquitin ligase COP1 were found for 10 µg AgNP only, and pathways associated to NF-kB signalling and chromatids separation were found for 50 µg AgNP. After 24 h exposure, proteins associated with mitochondrial pathways were found for 10 µg AgNP only, and cell cycling pathways were found for 50 µg AgNP only. These proteins may be associated to the cell response to AgNPs, which is analysed in paragraph 5.3-2.

Major differences in the composition of the cellular protein corona were found as a function of the exposure time. As expected, short incubation time presented less proteins identified per pathways due to a lower number of proteins forming the corona. Interestingly, we found an enrichment of pathways associated to cell division (G1/S transition, regulation of AURKA during mitotic and mitosis), translation (cellular and mitochondrial), and metabolism of proteins and polyamines for long incubation time, that were not present after 1 h exposure.

These results emphasize the necessity to accurately study the protein corona in each biological context. The NP-cell interaction may change the composition of the extracellular environment following cell response to NP exposure. The secretion of new proteins can lead to competition in protein adsorption depending on the protein affinity for the surface and to the reorganization of the protein corona.

Figure 66: g:GOST functional enrichment analysis of Reactome pathways for the cellular protein corona.

The Reactome pathway functional enrichment was performed using the proteins identified in the cellular protein corona: 100 proteins for 1 h 10 µg AgNP, the 104 proteins for 1 h 50 µg AgNP, 367 proteins for 24 h 10 µg AgNP and 377 proteins for 24 h 50 µg cellular protein corona.

5.3-2 Comparison of the cellular and acellular protein corona formed in the secretome

It is well known that the protein corona formation is a dynamic process, and that the composition of the protein corona evolves depending on the surrounding medium. However, the evolution of the secretome composition following NP exposure of epithelial cells and its effect on the protein corona composition has been rarely investigated. The analysis of the 'cellular protein corona' during cell exposure to NPs is particularly interesting to investigate

NP-cell interaction and NP uptake. as the extracellular environment will be conditionate *via* the secretion of biomolecules by the exposed cells (Albanese et al. 2014).

The acellular and cellular protein corona formed after 1h incubation/exposure to 10 µg and 50 µg AgNPs are presented in Figure 67. We observed differences between the cellular and acellular protein corona formed in the secretome for the same incubation or exposure time (1 h). For 10 µg AgNP corona, 10 proteins were common to the 2 conditions, whereas 63 were unique to the acellular corona and 90 were unique to the cellular corona (Figure 67a). For 50 µg AgNP corona, 16 proteins were common to the 2 conditions, whereas 74 were unique to the acellular corona and 88 were unique to the cellular corona (Figure 67b).

Among the 10 and 16 common proteins identified for 10 and 50 µg AgNPs, 9 proteins were common to the all conditions, only 1 was unique to 10 µg AgNP, while 7 were unique to 50 µg AgNP (Table 14). This effect could be due to differences in the secretome composition following Calu-3 cell exposure to AgNPs. The analysis of the secretome after treatment by AgNPs is in progress to document this effect.

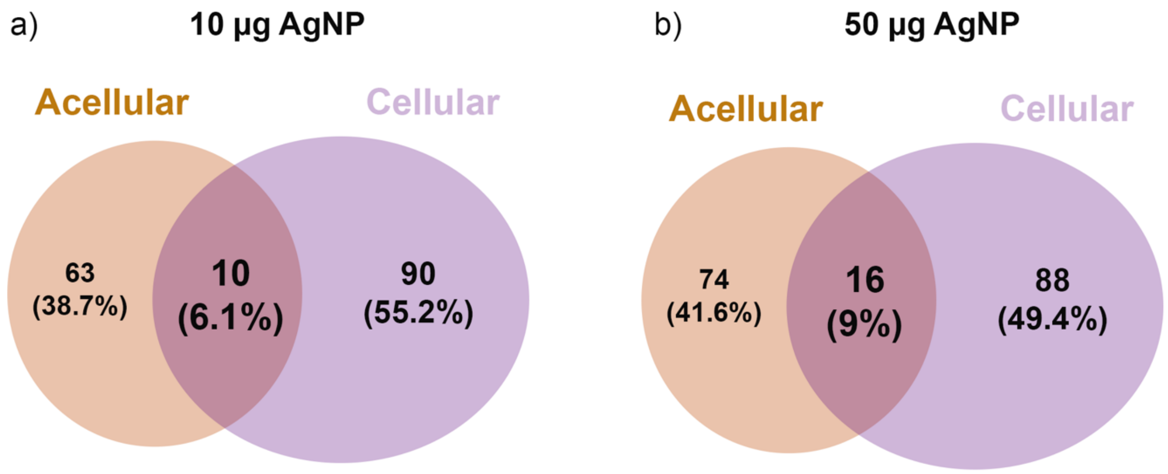

Figure 67: Comparison of AgNP acellular and cellular protein corona after 1 h incubation in the secretome or exposure of Calu-3 cells.

The total number of proteins and the percentages of common proteins are shown in a Venn diagram. (a) Qualitative comparison of the acellular and cellular protein corona identified for 10 µg AgNPs and (b) for 50 µg AgNP samples.

Table 14: Common proteins identified in the acellular and cellular protein corona for 10 and 50 µg AgNPs.

Condition	Gene name	Accession	Description
All	PSMB4	P28070	Proteasome subunit beta type-4
	GDI1	P31150	Rab GDP dissociation inhibitor alpha
	NUP205	Q92621	Nuclear proe complex protein Nup 205
	AHSA1	O95433	Activator of 90kDa heat shock protein ATPase homolog 1
	YBX1	P67809	Y-box-binding protein 1
	LRRC47	Q8N1G4	Leucine-rich repeat-containing protein 47
	TRIM25	Q14258	E3 ubiquitin/ISG15 ligase
	MDK	P21741	Midkine
	WDR3	Q9UNX4	WD repeat-containing protein 3
10 µg AgNP	MRPL41	Q8IXM3	39S ribosomal protein L41
50 µg AgNP	ANP32B	Q92688	Acidic leucine-rich nuclear phosphoprotein 32 family member B
	PCMT1	P22061	Protein-L-isoaspartate O-methyltransferase
	TAF15	Q16514	Transcription initiation factor TFIID subunit 12
	TROVE2	P10155	60 kDa SS-A/Ro ribonucleoprotein
	SUPT16H	Q9Y5B9	FACT complex subunit SPT16
	PDLIM5	Q96HC4	PDZ and LIM domain protein 5
	RBM28	Q9NW13	RNA-binding protein 28

5.3-3 Cellular responses of the Calu-3 epithelial barrier to AgNP exposure

In order to determine whether AgNPs induced adverse effects on the Calu-3 epithelial barrier that could also modify the secretome composition, we evaluated the epithelial integrity, the metabolic activity of the cells as well as the expression level of mucins, tight junction proteins, pro-inflammatory, metal homeostasis, and oxidative stress markers. The experimental design is represented in Figure 68. Calu-3 cells were cultured at ALI for 10 days allowing full epithelium differentiation. One day before NP exposure, the epithelial integrity and the cell viability were checked by measuring the TEER and by using the Alamar Blue assay. The cultures rested overnight allowing the secretion of a normal apical secretome. Then, the cells were exposed to 0, 10 or 50 µg/cm^2 AgNPs diluted in HBSS. 5 µl droplets were deposited on the cells as described in Chapter 2. The secretome with and without AgNPs was collected for the characterization of the cellular protein corona after 1, 24 and 48 h of exposure. The TEER value (Figure 68b) and LY permeability (Figure 68c) did not show significant changes between the controls and the treated samples, after 1, 24 and 48 h of treatment. Additionally, the metabolic activities did not change significantly between the controls and the treated samples except for 10 µg AgNP after 48 h, where a significant reduction of the metabolic activity was observed. Overall, our results show that a short and acute treatment with AgNPs did not affect the viability and integrity of the epithelial barrier in the Calu-3 model.

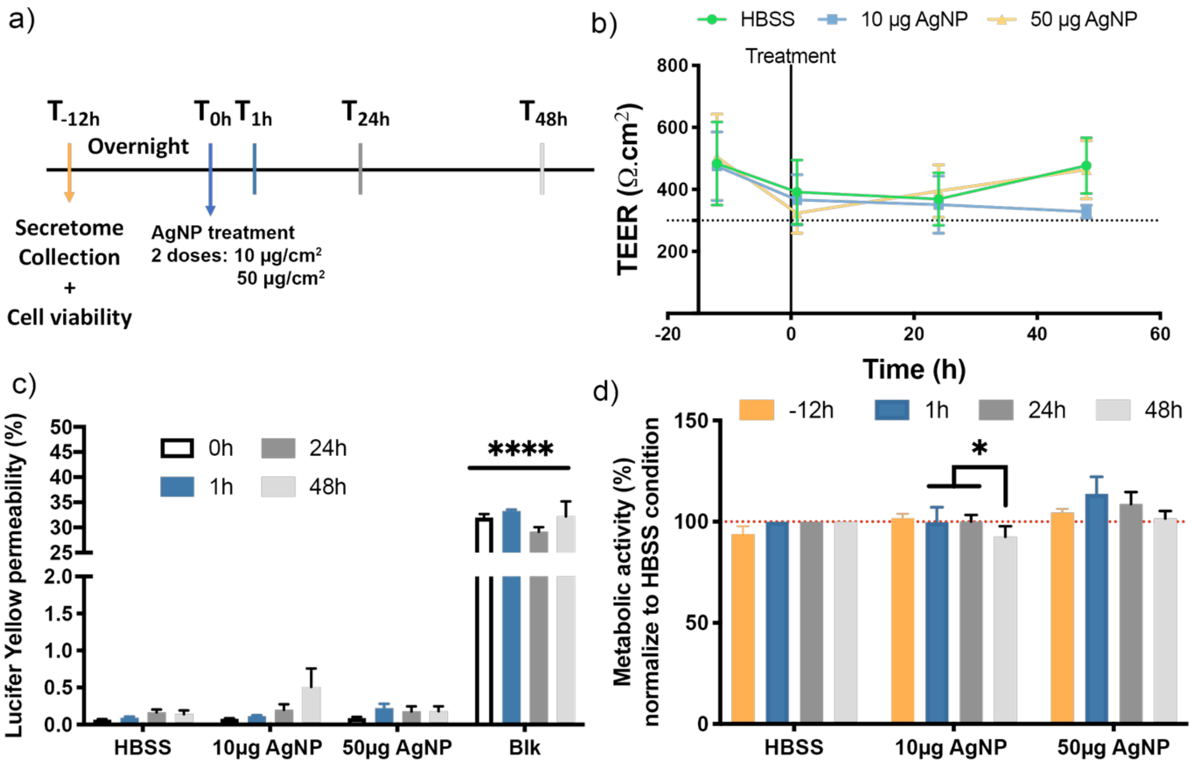

Figure 68: Investigation of Calu-3 epithelial integrity following exposure to AgNPs at ALI.

*(a) Experimental design for cell exposure to AgNPs and characterization of the cellular protein corona. (b) TEER (c) LY permeability and (d) Alamar blue cell viability assay. All measurements were performed 1 day before, 1 h, 24 h and 48 h after AgNP exposure. An empty insert was used as a negative control for LY measurement (Blk). N=3. * p-value < 0.05.*

The molecular responses of Calu-3 to AgNPs were further investigated by measuring the expression level of different markers by RT-qPCR (Figure 69 and Figure 70). The relative expression of the gel-forming mucins (Figure 69a and b), *muc5ac and muc5b*, did not show any significant difference following exposure to AgNPs compared to the control. The proteins associated with tight junctions (Figure 69c and d), ZO-1 and E-cadherin, did not show changes at the mRNA expression levels.

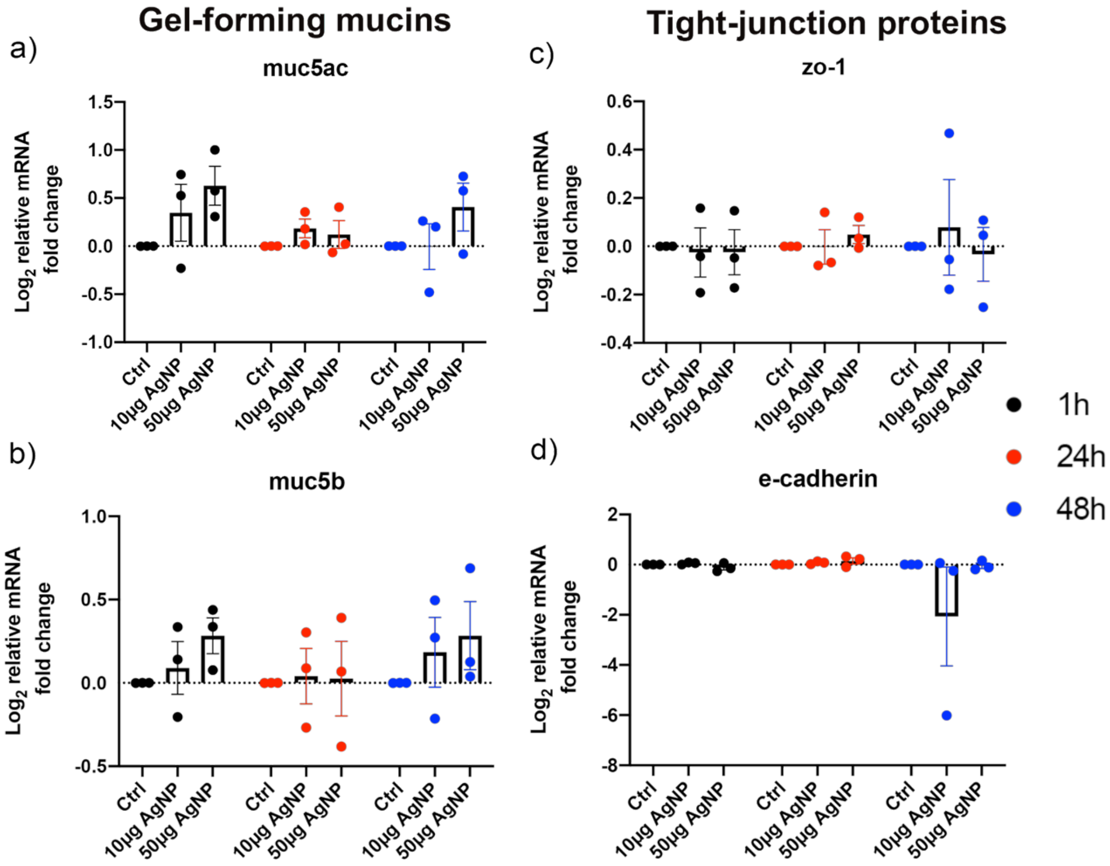

Figure 69: Gene expression levels of mucins and proteins associated to tight junctions.

The gel-forming mucins (a) muc5ac and (b) muc5b and tight junctions (c) ZO-1 and (d) E-cadherin associated proteins were quantified by qRT-PCR. Gene expression was analyzed by the $2^{-\Delta\Delta Ct}$ *method and normalized to the rpl19 housekeeping gene. Data shown as* Log_2 *fold-change normalized to the control for each time point. Results are expressed as mean ± SEM, n= 3.*

The mRNA expression levels of relevant target genes of pro-inflammatory and anti-oxidant responses were investigated after 1, 24 and 48 h of exposure to 10 and 50 µg AgNPs. For both AgNP concentrations, a pro-inflammatory response was triggered 1 h after the exposure. The expression of the IL-6 (Figure 70a), IL-8 (Figure 70b) and IL-1β (Figure 70c) interleukins were significantly increased after 1 h exposure. The log_2-fold increase was 0.98 (IL-6), 0.7 (IL-8) and 0.75 (IL-1β) for 10 µg AgNP, and 1.2 (IL-6), 1.14 (IL-8) and 0.8 (IL-1β) for 50 µg AgNP. This induction was no longer observed after 24 and 48 h of NPs exposure. The expression levels of TNFα (Figure 70d) did not significantly change, but tended to increase after 1 h (0.4- and 0.6-fold increase for 10 and 50 µg AgNP, respectively) as observed with the other cytokines. Surprisingly, a decreasing tendency in the expression level of IL-8 and IL-1β, and a significant decrease of IL-6 and TNFα (1.1- and 0.8-fold decrease respectively) were observed after 24 h exposure in a dose dependent manner.

The anti-oxidant response was investigated by measuring the expression levels of the heme-oxygenase (*hmox-1* gene) (Figure 70f). A significant increase in the expression level of *hmox-1* was observed after 1 h of treatment in a dose-dependent manner (0.98- and 3.1-fold increase for 10 and 50 µg AgNPs, respectively), as observed for the pro-inflammatory response. This induction was transient, and was no longer observed after 24 or 48 h exposure to AgNPs.

Metallothioneins (MTs) are metal-binding proteins that contribute to heavy metal detoxification. These proteins have a high affinity for mercury, cadmium and silver, and the detoxification of heavy metal is their main biological function (Lindeque et al. 2010). The mRNA expression levels of two MT isoforms, MT1X (Figure 70g) and MT2A (Figure 70h), were quantified. The AgNPs strongly induced the expression of *mt1x* and *mt2a* following 1 h of treatment (5.5- and 5.8-fold increase for 50 µg AgNPs). Although this expression decreased after 24 h, it remained significantly higher for the highest dose of 50 µg AgNPs (2.2- and 3-fold change at 24 h and 48 h respectively for *mt2a*).

Surprisingly, a dose-dependent decreasing tendency was observed in the expression level of human albumin (Figure 70e). Contrary to the other genes, albumin expression decreased with time showing a longer and more general stress response. Böhmert *et al.* showed similar results after the exposure of Caco-2 cells (differentiated on inserts) to AgNPs. The authors carried out a microarray analysis and reported the induction of the anti-oxidant response, pro-inflammatory and metal homeostasis genes, as well as the downregulation of albumin gene. They concluded that AgNPs induced morphological changes and oxidative stress in differentiated Caco-2 cells (Böhmert et al. 2015).

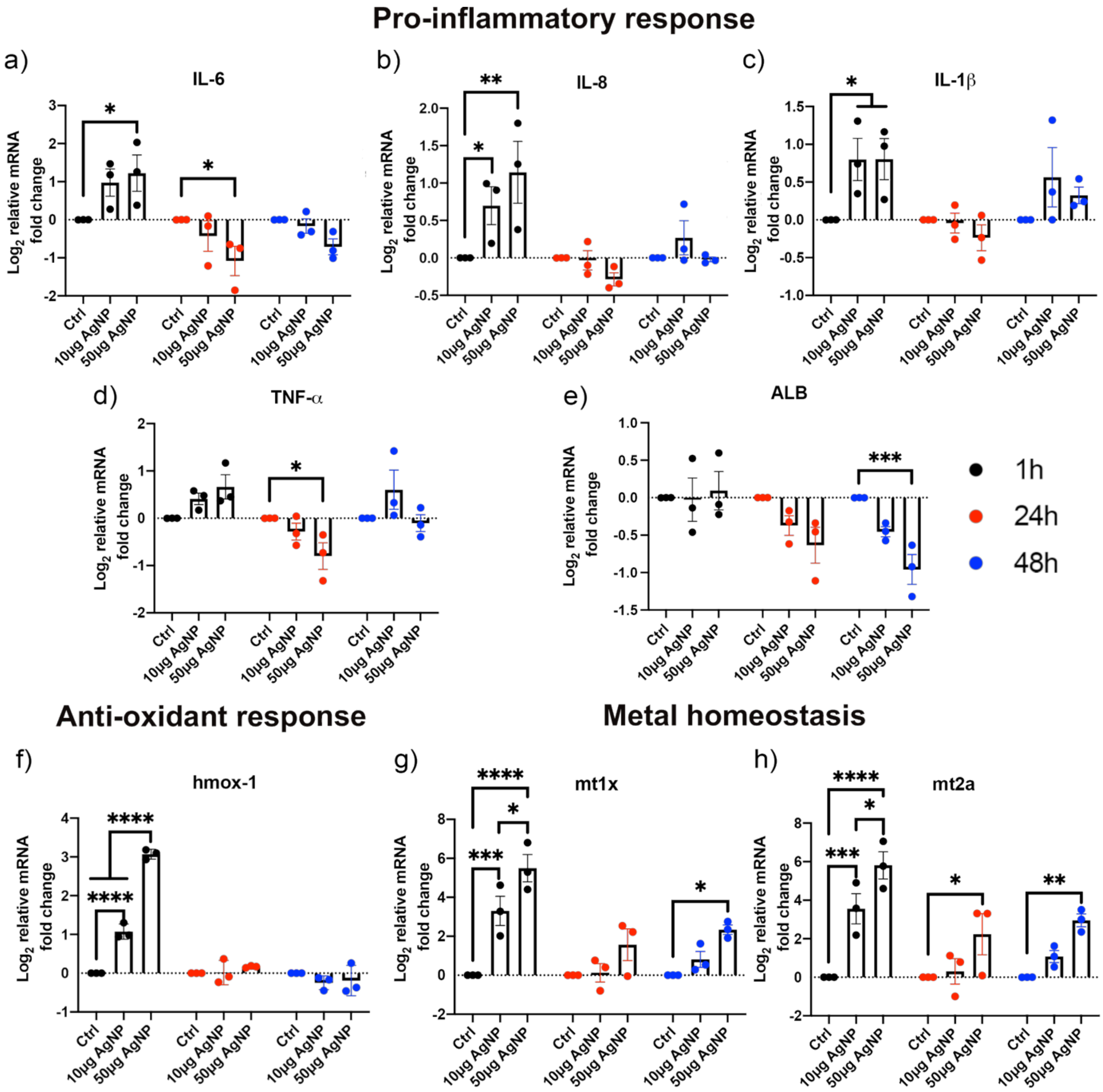

Figure 70: Gene expression levels for pro-inflammatory, anti-oxidant responses and metal homeostasis proteins.

Target genes for the pro-inflammatory response (a) il-6, (b) il-8, (c) il-1β and (d) tnf-α,; for the anti-oxidant response (e) hmox-1, and for metal detoxification and homeostasis (f) mt1x and (g) mt2a, were quantified by qRT-PCR. Gene expression was analyzed by the $2^{-\Delta\Delta Ct}$ *method and normalized to the rpl19 housekeeping gene. Data shown as* Log_2 *fold-change normalized to the control for each time point. Results are expressed as mean ± SEM, n= 3.*

5.4 Impact of the protein corona on the effect of AgNPs on macrophages

In addition to the analysis of the protein corona formed on AgNPs in the Calu-3 secretome, we investigated whether it could modify the cellular interactions and effects of AgNPs on other cell types. Indeed, different *in vitro* studies showed that proteins adsorbed on NPs can have a strong effect on NP uptake and toxicity on cells. For example, it was shown that the serum- and plasma-protein corona inhibited the uptake of AgNPs and silica NPs by human macrophages-like cells (THP-1) (Aoyama et al. 2016). For our experiments, we also used THP-1 cells that were differentiated into macrophages-like cells using Phorbol 12-myristate 13-acetate (PMA). The cytotoxicity, pro-inflammatory responses and AgNP uptake were analyzed in THP-1 following AgNP pre-incubation in the Calu-3 secretome, FBS or HBSS:RPMI (v/v) medium, in order to investigate the effect of the protein corona formed in airway lining fluid on the biological effects of AgNPs on macrophages.

THP-1 cells were exposed in a mixed medium of HBSS:RPMI (v/v), corresponding to conditions that did not affect cell viability for at least 24 h, as opposed to HBSS alone. RPMI medium was used with 0% FBS, and the medium was supplemented with essential amino acids, glutamax, sodium pyruvate and β-mercaptoethanol essential for THP-1 growth. To address the question of the role of the protein corona in the biological effects and toxicity of AgNPs, THP-1 cells were exposed either to bare AgNPs ('NP in HBSS:RPMI'), to AgNPs incubated in the Calu-3 secretome ('secretome-NP') or 4% FBS ('4%FBS-NP') for 1 h at 37°C with gentle mixing. Controls were exposed to HBSS:RPMI medium, 4% FBS or secretome only using the same volumes and concentrations to distinguish between the effects of proteins/buffers and the effects of the protein corona.

Exposure of THP-1 cells to 1 or 5 µg/mL AgNPs (corresponding to a total mass of 0.2 µg and 1 µg Ag, respectively) with or without a pre-formed protein corona did not induce significant changes in the cell viability following 4 or 24 h of exposure (Figure 71a). Instead of a decrease of cell viability, we observed a trend of increased metabolic activity following exposure to AgNPs in all the conditions. This trend was significant following exposure to 5 µg/mL secretome-NP. Other groups reported an increase in metabolic activity following exposure of A549 cells to subtoxic doses of ZnO NPs. Those results could indicate an initial survival response to internalized NPs, which was not observed in higher NPs concentrations, where cell death is induced (Lovén et al. 2021).

The pro-inflammatory response was investigated by quantifying the release of IL-8 after 24 h of exposure to AgNPs. The mean of only 2 independent biological replicates is shown for IL-8, which explains why no statistical analysis was performed (Figure 71b). We observed that the secretome alone induced a higher production of IL-8 compared to the control, either because it already contained IL-8 and/or because it had a stimulating effect on macrophages. The proteomic analysis of the Calu-3 secretome (Chapter 4) did not detected IL-8 in the secretome, however the ELISA measurement identified the production of IL-8 in Calu-3 secretome (data not shown). A tendency of a dose-dependent IL-8 release was observed in all conditions following exposure to AgNPs, whether or not AgNPs were pre-coated with a protein corona.

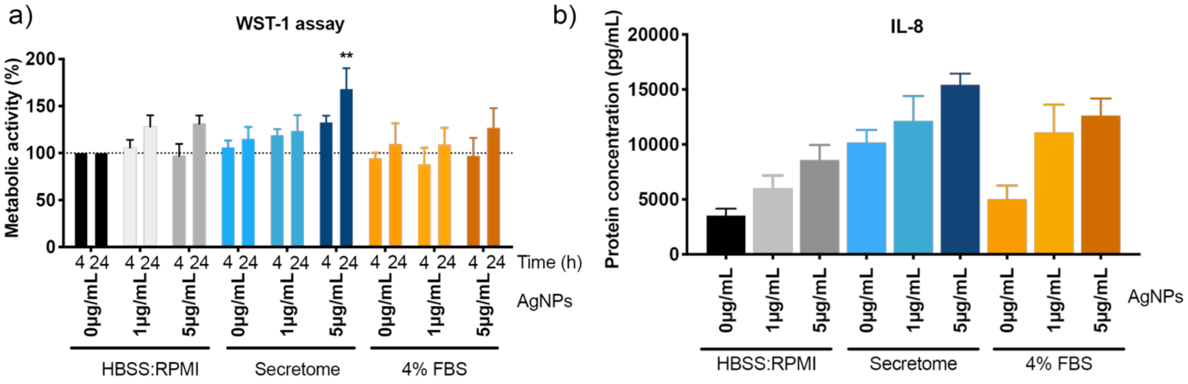

Figure 71: Macrophage viability and cytokine release following exposure to bare AgNPs or to AgNPs pre-incubated with Calu-3 secretome (secretome-NP) or FBS (4%FBS-NP).

THP-1 cells differentiated into macrophage-like cells were exposed to bare AgNPs (grey), secretome-AgNPs (blue), 4%FBS-AgNPs (orange), diluted in HBSS:RPMI medium. Cells exposed to HBSS:RPMI, secretome, or 4% FBS without NPs were used as controls. (a) THP-1 metabolic activity measured after 4 h and 24 h of exposure using WST-1 assay. Expressed in % compared to the control (exposed to HBSS:RPMI only). (b) The secretion of IL-8 (pg/mL) measured by ELISA after 24 h exposure to AgNPs. Metabolic activity data: mean ± SEM of 4 biological replicates. ELISA data: mean ± SEM of 2 biological replicates.

The uptake of AgNPs by macrophage-like cells was analyzed by transmission electron microscopy (TEM) (Figure 72). The observations of black particles which size matches AgNP diameter inside the cells suggest that AgNPs were internalized by macrophages in all conditions, although a chemical analysis by ICP-MS or TEM-EDX would be needed to confirm silver uptake. NPs were located in intracellular vesicles in the cytoplasm, independently of their pre-formed protein corona. However, with this methodology, it is difficult to determine whether there is a difference in the amount of internalized AgNPs depending on the protein corona. A quantitative analysis will be necessary to determine a potential role of the protein corona in AgNP uptake by THP-1 cells.

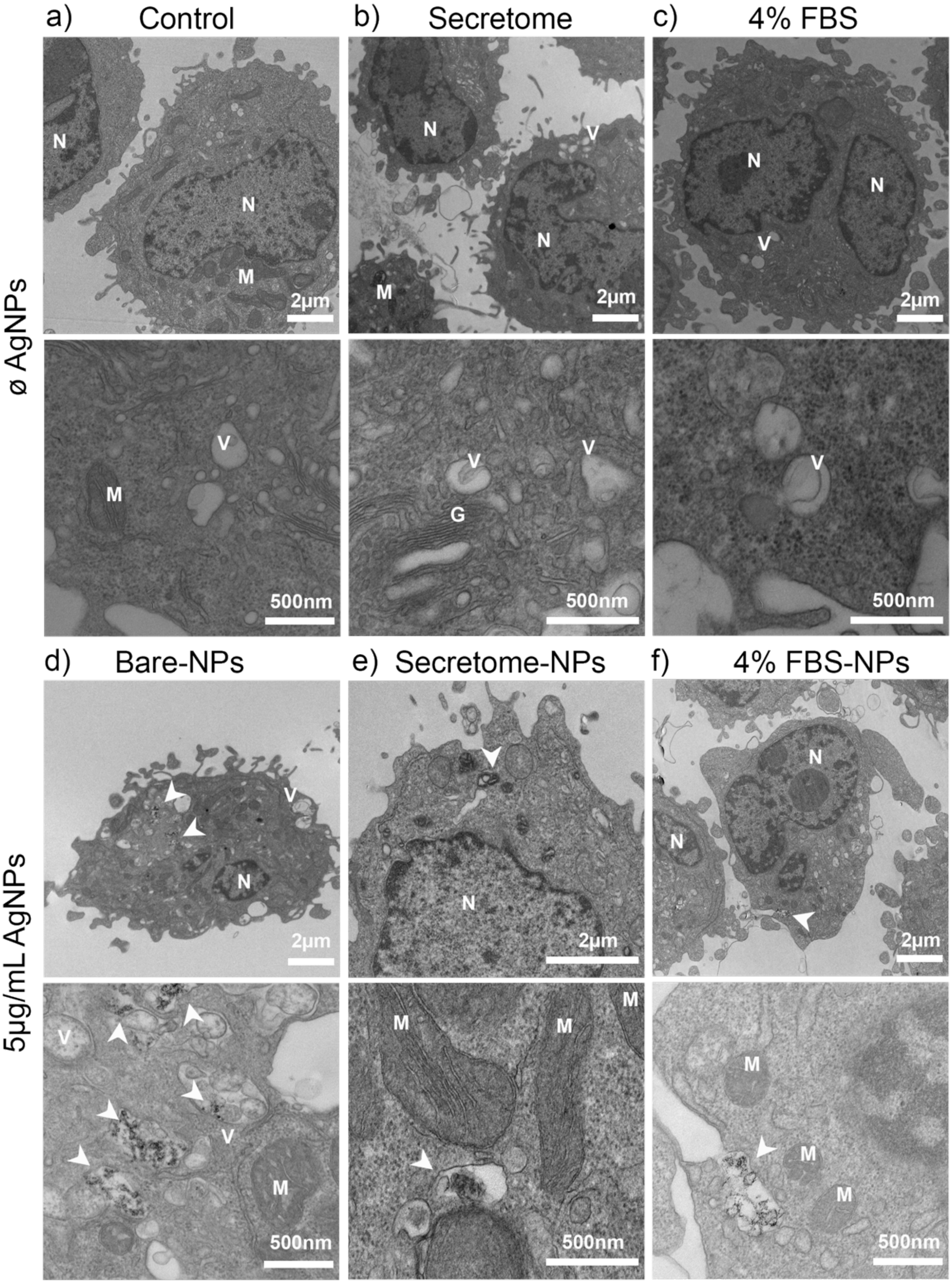

Figure 72: Transmission Electron Microscopy observation of AgNP internalization by THP-1 cells following the formation of a protein corona in the secretome or in FBS.

As a control, cells were treated with (a) HBSS:RPMI, (b) secretome and (c) 4% FBS. For the treatments, cells were exposed to 5 µg/mL of AgNP pre-incubated with (d) HBSS:RPMI (bare-NP), (e) secretome (secretome-NP) and (f) 4% FBS (FBS-NP) for 4 h. White arrows indicate NPs, FBS: fetal bovine serum, M: mitochondria, N: nucleus, V: vesicles, G: Golgi apparatus.

5.5 Discussion

In this chapter, we characterized the protein corona that forms on silver nanoparticles in an airway lining fluid, the apical secretome of the Calu-3 epithelial barrier. Two different protocols were used: AgNPs were incubated in the collected secretome ('acellular' protein corona), or directly with Calu-3 cells, allowing the secretome composition to change in response to AgNP exposure ('cellular' protein corona).

NP isolation for protein corona analysis

Reproducible methods are needed to separate NPs with their corona from the biological medium and the free proteins for the analysis of the adsorbed proteins. Ideally, NPs should be isolated without altering the composition of the protein corona, to avoid the loss of loosely bound proteins (the soft corona) or the reshuffling of the protein corona during the separation step. In the literature, different methods have been employed for NP-protein corona separation, each of them with some limitations. The most common method is centrifugation. The main limitation of this method is the loss of loosely bound proteins and the possibility to precipitate free proteins at the same time as NPs. Moreover, this method is difficult to apply to low density materials. Protein complexes can sediment during the centrifugation process, leading to misinterpretation when some free proteins are counted as corona components. A large number of sedimented proteins (false-positives) were identified by SDS-PAGE during our first experiment with the cellular protein corona formed with Calu-3 cells in the fresh secretome (Figure 55c). The viscosity of the mucosal secretion favored the sedimentation of mucins that may trap other proteins during centrifugation. The freezing/thawing cycles improved this step by limiting the amount of proteins that precipitate during centrifugation (Figure 56b), possibly by altering the mucus network.

Moreover, the analysis of the protein corona formed on magnetic Fe_3O_4 NPs using Calu-3 secretome confirmed the improvement of the centrifugation protocol we set up (including freezing/thawing cycle). The use of Fe_3O_4 NPs allowed us to compare the magnetic and centrifugation separation methods for the analysis of the protein corona in the secretome. We obtained similar protein corona profiles with both methods, and confirmed that the freezing/thawing cycle considerably reduced the sedimentation of false positive proteins from the secretome during centrifugation. However, the high sensitivity of the LC-MS/MS analysis showed the presence of free proteins sedimented in control samples after the centrifugation (such as MUC5AC, MUC5B, LNC2) that we removed from the analysis of the proteomic data.

Nevertheless, the acellular and cellular protein corona of AgNPs were prepared following the same separation protocol, so that we can be relatively confident in the comparative analysis of their composition.

Magnetic separation is an attractive method as it can better preserve the full protein corona compared to centrifugation. However, it can be applied to magnetic NPs only. Pisani *et al.* compared the composition of the protein corona formed on silica NPs with a magnetic core in human serum, using either centrifugation or magnetic separation (C. Pisani et al. 2017). The authors observed differences in the relative protein quantities in the protein corona depending on the separation method. Centrifugation applied stronger forces compared to magnetic separation, and potentially removed weakly bounded proteins, destabilizing protein-NP or protein-protein interactions in the corona, leading to a modification of the protein corona during the separation step.

Alternative methods using chromatography for NP isolation exist, such as size exclusion chromatography (SEC) and asymmetric flow-field-flow fractionation (A4F). SEC can be applied to various NPs and biological media. It is also less perturbing than centrifugation (Cedervall, Lynch, Lindman, et al. 2007). Monopoli *et al.* compared centrifugation, size exclusion chromatography, and magnetic separation for the analysis of the protein corona formed on magnetic silica NPs in human plasma (MONOPOLI et al. 2013). The authors concluded that the protein corona composition remains very similar, independently of the separation method, and that none of the techniques applied promoted a strong material loss. However, using cryoTEM for imaging the protein corona formed by purified haemoglobin on silica NPs, we observed a loss of weakly bound proteins following centrifugation (Sanchez-Guzman et al. 2020). Therefore, the effect of the separation method on the protein corona may depend on the nature of the NPs and of the adsorbed proteins.

The choice of the isolation method also depends on the biological matrix that is studied (Böhmert et al. 2020). As shown in our experimental results, centrifugation may be more perturbing for viscous mucus samples compared to human serum, and additional protocol adaptation were needed. In our project, we studied pure silver nanoparticles, so that magnetic separation was not an option. However, we have started developing an isolation protocol by SEC to separate AgNPs from free proteins in the secretome. SEC has been reported as having a good potential for NP-protein corona isolation from complex matrices and it has been found less perturbating than centrifugation. The first results were not conclusive because of the high dilution factor of the sample following protein separation by chromatography. One limitation of the SEC method is the low throughput and incomplete protein recovery. In our case, we did not have large enough secretome samples (in terms of volume and protein concentration compared to human serum for example) to detect proteins following NP separation. Further developments and technical tests would be needed before we apply this technique to the analysis of the protein corona in the secretome.

Protein corona in airway lining fluid

The study of the formation and composition of the biomolecular corona on NPs is relatively recent. It has mainly started by the analysis of the protein corona in serum, cell culture media, or cell homogenates, which allowed the identification of a number of factors controlling its formation (Lundqvist et al. 2008; Mathé et al. 2013). Moreover, the effects of adsorption on protein structure and activity have been investigated at a molecular level based on single protein studies (Sanchez-Guzman et al. 2020; W. Zhang et al. 2015; Verma et al. 2018). Recently, the analysis of the biomolecular corona has been extended to other biological matrices, such as intestinal fluids, urine, or food components, and to a wider range of nanomaterials (Böhmert et al. 2020).

The inhaled NPs encounter the biological fluids present at the different levels of the respiratory tract, such as the epithelial lining fluid and the surfactant. The analysis of the broncho-alveolar lavage (BAL) revealed a different protein composition compared to blood fluids, with specific proteins such as mucins and clusterin surfactant proteins that form specific structures (mucus at the bronchial level and lamellar bodies in the alveoli) (Jinzhi Chen et al. 2008). Serum albumin, complement proteins and apolipoproteins, among others, are both present in blood and broncho-alveolar fluids.

To date, very few studies have investigated the formation of the protein corona on NPs in the airway lining fluid. Kumar *et al.* investigated the protein corona formation on silica and poly(vinyl) acetate NPs using hBAL from healthy donors. The authors identified surfactant proteins (A and B), serum albumin and complement proteins (C3 and C4) among the most abundant proteins of the corona. Furthermore, they observed an enrichment of immunoregulatory proteins, which can promote phagocytosis.

In our project, we studied the formation of the protein corona in the secretome of the bronchial epithelial barrier using Calu-3 cells. Collecting the bronchial secretome *in vitro* has several advantages: it is less invasive than the collection of BAL in healthy individuals, it is specific to one lung level and/or cell type, it allows to expose cells to NPs and to take into account their effect on the evolution of the secretome. Secretions from other cell types were also used in another protein corona study (Albanese et al. 2014). The authors investigated the effect of the protein corona on the uptake of gold NPs by A549 cells as a function of time. They observed that cells secretions in the extracellular environment changed after NP exposure, which altered NP-cell interactions by modulating the aggregation state and the biological identity of the NPs.

We identified intracellular proteins in the corona of AgNPs formed in the secretome. For the analysis of the secretome in chapter 4, we excluded the intracellular proteins from the proteomic data in order to investigate the profile of extracellular proteins responsible for the defence mechanisms of the epithelial barrier. For the protein corona analysis, it did not seem relevant to exclude the intracellular proteins because they are indeed real components of the secretome, and hence of the protein corona. These intracellular proteins were also observed in primary cultures, as well as in BAL, suggesting that the process of cell turnover both *in vitro* and *in vivo* is accompanied by the release of intracellular proteins. The fact that these proteins were observed following the incubation of AgNPs both in cellular and acellular conditions shows that their presence was not linked to AgNP cytotoxicity. Moreover, no loss of viability and no alteration of the barrier integrity were observed following exposure to 10 μg/cm^2 AgNP or 50 μg/cm^2 AgNP for 48 h, confirming that these conditions were not cytotoxic for Calu-3 cells at ALI. The comparison of the protein corona formed on AgNPs in the secretome with or without cells revealed several effects: i) the protein corona was richer in terms of protein diversity when formed in the presence of cells, ii) this diversity increased with time, iii) the fraction of intracellular and organelle proteins increased with time in the protein corona. These results suggest that the cellular response to AgNPs induced changes in the protein corona composition, which could be triggered by a modification of the secretome following exposure. However, some differences between the acellular and cellular corona might be due to protein degradation process. The protein degradation rate is dependent on the protein type adsorbed on the NPs (Ma, Bai, and Jiang 2015). For the acellular condition, the protein corona could be more affected than in cellular corona by the lacking of protein renewal.

Although we did not observe any cytotoxicity, the analysis of the gene expression associated with inflammation, metallic and oxidative stress showed that some of them were modulated when Calu-3 cells were exposed to AgNPs. This analysis was performed by RT-qPCR for a limited number of genes, but other unknown genes could be modulated as well following AgNP exposure. The microarray using Caco-2 cells exposed to AgNP and Ag^+, revealed the induction of anti-oxidant response, pro-inflammatory and metal homeostasis genes (Böhmert et al. 2015).

Interestingly, we both reported a downregulation of albumin gene, which is related to cellular stress (Böhmert et al. 2015). The analysis of the secretome by LC-MS/MS before and after exposure of Calu-3 cells to AgNPs has been performed. The analysis of the proteomic data is in progress. This experiment will help us to determine whether significant changes in the cellular secretions occurred (on the apical side) following exposure to AgNPs.

Another aspect to consider is the evolution of the protein corona with time (Cédric Pisani, Gaillard, et al. 2017; Monopoli et al. 2012). The biomolecular corona is constantly reshuffled depending on the protein affinity for the surface, the composition of the surrounding medium, and the dynamic conditions that may apply. In this respect, the acellular and cellular protein corona formed in the secretome with and without cells can help us understand the processes that trigger its evolution. We identified a higher number of different proteins in the cellular protein corona following 24 h exposure compared to 1h. In addition, the protein abundances also changed with time, as observed for example with TUBB8 and CCL20, which became more abundant in the protein corona at 24 h compared to 1 h. This observation could be explained by an increase in TUBB8 and TUBB20 protein concentration in the secretome and/or a high protein affinity for AgNPs. Indeed, one model suggests that the protein corona is formed by high abundant low affinity proteins first, which would be replaced in part by low abundance high affinity proteins with time, a competition mechanism called the Vroman effect (Monopoli et al. 2012). However, the cellular role in shaping the protein corona must now be included when modeling its formation and evolution to take into account the feedback loop of the effects of NPs on cells (Albanese et al. 2014). The exposure of cells to NPs induces the depletion or secretion of different biomolecules resulting in changes in the extracellular environment. The evolution of the biological fluid can in turn impact the protein corona composition and modulate its biological identity.

In addition to proteins, other biomolecules adsorbed on AgNPs may play a role, such as lipids and polysaccharides. Lipidomic analysis found different adsorbed lipids in function of the NPs nature. Lipid-NPs were able to adsorb higher amount of lipids per surface compared to PEG- or PLGA-NPs, though both NPs exhibited a similar lipid corona composition (Raesch et al. 2015) These biomolecules could also compete with the proteins for the adsorption on NP surface, affecting the composition of the protein corona.

Role of the protein corona in the effects of AgNPs on macrophages

The analysis of the cellular effects of AgNPs on THP-1 macrophages following pre-incubation in HBSS:RPMI medium only, in the secretome of Calu-3 cells, or in 4% FBS, showed that different protein corona induced different inflammatory responses. These preliminary results underline the role of the biomolecular corona in NP biological effects, as shown by others. Shaw *et al.* reported differences in diesel and carbon black NP uptake and pro-inflammatory response in macrophages-like cells (THP-1 cells) following incubation in human BAL or plasma. While plasma-corona did not induce inflammatory response in macrophages, BAL-corona induced the secretion of IL-8 (Shaw et al. 2016). Aoyama *et al*. reported that clusterin adsorbed on silver and silica NPs suppressed their uptake by THP-1 cells (Aoyama et al. 2016). These studies highlight the role of the protein corona on the biological fate and toxicity of NPs, and the importance of choosing the relevant biological fluid for nanotoxicology studies.

Additional experiments will be needed to elucidate the effect of the protein corona formed in airway lining fluids on the toxicity of NPs and the underlying mechanisms. The same study could be performed on primary cell cultures to take into account the cellular response of the other bronchial epithelial cells. We could also take advantage of the long-term cell culture to investigate the evolution of the cellular response and protein corona at the same time following chronic and repeated exposure. In our experiments, macrophages could not be exposed to AgNPs with their ‘cellular protein corona’ due to the limited amount of material available. Co-culture cellular models could be used *in vitro* to study the response on different cell types at the same time, while preserving the protein corona formation in relevant airway lining fluids. Such model could include macrophages on the apical side of the epithelial barrier, and fibroblasts on the basal side. Recently, He *et al*. established a co-culture model using Calu-3 cells and human macrophages-like cells (monocytes-derived macrophages), which can be kept in cultures for 10 days (He et al. 2021). This model could be used to study the cellular response in a complex biological fluid.

Moreover, NPs may translocate through the epithelial barrier before reaching the fibroblasts, so that the protein corona formed in the secretome would probably be modified following NP uptake by epithelial cells. As the analysis of the protein corona inside cells remains a technical challenge (Hu et al. 2021), probing its effect in advanced cell and tissue models may help getting around this difficulty.

All these studies reflect the role of the protein corona on the fate and toxic effect of different nanoparticles and the importance of choosing the correct biological fluid depending for the toxicological assessment of NP toxicity *in vitro*.

5.6 Conclusion

We established a method to isolate NPs and adsorbed proteins from the mucus samples reducing false positive and negative results. However, further improvements are needed by implementing other techniques such as size-exclusion chromatography.

We analysed the composition of the protein corona formed on AgNPs in the secretome of Calu-3 cells. We compared the corona formation as a function of protein/NP ratio, incubation time, and cellular responses. These results highlighted the necessity of studying the formation of the protein corona under physiological conditions due to their high capacity of change and evolution. In addition, the cellular responses to NP exposure, not taken in consideration under acellular condition, are playing an important role in the modification of the biological fluid inducing changes in biological media composition and therefore in the protein corona.

Then, we investigated the biological role of the protein corona in the cellular interactions of AgNPs with macrophages. The presence or not of a protein corona formed by incuation with secretome or FBS proteins seems to induce different pro-inflammatory responses and highlighted the specific functions of some of the proteins involved.

Chapter 6: General discussion and perspectives

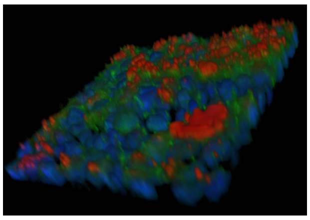

Calu-3 culture for nanotoxicology studies

- Large porosity insert and reduction of FBS supplementation
- Long-term cultures (up to 28 days)
- Characterization:
  - Morphological: tight-junctions, mucus vesicles
  - Functional: mucus production

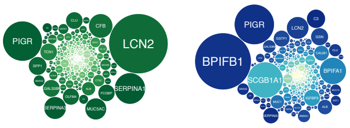

Validation of Calu-3 culture using MucilAir^{TM} cultures

- Long-term characterization of the epithelial barrier
- Characterization of Calu-3 and MucilAir^{TM} apical secretomes
- Evolution of the secretome composition with time
- Biological role of secreted proteins in both cultures

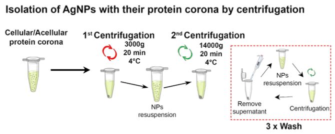

Methods for NP isolation

- Adaptation of the centrifugation method to separate NPs from mucus
- Comparison with magnetic isolation

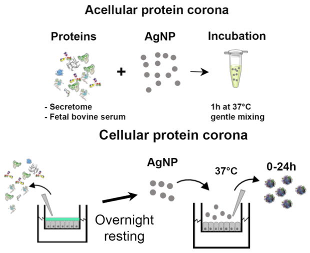

Formation of the protein corona in secretomes

- Formation of a protein corona on AgNPs in a static (without cells) and dynamic (with cells for 1 h or 24 h) biological fluid
- Comparison of two NP concentrations to investigate the effect of protein/NP ratio on the composition of the protein corona
- Proteomic analysis of the corona by SDS-PAGE and LC-MS/MS

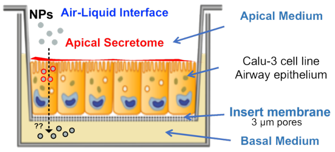

Cellular responses of Calu-3 cultures exposed to AgNPs

- 10 and 50 µg/cm² of AgNPs did not alter the epithelial barrier integrity
- No significant changes of the metabolic activity
- Activation of pro-inflammatory and anti-oxidant responses
- Activation of metal detoxification and metal homeostasis

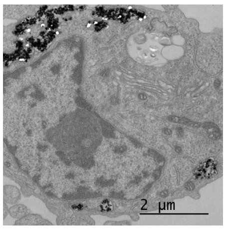

Role of the protein corona on macrophages

- Uptake of bare AgNPs or AgNPs with a protein corona formed in FBS or in the secretome observed by TEM
- Significant induction of the metabolic activity of macrophages by secretome-AgNPs

Figure 73: Summary of the main results obtained during my thesis.

The aim of this study was to investigate the interactions between nanoparticles and the lung fluids in order to better understand the potential toxicological effects resulting from NP inhalation. To carry out this project, silver nanoparticles were used as a model of nanoparticles and a 3D *in vitro* model of the human bronchial epithelium was established using the Calu-3 cell line. Calu-3 cells have been widely used in pharmacology research for their capacity to establish a tight barrier. To adapt the model to nanotoxicology and the study of NP-protein interactions, the model was modified with the cells cultured at the air-liquid interface on large-porosity inserts and with reduced FBS supplementation in the basal medium. The composition of the secretome produced by Calu-3 cells was characterized by proteomics. It showed high similarities with the airway surface liquid protein composition produced *in vitro* by primary cells (Sanchez-Guzman et al. 2021), and with a broncho-alveolar lavage from a healthy donor (this thesis) (Jinzhi Chen et al. 2008). Using this model provided insight in the formation of the protein corona in the airway fluid and its evolution following cell exposure to NPs. Furthermore, the model can be used to follow NP internalization and translocation through the epithelial barrier as well as for chronic toxicity studies as the culture can be maintained over several weeks.

The originality of our study was to investigate the corona formation on NP from an airway fluid. In a biological fluid, the adsorption of proteins on the surface of NPs is an early process that leads to major changes in the physicochemical properties and biological effects of the NPs. Proteins show different affinities for a solid surface, so that some proteins may or may not adsorb onto NPs, depending on the protein structure and biochemical properties on one hand, and the NP physicochemical properties (size, shape, and surface chemistry) on the other hand (Lundqvist et al. 2008). The pH, ionic strength and medium composition also play a role in protein adsorption (Sanchez-Guzman et al. 2020). Numerous studies investigated the composition and dynamics of the protein corona using different biological systems, for example in serum or plasma (Kumar et al. 2016; C. Pisani et al. 2017), following direct cell exposure to NPs (Albanese et al. 2014; Bertoli et al. 2016), or *in vivo* (Hadjidemetriou et al. 2015). Plasma, serum, blood and bronchoalveolar lavage have been used to study protein corona formation on different types of NPs. Cedervall *et al.* reported different protein adsorption patterns on *N-isopropylacrylamide-N-tert-butylacrylamide* (NIPAM-BAM) co-polymer NPs after incubation with varying concentrations of plasma proteins (Cedervall, Lynch, Foy, et al. 2007).

Several studies using blood sample identified serum albumin, apolipoprotein, fibrinogen, coagulation factors and complement proteins among the most abundant proteins adsorbed on liposomal NPs (Caracciolo et al. 2014), silica NPs (Cédric Pisani, Rascol, et al. 2017), gold NPs and silver NPs (W. Lai et al. 2017). The use of other biological fluids, such as the respiratory lining fluid, lead to the formation of a protein coronas with a different composition. Kumar *et al.* identified an enrichment in immunoregulatory proteins on silica and poly(vinyl) acetate (PVAc) NPs after incubation in human bronchoalveolar lavage (Kumar et al. 2016). In this study, the authors identified serum albumin, apolipoproteins, and complement proteins in the protein corona, which are common with protein coronas formed in serum. Proteins specific of bronchoalveolar lavage, such as pulmonary surfactant and BPI-fold containing families, were also identified in the protein corona. In our study, we characterized the formation of the protein corona in the secretome samples. We observed a protein pattern different from the protein corona formed in human serum or plasma reported in other studies. Here, we reported an evolution of the pattern of protein corona as a function of NP concentration, time of exposure and biological fluid (acellular or cellular corona). We did not identify serum albumin or apolipoproteins in any of the protein coronas. Instead, these coronas were formed by proteins associated to the secretome or the cells such as proteasome proteins, chemokine, complement proteins, tight junctions, among others.

The corona formation on NP from an airway fluid was investigated in presence or not of cells showing a dynamic process related to cell responses to NP exposure.

Pisani *et al.* previously showed that the formation of the protein corona is a dynamic process and that the composition of the protein corona evolves with time (Pisani *et al.*, 2017). To address more accurately the formation of the protein corona formation in complex biological fluids, *in vitro* and *in vivo* experiments have been developed. Cox *et al.* investigated the evolution of the protein corona evolution using an *in vitro* model of the blood-brain-barrier (A. Cox et al. 2018). The establishment of the model on inserts allowed the investigation of the evolution of the protein corona after NP translocation. The authors observed a different protein corona on the same NPs before and after translocation, supporting the evolution of the protein corona with its biological environment. In our study, we investigated the formation of the protein corona during the exposure of the bronchial epithelium to AgNPs *in vitro*. Our Calu-3 model was developed on inserts with a 3 µm porosity, so that NP translocation through the epithelium could be later investigated. The use of *in vitro* models to analyze the protein corona provides more relevant results compared to the analysis of acellular protein corona (that is in biological fluids but without cells). Cell exposure to NPs can induce cellular responses producing changes in the biological fluid composition. These changes may lead to a modification of the protein corona, which can result in changes in NP internalization, translocation, or toxicity. One limitation of *in vitro* models is the use of cell culture media, which are usually supplemented with FBS, potentially bringing exogenous proteins to the system.

The composition of the protein corona has also been investigated *in vivo*, though it can be challenging to collect NPs in the whole organism. Circulating NPs were collected from the blood in most cases. Hadjidemetriou *et al.* reported differences in the composition of the protein corona formed onto liposomal NPs either *in vitro* or *in vivo* in mice. The protein corona formed *in vivo* exhibited a larger protein variety. However, the amount of adsorbed proteins per NP was similar *in vitro* and *in vivo*, suggesting that blood composition, blood flow, and/or contacts with the endothelial and circulating cells may have an impact on the formation of the protein corona (Hadjidemetriou et al. 2015). In our study, we also reported differences between the acellular and cellular protein corona formed on AgNPs in the secretome, with a richer composition in the cellular conditions. In addition, the cellular protein corona formed on silver NPs following 24 h exposure of the Calu-3 cells was composed of a larger number of different proteins compared to 1 h exposure. These changes could be explained by changes in the biological fluid induced by the cell response to NP exposure. The ongoing proteomic analysis on the secretome (not absorbed onto NP) of AgNP treated and untreated Calu-3 cultures will tell us about changes in the protein profile and whether the new proteins observed after 24 hours are the result of the cellular responses to AgNPs.

One limitation of the study of the protein corona *in vivo* is the specie difference. The effect of the specie on the composition of the protein corona was shown *in vitro* in biological fluids. Caracciolo *et al.* reported different protein corona compositions on liposomal NPs after incubation with mice or human plasma. Since some liposomal formulations failed to reproduce the effects observed in mice to humans, changes in the protein corona suggest a possible additional explanation (Caracciolo et al. 2014).

The corona formation on AgNPs from an airway fluid modified macrophage response. New tools and models will help us to better understand the functions and cellular effects of the protein corona on cells exposed to NPs. *In vitro* models can be used to follow NP internalization and translocations. Bertoli *et al.* studied the evolution of the protein corona after NP internalization. The authors reported that part of the protein corona may be degraded in the lysosomes (Bertoli et al. 2016). Using the same strategy, the Calu-3 model could be used to investigate the evolution of the protein corona inside cells. The analysis of the protein corona inside cells is challenging: NPs must be recovered from the cells and/or organelles without modifying the biomolecular corona, a low number of NPs may be internalized by cells, and a lower number of NPs may be recovered for quantitative and qualitative proteomics. Further investigation is required to develop new strategies to analyse the intracellular protein corona.

In addition to the analysis of the biomolecular corona composition, other studies have investigated the changes induced by adsorption on the protein structure and activity. The changes of oxyhemoglobin secondary structure was investigated following formation of a hard or soft protein corona on silica NPs using cryoTEM and synchrotron-radiation circular dichroism (Sanchez-Guzman et al. 2020). This represents a first step towards the analysis of the protein corona *in situ*. Additionally, the use of molecular dynamic simulation is a promising approach to predict protein affinity and structural changes during their interaction with NPs.

Understanding NP-protein interactions is also important for the development of nanomedical applications. Richards *et al.* presented a gold NPs functionalized with bovine serum proteins, which provide protection against NPs fouling and improved the delivery of Ontruzant (an antibody against tumoral biomarkers) specifically to the tumoral tissue (Richards et al. 2021). Mixing inactivated influenza viral particles with silver NPs promoted mice protection against lethal viral infections. AgNPs boosted the immune system and favoured the production of mucosal antibodies against the influenza virus (Sanchez-Guzman et al. 2019). Thus, it would be interesting to know whether adsorption of viral particles, viral proteins, and/or host proteins participated in the building of the immune response. The cellular model and the methodologies that have been developed in this thesis could contribute to the development of such studies.

References

Ahmad, S, A Ahmad, K B Neeves, T Hendry-Hofer, J E Loader, C W White, and L Veress. 2014. “In Vitro Cell Culture Model for Toxic Inhaled Chemical Testing.” *J. Vis. Exp* 87: 51539. https://doi.org/10.3791/51539.

Al-Nasiry, Salwan, N Geusens, M. Hanssens, C. Luyten, and R. Pijnenborg. 2007. “The Use of Alamar Blue Assay for Quantitative Analysis of Viability, Migration and Invasion of Choriocarcinoma Cells.” *Human Reproduction* 22 (5): 1304–9. https://doi.org/10.1093/humrep/dem011.

Albanese, Alexandre, Carl D. Walkey, Jonathan B. Olsen, Hongbo Guo, Andrew Emili, and Warren C.W. Chan. 2014. “Secreted Biomolecules Alter the Biological Identity and Cellular Interactions of Nanoparticles.” *ACS Nano* 8 (6): 5515–26. https://doi.org/10.1021/nn4061012.

Anandhakumar, S., V. Mahalakshmi, and Ashok M. Raichur. 2012. “Silver Nanoparticles Modified Nanocapsules for Ultrasonically Activated Drug Delivery.” *Materials Science and Engineering: C* 32 (8): 2349–55. https://doi.org/10.1016/J.MSEC.2012.07.006.

Aoyama, Michihiko, Katsutomo Hata, Kazuma Higashisaka, Kazuya Nagano, Yasuo Yoshioka, and Yasuo Tsutsumi. 2016. “Clusterin in the Protein Corona Plays a Key Role in the Stealth Effect of Nanoparticles against Phagocytes.” *Biochemical and Biophysical Research Communications* 480 (4): 690–95. https://doi.org/10.1016/j.bbrc.2016.10.121.

Arsalane, Karim, Fabrice Broeckaert, Bernard Knoops, Murielle Wiedig, Gerard Toubeau, and Alfred Bernard. 2000. “Clara Cell Specific Protein (CC16) Expression after Acute Lung Inflammation Induced by Intratracheal Lipopolysaccharide Administration.” *American Journal of Respiratory and Critical Care Medicine* 161 (5): 1624–30. https://doi.org/10.1164/AJRCCM.161.5.9812157.

Aufderheide, Michaela, Wolf Dieter Heller, Olaf Krischenowski, Niklas Möhle, and Dieter Hochrainer. 2017. “Improvement of the CULTEX® Exposure Technology by Radial Distribution of the Test Aerosol.” *Experimental and Toxicologic Pathology* 69 (6): 359–65. https://doi.org/10.1016/j.etp.2017.02.004.

Babu, Polani B.Ramesh, Aaron Chidekel, and Thomas H. Shaffer. 2004. “Protein Composition of Apical Surface Fluid from the Human Airway Cell Line Calu-3: Effect of Ion Transport Mediators.” *Clinica Chimica Acta* 347 (1–2): 81–88. https://doi.org/10.1016/j.cccn.2004.04.006.

Baimanov, Didar, Rong Cai, and Chunying Chen. 2019. “Understanding the Chemical Nature of Nanoparticle-Protein Interactions.” *Bioconjugate Chemistry* 30 (7): 1923–37. https://doi.org/10.1021/acs.bioconjchem.9b00348.

Bals, Robert, Daniel J. Weiner, and James M. Wilson. 1999. “The Innate Immune System in Cystic Fibrosis Lung Disease.” *Journal of Clinical Investigation* 103 (3): 303–7. https://doi.org/10.1172/JCI6277.

Bansil, Rama, and Bradley S Turner. 2018. “The Biology of Mucus : Composition , Synthesis and Organization ☆.” *Advanced Drug Delivery Reviews* 124: 3–15. https://doi.org/10.1016/j.addr.2017.09.023.

Barbalinardo, Marianna, Federico Caicci, Massimiliano Cavallini, and Denis Gentili. 2018. “Protein Corona Mediated Uptake and Cytotoxicity of Silver Nanoparticles in Mouse Embryonic Fibroblast.” *Small* 14 (34): 1–8. https://doi.org/10.1002/smll.201801219.

Bedward, Michael, David Eppstein, and Menzel Peter. 2018. “Package ‘ Packcircles ’ R Package Version 0.3.3.” https://cran.r-project.org/package=packcircles.

Bertoli, Filippo, David Garry, Marco P. Monopoli, Anna Salvati, and Kenneth A. Dawson. 2016. “The Intracellular Destiny of the Protein Corona: A Study on Its Cellular Internalization and Evolution.” *ACS Nano* 10 (11): 10471–79. https://doi.org/10.1021/acsnano.6b06411.

Bissell, Mina J., Aylin Rizki, and I. Saira Mian. 2003. “Tissue Architecture: The Ultimate Regulator of Breast Epithelial Function.” *Current Opinion in Cell Biology*. https://doi.org/10.1016/j.ceb.2003.10.016.

Bobyk, Laure, Adeline Tarantini, David Beal, Giulia Veronesi, Isabelle Kieffer, Sylvie Motellier, Eugenia Valsami-Jones, et al. 2021. “Toxicity and Chemical Transformation of Silver Nanoparticles in A549 Lung Cells: Dose-Rate-Dependent Genotoxic Impact.” *Environmental Science: Nano* 8 (3): 806–21. https://doi.org/10.1039/d0en00533a.

Böhmert, Linda, Birgit Niemann, Dajana Lichtenstein, Sabine Juling, Birgit Niemann, Dajana Lichtenstein, Sabine Juling, and Alfonso Lampen. 2015. “Molecular Mechanism of Silver Nanoparticles in Human Intestinal Cells Molecular Mechanism of Silver Nanoparticles in Human Intestinal Cells” 5390. https://doi.org/10.3109/17435390.2014.980760.

Böhmert, Linda, Linn Voß, Valerie Stock, Albert Braeuning, Alfonso Lampen, and Holger Sieg. 2020. “Isolation Methods for Particle Protein Corona Complexes from Protein-Rich Matrices.” *Nanoscale Advances* 2 (2): 563–82. https://doi.org/10.1039/c9na00537d.

Bonvin, Debora, Ulrich Aschauer, Duncan T. L. Alexander, Diego Chiappe, Marc Moniatte, Heinrich Hofmann, and Marijana Mionić Ebersold. 2017. “Protein Corona: Impact of Lymph Versus Blood in a Complex In Vitro Environment.” *Small* 13 (29): 1700409. https://doi.org/10.1002/smll.201700409.

Borrok, M. Jack, Antonio DiGiandomenico, Nurten Beyaz, Gabriela M. Marchetti, Arnita S. Barnes, Kristen J. Lekstrom, Sandrina S. Phipps, et al. 2018. “Enhancing IgG Distribution to Lung Mucosal Tissue Improves Protective Effect of Anti-Pseudomonas Aeruginosa Antibodies.” *JCI Insight* 3 (12). https://doi.org/10.1172/jci.insight.97844.

Botelho, Danielle, Bey F. Leo, Christopher Massa, Srijata Sarkar, Terry Tetley, Kian F. Chung, Shu Chen, et al. 2018. “Exposure to Silver Nanospheres Leads to Altered Respiratory Mechanics and Delayed Immune Response in an in Vivo Murine Model.” *Frontiers in Pharmacology* 9 (MAR): 1–9. https://doi.org/10.3389/fphar.2018.00213.

Bovard, David, Albert Giralt, Keyur Trivedi, Laurent Neau, Petros Kanellos, Anita Iskandar, Athanasios Kondylis, et al. 2020. “Comparison of the Basic Morphology and Function of 3D Lung Epithelial Cultures Derived from Several Donors.” *Current Research in Toxicology* 1 (June): 56–69. https://doi.org/10.1016/j.crtox.2020.08.002.

Braakhuis, Hedwig M., Flemming R. Cassee, Paul H.B. Fokkens, Liset J.J. De La Fonteyne, Agnes G. Oomen, Petra Krystek, Wim H. De Jong, Henk Van Loveren, and Margriet V.D.Z. Park. 2016. “Identification of the Appropriate Dose Metric for Pulmonary Inflammation of Silver Nanoparticles in an Inhalation Toxicity Study.” *Nanotoxicology* 10 (1): 63–73. https://doi.org/10.3109/17435390.2015.1012184.

Braakhuis, Hedwig M., Samantha K. Kloet, Sanja Kezic, Frieke Kuper, Margriet V.D.Z. Park, Susann Bellmann, Meike van der Zande, et al. 2015. “Progress and Future of in Vitro Models to Study Translocation of Nanoparticles.” *Archives of Toxicology* 89 (9): 1469–95. https://doi.org/10.1007/s00204-015-1518-5.

Brookes, Oliver, Sonja Boland, René Lai Kuen, Dorian Miremont, Jamileh Movassat, and Armelle Baeza-Squiban. 2021. “Co-Culture of Type I and Type II Pneumocytes as a Model of Alveolar Epithelium.” *Plos One* 16 (9): e0248798. https://doi.org/10.1371/journal.pone.0248798.

Brunner, Daniel, Jürgen Frank, Helmut Appl, Harald Schöffl, Walter Pfaller, and Gerhard Gstraunthaler. 2010. “Serum-Free Cell Culture: The Serum-Free Media Interactive Online Database.” *ALTEX* 27 (1): 53–62. https://doi.org/10.14573/altex.2010.1.53.

Bustamante-Marin, Ximena M., and Lawrence E. Ostrowski. 2017. “Cilia and Mucociliary Clearance.” *Cold Spring Harbor Perspectives in Biology* 9 (4): a028241. https://doi.org/10.1101/cshperspect.a028241.

Button, Brian, Li Heng Cai, Camille Ehre, Mehmet Kesimer, David B. Hill, John K. Sheehan, Richard C. Boucher, and Michael Rubinstein. 2012. “A Periciliary Brush Promotes the Lung Health by Separating the Mucus Layer from Airway Epithelia.” *Science* 337 (6097): 937–41. https://doi.org/10.1126/science.1223012.

Cao, Xuefei, Jayme P Coyle, Rui Xiong, Yiying Wang, Robert H Heflich, Baiping Ren, William M Gwinn, Patrick Hayden, and Liying Rojanasakul. 2020. “Invited Review: Human Air-Liquid-Interface Organotypic Airway Tissue Models Derived from Primary Tracheobronchial Epithelial Cells-Overview and Perspectives.” https://doi.org/10.1007/s11626-020-00517-7/Published.

Caracciolo, G., D. Pozzi, A. L. Capriotti, C. Cavaliere, S. Piovesana, G. La Barbera, A. Amici, and A. Laganà. 2014. “The Liposome-Protein Corona in Mice and Humans and Its Implications for in Vivo Delivery.” *Journal of Materials Chemistry B* 2 (42): 7419–28. https://doi.org/10.1039/c4tb01316f.

Castell, José V., M. Teresa Donato, and María José Gómez-Lechón. 2005. “Metabolism and Bioactivation of Toxicants in the Lung. The in Vitro Cellular Approach.” *Experimental and Toxicologic Pathology* 57 (SUPPL. 1): 189–204. https://doi.org/10.1016/j.etp.2005.05.008.

Cedervall, Tommy, Iseult Lynch, Martina Foy, Tord Berggård, Seamas C. Donnelly, Gerard Cagney, Sara Linse, and Kenneth A. Dawson. 2007. “Detailed Identification of Plasma Proteins Adsorbed on Copolymer Nanoparticles.” *Angewandte Chemie - International Edition* 46 (30): 5754–56. https://doi.org/10.1002/anie.200700465.

Cedervall, Tommy, Iseult Lynch, Stina Lindman, T. Berggard, Eva Thulin, Hanna Nilsson, Kenneth A. Dawson, et al. 2007. “Understanding the Nanoparticle-Protein Corona Using Methods to Quantify Exchange Rates and Affinities of Proteins for Nanoparticles.” *Proceedings of the National Academy of Sciences* 104 (7): 2050–55. https://doi.org/10.1073/pnas.0608582104.

Cha, Sang Ho, Jin Hong, Matt McGuffie, Bongjun Yeom, J. Scott Vanepps, and Nicholas A. Kotov. 2015. “Shape-Dependent Biomimetic Inhibition of Enzyme by Nanoparticles and Their Antibacterial Activity.” *ACS Nano* 9 (9): 9097–9105. https://doi.org/10.1021/acsnano.5b03247.

Chairuangkitti, Porntipa, Somsong Lawanprasert, Sittiruk Roytrakul, Sasitorn Aueviriyavit, Duangkamol Phummiratch, Kornphimol Kulthong, Pithi Chanvorachote, and Rawiwan Maniratanachote. 2013. “Silver Nanoparticles Induce Toxicity in A549 Cells via ROS-Dependent and ROS-Independent Pathways.” *Toxicology in Vitro : An International Journal Published in Association with BIBRA* 27 (1): 330–38. https://doi.org/10.1016/j.tiv.2012.08.021.

Chan, Yvonne R., Jessica S. Liu, Derek A. Pociask, Mingquan Zheng, Timothy A. Mietzner, Thorsten Berger, Tak W. Mak, et al. 2009. “Lipocalin 2 Is Required for Pulmonary Host Defense against Klebsiella Infection.” *The Journal of Immunology* 182 (8): 4947–56. https://doi.org/10.4049/jimmunol.0803282.

Chang, Natasha C, Mai Nguyen, Marc Germain, and Gordon C Shore. 2009. “Antagonism of Beclin 1-Dependent Autophagy by BCL-2 at the Endoplasmic Reticulum Requires NAF-1.” *The EMBO Journal* 29 (3): 606–18. https://doi.org/10.1038/emboj.2009.369.

Chen, Jinzhi, Soyoung Ryu, Sina A. Gharib, David R. Goodlett, and Lynn M. Schnapp. 2008. “Exploration of the Normal Human Bronchoalveolar Lavage Fluid Proteome.” *Proteomics - Clinical Applications* 2 (4): 585–95. https://doi.org/10.1002/prca.200780006.

Chen, Jiong, Chun mao Han, Xiao wei Lin, Zhi jian Tang, and Shi jie Su. 2006. “Effect of Silver Nanoparticle Dressing on Second Degree Burn Wound.” *Zhonghua Wai Ke Za Zhi [Chinese Journal of Surgery]* 44 (1): 50–52. http://www.ncbi.nlm.nih.gov/pubmed/16620649.

Chen, Yue, Zhe Wang, Ming Xu, Xiang Wang, Rui Liu, Qian Liu, Zhihong Zhang, et al. 2014. “Nanosilver Incurs an Adaptive Shunt of Energy Metabolism Mode to Glycolysis in Tumor and Nontumor Cells.” *ACS Nano* 8 (6): 5813–25. https://doi.org/10.1021/nn500719m.

Cingolani, Emanuela, Safar Alqahtani, Robyn C. Sadler, David Prime, Snjezana Stolnik, and Cynthia Bosquillon. 2019. “In Vitro Investigation on the Impact of Airway Mucus on Drug Dissolution and Absorption at the Air-Epithelium Interface in the Lungs.” *European Journal of Pharmaceutics and Biopharmaceutics* 141 (August): 210–20. https://doi.org/10.1016/j.ejpb.2019.05.022.

Cornu, Raphaël, Claire Chrétien, Yann Pellequer, Hélène Martin, and Arnaud Béduneau. 2020. “Small Silica Nanoparticles Transiently Modulate the Intestinal Permeability by Actin Cytoskeleton Disruption in Both Caco-2 and Caco-2/HT29-MTX Models.” *Archives of Toxicology* 94 (4): 1191–1202. https://doi.org/10.1007/s00204-020-02694-6.

Cox, Alysia, Patrizia Andreozzi, Roberta Dal Magro, Fabio Fiordaliso, Alessandro Corbelli, Laura Talamini, Clizia Chinello, et al. 2018. “Evolution of Nanoparticle Protein Corona across the Blood-Brain Barrier.” *ACS Nano* 12 (7): 7292–7300. https://doi.org/10.1021/acsnano.8b03500.

Cox, Jürgen, Nadin Neuhauser, Annette Michalski, Richard A. Scheltema, Jesper V. Olsen, and Matthias Mann. 2011. “Andromeda: A Peptide Search Engine Integrated into the MaxQuant Environment.” *Journal of Proteome Research* 10 (4): 1794–1805. https://doi.org/10.1021/pr101065j.

Cukierman, Edna, Roumen Pankov, Daron R Stevens, and Kenneth M Yamada. 1998. “Taking Cell-Matrix Adhesions to the Third Dimension.” *J. Appl. Physiol* 14: 15432. https://doi.org/10.1126/science.1065874.

Dagani, RON. 2003. “Nanomaterials: Safe or Unsafe?” In *Chemical and Engineering News*, 81:30–33. https://doi.org/10.1021/cen-v081n017.p030.

Docter, D, D Westmeier, M Markiewicz, S Stolte, S K Knauer, and R. H. Stauber. 2015. “The Nanoparticle Biomolecule Corona: Lessons Learned - Challenge Accepted?” *Chemical Society Reviews* 44 (17): 6094–6121. https://doi.org/10.1039/c5cs00217f.

Dong, Y, G F T Poon, A A Arif, S S M Lee-Sayer, M Dosanjh, and P Johnson. 2017. “The Survival of Fetal and Bone Marrow Monocyte-Derived Alveolar Macrophages Is

Promoted by CD44 and Its Interaction with Hyaluronan." *Mucosal Immunology 2018 11:3* 11 (3): 601–14. https://doi.org/10.1038/mi.2017.83.

Dwivedi, Aishwarya M., Swapna Upadhyay, Gunnar Johanson, Lena Ernstgård, and Lena Palmberg. 2018. "Inflammatory Effects of Acrolein, Crotonaldehyde and Hexanal Vapors on Human Primary Bronchial Epithelial Cells Cultured at Air-Liquid Interface." *Toxicology in Vitro* 46: 219–28. https://doi.org/10.1016/j.tiv.2017.09.016.

Echegoyen, Yolanda, and Cristina Nerín. 2013. "Nanoparticle Release from Nano-Silver Antimicrobial Food Containers." *Food and Chemical Toxicology* 62: 16–22. https://doi.org/10.1016/j.fct.2013.08.014.

Eckert, Judith J., and Tom P. Fleming. 2008. "Tight Junction Biogenesis during Early Development." *Biochimica et Biophysica Acta - Biomembranes* 1778 (3): 717–28. https://doi.org/10.1016/j.bbamem.2007.09.031.

Fang, Ye, and Richard M Eglen. 2017. "Three-Dimensional Cell Cultures in Drug Discovery and Development." https://doi.org/10.1177/1087057117696795.

Fasquelle, François, Rodolphe Carpentier, Bastien Demouveaux, Jean Luc Desseyn, and Didier Betbeder. 2020. "Importance of the Phospholipid Core for Mucin Hydrogel Penetration and Mucosal Cell Uptake of Maltodextrin Nanoparticles." *ACS Applied Bio Materials* 3 (9): 5741–49. https://doi.org/10.1021/acsabm.0c00521.

Feng, Yanlin, Guorui Wang, Yun Chang, Yan Cheng, Bingbing Sun, Liming Wang, Chunying Chen, and Haiyuan Zhang. 2019. "Electron Compensation Effect Suppressed Silver Ion Release and Contributed Safety of Au@Ag Core-Shell Nanoparticles." *Nano Letters*. https://doi.org/10.1021/acs.nanolett.9b01293.

Ferruzza, Simonetta, Carlotta Rossi, Yula Sambuy, and Maria Laura Scarino. 2013. "Serum-Reduced and Serum-Free Media for Differentiation of Caco-2 Cells." *Altex* 30 (2): 159–68. https://doi.org/10.14573/altex.2013.2.159.

Florea, Bogdan I., Maria L. Cassara, Hans E. Junginger, and Gerrit Borchard. 2003. "Drug Transport and Metabolism Characteristics of the Human Airway Epithelial Cell Line Calu-3." *Journal of Controlled Release* 87 (1–3): 131–38. https://doi.org/10.1016/S0168-3659(02)00356-5.

Forti, Efrat, Susan Salovaara, Yuksel Cetin, Anna Bulgheroni, Richard Tessadri, Paul Jennings, Walter Pfaller, and Pilar Prieto. 2011. "In Vitro Evaluation of the Toxicity Induced by Nickel Soluble and Particulate Forms in Human Airway Epithelial Cells." *Toxicology in Vitro* 25 (2): 454–61. https://doi.org/10.1016/j.tiv.2010.11.013.

Foster, Matthew W., J. Will Thompson, Loretta G. Que, Ivana V. Yang, David A. Schwartz, M. Arthur Moseley, and Harvey E. Marshall. 2013. "Proteomic Analysis of Human Bronchoalveolar Lavage Fluid after Subsgemental Exposure." *Journal of Proteome Research* 12 (5): 2194–2205. https://doi.org/10.1021/pr400066g.

Franco-Molina, Moisés A., Edgar Mendoza-Gamboa, Crystel A. Sierra-Rivera, Ricardo A. Gómez-Flores, Pablo Zapata-Benavides, Paloma Castillo-Tello, Juan Manuel Alcocer-González, Diana F. Miranda-Hernández, Reyes S. Tamez-Guerra, and Cristina Rodríguez-Padilla. 2010. "Antitumor Activity of Colloidal Silver on MCF-7 Human Breast Cancer Cells." *Journal of Experimental and Clinical Cancer Research* 29 (1): 148. https://doi.org/10.1186/1756-9966-29-148.

Garcés, Mariana, Lourdes Cáceres, Diego Chiappetta, Natalia Magnani, and Pablo Evelson. 2021. "Current Understanding of Nanoparticle Toxicity Mechanisms and Interactions with

Biological Systems." *New Journal of Chemistry* 45 (32): 14328–44. https://doi.org/10.1039/d1nj01415c.

García-Salvador, Adrián, Alberto Katsumiti, Elena Rojas, Carol Aristimuño, Mónica Betanzos, Marta Martínez-Moro, Sergio E. Moya, and Felipe Goñi-De-cerio. 2021. "A Complete in Vitro Toxicological Assessment of the Biological Effects of Cerium Oxide Nanoparticles: From Acute Toxicity to Multi-Dose Subchronic Cytotoxicity Study." *Nanomaterials* 11 (6). https://doi.org/10.3390/nano11061577.

Geng, Yan, Paul Dalhaimer, Shenshen Cai, Richard Tsai, Manorama Tewari, Tamara Minko, and Dennis E. Discher. 2007. "Shape Effects of Filaments versus Spherical Particles in Flow and Drug Delivery." *Nature Nanotechnology* 2 (4): 249–55. https://doi.org/10.1038/nnano.2007.70.

George, Isabelle, Sandra Vranic, Sonja Boland, Arnaud Courtois, and Armelle Baeza-Squiban. 2015. "Development of an in Vitro Model of Human Bronchial Epithelial Barrier to Study Nanoparticle Translocation." *Toxicology in Vitro* 29 (1): 51–58. https://doi.org/10.1016/j.tiv.2014.08.003.

Gerde, Per, Pär Ewing, Lena Låstbom, Åke Ryrfeldt, Juri Waher, and Göran Lidén. 2004. "A Novel Method to Aerosolize Powder for Short Inhalation Exposures at High Concentrations: Isolated Rat Lungs Exposed to Respirable Diesel Soot." Edited by Amitava Mukherjee. *Inhalation Toxicology* 16 (1): 45–52. https://doi.org/10.1080/08958370490258381.

Gliga, Anda R., Sara Skoglund, Inger Odnevall Wallinder, Bengt Fadeel, and Hanna L. Karlsson. 2014. "Size-Dependent Cytotoxicity of Silver Nanoparticles in Human Lung Cells: The Role of Cellular Uptake, Agglomeration and Ag Release." *Particle and Fibre Toxicology* 11 (1): 1–17. https://doi.org/10.1186/1743-8977-11-11.

Gminski, Richard, Tao Tang, and Volker Mersch-Sundermann. 2010. "Cytotoxicity and Genotoxicity in Human Lung Epithelial A549 Cells Caused by Airborne Volatile Organic Compounds Emitted from Pine Wood and Oriented Strand Boards." *Toxicology Letters* 196 (1): 33–41. https://doi.org/10.1016/j.toxlet.2010.03.015.

Gonzalez-Galarza, Faviel F., Craig Lawless, Simon J. Hubbard, Jun Fan, Conrad Bessant, Henning Hermjakob, and Andrew R. Jones. 2012. "A Critical Appraisal of Techniques, Software Packages, and Standards for Quantitative Proteomic Analysis." *OMICS A Journal of Integrative Biology* 16 (9): 431–42. https://doi.org/10.1089/omi.2012.0022.

Grainger, Christopher I., Leona L. Greenwell, David J. Lockley, Gary P. Martin, and Ben Forbes. 2006. "Culture of Calu-3 Cells at the Air Interface Provides a Representative Model of the Airway Epithelial Barrier." *Pharmaceutical Research* 23 (7): 1482–90. https://doi.org/10.1007/s11095-006-0255-0.

Gray, Thomas E., Karen Guzman, C. William Davis, Lubna H. Abdullah, and Paul Nettesheim. 1996. "Mucociliary Differentiation of Serially Passaged Normal Human Tracheobronchial Epithelial Cells." *American Journal of Respiratory Cell and Molecular Biology* 14 (1): 104–12. https://doi.org/10.1165/ajrcmb.14.1.8534481.

Gref, R., M. Lück, P. Quellec, M. Marchand, E. Dellacherie, S. Harnisch, T. Blunk, and R. H. Müller. 2000. "'Stealth' Corona-Core Nanoparticles Surface Modified by Polyethylene Glycol (PEG): Influences of the Corona (PEG Chain Length and Surface Density) and of the Core Composition on Phagocytic Uptake and Plasma Protein Adsorption." *Colloids and Surfaces B: Biointerfaces* 18 (3–4): 301–13. https://doi.org/10.1016/S0927-7765(99)00156-3.

Groneberg, D A, P R Eynott, S Lim, T Oates, R Wu, I Carlstedt, P Roberts, et al. 2002. "Expression of Respiratory Mucins in Fatal Status Asthmaticus and Mild Asthma." *Histopathology*. Vol. 40.

Gstraunthaler, Gerhard, Toni Lindl, and Jan Van Der Valk. 2013. "A Plea to Reduce or Replace Fetal Bovine Serum in Cell Culture Media." *Cytotechnology* 65 (5): 791–93. https://doi.org/10.1007/s10616-013-9633-8.

Guglani, Lokesh, Radha Gopal, Javier Rangel-Moreno, Beth Fallert Junecko, Yinyao Lin, Thorsten Berger, Tak W. Mak, et al. 2012. "Lipocalin 2 Regulates Inflammation during Pulmonary Mycobacterial Infections." *PLoS ONE* 7 (11): 1–11. https://doi.org/10.1371/journal.pone.0050052.

Gupta, Richa, Giorgia Radicioni, Sabri Abdelwahab, Hong Dang, Jerome Carpenter, Michael Chua, Piotr A. Mieczkowski, John T. Sheridan, Scott H. Randell, and Mehmet Kesimer. 2019. "Intercellular Communication between Airway Epithelial Cells Is Mediated by Exosome-like Vesicles." *American Journal of Respiratory Cell and Molecular Biology* 60 (2): 209–20. https://doi.org/10.1165/rcmb.2018-0156OC.

Hadjidemetriou, Marilena, Zahraa Al-Ahmady, Mariarosa Mazza, Richard F. Collins, Kenneth Dawson, and Kostas Kostarelos. 2015. "In Vivo Biomolecule Corona around Blood-Circulating, Clinically Used and Antibody-Targeted Lipid Bilayer Nanoscale Vesicles." *ACS Nano* 9 (8): 8142–56. https://doi.org/10.1021/acsnano.5b03300.

Hattrup, Christine L, and Sandra J Gendler. 2008. "Structure and Function of the Cell Surface (Tethered) Mucins." https://doi.org/10.1146/annurev.physiol.70.113006.100659.

He, Rui-Wen Wen, Hedwig M. Braakhuis, Rob J. Vandebriel, Yvonne C.M. Staal, Eric R. Gremmer, Paul H.B. Fokkens, Claudia Kemp, Jolanda Vermeulen, Remco H.S. Westerink, and Flemming R. Cassee. 2021. "Optimization of an Air-Liquid Interface in Vitro Cell Co-Culture Model to Estimate the Hazard of Aerosol Exposures." *Journal of Aerosol Science* 153 (October 2020): 105703. https://doi.org/10.1016/j.jaerosci.2020.105703.

Hinderliter, Paul M., Kevin R. Minard, Galya Orr, William B. Chrisler, Brian D. Thrall, Joel G. Pounds, and Justin G. Teeguarden. 2010. "ISDD: A Computational Model of Particle Sedimentation, Diffusion and Target Cell Dosimetry for in Vitro Toxicity Studies." *Particle and Fibre Toxicology* 7 (1): 36. https://doi.org/10.1186/1743-8977-7-36.

Hu, Bin, Chuan Wang, Beibei Chen, and Man He. 2021. "Composition of Intracellular Protein Corona around Nanoparticles during Internalization." *ACS Nano* 15 (2): 3108–22. https://doi.org/10.1021/acsnano.0c09649.

Huff, Mary E., Lesley J. Page, William E. Balch, and Jeffery W. Kelly. 2003. "Gelsolin Domain 2 Ca2+ Affinity Determines Susceptibility to Furin Proteolysis and Familial Amyloidosis of Finnish Type." *Journal of Molecular Biology* 334 (1): 119–27. https://doi.org/10.1016/j.jmb.2003.09.029.

Hussell, Tracy, and Thomas J. Bell. 2014. "Alveolar Macrophages: Plasticity in a Tissue-Specific Context." *Nature Reviews Immunology* 14 (2): 81–93. https://doi.org/10.1038/nri3600.

Imaninezhad, Mozhdeh, Joseph Schober, David Griggs, Peter Ruminski, Irma Kuljanishvili, and Silviya Petrova Zustiak. 2018. "Cell Attachment and Spreading on Carbon Nanotubes Is Facilitated by Integrin Binding." *Frontiers in Bioengineering and Biotechnology* 6 (SEP): 1–12. https://doi.org/10.3389/fbioe.2018.00129.

Jeong, Mi Ho, Ha Ryong Kim, In Jae Bang, So Hee Yoo, Sang Jin Lee, Kyu Hong Lee, and Kyu Hyuck Chung. 2019. "In Vitro Model for Predicting Acute Inhalation Toxicity by Using a Calu-3 Epithelium Cytotoxicity Assay." *Journal of Pharmacological and Toxicological Methods* 98 (July 2018): 106576. https://doi.org/10.1016/j.vascn.2019.04.002.

Ji, Jie, Anna Hedelin, Maria Malmlöf, Vadim Kessler, Gulaim Seisenbaeva, Per Gerde, and Lena Palmberg. 2017. "Development of Combining of Human Bronchial Mucosa Models with XposeALI® for Exposure of Air Pollution Nanoparticles." *PLoS ONE* 12 (1). https://doi.org/10.1371/journal.pone.0170428.

Jo, Mi Seong, Jin Kwon Kim, Younghun Kim, Hoi Pin Kim, Hee Sang Kim, Kangho Ahn, Ji Hyun Lee, et al. 2020. "Mode of Silver Clearance Following 28-Day Inhalation Exposure to Silver Nanoparticles Determined from Lung Burden Assessment Including Post-Exposure Observation Periods." *Archives of Toxicology* 94 (3): 773–84. https://doi.org/10.1007/s00204-020-02660-2.

Joshi, Nikita, James M. Walter, and Alexander V. Misharin. 2018. "Alveolar Macrophages." *Cellular Immunology* 330 (December 2017): 86–90. https://doi.org/10.1016/j.cellimm.2018.01.005.

Kensler, Thomas W., Nobunao Wakabayashi, and Shyam Biswal. 2007. "Cell Survival Responses to Environmental Stresses via the Keap1-Nrf2-ARE Pathway." *Annual Review of Pharmacology and Toxicology* 47: 89–116. https://doi.org/10.1146/annurev.pharmtox.46.120604.141046.

Klein, Géraldine, Stéphanie Devineau, Jean Christophe Aude, Yves Boulard, Hélène Pasquier, Jean Labarre, Serge Pin, and Jean Philippe Renault. 2016. "Interferences of Silica Nanoparticles in Green Fluorescent Protein Folding Processes." *Langmuir* 32 (1): 195–202. https://doi.org/10.1021/acs.langmuir.5b03890.

Klein, Sebastian G, Tommaso Serchi, Lucien Hoffmann, Brunhilde Blömeke, and Arno C Gutleb. 2013. "An Improved 3D Tetraculture System Mimicking the Cellular Organisation at the Alveolar Barrier to Study the Potential Toxic Effects of Particles on the Lung." *Particle and Fibre Toxicology* 10 (1): 31. https://doi.org/10.1186/1743-8977-10-31.

Knight, Darryl A., and Stephen T. Holgate. 2003. "The Airway Epithelium: Structural and Functional Properties in Health and Disease." *Respirology* 8 (4): 432–46. https://doi.org/10.1046/j.1440-1843.2003.00493.x.

Kolde, R. 2019. "Pheatmap: Pretty Heatmaps. R Package Version 1.0.12." https://cran.r-project.org/package=pheatmap.

Konar, Mouli, Ashwin Mathew, and Swagata Dasgupta. 2019. "Effect of Silica Nanoparticles on the Amyloid Fibrillation of Lysozyme." *ACS Omega* 4 (1): 1015–26. https://doi.org/10.1021/acsomega.8b03169.

Konduru, Nagarjun V., Ramon M. Molina, Archana Swami, Flavia Damiani, Georgios Pyrgiotakis, Paulo Lin, Patrizia Andreozzi, et al. 2017. "Protein Corona: Implications for Nanoparticle Interactions with Pulmonary Cells." *Particle and Fibre Toxicology*. https://doi.org/10.1186/s12989-017-0223-3.

Kreda, Silvia M., Seiko F. Okada, Catharina A. Van Heusden, Wanda O'neal, Sherif Gabriel, Lubna Abdullah, C. William Davis, Richard C. Boucher, and Eduardo R. Lazarowski. 2007. "Coordinated Release of Nucleotides and Mucin from Human Airway Epithelial Calu-3 Cells." *Journal of Physiology* 584 (1): 245–59.

https://doi.org/10.1113/jphysiol.2007.139840.

Kreft, Mateja Erdani, Urška Dragin Jerman, Eva Lasič, Neli Hevir-Kene, Tea Lanišnik Rižner, Luka Peternel, and Katja Kristan. 2015. “The Characterization of the Human Cell Line Calu-3 under Different Culture Conditions and Its Use as an Optimized in Vitro Model to Investigate Bronchial Epithelial Function.” *European Journal of Pharmaceutical Sciences* 69: 1–9. https://doi.org/10.1016/j.ejps.2014.12.017.

Kuehn, Anna, Stephanie Kletting, Cristiane De Souza Carvalho-Wodarz, Urska Repnik, Gareth Griffiths, Ulrike Fischer, Eckart Meese, et al. 2016. “Human Alveolar Epithelial Cells Expressing Tight Junctions to Model the Air-Blood Barrier.” *Altex* 33 (3): 251–60. https://doi.org/10.14573/altex.1511131.

Kumar, Abhinav, Elif Melis Bicer, Anna Babin Morgan, Paul E. Pfeffer, Marco Monopoli, Kenneth A. Dawson, Jonny Eriksson, et al. 2016. “Enrichment of Immunoregulatory Proteins in the Biomolecular Corona of Nanoparticles within Human Respiratory Tract Lining Fluid.” *Nanomedicine: Nanotechnology, Biology, and Medicine* 12 (4): 1033–43. https://doi.org/10.1016/j.nano.2015.12.369.

Lai, Samuel K., Ying-Ying Wang, and Justin Hanes. 2009. “Mucus-Penetrating Nanoparticles for Drug and Gene Delivery to Mucosal Tissues.” *Advanced Drug Delivery Reviews* 61 (2): 158–71. https://doi.org/10.1016/j.addr.2008.11.002.

Lai, Wenjia, Qingsong Wang, Lumeng Li, Zhiyuan Hu, Jiankui Chen, and Qiaojun Fang. 2017. “Interaction of Gold and Silver Nanoparticles with Human Plasma: Analysis of Protein Corona Reveals Specific Binding Patterns.” *Colloids and Surfaces B: Biointerfaces* 152: 317–25. https://doi.org/10.1016/j.colsurfb.2017.01.037.

Lancaster, Madeline A., and Juergen A. Knoblich. 2014. “Organogenesisin a Dish: Modeling Development and Disease Using Organoid Technologies.” *Science* 345 (6194). https://doi.org/10.1126/science.1247125.

Landsiedel, Robert, Lan Ma-Hock, Karin Wiench, Wendel Wohlleben, and Ursula G. Sauer. 2017. “Safety Assessment of Nanomaterials Using an Advanced Decision-Making Framework, the DF4nanoGrouping.” *Journal of Nanoparticle Research* 19 (5). https://doi.org/10.1007/s11051-017-3850-6.

LeMessurier, Kim S., Meenakshi Tiwary, Nicholas P. Morin, and Amali E. Samarasinghe. 2020. “Respiratory Barrier as a Safeguard and Regulator of Defense Against Influenza A Virus and Streptococcus Pneumoniae.” *Frontiers in Immunology* 11 (February). https://doi.org/10.3389/fimmu.2020.00003.

Lemmer, Hendrik Jr, and Josias H. Hamman. 2013. “Paracellular Drug Absorption Enhancement through Tight Junction Modulation.” *Expert Opinion on Drug Delivery* 10 (1): 103–14. https://doi.org/10.1517/17425247.2013.745509.

Lenz, Anke Gabriele, Erwin Karg, Ellen Brendel, Helga Hinze-Heyn, Konrad L Maier, Oliver Eickelberg, Tobias Stoeger, and Otmar Schmid. 2013. “Inflammatory and Oxidative Stress Responses of an Alveolar Epithelial Cell Line to Airborne Zinc Oxide Nanoparticles at the Air-Liquid Interface: A Comparison with Conventional, Submerged Cell-Culture Conditions.” *BioMed Research International* 2013: 12. https://doi.org/10.1155/2013/652632.

Lindeque, J.Z., O. Levanets, R. Louw, and F.H. van der Westhuizen. 2010. “The Involvement of Metallothioneins in Mitochondrial Function and Disease.” *Current Protein & Peptide Science* 11 (4): 292–309. https://doi.org/10.2174/138920310791233378.

Liu, Yang, Jennifer A. Bartlett, Marissa E. Di, Jennifer M. Bomberger, Yvonne R. Chan, Lokesh Gakhar, Rama K. Mallampalli, Paul B. McCray, and Y. Peter Di. 2013. "SPLUNC1/BPIFA1 Contributes to Pulmonary Host Defense against Klebsiella Pneumoniae Respiratory Infection." *American Journal of Pathology* 182 (5): 1519–31. https://doi.org/10.1016/j.ajpath.2013.01.050.

Loboda, Agnieszka, Milena Damulewicz, Elzbieta Pyza, Alicja Jozkowicz, and Jozef Dulak. 2016. "Role of Nrf2/HO-1 System in Development, Oxidative Stress Response and Diseases: An Evolutionarily Conserved Mechanism." *Cellular and Molecular Life Sciences* 73 (17): 3221–47. https://doi.org/10.1007/s00018-016-2223-0.

Loman, Stoffer, Jiri Radl, Henk M. Jansen, Theo A. Out, and René Lutter. 1997. "Vectorial Transcytosis of Dimeric IgA by the Calu-3 Human Lung Epithelial Cell Line: Upregulation by IFN-γ." *American Journal of Physiology - Lung Cellular and Molecular Physiology* 272 (5 16-5): 951–58. https://doi.org/10.1152/ajplung.1997.272.5.l951.

Londino, James D., James F. Collawn, and Sadis Matalon. 2015. *Regulation of Airway Lining Fluid in Health and Disease*. *Comparative Biology of the Normal Lung: Second Edition*. Second Edi. Elsevier Inc. https://doi.org/10.1016/B978-0-12-404577-4.00023-0.

Loret, Thomas, Emmanuel Peyret, Marielle Dubreuil, Olivier Aguerre-Chariol, Christophe Bressot, Olivier le Bihan, Tanguy Amodeo, et al. 2016. "Air-Liquid Interface Exposure to Aerosols of Poorly Soluble Nanomaterials Induces Different Biological Activation Levels Compared to Exposure to Suspensions." *Particle and Fibre Toxicology* 13 (1). https://doi.org/10.1186/s12989-016-0171-3.

Lovén, Karin, Julia Dobric, Deniz A. Bölükbas, Monica Kåredal, Sinem Tas, Jenny Rissler, Darcy E. Wagner, and Christina Isaxon. 2021. "Toxicological Effects of Zinc Oxide Nanoparticle Exposure: An in Vitro Comparison between Dry Aerosol Air-Liquid Interface and Submerged Exposure Systems." *Nanotoxicology* 15 (4): 494–510. https://doi.org/10.1080/17435390.2021.1884301.

Lundqvist, Martin, and Tommy Cedervall. 2020. "Three Decades of Research about the Corona Around Nanoparticles : Lessons Learned and Where to Go Now" 2000892. https://doi.org/10.1002/smll.202000892.

Lundqvist, Martin, Johannes Stigler, Giuliano Elia, Iseult Lynch, Tommy Cedervall, and Kenneth A. Dawson. 2008. "Nanoparticle Size and Surface Properties Determine the Protein Corona with Possible Implications for Biological Impacts." *Proceedings of the National Academy of Sciences of the United States of America* 105 (38): 14265–70. https://doi.org/10.1073/pnas.0805135105.

Luther, Eva M., Maike M. Schmidt, Joerg Diendorf, Matthias Epple, and Ralf Dringen. 2012. "Upregulation of Metallothioneins after Exposure of Cultured Primary Astrocytes to Silver Nanoparticles." *Neurochemical Research* 37 (8): 1639–48. https://doi.org/10.1007/s11064-012-0767-4.

Ma, Zhifang, Jing Bai, and Xiue Jiang. 2015. "Monitoring of the Enzymatic Degradation of Protein Corona and Evaluating the Accompanying Cytotoxicity of Nanoparticles." *ACS Applied Materials & Interfaces* 7 (32): 17614–22. https://doi.org/10.1021/acsami.5b05744.

Madlova, M., S. A. Jones, I. Zwerschke, Y. Ma, R. C. Hider, and B. Forbes. 2009. "Poly(Vinyl Alcohol) Nanoparticle Stability in Biological Media and Uptake in Respiratory Epithelial Cell Layers in Vitro." *European Journal of Pharmaceutics and Biopharmaceutics* 72 (2): 438–43. https://doi.org/10.1016/j.ejpb.2009.01.009.

Mailliard, William S., Harry T. Haigler, and David D. Schlaepfer. 1996. “Calcium-Dependent Binding of S100C to the N-Terminal Domain of Annexin I.” *Journal of Biological Chemistry* 271 (2): 719–25. https://doi.org/10.1074/jbc.271.2.719.

Maiorano, Gabriele, Stefania Sabella, Barbara Sorce, Virgilio Brunetti, Maria Ada Malvindi, Roberto Cingolani, and Pier Paolo Pompa. 2010. “Effects of Cell Culture Media on the Dynamic Formation of Protein-Nanoparticle Complexes and Influence on the Cellular Response.” *ACS Nano* 4 (12): 7481–91. https://doi.org/10.1021/nn101557e.

Majorek, Karolina A., Przemyslaw J. Porebski, Arjun Dayal, Matthew D. Zimmerman, Kamila Jablonska, Alan J. Stewart, Maksymilian Chruszcz, and Wladek Minor. 2012. “Structural and Immunologic Characterization of Bovine, Horse, and Rabbit Serum Albumins.” *Molecular Immunology* 52 (3–4): 174–82. https://doi.org/10.1016/j.molimm.2012.05.011.

Mathé, Christelle, Stéphanie Devineau, Jean-Christophe Christophe Aude, Gilles Lagniel, Stéphane Chédin, Véronique Legros, Marie-Hélène Hélène Mathon, et al. 2013. “Structural Determinants for Protein Adsorption/Non-Adsorption to Silica Surface.” *PLoS ONE* 8 (11): 1–13. https://doi.org/10.1371/journal.pone.0081346.

Mathias, Neil R., Julita Timoszyk, Paul I. Stetsko, John R. Megill, Ronald L. Smith, and Doris A. Wall. 2002. “Permeability Characteristics of Calu-3 Human Bronchial Epithelial Cells: In Vitro-in Vitro Correlation to Predict Lung Absorption in Rats.” *Journal of Drug Targeting* 10 (1): 31–40. https://doi.org/10.1080/10611860290007504.

McDonald, Braedon, and Paul Kubes. 2015. “Interactions between CD44 and Hyaluronan in Leukocyte Trafficking.” *Frontiers in Immunology* 0 (FEB): 68. https://doi.org/10.3389/FIMMU.2015.00068.

Meyer, Megan, and Ilona Jaspers. 2015. “Respiratory Protease/Antiprotease Balance Determines Susceptibility to Viral Infection and Can Be Modified by Nutritional Antioxidants.” *J Physiol Lung Cell Mol Physiol* 308: 1189–1201. https://doi.org/10.1152/ajplung.00028.2015.-The.

Milani, Silvia, Francesca Baldelli Bombelli, Andrzej S. Pitek, Kenneth A. Dawson, and Joachim Rädler. 2012. “Reversible versus Irreversible Binding of Transferrin to Polystyrene Nanoparticles: Soft and Hard Corona.” *ACS Nano* 6 (3): 2532–41. https://doi.org/10.1021/nn204951s.

Monopoli, Marco P., Christoffer Åberg, Anna Salvati, and Kenneth A. Dawson. 2012. “Biomolecular Coronas Provide the Biological Identity of Nanosized Materials.” *Nature Nanotechnology*. https://doi.org/10.1038/nnano.2012.207.

Monopoli, Marco P., Dorota Walczyk, Abigail Campbell, Giuliano Elia, Iseult Lynch, Francesca Baldelli Bombelli, and Kenneth A. Dawson. 2011. “Physical-Chemical Aspects of Protein Corona: Relevance to in Vitro and in Vivo Biological Impacts of Nanoparticles.” *Journal of the American Chemical Society* 133 (8): 2525–34. https://doi.org/10.1021/ja107583h.

MONOPOLI, MARCO P., SHA WAN, FRANCESCA BALDELLI BOMBELLI, EUGENE MAHON, and KENNETH A. DAWSON. 2013. “COMPARISONS OF NANOPARTICLE PROTEIN CORONA COMPLEXES ISOLATED WITH DIFFERENT METHODS.” *Nano LIFE* 03 (04): 1343004. https://doi.org/10.1142/S1793984413430046.

Monopoli, Marco P, Andrzej S. Pitek, Iseult Lynch, and Kenneth A. Dawson. 2013. “Formation and Characterization of the Nanoparticle–Protein Corona.” In *Methods in Molecular*

Biology (Clifton, N.J.), 1025:137–55. https://doi.org/10.1007/978-1-62703-462-3_11.

Morgenroth, Konrad, and Michael Ebsen. 2008. “Anatomy.” *Mechanical Ventilation: Clinical Applications and Pathophysiology*, 69–85. https://doi.org/10.1016/B978-0-7216-0186-1.50012-0.

Moustaoui, Hanane, Justine Saber, Ines Djeddi, Qiqian Liu, Dania Movia, Adriele Prina-Mello, Jolanda Spadavecchia, Marc Lamy De La Chapelle, and Nadia Djaker. 2019. “A Protein Corona Study by Scattering Correlation Spectroscopy: A Comparative Study between Spherical and Urchin-Shaped Gold Nanoparticles.” *Nanoscale* 11 (8): 3665–73. https://doi.org/10.1039/c8nr09891c.

Mülhopt, Sonja, Marco Dilger, Silvia Diabaté, Christoph Schlager, Tobias Krebs, Ralf Zimmermann, Jeroen Buters, et al. 2016. “Toxicity Testing of Combustion Aerosols at the Air-Liquid Interface with a Self-Contained and Easy-to-Use Exposure System.” *Journal of Aerosol Science* 96: 38–55. https://doi.org/10.1016/j.jaerosci.2016.02.005.

Mura, Simona, Hervé Herve Hillaireau, Julien Nicolas, Saadia Kerdine-ro, Benjamin Le Droumaguet, Claudine Delome, Saadia Kerdine-Römer, et al. 2011. “Biodegradable Nanoparticles Meet the Bronchial Airway Barrier: How Surface Properties Affect Their Interaction with Mucus and Epithelial Cells.” *Biomacromolecules* 12 (11): 4136–43. https://doi.org/10.1021/bm201226x.

Netsomboon, Kesinee, and Andreas Bernkop-Schnürch. 2016. “Mucoadhesive vs. Mucopenetrating Particulate Drug Delivery.” *European Journal of Pharmaceutics and Biopharmaceutics* 98: 76–89. https://doi.org/10.1016/j.ejpb.2015.11.003.

Noguchi, Masafumi, Kana T Furukawa, and Mitsuru Morimoto. 2021. “Pulmonary Neuroendocrine Cells: Physiology, Tissue Homeostasis and Disease.” *DMM Disease Models and Mechanisms*. https://doi.org/10.1242/DMM.046920.

Oberdörster, Günter, Eva Oberdörster, and Jan Oberdörster. 2005. “Nanotoxicology: An Emerging Discipline Evolving from Studies of Ultrafine Particles.” *Environmental Health Perspectives* 113 (7): 823–39. https://doi.org/10.1289/ehp.7339.

Opdenakker, Ghislain, Philippe E. Van Den Steen, and Jo Van Damme. 2001. “Gelatinase B: A Tuner and Amplifier of Immune Functions.” *Trends in Immunology* 22 (10): 571–79. https://doi.org/10.1016/S1471-4906(01)02023-3.

Panas, A., C. Marquardt, O. Nalcaci, H. Bockhorn, W. Baumann, H.-R. Paur, S. Mülhopt, S. Diabaté, and C. Weiss. 2013. “Screening of Different Metal Oxide Nanoparticles Reveals Selective Toxicity and Inflammatory Potential of Silica Nanoparticles in Lung Epithelial Cells and Macrophages.” *Https://Doi.Org/10.3109/17435390.2011.652206* 7 (3): 259–73. https://doi.org/10.3109/17435390.2011.652206.

Park, Sung Jean. 2020. “Protein–Nanoparticle Interaction: Corona Formation and Conformational Changes in Proteins on Nanoparticles.” *International Journal of Nanomedicine* 15: 5783–5802. https://doi.org/10.2147/IJN.S254808.

Patel, Jignesh, Dhananjay Pal, Veena Vangala, Mohit Gandhi, and Ashim K. Mitra. 2002. “Transport of HIV-Protease Inhibitors across 1α,25di-Hydroxy Vitamin D3-Treated Calu-3 Cell Monolayers: Modulation of p-Glycoprotein Activity.” *Pharmaceutical Research* 19 (11): 1696–1703. https://doi.org/10.1023/A:1020761514471.

Patwa, Apeksh, and Amit Shah. 2015. “Anatomy and Physiology of Respiratory System Relevant to Anaesthesia.” *Indian Journal of Anaesthesia* 59 (9): 533–41. https://doi.org/10.4103/0019-5049.165849.

Pazos, Patricia, Monica Boveri, Alessandra Gennari, Juan Casado, Fernando Fernandez, and Pilar Prieto. 2004. “Culturing Cells without Serum: Lessons Learnt Using Molecules of Plant Origin.” *Altex* 21 (2): 67–72.

Pierce, R. J., and C. J. Worsnop. 1999. “Upper Airway Function and Dysfunction in Respiration.” *Clinical and Experimental Pharmacology and Physiology* 26 (1): 1–10. https://doi.org/10.1046/j.1440-1681.1999.02988.x.

Pisani, C., J. C. Gaillard, Christophe Dorandeu, Clarence Charnay, Y. Guari, J. Chopineau, J. M. Devoisselle, J. Armengaud, and O. Prat. 2017. “Experimental Separation Steps Influence the Protein Content of Corona around Mesoporous Silica Nanoparticles.” *Nanoscale* 9 (18): 5769–72. https://doi.org/10.1039/C7NR01654A.

Pisani, Cédric, Jean-Charles Gaillard, Michaël Odorico, Jeff L. Nyalosaso, Clarence Charnay, Yannick Guari, Joël Chopineau, Jean-Marie Devoisselle, Jean Armengaud, and Odette Prat. 2017. “The Timeline of Corona Formation around Silica Nanocarriers Highlights the Role of the Protein Interactome.” *Nanoscale* 9 (5): 1840–51. https://doi.org/10.1039/c6nr04765c.

Pisani, Cédric, Estelle Rascol, Christophe Dorandeu, Jean Charles Gaillard, Clarence Charnay, Yannick Guari, Joël Chopineau, Jean Armengaud, Jean Marie Devoisselle, and Odette Prat. 2017. “The Species Origin of the Serum in the Culture Medium Influences the in Vitro Toxicity of Silica Nanoparticles to HepG2 Cells.” Edited by Valentin Ceña. *PLoS ONE* 12 (8): e0182906. https://doi.org/10.1371/journal.pone.0182906.

Progress, Medical, John V. Fahy, and Burton F. Dickey. 2010. “Airway Mucus Function and Dysfunction.” *New England Journal of Medicine* 363 (23): 2233–47. https://doi.org/10.1056/nejmra0910061.

Raesch, Simon Sebastian, Stefan Tenzer, Wiebke Storck, Alexander Rurainski, Dominik Selzer, Christian Arnold Ruge, Jesus Perez-gil, Ulrich Friedrich Schaefer, and Claus-michael Michael Lehr. 2015. “Proteomic and Lipidomic Analysis of Nanoparticle Corona upon Contact with Lung Surfactant Reveals Differences in Protein, but Not Lipid Composition.” *ACS Nano* 9 (12): 11872–85. https://doi.org/10.1021/acsnano.5b04215.

Raj, Silpa, Shoma Jose, U. S. Sumod, and M. Sabitha. 2012. “Nanotechnology in Cosmetics: Opportunities and Challenges.” *Journal of Pharmacy and Bioallied Sciences* 4 (3): 186–93. https://doi.org/10.4103/0975-7406.99016.

Ramezani, Fatemeh, and Hashem Rafii-Tabar. 2015. “An In-Depth View of Human Serum Albumin Corona on Gold Nanoparticles.” *Molecular BioSystems* 11 (2): 454–62. https://doi.org/10.1039/c4mb00591k.

Rauch, Caroline, Elisabeth Feifel, Eva Maria Amann, Hans Peter Spötl, Harald Schennach, Walter Pfaller, and Gerhard Gstraunthaler. 2011. “Alternatives to the Use of Fetal Bovine Serum: Human Platelet Lysates as a Serum Substitute in Cell Culture Media.” *Altex* 28 (4): 305–16. https://doi.org/10.14573/altex.2011.4.305.

Rawlins, Emma L., Tadashi Okubo, Yan Xue, David M. Brass, Richard L. Auten, Hiroshi Hasegawa, Fan Wang, and Brigid L.M. Hogan. 2009. “The Role of Scgb1a1+ Clara Cells in the Long-Term Maintenance and Repair of Lung Airway, but Not Alveolar, Epithelium.” *Cell Stem Cell* 4 (6): 525–34. https://doi.org/10.1016/j.stem.2009.04.002.

Rayner, Rachael E, Patrudu Makena, Gaddamanugu L Prasad, and Estelle Cormet-boyaka. 2019. “Optimization of Normal Human Bronchial Epithelial (NHBE) Cell 3D Cultures for in Vitro Lung Model Studies,” no. November 2018: 2–11.

https://doi.org/10.1038/s41598-018-36735-z.

Rejman, Joanna, Volker Oberle, Inge S. Zuhorn, and Dick Hoekstra. 2004. “Size-Dependent Internalization of Particles via the Pathways of Clathrin-and Caveolae-Mediated Endocytosis.” *Biochemical Journal* 377 (1): 159–69. https://doi.org/10.1042/BJ20031253.

Reynolds, Susan D, and Alvin M Malkinson. 2010. “Clara Cell: Progenitor for the Bronchiolar Epithelium.” *The International Journal of Biochemistry & Cell Biology* 42: 1–4. https://doi.org/10.1016/j.biocel.2009.09.002.

Richards, Daniel A., Michael R. Thomas, Peter A. Szijj, James Foote, Yiyun Chen, João C.F. Nogueira, Vijay Chudasama, and Molly M. Stevens. 2021. “Employing Defined Bioconjugates to Generate Chemically Functionalised Gold Nanoparticles for: In Vitro Diagnostic Applications.” *Nanoscale* 13 (27): 11921–31. https://doi.org/10.1039/d1nr02584h.

Ridley, Caroline, and David J Thornton. 2018. “Mucins : The Frontline Defence of the Lung” 0: 1–8.

Riese, Richard J., Paula R. Wolf, Dieter Brömme, Lisa R. Natkin, José A. Villadangos, Hidde L. Ploegh, and Harold A. Chapman. 1996. “Essential Role for Cathepsin S in MHC Class II-Associated Invariant Chain Processing and Peptide Loading.” *Immunity* 4 (4): 357–66. https://doi.org/10.1016/S1074-7613(00)80249-6.

Ritz, Sandra, Susanne Schöttler, Niklas Kotman, Grit Baier, Anna Musyanovych, Jörg Kuharev, Katharina Landfester, et al. 2015. “Protein Corona of Nanoparticles: Distinct Proteins Regulate the Cellular Uptake.” *Biomacromolecules* 16 (4): 1311–21. https://doi.org/10.1021/acs.biomac.5b00108.

Rogers, Duncan F. 2003. “The Airway Goblet Cell.” *International Journal of Biochemistry and Cell Biology* 35 (1): 1–6. https://doi.org/10.1016/S1357-2725(02)00083-3.

Rose, Mary Callaghan, William S. Lynn, and Bernard Kaufman. 1979. “Resolution of the Major Components of Human Lung Mucosal Gel and Their Capabilities for Reaggregation and Gel Formation.” *Biochemistry* 18 (18): 4030–37. https://doi.org/10.1021/bi00585a029.

Rothen-Rutishauser, Barbara, Fabian Blank, Christian Mühlfeld, and Peter Gehr. 2008. “In Vitro Models of the Human Epithelial Airway Barrier to Study the Toxic Potential of Particulate Matter.” *Expert Opinion on Drug Metabolism and Toxicology* 4 (8): 1075–89. https://doi.org/10.1517/17425255.4.8.1075.

Rothen-Rutishauser, Barbara M, Stephen C. Kiama, and Peter Gehr. 2005. “A Three-Dimensional Cellular Model of the Human Respiratory Tract to Study the Interaction with Particles.” *American Journal of Respiratory Cell and Molecular Biology* 32 (4): 281–89. https://doi.org/10.1165/rcmb.2004-0187OC.

Sachyani, Dana, Meidan Dvir, Roi Strulovich, Giancarlo Tria, William Tobelaim, Asher Peretz, Olaf Pongs, Dmitri Svergun, Bernard Attali, and Joel A. Hirsch. 2014. “Structural Basis of a Kv7.1 Potassium Channel Gating Module: Studies of the Intracellular C-Terminal Domain in Complex with Calmodulin.” *Structure* 22 (11): 1582–94. https://doi.org/10.1016/j.str.2014.07.016.

Samuel, U., and J. P. Guggenbichler. 2004. “Prevention of Catheter-Related Infections: The Potential of a New Nano-Silver Impregnated Catheter.” *International Journal of Antimicrobial Agents* 23 (SUPPL. 1): 75–78. https://doi.org/10.1016/j.ijantimicag.2003.12.004.

Sanchez-Guzman, Daniel, Sonja Boland, Oliver Brookes, Claire Mc Cord, René Lai Kuen, Valentina Sirri, Armelle Baeza Squiban, and Stéphanie Devineau. 2021. “Long-Term Evolution of the Epithelial Cell Secretome in Preclinical 3D Models of the Human Bronchial Epithelium.” *Scientific Reports* 11 (1): 1–14. https://doi.org/10.1038/s41598-021-86037-0.

Sanchez-Guzman, Daniel, Gaël Giraudon--Colas, Laurent Marichal, Yves Boulard, Frank Wien, Jéril Degrouard, Armelle Baeza-Squiban, Serge Pin, Jean Philippe Renault, and Stéphanie Devineau. 2020. “ In Situ Analysis of Weakly Bound Proteins Reveals Molecular Basis of Soft Corona Formation .” *ACS Nano* 14 (7): 9073–88. https://doi.org/10.1021/acsnano.0c04165.

Sanchez-Guzman, Daniel, Pierre Le Guen, Berengere Villeret, Nuria Sola, Remi Le Borgne, Alice Guyard, Alix Kemmel, Bruno Crestani, Jean-Michel Michel Sallenave, and Ignacio Garcia-Verdugo. 2019. “Silver Nanoparticle-Adjuvanted Vaccine Protects against Lethal Influenza Infection through Inducing BALT and IgA-Mediated Mucosal Immunity.” *Biomaterials* 217. https://doi.org/10.1016/j.biomaterials.2019.119308.

Sarkar, Biplab, Suresh K. Verma, Javed Akhtar, Surya Prakash Netam, Sanjay Kr Gupta, Pritam Kumar Panda, and Koel Mukherjee. 2018. “Molecular Aspect of Silver Nanoparticles Regulated Embryonic Development in Zebrafish (Danio Rerio) by Oct-4 Expression.” *Chemosphere* 206: 560–67. https://doi.org/10.1016/j.chemosphere.2018.05.018.

Saxena, Ashish, Matthew S. Walters, Jae Hung Shieh, Ling Bo Shen, Kazunori Gomi, Robert J. Downey, Ronald G. Crystal, and Malcolm A.S. Moore. 2021. “Extracellular Vesicles from Human Airway Basal Cells Respond to Cigarette Smoke Extract and Affect Vascular Endothelial Cells.” *Scientific Reports* 11 (1). https://doi.org/10.1038/S41598-021-85534-6.

Serrano, Alicia G., and Jesús Pérez-Gil. 2006. “Protein-Lipid Interactions and Surface Activity in the Pulmonary Surfactant System.” *Chemistry and Physics of Lipids* 141 (1–2): 105–18. https://doi.org/10.1016/j.chemphyslip.2006.02.017.

Servin, Alia, Wade Elmer, Arnab Mukherjee, Roberto De la Torre-Roche, Helmi Hamdi, Jason C. White, Prem Bindraban, and Christian Dimkpa. 2015. “A Review of the Use of Engineered Nanomaterials to Suppress Plant Disease and Enhance Crop Yield.” *Journal of Nanoparticle Research* 17 (2): 1–21. https://doi.org/10.1007/s11051-015-2907-7.

Shaw, Catherine A, Gysell M. Mortimer, Zhou J Deng, Edwin S. Carter, Shea P Connell, Mark R Miller, Rodger Duffin, David E Newby, Patrick W.F. Hadoke, and Rodney F Minchin. 2016. “Protein Corona Formation in Bronchoalveolar Fluid Enhances Diesel Exhaust Nanoparticle Uptake and Pro-Inflammatory Responses in Macrophages.” *Nanotoxicology* 10 (7): 981–91. https://doi.org/10.3109/17435390.2016.1155672.

Shweiki, Mhd H.D.Rami Al, Susann Mönchgesang, Petra Majovsky, Domenika Thieme, Diana Trutschel, and Wolfgang Hoehenwarter. 2017. “Assessment of Label-Free Quantification in Discovery Proteomics and Impact of Technological Factors and Natural Variability of Protein Abundance.” *Journal of Proteome Research* 16 (4): 1410–24. https://doi.org/10.1021/acs.jproteome.6b00645.

Silva, Rona M., Donald S. Anderson, Lisa M. Franzi, Janice L. Peake, Patricia C. Edwards, Laura S. Van Winkle, and Kent E. Pinkerton. 2015. “Pulmonary Effects of Silver Nanoparticle Size, Coating, and Dose over Time upon Intratracheal Instillation.” *Toxicological Sciences* 144 (1): 151–62. https://doi.org/10.1093/toxsci/kfu265.

Singh, Surya, and Hari Singh Nalwa. 2007. “Nanotechnology and Health Safety - Toxicity and Risk Assessments of Nanostructured Materials on Human Health.” *Journal of*

Nanoscience and Nanotechnology 7 (9): 3048–70. https://doi.org/10.1166/jnn.2007.922.

Smith-Dupont, K B, C E Wagner, J Witten, K Conroy, H Rudoltz, K Pagidas, V Snegovskikh, M House, and K. Ribbeck. 2017. “Probing the Potential of Mucus Permeability to Signify Preterm Birth Risk.” *Scientific Reports* 7 (1). https://doi.org/10.1038/s41598-017-08057-z.

Stentebjerg-Andersen, Anna, Ingrid Vedsted Notlevsen, Birger Brodin, and Carsten Uhd Nielsen. 2011. “Calu-3 Cells Grown under AIC and LCC Conditions: Implications for Dipeptide Uptake and Transepithelial Transport of Substances.” *European Journal of Pharmaceutics and Biopharmaceutics* 78 (1): 19–26. https://doi.org/10.1016/j.ejpb.2010.12.030.

Stucki, Janick D, Nina Hobi, Artur Galimov, Andreas O Stucki, Nicole Schneider-Daum, Claus-Michael Lehr, Hanno Huwer, et al. 2018. “Medium Throughput Breathing Human Primary Cell Alveolus-on-Chip Model OPEN.” *SCIENTIfIC RepoRTS* | 8: 14359. https://doi.org/10.1038/s41598-018-32523-x.

Takeuchi, Hirofumi, Hiromitsu Yamamoto, and Yoshiaki Kawashima. 2001. “Mucoadhesive Nanoparticulate Systems for Peptide Drug Delivery.” *Advanced Drug Delivery Reviews* 47 (1): 39–54. https://doi.org/10.1016/S0169-409X(00)00120-4.

Tecle, Tesfaldet, Shweta Tripathi, and Kevan L Hartshorn. 2010. “Defensins and Cathelicidins in Lung Immunity.” *Innate Immunity*. https://doi.org/10.1177/1753425910365734.

Tenzer, Stefan, Dominic Docter, Jörg Kuharev, Anna Musyanovych, Verena Fetz, Rouven Hecht, Florian Schlenk, et al. 2013. “Rapid Formation of Plasma Protein Corona Critically Affects Nanoparticle Pathophysiology.” *Nature Nanotechnology* 8 (10): 772–81. https://doi.org/10.1038/nnano.2013.181.

Teodoro, João S., Anabela M. Simões, Filipe V. Duarte, Anabela P. Rolo, Richard C. Murdoch, Saber M. Hussain, and Carlos M. Palmeira. 2011. “Assessment of the Toxicity of Silver Nanoparticles in Vitro: A Mitochondrial Perspective.” *Toxicology in Vitro* 25 (3): 664–70. https://doi.org/10.1016/j.tiv.2011.01.004.

Tibbitt, Mark W., and Kristi S. Anseth. 2009. “Hydrogels as Extracellular Matrix Mimics for 3D Cell Culture.” *Biotechnology and Bioengineering* 103 (4): 655–63. https://doi.org/10.1002/bit.22361.

Tripathi, S., J. Batra, W. Cao, K. Sharma, J. R. Patel, P. Ranjan, A. Kumar, et al. 2013. “Influenza A Virus Nucleoprotein Induces Apoptosis in Human Airway Epithelial Cells: Implications of a Novel Interaction between Nucleoprotein and Host Protein Clusterin.” *Cell Death and Disease* 4 (3). https://doi.org/10.1038/cddis.2013.89.

Turner, Jonathan, and Carol E. E Jones. 2009. “Regulation of Mucin Expression in Respiratory Diseases.” *Biochemical Society Transactions* 37 (4): 877–81. https://doi.org/10.1042/BST0370877.

Tyanova, Stefka, Tikira Temu, Pavel Sinitcyn, Arthur Carlson, Marco Y. Hein, Tamar Geiger, Matthias Mann, and Jürgen Cox. 2016. “The Perseus Computational Platform for Comprehensive Analysis of (Prote)Omics Data.” *Nature Methods* 13 (9): 731–40. https://doi.org/10.1038/nmeth.3901.

Upadhyay, Swapna, and Lena Palmberg. 2018. “Air-Liquid Interface: Relevant in Vitro Models for Investigating Air Pollutant-Induced Pulmonary Toxicity.” *Toxicological Sciences*. https://doi.org/10.1093/toxsci/kfy053.

Vance, Marina E, Todd Kuiken, Eric P Vejerano, Sean P Mcginnis, Michael F Hochella, David

Rejeski, and Matthew S Hull. 2015. “Nanotechnology in the Real World: Redeveloping the Nanomaterial Consumer Products Inventory.” *Beilstein J. Nanotechnol* 6: 1769–80. https://doi.org/10.3762/bjnano.6.181.

Verma, Suresh K., Ealisha Jha, Pritam Kumar Panda, Arun Thirumurugan, Shubhransu Patro, S. K.S. Parashar, and Mrutyunjay Suar. 2018. “Molecular Insights to Alkaline Based Bio-Fabrication of Silver Nanoparticles for Inverse Cytotoxicity and Enhanced Antibacterial Activity.” *Materials Science and Engineering C* 92 (July): 807–18. https://doi.org/10.1016/j.msec.2018.07.037.

Voynow, Judith A, and Bruce K Rubin. 2009. “Mucins , Mucus , and Sputum CHEST Translating Basic Research Into Clinical Practice Mucins , Mucus , and Sputum *.” https://doi.org/10.1378/chest.08-0412.

Vranic, Sandra, Ilse Gosens, Nicklas Raun Jacobsen, Keld A. Jensen, Bas Bokkers, Ali Kermanizadeh, Vicki Stone, et al. 2017. “Impact of Serum as a Dispersion Agent for in Vitro and in Vivo Toxicological Assessments of TiO2 Nanoparticles.” *Archives of Toxicology* 91 (1): 353–63. https://doi.org/10.1007/s00204-016-1673-3.

Vranic, Sandra, Artur Filipe Rodrigues, Maurizio Buggio, Leon Newman, Michael R.H. White, David G. Spiller, Cyrill Bussy, and Kostas Kostarelos. 2018. “Live Imaging of Label-Free Graphene Oxide Reveals Critical Factors Causing Oxidative-Stress-Mediated Cellular Responses.” *ACS Nano*. https://doi.org/10.1021/acsnano.7b07734.

Vroman, L. 1962. “Effect of Adsorbed Proteins on the Wettability of Hydrophilic and Hydrophobic Solids.” *Nature* 196 (4853): 476–77. https://doi.org/10.1038/196476a0.

Vu, Vincent Q. 2011. “Ggbiplot: A Ggplot2 Based Biplot. R Package Version 0.55.” http://github.com/vqv/ggbiplot.

Wadhwa, Ridhima, Keshav Raj Paudel, Li Hian Chin, Chian Ming Hon, Thiagarajan Madheswaran, Gaurav Gupta, Jithendra Panneerselvam, et al. 2021. “Anti-Inflammatory and Anticancer Activities of Naringenin-Loaded Liquid Crystalline Nanoparticles in Vitro.” *Journal of Food Biochemistry* 45 (1): e13572. https://doi.org/10.1111/JFBC.13572.

Wagner, C E, K M Wheeler, and K Ribbeck. 2018. “Mucins and Their Role in Shaping the Functions of Mucus Barriers.”

Walkey, Carl D., and Warren C.W. Chan. 2012. “Understanding and Controlling the Interaction of Nanomaterials with Proteins in a Physiological Environment.” *Chemical Society Reviews* 41 (7): 2780–99. https://doi.org/10.1039/c1cs15233e.

Wallace, Louisa E., Mengying Liu, Frank J.M. van Kuppeveld, Erik de Vries, and Cornelis A.M. de Haan. 2021. “Respiratory Mucus as a Virus-Host Range Determinant.” *Trends in Microbiology*, 1–10. https://doi.org/10.1016/j.tim.2021.03.014.

Walters, Matthew S, Kazunori Gomi, Beth Ashbridge, Malcolm A S Moore, Vanessa Arbelaez, Jonna Heldrich, Bi-Sen Ding, Shahin Rafii, Michelle R Staudt, and Ronald G Crystal. 2013. “Generation of a Human Airway Epithelium Derived Basal Cell Line with Multipotent Differentiation Capacity.” http://www.mskcc.org/research/molecular-cytogenetics.

Wang, Zhe, Tian Xia, and Sijin Liu. 2015. “Mechanisms of Nanosilver-Induced Toxicological Effects: More Attention Should Be Paid to Its Sublethal Effects.” *Nanoscale* 7 (17): 7470–81. https://doi.org/10.1039/C5NR01133G.

Weber, Claudia, Svenja Morsbach, and Katharina Landfester. 2019. “Possibilities and

Limitations of Different Separation Techniques for the Analysis of the Protein Corona." *Angewandte Chemie - International Edition*. Wiley-VCH Verlag. https://doi.org/10.1002/anie.201902323.

Webster, Megan J., and Robert Tarran. 2018. *Slippery When Wet: Airway Surface Liquid Homeostasis and Mucus Hydration*. *Current Topics in Membranes*. Vol. 81. Elsevier Ltd. https://doi.org/10.1016/bs.ctm.2018.08.004.

Whitsett, Jeffrey A., and Theresa Alenghat. 2015. "Respiratory Epithelial Cells Orchestrate Pulmonary Innate Immunity." *Nature Immunology* 16 (1): 27–35. https://doi.org/10.1038/ni.3045.

Winzen, S., S. Schoettler, G. Baier, C. Rosenauer, V. Mailaender, K. Landfester, and K. Mohr. 2015. "Complementary Analysis of the Hard and Soft Protein Corona: Sample Preparation Critically Effects Corona Composition." *Nanoscale* 7 (7): 2992–3001. https://doi.org/10.1039/c4nr05982d.

Wu, Hong, Eric Santoni-Rugiu, Elisabeth Ralfkiaer, Bo T Porse, Claus Moser, Niels Høiby, Niels Borregaard, and Jack B Cowland. 2010. "Lipocalin 2 Is Protective against E. Coli Pneumonia." *Respiratory Research* 11: 96. https://doi.org/10.1186/1465-9921-11-96.

Xi, Wen-Song, Jia-Bei Li, Yuan-Yuan Liu, Hao Wu, Aoneng Cao, and Haifang Wang. 2021. "Cytotoxicity and Genotoxicity of Low-Dose Vanadium Dioxide Nanoparticles to Lung Cells Following Long-Term Exposure." *Toxicology* 459 (July): 152859. https://doi.org/10.1016/j.tox.2021.152859.

Xiao, Yansen, Min Cong, Jiatao Li, Dasa He, Qiuyao Wu, Pu Tian, Yuan Wang, et al. 2021. "Cathepsin C Promotes Breast Cancer Lung Metastasis by Modulating Neutrophil Infiltration and Neutrophil Extracellular Trap Formation." *Cancer Cell* 39 (3): 423-437.e7. https://doi.org/10.1016/j.ccell.2020.12.012.

Xu, Gang, Zhangchuan Xia, Feiyan Deng, Lin Liu, Qiming Wang, Yi Yu, Fubing Wang, et al. 2019. "Inducible LGALS3BP/90K Activates Antiviral Innate Immune Responses by Targeting TRAF6 and TRAF3 Complex." *PLoS Pathogens* 15 (8): 1–22. https://doi.org/10.1371/journal.ppat.1008002.

Yang, Ying Fei, Wei Ming Wang, Chi Yun Chen, Tien Hsuan Lu, and Chung Min Liao. 2019. "Assessing Human Exposure Risk and Lung Disease Burden Posed by Airborne Silver Nanoparticles Emitted by Consumer Spray Products." *International Journal of Nanomedicine* 14: 1687–1703. https://doi.org/10.2147/IJN.S171510.

Yonker, Lael M, Hongmei Mou, Kengyeh K Chu, Michael A Pazos, Huimin Leung, Dongyao Cui, Jinhyeob Ryu, et al. 2017. "Development of a Primary Human Co-Culture Model of Inflamed Airway Mucosa." *Scientific Reports* 7 (1). https://doi.org/10.1038/s41598-017-08567-w.

Yu, Chih-chieh, Jum-suk Ko, Tomohiko Ai, Wen-chin Tsai, Zhenhui Chen, Michael Rubart, Matteo Vatta, Thomas H Everett, Alfred L George, and Peng-sheng Chen. 2016. "Arrhythmogenic Calmodulin Mutations Impede Activation of Small-Conductance Calcium-Activated Potassium Current." *Heart Rhythm* 13 (8): 1716–23. https://doi.org/10.1016/j.hrthm.2016.05.009.

Zhang, Fan, Grace V. Aquino, Amjad Dabi, and Erica D. Bruce. 2019. "Assessing the Translocation of Silver Nanoparticles Using an in Vitro Co-Culture Model of Human Airway Barrier." *Toxicology in Vitro* 56 (December 2018): 1–9. https://doi.org/10.1016/j.tiv.2018.12.013.

Zhang, Ruijia, Hui Zhang, Baowei Chen, and Tiangang Luan. 2020. “Fetal Bovine Serum Attenuating Perfluorooctanoic Acid-Inducing Toxicity to Multiple Human Cell Lines via Albumin Binding.” *Journal of Hazardous Materials* 389 (January): 122109. https://doi.org/10.1016/j.jhazmat.2020.122109.

Zhang, Wanju, Qingbo Zhang, Fang Wang, Lian Yuan, Ziqiang Xu, Fenglei Jiang, and Yi Liu. 2015. “Comparison of Interactions between Human Serum Albumin and Silver Nanoparticles of Different Sizes Using Spectroscopic Methods.” *Luminescence* 30 (4): 397–404. https://doi.org/10.1002/bio.2748.

Zhang, Yu Shrike, Kan Yue, Julio Aleman, Kamyar Mollazadeh-Moghaddam, Syeda Mahwish Bakht, Jingzhou Yang, Weitao Jia, et al. 2017. “3D Bioprinting for Tissue and Organ Fabrication.” *Annals of Biomedical Engineering* 45 (1): 148–63. https://doi.org/10.1007/s10439-016-1612-8.

Zhu, Yan, Aaron Chidekel, and Thomas H. Shaffer. 2010. “Cultured Human Airway Epithelial Cells (Calu-3): A Model of Human Respiratory Function, Structure, and Inflammatory Responses.” *Critical Care Research and Practice* 2010: 1–8. https://doi.org/10.1155/2010/394578.

Zia, Fatima, Michaela Kendall, Steve P. Watson, and Paula M. Mendes. 2018. “Platelet Aggregation Induced by Polystyrene and Platinum Nanoparticles Is Dependent on Surface Area.” *RSC Advances* 8 (66): 37789–94. https://doi.org/10.1039/C8RA07315E.

Annex I

Sanchez-Guzman, Daniel, Sonja Boland, Oliver Brookes, Claire Mc Cord, René Lai Kuen, Valentina Sirri, Armelle Baeza Squiban, and Stéphanie Devineau.

Long-Term Evolution of the Epithelial Cell Secretome in Preclinical 3D Models of the Human Bronchial Epithelium

Scientific Reports 2021

DOI: https://doi.org/10.1038/s41598-021-86037-0

Data availability: PRIDE database repository-PXD024242 scientific reports

OPEN

Long-term evolution of the epithelial cell secretome in preclinical 3D models of the human bronchial epithelium

Daniel Sanchez-Guzman[1], Sonja Boland[1], Oliver Brookes[1], Claire Mc Cord[1], René Lai Kuen[2], Valentina Sirri[1], Armelle Baeza Squiban[1,3] & Stéphanie Devineau[1,3]✉

The human bronchial epithelium is the first line of defense against atmospheric particles, pollutants, and respiratory pathogens such as the novel SARS-CoV-2. The epithelial cells form a tight barrier and secrete proteins that are major components of the mucosal immune response. Functional in vitro models of the human lung are essential for screening the epithelial response and assessing the toxicity and barrier crossing of drugs, inhaled particles, and pollutants. However, there is a lack of models to investigate the effect of chronic exposure without resorting to animal testing. Here, we developed a 3D model of the human bronchial epithelium using Calu-3 cell line and demonstrated its viability and functionality for 21 days without subculturing. We investigated the effect of reduced Fetal Bovine Serum supplementation in the basal medium and defined the minimal supplementation needed to maintain a functional epithelium, so that the amount of exogenous serum proteins could be reduced during drug testing. The long-term evolution of the epithelial cell secretome was fully characterized by quantitative mass spectrometry in two preclinical models using Calu-3 or primary NHBE cells. 408 common secreted proteins were identified while significant differences in protein abundance were observed with time, suggesting that 7–10 days are necessary to establish a mature secretome in the Calu-3 model. The associated Reactome pathways highlight the role of the secreted proteins in the immune response of the bronchial epithelium. We suggest this preclinical 3D model can be used to evaluate the long-term toxicity of drugs or particles on the human bronchial epithelium, and subsequently to investigate their effect on the epithelial cell secretions.

With a daily inhaled volume of 10 m^3 per individual, the respiratory tract is the main route of exposure to atmospheric particles, pollutants, and respiratory pathogens. The epithelia that line the respiratory tract are covered by lung lining fluid, consisting of mucus in the upper airways and surfactant in the alveoli, which exhibits mechanical, antimicrobial, and antioxidant functions to protect the epithelium[1]. The inhalation of exogenous compounds (drugs, atmospheric particles, pollutants) or pathogens (bacteria, viruses) can induce pro-inflammatory epithelial response, release of danger signals to the immune system, cell migration, and cell death[2,3]. The agent can also translocate through the intact or damaged epithelial barrier causing potential systemic effects[4,5].

The toxicological assessment of drugs and particles following exposure by inhalation has long relied on in vivo studies[6,7]. However, the limited number of compounds that can be tested, the interspecies variability, the associated cost and ethical concerns have supported the development of alternative in vitro models of the human upper and lower airways[8–10]. Functional bronchial epithelium models were developed to investigate the toxicity and translocation of various agents[11,12]. These models have greatly promoted our understanding of the epithelial response and supported the identification of the adverse outcome pathways of toxic compounds.

The available models of the human bronchial epithelium using cell lines can be used to study acute toxicity following short-term exposure, usually 24 or 48 h[13,14]. However there is a lack of functional models to investigate the long-term toxicity of drugs or pollutants following chronic exposure or repeated exposure at low doses. The difficulties associated with long-term cell cultures (without subculturing) are decreased cell viability, divergence and changes in cellular features, and stratification due to continuous proliferation. The development of in vitro

[1]Université de Paris, BFA, UMR 8251, CNRS, 75013 Paris, France. [2]Cellular and Molecular Imaging Facility, US25 Inserm-3612 CNRS, Faculté de Pharmacie de Paris, Université de Paris, Paris, France. [3]These authors contributed equally: Armelle Baeza Squiban and Stéphanie Devineau. ✉email: stephanie.devineau@u-paris.fr

https://doi.org/10.1038/s41598-021-86037-0

lung models to investigate the chronic toxicity of exogenous agents by inhalation is therefore a key step in the field of predictive toxicology.

Primary normal human bronchial epithelial (NHBE) cells collected from healthy donors are commercially available. NHBE cells can be cultured on porous membranes (inserts) at the air liquid interface (ALI), which leads to their differentiation into a mucociliary epithelium after 3–4 weeks. Composed of epithelial cells, including ciliated and goblet cells, these cultures can be maintained for several weeks at ALI with minor modifications[15]. They represent one of the best options to evaluate the long-term effect of a compound on the bronchial epithelium. However, high cost, low rate of cell expansion before differentiation, time required to establish a stable differentiated epithelium, and donor variability, limit their use for high throughput toxicological screening[16,17].

The human Calu-3 lung adenocarcinoma cell line (ATCC HTB-55) is an interesting alternative to primary cells for the development of robust and low-cost models of the human bronchial epithelium for toxicological assessment. The Calu-3 cells differentiate into a functional tight epithelium when cultured on inserts at ALI. Even though the resulting epithelium is limited to one cell type, it exhibits features specific to the human bronchial epithelium such as a tight epithelial barrier, mucus secretion, receptor expression, and cytokine production among others[9,18–23]. Expert panels and pre-validation assays have put forward the Calu-3 model of the bronchial epithelium for drug screening[24–26]. Readers may refer to reviews for more details about this cell line[25,27–29]. Other lung cell lines could be used as in vitro models, such as the epithelial BEAS-2B, NCI-H292, and 16HBE cell lines[30–32]. Contrary to BEAS-2B, NCI-H292, and 16HBE, the Calu-3 cell line can simultaneously form a tight epithelium at ALI and secrete mucus[33]. Hence, we selected the Calu-3 cell line for this study.

The mucus secreted by airway epithelial cells plays a key role in the protection against and clearance of particles and pathogens[34]. Secreted proteins in the mucus are involved in the cell-to-cell communication and the mucosal immune response[35]. Changes in cell secretions are associated with pulmonary diseases including COPD, asthma, and lung cancers[36,37]. However, little is known about the evolution of the epithelial cell secretion with time, especially for long periods (2–4 weeks) studied in the context of chronic toxicity studies. In addition, the drug or the inhaled particles may alter the epithelial cell secretion profiles, which is an important element of the epithelium response[38].

Here, we developed a 3D model of the human bronchial epithelium using Calu-3 cells and investigated its viability, morphology, and functionality for 21 days following differentiation at ALI. Barrier function of the epithelium, protein secretion, and the composition of the apical secretome were monitored over time in the Calu-3 model of the bronchial epithelium. Reduced FBS (fetal bovine serum) supplementation was tested in the basal medium in long-term cell cultures. Minimizing the intake of exogenous proteins is important for the long-term toxicological study of both drugs and particles. FBS is composed of more than 1800 proteins and 4000 metabolites with high batch-to-batch variability[39]. Some drugs can form complexes with serum protein, which changes their bioavailability. Nanoparticles are prone to adsorb proteins on their surface, forming a so-called protein corona that drives cell-nanoparticle interactions[40,41], an effect that is amplified when cells and serum from different species are used[42]. A minimal FBS supplementation of 4% was defined for long-term cell cultures in our Calu-3 model.

The epithelial cell secretions of models based on Calu-3 and on primary NHBE cells from three healthy donors were characterized from 4 to 18 days at ALI by quantitative mass spectrometry. We observed that the same proteins were secreted in both models, albeit with differences in abundance with time and between models. The time evolution of the secretome of the Calu-3 cells shows that a stable and mature secretome was established after 7–10 days at ALI. The Reactome pathway analysis of the Calu-3 and NHBE secretome highlighted the role of the secreted proteins in the mucosal immune response in vitro. We suggest this pre-clinical model can be used to evaluate the chronic toxicity of drugs, particles or pollutants following single or repeated exposure by inhalation, and to investigate their effect on the epithelial cell secretions.

Results

Long-term cultures of Calu-3 cells at the air–liquid interface with minimal FBS supplementation.

First, we developed a protocol to establish a long-term culture of Calu-3 cells at the air–liquid interface (Fig. 1a). Calu-3 cells were grown on Transwell inserts with a 3 µm pore diameter with MEM supplemented with 10% FBS in both the apical and basal compartments (submerged conditions). We did not observe any cell migration through the pores, nor cell growth on the basal side of the insert membrane. The cultures were maintained in submerged conditions for approximately 7 days until a TEER ≥ 700 Ω cm^2 was obtained, corresponding to a confluent culture. Calu-3 differentiation was initiated by changing culture conditions from submerged to ALI by removing the apical medium, without addition of any inducer. One day after ALI, the basal medium was replaced with MEM containing 0–8% FBS corresponding to our experimental conditions. We used these conditions to determine the effect of FBS concentration on the viability and functionality of the human bronchial epithelium in our 3D model for a 4-week period. The objective was to define the minimal FBS supplementation needed to maintain a functional epithelium over a 4-week period so that the amount of exogenous serum proteins could be reduced during drug testing.

The formation of the epithelial barrier was monitored by measuring the trans-epithelial electrical resistance (TEER) before ALI and for a 4-week period (Fig. 1b). The TEER increases with the formation of tight junctions, which leads to a reduction in paracellular ion/electron transport. A TEER > 300 Ω cm^2 is associated with a tight epithelium at ALI[43]. We observed an increase of the TEER with a maximum value of 940 ± 69 Ω cm^2 at day 7 in submerged conditions. At day 8 (day 1 after ALI), the TEER decreased to 682 ± 76 Ω cm^2. A TEER > 300 Ω cm^2 was maintained for at least 18 days after establishing ALI (corresponding to a total number of 25 days in culture) (Figs. 1b, S1). Interestingly, a TEER equal or higher to this minimal value was measured even without any FBS in the basal medium. The highest TEER value was observed with 2% FBS. Similar values were measured with

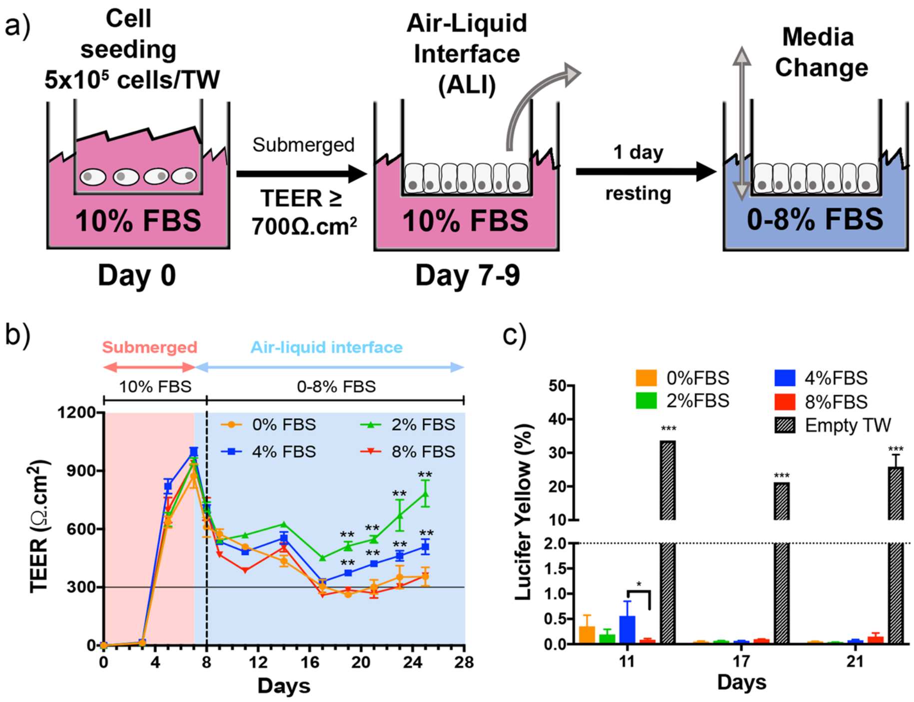

Figure 1. Development of a 3D model of the human bronchial epithelial using Calu-3 cells for long-term toxicity studies. (**a**) Schematic of the experimental protocol to establish long-term cultures of Calu-3 cells. Cells were grown on Transwell inserts with a 3-μm pore diameter. Cell differentiation was induced by changing culture conditions from submerged to ALI. The barrier integrity of the epithelium was assessed by the measurement of the trans-epithelial electrical resistance (TEER) and the paracellular permeability (Lucifer Yellow (LY) permeability assay). (**b**) Evolution of the TEER for 21 days in a representative experiment (n = 3). A TEER > 300 Ω cm^2 (horizontal line) is associated with a tight epithelium (n = 3). (**c**) Measurement of the paracellular permeability with the LY assay at 11, 17, and 21 days. An empty Transwell insert was used as a negative control. A LY permeability < 2% (dotted line) is associated with a tight epithelium (n = 3). Significant differences between conditions (FBS %) *P < 0.01. **P < 0.05, ***P < 0.001.

0, 4, and 8% FBS. These results show that a decrease of FBS percentage in the basal medium does not alter the barrier integrity of the bronchial epithelium in long-term cultures. We monitored the TEER of two additional Calu-3 models prepared at different cell passages to check for the variability of the TEER measurement in Calu-3 cultures (Fig. S1). The three biological replicates shown in Fig. S1 correspond to Calu-3 cells thawed and cultured independently on different days. Similar results were obtained with a TEER > 300 Ω cm^2 in all the experiments up to 21 days after ALI.

The paracellular permeability of the epithelium was measured using the Lucifer Yellow (LY) permeability assay to confirm the TEER results (Fig. 1c). A LY permeability < 2% was measured in all conditions, confirming the integrity of the bronchial epithelium for 21 days with reduced FBS supplementation in the basal medium. We compared the TEER measurement and LY permeability of 236 different samples with tight or damaged epithelial barrier (Fig. S2). This broad analysis confirmed the minimal TEER value of 300 Ω cm^2 defined for a tight epithelium in our experimental conditions. Therefore, the variations of the TEER above this limit (e.g. between 300 and 800 Ω cm^2) do not reflect alteration in the barrier function of the epithelium. Higher values may be due to differences in the epithelium thickness or in ion secretion[28]. The EdU (5-ethynyl-2′-deoxyuridine) cell proliferation assay confirmed that Calu-3 cells can proliferate with reduced FBS supplementation in the basal medium (Fig. S3).

Then, we studied the effect of reduced FBS supplementation on protein secretion by epithelial cells for 17 days at ALI. The total protein and glycoprotein concentrations of the apical secretome of the Calu-3 cells were measured at day 3, 10, and 17 after ALI (Fig. 2a,b). The apical secretome was collected every 2 days in this experiment to avoid bias due to protein accumulation. We observed a significant increase in protein secretion both with time and with FBS percentage (Fig. 2a). This result may reflect an increasing metabolic activity of Calu-3 cells at ALI with time, and a reduced metabolic activity when cells have a lower FBS supply. However, a different trend was observed when looking at glycoproteins specifically, among which mucins would be the most abundant. The glycoprotein concentration was normalized to the total protein concentration at each day. A steady normalized glycoprotein concentration was measured over time for the 2, 4, 8% FBS conditions, while a significant increase was observed without supplementation (Fig. 2b). This result indicates that glycoprotein secretion by the epithelial cells is stable once the epithelial barrier is well established for cells cultured with reduced FBS supplementation, while a lack of FBS induces hypersecretion of glycoproteins by Calu-3 cells at ALI.

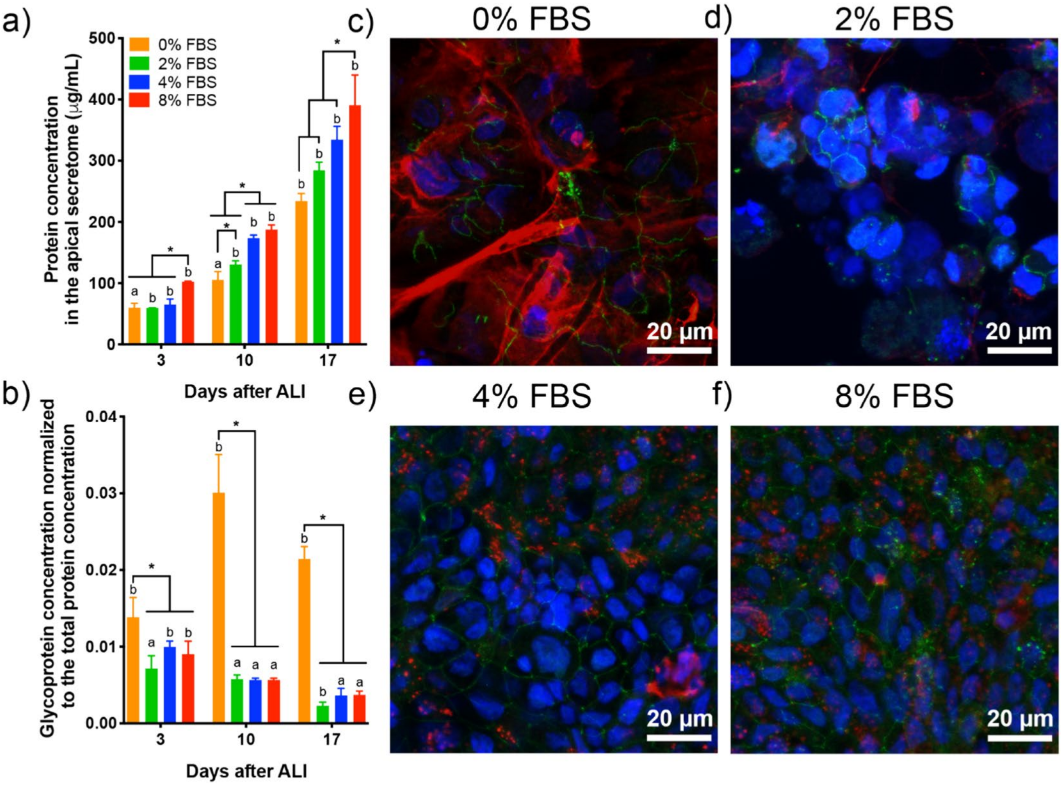

Figure 2. Effect of lower FBS supplementation on the apical secretion by Calu-3 cells in long-term cultures. (**a**) Total protein and (**b**) glycoprotein concentration in the apical secretome of Calu-3 cells supplemented with 0, 2, 4, 8% FBS at day 3, 10 and 17 after ALI. The glycoprotein concentration was normalized to the total protein concentration. (**c**–**f**) Immunolabelling of ZO-1 (green) and MUC5AC (red) in DAPI-stained Calu-3 cells at day 17 after ALI. The cell cultures were supplemented with 0 (**c**), 2 (**d**), 4 (**e**), and 8% FBS. Each image is the z-projection of 10 slides. (n = 3) $^{*}P < 0.01$ ^{a,b}statistically different between days.

To determine whether glycoprotein secretion included mucin secretion in the apical secretome, immunolabelling and confocal microscopy imaging of the gel-forming mucin MUC5AC and the tight-junction associated protein zonula occludens-1 (ZO-1) was performed on Calu-3 cells 17 days after ALI (Fig. 2c–f). MUC5AC staining appears as small dots distributed in the apical region of the cell for the 0, 2, 4, 8% FBS conditions, confirming mucus secretion in long-term Calu-3 cell cultures at ALI. Mucus secretion is usually partially or totally lost during the washes in the cell fixation protocol. Similar MUC5AC staining was observed with 4 and 8% FBS supplementation. ZO-1 staining confirmed the presence of tight junction in long-term Calu-3 cultures, making them a good model of the human bronchial epithelium for chronic toxicity studies with reduced FBS supplementation.

A distinct MUC5AC staining was observed in the case of Calu-3 cells cultured without FBS. Large patches of MUC5AC were visible on the epithelium surface, forming thick mucus filaments. The hypersecretion of mucin was confirmed by qRT-PCR with the up-regulation of *muc5ac* in Calu-3 cells deprived of FBS compared to cells cultured with 10% FBS in the basal medium (Fig. S4). Up-regulation of serum albumin (*alb*) and the tight junction associated protein, zonula occludens-1 (*zo1*), was also observed. Surprisingly, significant down-regulation of *muc5b* was seen in Calu-3 cells supplemented with 2% FBS, while no change occurred at 0% suggesting that mucus hypersecretion was mediated by MUC5AC in conditions without FBS. This feature is reminiscent of mucus hypersecretion described in respiratory diseases, including asthma, COPD, and lung cancers[44–46]. In our model, the hypersecretion of MUC5AC by Calu-3 cells, derived from a lung adenocarcinoma, was induced by deprivation of any FBS supplementation only, while no visible over-production of MUC5AC was observed in long-term cell cultures with reduced FBS supplementation (Fig. 2).

We observed that Calu-3 cells could be maintained for 18 days at ALI with reduced FBS supplementation. With 4% FBS supplementation in the basal medium, Calu-3 cells exhibit good functionality and viability, as evidenced by the TEER measurement, the LY permeability assay, the analysis of the protein secretion, and MUC5AC immunolabelling. Transmission electron microscopy images of the bronchial epithelium formed by Calu-3 cells cultured with a reduced FBS supplementation of 4% are shown 8 days after ALI in Fig. S5. Calu-3 cells formed an epithelium monolayer with visible tight junctions and a high number of secretory vesicles in some cells[33]. The release of mucus vesicles (or granules) at the apical side of the epithelium was also observed (Fig. S5e). Based on these observations, we chose a minimal FBS supplementation of 4% to characterize the epithelial cell secretions in a 3D model of the human bronchial epithelium in the second part of this study.

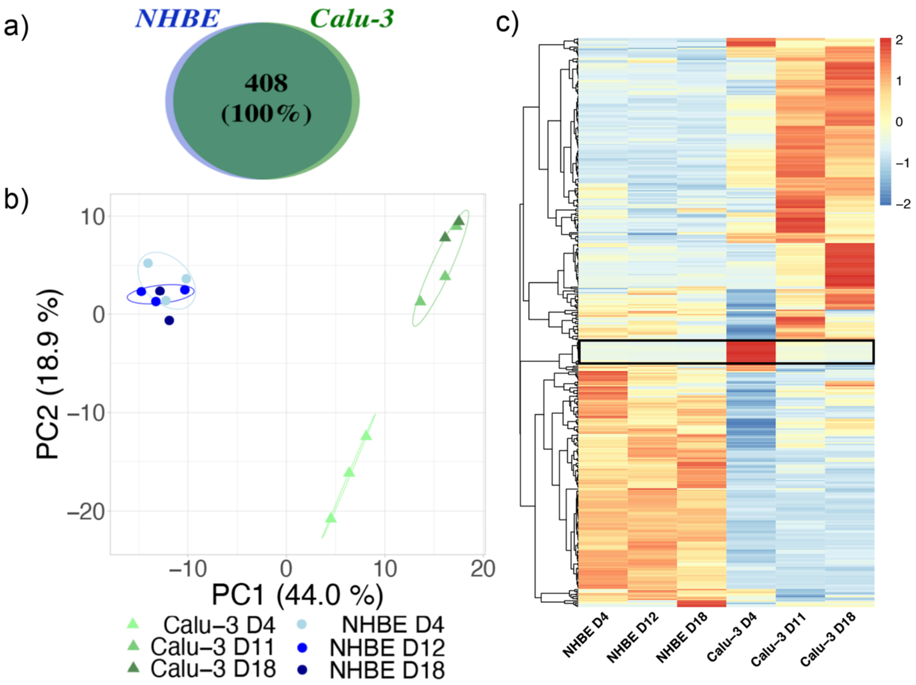

Figure 3. Proteomic analysis of the apical secretome of the human bronchial epithelium in Calu-3 and NHBE models. (**a**) Qualitative analysis of the extracellular proteins of Calu-3 and NHBE cells at day 4, day 11 (Calu-3) or 12 (NHBE), and day 18 after ALI. The total number of proteins and the percentage of common proteins are shown in a Venn diagram. (**b**) Comparison of the abundance of extracellular proteins by Principal Component Analysis (PCA). The analysis was performed at day 4, day 11 (Calu-3) or 12 (NHBE), and day 18. The different donors (NHBE cells) and biological replicates (Calu-3 cells) are represented for each condition and circled on the graph. The percentage associated with each principal component is indicated in the axis legend. (**c**) Heat map of extracellular proteins identified in the apical secretome of Calu-3 cells and NHBE cells at day 4, 11–12, and 18 after ALI. A protein set showing a large difference at day 4 in the secretome of Calu-3 cells is highlighted by a black rectangle.

Quantitative proteomic analysis of the secretome in Calu-3 and NHBE models. We characterized the secretome of Calu-3 cells in long-term cell cultures by label-free quantitative mass spectrometry. The apical secretome was collected in Hanks' balanced salt solution (HBSS) at day 4, 11, and 18 after ALI for analysis. We performed the same experiment with NHBE cells to compare the composition of the epithelial cell secretions in Calu-3 and NHBE models of the human bronchial epithelium. All the experiments were performed in biological and technical triplicates. In the case of primary cells, NHBE cells from 3 healthy donors were used and the apical secretome collected in HBSS at day 4, 12, and 18 after ALI. The NHBE cells were cultured on inserts with a 0.4 µm pore diameter following the provider's instructions. The commercial cell culture medium used for NHBE cells is serum free (details on growth factors or other additives were not disclosed by the provider).

A total number of 1685 proteins were identified in the apical secretome of Calu-3 and NHBE cells at all time points. The full protein list is presented in the Supplementary dataset 1. These proteins include several intracellular proteins that may originate from dead cells and cell debris, which are collected with the secretome during washes. Extracellular proteins were selected using the Proteome Discover database. We identified 408 extracellular proteins in the apical secretome of Calu-3 and NHBE cells (Fig. 3). Each protein was identified in at least two biological replicates, showing that little difference exists between cell batches (in the case of Calu-3 cell lines) or donors (in the case of NHBE primary cells). Interestingly, the same proteins were identified in the secretome of Calu-3 and NHBE cells, indicating a very high similarity in the epithelial cell secretome in the Calu-3 and NHBE model over time (Fig. 3a).

The abundance of each protein was analyzed so that we could determine whether one protein was more or less secreted in one condition, either between the Calu-3 and the NHBE model, or as a function of time. To get an overview of the proteomic pattern for each condition, a principal component analysis (PCA) of the quantitative proteomic data was performed. The plot of the two main eigenvectors PC1 and PC2 is shown in Fig. 3b. This analysis shows that the secretomes of NHBE cells form a single cluster that differs from the secretome of Calu-3 cells at all time points. No difference in the secretome of NHBE cells with time or between donors was observed in this analysis, suggesting a high stability of the NHBE culture over time and little difference in the secretions of the epithelial cells between donors. Note that both male and female healthy donors of different ages were considered in this study. On the contrary, Calu-3 secretomes form two separate clusters at day 4, and at day 11 and 18 after ALI respectively. This analysis suggests that the protein abundance in the apical secretome of Calu-3 cells may evolve during the first days at ALI until it stabilizes and forms a mature secretome.

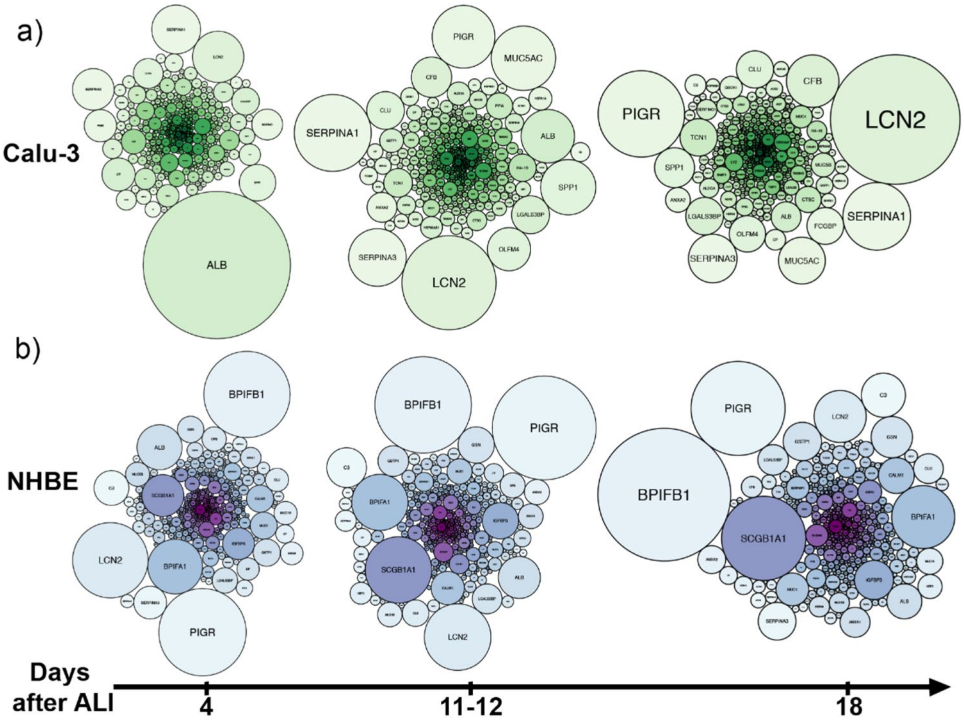

Figure 4. Time evolution of the secretome of Calu-3 and NHBE cells. Schematic representing the proteins secreted by Calu-3 (**a**) and NHBE (**b**) cells as a function of their abundance at day 4, 11–12, and 18 after ALI. A larger sphere denotes a higher protein abundance. Proteins are designated by their corresponding gene. Human serum albumin (*alb*), neutrophil gelatinase-associated lipocalin (*lcn2*), polymeric immunoglobulin receptor (*pigr*), alpha-1-antitrypsin (*serpina1*), BPI fold containing family B member 1 (*bpfib1*). The full protein list is detailed in Table S1.

The relative abundance of the 408 extracellular proteins identified in the secretome of Calu-3 and NHBE cells is shown in a heat map in Fig. 3c. This analysis confirms the high level of similarity of the apical secretome of NHBE cells as a function of time. On the contrary, larger variations in protein abundances are observed at day 4 compared to day 11 and 18 after ALI in the case of Calu-3 cells. The detailed analysis shows that these differences are usually associated with an increase of the protein concentration with time between day 4 and day 11 after ALI. However, a cluster of proteins showed a different trend, with a higher abundance in the secretome of Calu-3 cells at day 4 compared to day 11 and 18 after ALI (Fig. 3c).

Differences in protein abundances were clearly observed between the secretome of NHBE and Calu-3 cells at each time point. This result shows that, despite a high degree of similarity in terms of protein composition, the epithelial cell secretions differ in their protein abundance and temporal evolution in the Calu-3 and NHBE models.

To get a better view of these differences, the secreted proteins of each model were represented as a function of time using a sphere diagram (Fig. 4). The most abundant protein in the secretome of Calu-3 cells at day 4 was serum albumin (ALB), which abundance then decreases at day 11 and 18 after ALI. The potential contamination of the apical secretome by bovine serum albumin from the basal medium was checked using two methods: first, the peptide sequence analysis showed higher sequence homology with *Homo sapiens* versus *Bos Taurus* serum albumin using the Swissprot database; secondly, up-regulation of HSA expression in Calu-3 cells was evidenced by qRT-PCR in Calu-3 cells (Fig. S4). Serum albumin is a major component of lung lining fluid[47]. We hypothesize that the hypersecretion of serum albumin by Calu-3 cells a few days after ALI is related to the control of the osmotic pressure in an immature epithelium. This is supported by the secretion of Hsp90, a heat shock protein secreted by normal cells in case of tissue injury that also promotes cancer cell motility[48]. A basal level of secretion of serum albumin was then observed in both models.

At day 11 and 18 after ALI, similar features were observed in the apical secretome of Calu-3 cells, suggesting that the secretome becomes more stable after 7–10 days at ALI in this model. Proteins involved in the formation of the mucus layer such as MUCA5AC, and in cell communication and defense mechanisms, such as the neutrophil gelatinase associated lipocalin (*lcn2*), the polymeric immunoglobulin receptor (*pigr*), alpha-1-antitrypsin (*serpina1*) and alpha-1-antichymotrypsin (*serpina3*) became more abundant in the mature secretome of Calu-3 cells (Fig. 4a). Clusterin (*clu*), an extracellular chaperone protein associated with the folding of secreted proteins; galectin-3 binding protein (*lgals3bp*), a glycoprotein associated with the innate immune response of epithelial cells[49]; and annexin A2 (*anxa2*), which is involved in the cell secretory machinery, were also identified as main components of the mature secretome of Calu-3 cells. Annexin A2 can be trafficked across the membrane of the

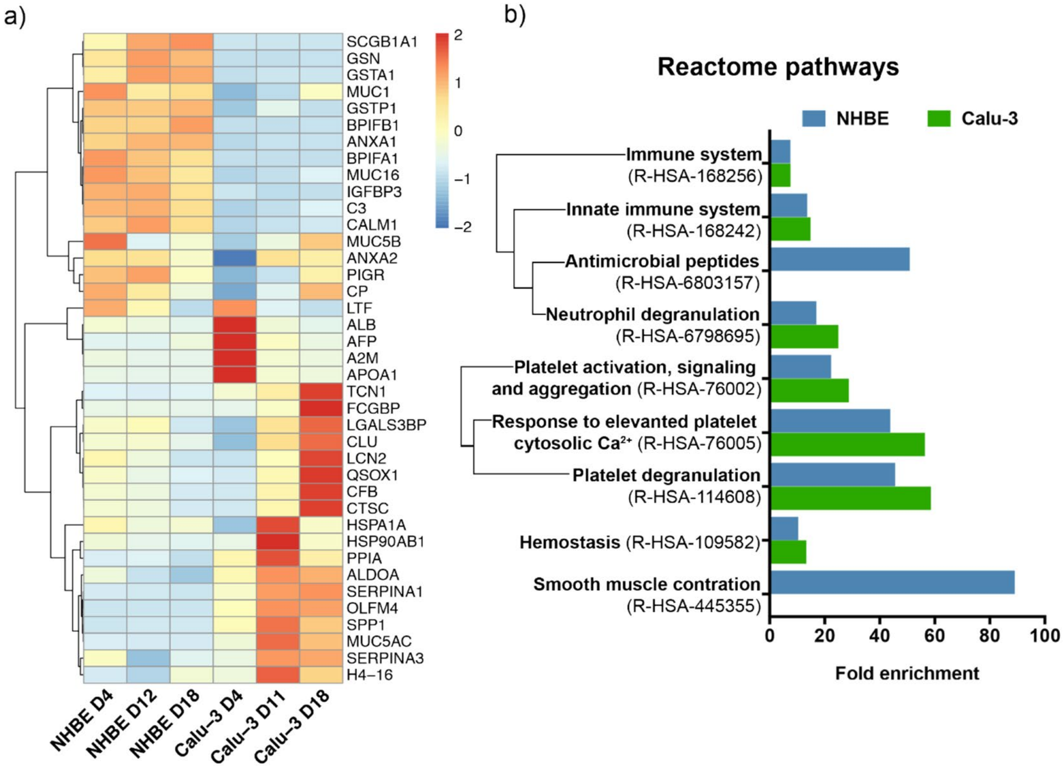

Figure 5. Analysis of the biological pathways associated with the secreted proteins in the Calu-3 and NHBE models. (**a**) Heat map of the 20 most abundant proteins secreted by Calu-3 and NHBE cells at day 4, 11–12, and 18 after ALI. Proteins are designated by their corresponding gene. (**b**) Reactome pathways associated with the extracellular proteins identified in the apical secretome of Calu-3 cells (in green) and NHBE cells (in blue) at day 11–12 and 18 after ALI. ($P < 0.05$ for each fold enrichment).

lung epithelial cells during the secretion of extracellular vesicles (EVs)[50], which suggests that proteins identified in the apical secretome of Calu-3 cells include exosomal proteins[35].

The comparison of the apical secretome of Calu-3 and NHBE cells shows that neutrophil gelatinase associated lipocalin, polymeric immunoglobulin receptor, clusterin, galectin-3 binding protein, and annexin 2 were secreted at high levels in both models. Other major components of NHBE cell secretome included uteroglobin (*scgb1a1*) and the BPI fold containing family A (*bpifa1*) and B (*bpifb1*), which are involved in the defense mechanisms of the epithelium (Fig. 4b).

Comparison of the long-term evolution of Calu-3 and NHBE cell secretomes. In order to better understand the long-term evolution of the epithelial cell secretome, the 20 most abundant proteins secreted by Calu-3 and NHBE cells (Top 20) were compared at each time point (Fig. 5a, Table S2). The heat map highlights the temporal evolution of each protein and the differences between the main components of the secretome of Calu-3 and NHBE cells.

The NHBE secretome was broadly stable for 3 weeks, except for a few proteins whose abundance tended to decrease a little (*muc5ab*, *muc1*, *serpina3*). Some proteins highly abundant in the NHBE secretome are secreted at lower levels by Calu-3 cells, such as gelsolin (*gsn*), glutathione S-transferases (*gsta*, *gstp1*), annexin 1 (*anxa1*), MUC16 (*muc16*), insulin-like growth factor-binding protein 3 (*igfbp3*), Complement C3 (*c3*) and calmodulin-1 (*calm1*). Gelsolin (*gsn*) breaks down actin filaments released by dying cells. Its secretion by epithelial cells is triggered by interleukin-4[51]. Gelsolin was detected at a lower level in Calu-3 secretome, suggesting a basal level of secretion of gelsolin in this model. Antimicrobial peptides were also secreted by NHBE cells, such as the BPI fold-containing family A and B members 1 (*bpifa1*, *bpifb1*).

The proteins secreted by Calu-3 cells can be clustered according to their time evolution during a period of 3 weeks: (1) highly secreted proteins during the first days at ALI, (2) highly secreted proteins in the mature secretome, (3) proteins with basal level of secretion. In addition, three proteins in the Top 20 showed a transient increase in secretion at day 11 after ALI: HSP70, HSP90, and the peptidyl prolyl isomerase A (*ppia*), which catalyses the folding of extracellular matrix proteins[52].

The highly secreted proteins during the first days at ALI were serum albumin, α-2-macroglobulin (*a2m*), α-fetoprotein (*afp*), and apolipoprotein A1 (*apoa1*). The presence of α-fetoprotein was reported in the bronchoalveolar lavage (BAL) of patients with lung adenocarcinoma[53], suggesting its secretion could be specific to the Calu-3 cell line in the immature epithelium. This hypothesis is consistent with the higher level of secretion of albumin at this time point. α-2-macroglobulin contributes to the control of protease activity in the lung

Reactome pathway	Top 20 NHBE + Calu-3	Top 20 NHBE	Top 20 Calu-3
Immune system	*anxa2* *clu* *lcn2* *pigr* *serpina3*	*anxa1* *bpifa1* *bpifb1* *c3* *calm1* *gsn* *gstp1* *muc1* *muc16*	*cfb* *ctsc* *muc5ac* *olfm4* *serpina1* *tcn1*
Innate immune system	*anxa2* *clu* *lcn2* *pigr* *serpina3*	*bpifa1* *bpifb1* *c3* *calm1* *gsn* *gstp1* *muc1* *muc16*	*cfb* *ctsc* *muc5ac* *olfm4* *serpina1* *tcn1*
Antimicrobial peptide		*bpifa1* *bpifb1* *clu* *lcn2*	
Neutrophil degranulation	*anxa2* *lcn2* *pigr* *serpina3*	*c3* *gsn* *gstp1*	*ctsc* *olfm4* *serpina1* *tcn1*
Platelet activation, signalling and aggregation	*alb* *clu* *lgals3bp* *serpina3*	*calm1*	*serpina1*
Response to elevated platelet cytosolic Ca^{2+}	*alb* *clu* *lgals3bp* *serpina3*	*calm1*	*serpina1*
Platelet degranulation	*alb* *clu* *lgals3bp* *serpina3*	*calm1*	*serpina1*
Homeostasis	*serpina3* *alb* *clu* *lgals3bp* *anxa2*	*calm1*	*serpina1*
Smooth muscle contraction		*anxa1* *calm1*	

Table 1. List of the biological pathways and their associated proteins identified in the secretome of NHBE and/or Calu-3 cells at day 11–12 and 18 after ALI. Only the 20 most abundant proteins were considered. Proteins are designated by their corresponding gene. The description of each protein is given in Table S2.

lining fluid. The secretion of apoA1 by epithelial cells was recently linked to the regulation of the innate immune response following airway inflammation[54].

Proteins more specific to the mature secretome of Calu-3 epithelial cells include the major gel-forming mucins MUC5AC and MUC5B, and to a smaller extent the tethered mucins MUC1 and MUC16[55]. MUC1 and MUC16 are anchored to the cell membrane, which can explain their lower abundance in the analysis of the secretome. Protease inhibitors [α1-antitrypsin (*serpina1*), α1- antichymotrypsin (*serpina3*)], proteases [cathepsin C (*ctsc*)], immunoglobulin G (*fcgbp*), Complement factor B (*cfb*), and olfactomedin4 (*olfm4*), a glycoprotein involved in the innate immune response, were also secreted at higher levels after 11 and 18 days at ALI in the Calu-3 model. To explore the biological role and interactions of the main components of the epithelial cell secretions further, we performed a Reactome pathway analysis of the Calu-3 and NHBE secretomes.

Biological pathways associated with the secretome of Calu-3 and NHBE cells.

The biological pathways associated with the secreted proteins were analysed using the Reactome database. We selected the proteins secreted both at day 11–12 and 18 after ALI for this analysis, which correspond to the proteins forming a stable and mature secretome in Calu-3 and NHBE models. The Reactome pathways associated with the secretome of Calu-3 and NHBE cells in long-term cultures are presented in Fig. 5b and Table 1. The secreted proteins are strongly associated with the immune response both in Calu-3 and NHBE models. This response involves the innate immune response, the neutrophil degranulation, and antimicrobial peptides (*bpifa1, bpifb1, clu, lcn2*)[56,57]. The proteins secreted by the epithelial cells, such as lipocalin 2, BPI fold containing family A and B members, and clusterin, are essential elements of the mucosal immune defense against pulmonary infections[58].

The biological pathways associated with hemostasis and platelet activation include albumin and calmodulin-1 (*calm1*), a calcium-binding protein that modulates the ion channel activity. These proteins may contribute to the regulation of the osmotic pressure in the epithelium[59].

Expression of SARS-CoV-2 receptors in preclinical 3D model of the human bronchial epithelium. The infection of Calu-3 cells by SARS-CoV-2 was recently reported[60,61]. The ACE-2 (angiotensin-converting enzyme 2) receptor and the neuropilin-1 receptor, which are involved in SARS-CoV-2 infection of the lung epithelial cells[62,63], were both expressed by Calu-3 cells for 4 weeks in our 3D model of human bronchial epithelium (Supplementary dataset 1). Proteomic analysis of cell extracts and qRT-PCR will be performed to confirm the levels of expression of these receptors in long-term Calu-3 cell cultures. The presence of these receptors could support the use of this preclinical model for testing novel therapeutic strategies against COVID-19[64–66].

Discussion

The objectives of this study were to develop a preclinical model of the human bronchial epithelium using the Calu-3 cell line for chronic toxicity study with minimal FBS supplementation, and to characterize the time evolution of the epithelial cell secretions. The Calu-3 cells were maintained for 21 days at ALI without subculturing and showed good viability and functionality, making it a relevant model for chronic toxicity studies of inhaled drugs, particles or pollutants. Here, we adapted the Calu-3 model for long-term nanotoxicology studies for repeated and chronic exposure to inhaled NPs by culturing cells on inserts with a 3-µm pore diameter. A larger pore size allows the analysis of NP translocation through the epithelial barrier[9]. Compared to primary cell models, the main advantages of the Calu-3 model are the availability, low cost, absence of donor variability, and the formation of a tight epithelium on inserts with a 3-µm pore diameter with excellent barrier properties without addition of any drug[15,21,22,67]. In comparison, the growth of NHBE cells is not possible on membranes with such a large porosity, and is limited to inserts with a 0.4-µm pore diameter. The disadvantages of the Calu-3 model are the presence of only one cell type, an abnormal karyotype, and the growth of polyps in certain conditions (data not shown). Some differences in anion secretion during transepithelial fluid transport were also reported[28].

Another advantage of 3D models is the possibility to establish co-cultures to mimic cellular interactions between different cell types in vitro. For instance, co-cultures of the epithelial cells with macrophages and fibroblasts on the apical and basal side of the bronchial epithelium respectively were used to investigate the fibrogenic potential in toxicology studies[68]. Our long-term culture model could be of particular interest regarding the development of this pathology. Interestingly, in the case of silver NPs, Braakhuis et al. showed that a simple in vitro model could better predict the pulmonary toxicity when compared to in vivo inhalation studies than co-cultures with endothelial cells and macrophages[14].

We determined a minimal FBS supplementation of 4% in the basal medium of Calu-3 cells to maintain a functional epithelium for 21 days at ALI. While cells cannot be deprived of serum, reducing the FBS supplementation is relevant in a lung model for testing drug or particle toxicity. On one hand, drugs may form complexes with serum proteins, reducing their bioavailability or triggering allergic responses; and NPs are covered by adsorbed proteins (the biomolecular corona) which defines their biological identity and cellular interactions. On the other hand, more than 1800 proteins and 4000 metabolites compose FBS, the concentrations of which vary greatly between batches[39]. Therefore, supplementation introduces a degree of complexity and variability that can have a substantial impact on the results. Here we advise to use minimal FBS supplementation for toxicity testing to reduce this risk. Future solutions may be provided with the use of serum substitutes and serum-free culture conditions.

On the apical side, the epithelial cell secretions structure the mucus that forms, with the tight epithelium, the first line of defense against particles and pathogens at the bronchial level[69]. The composition of the secretome and its evolution are therefore key elements of lung models. Our analysis of the apical secretome of Calu-3 and NHBE epithelia in long-term cultures shows high similarity between the two models, despite the difference in cell types. The same proteins are secreted, albeit with different abundances. While the NHBE secretome shows little variability with time, an evolution of Calu-3 secretions was clearly visible from 4 to 18 days at ALI. Based on this observation, we suggest that a stable and mature secretome is established after 11 days at ALI in the Calu-3 model.

The epithelial cell secretions, which include mucins and a large range of enzymes as well as antimicrobial peptides such as lipocalin 2, are key components of the mucosal immune defense against xenobiotics and pathogens. The Reactome biological pathway analysis shows their strong relation with the immune response of the epithelium. Proteins secreted by the Calu-3 and NHBE models of the bronchial epithelium were also identified in the human BAL of healthy individuals[70]. Shaw et al. showed that the biomolecular corona formed on diesel exhaust nanoparticles (DNEPs) in BAL induced an inflammatory response in macrophages and increased cell uptake, an effect unseen when the DNEPs were incubated in plasma[40]. Differences in the uptake of oxide NPs by rat alveolar macrophages in vivo was related by Konduru et al. to differences in their protein corona composition following incubation in rat lung lining fluid[41]. These studies highlight the role of the epithelial cell secretions on the mucosal immune response and on the fate of the inhaled particles.

Exosomal proteins, such as annexin A2, were also noted in the secretome of Calu-3 cells by Gupta et al., suggesting that extracellular vesicles EVs were produced by the bronchial epithelium in our model[50]. The proteomic analysis of the lung EVs was recently provided by Gupta et al. for the Calu-3 cell line[35]. The authors demonstrated that lung EVs played a central role in the epithelial cell communication in the upper airways. These results confirm the biological relevance of the Calu-3 model for long-term toxicity studies and the essential role of the epithelial cell secretions in the lung response.

Finally, diseases such as COPD and cystic fibrosis can alter mucus secretion[46]. The analysis of the BAL of atopic asthmatics showed altered proteomic profiles, which result in different biomolecular corona on inhaled particles[71]. The interaction of an inhaled agent (drug, particle, pollutant) with the mucus and its effect on mucus secretion are two essential aspects of the epithelial response, especially for chronic exposure. The secretome profile provided here can be used as a reference to investigate the effect of drugs on the epithelial cell secretions over time.

Taking advantage of microfabrication techniques, advanced lung models such as lung-on-chip have been developed to recapitulate other biological lung features such as breathing cycle, deep lung morphology, and airflow in the alveoli[72,73]. Using the Calu-3 cell line, functional and mucus producing lung-on-chip models could be developed to investigate the effect of exogenous compounds on mucus evolution and/or alteration in vitro. The immortalized BSi-NC1 cells developed by Crystal's group also represent an interesting model to establish a tight epithelium with both ciliated and non-ciliated cells following differentiation at ALI[74].

To conclude, a functional in vitro model of the human bronchial epithelium using Calu-3 cell line was developed as an alternative to primary NHBE cells. A minimal FBS supplementation in the basal medium was defined to maintain a functional epithelium for 21 days at the air liquid interface, so that the amount of exogenous serum proteins could be reduced during drug testing. The nature and the biological pathways associated with the secreted proteins confirmed their key role in the mucosal immune response of the lung. We suggest this preclinical 3D model can be used to evaluate the long-term toxicity of drugs or particles on the human bronchial epithelium, and subsequently to investigate their effect on the epithelial cell secretions.

Methods

3D model of the human bronchial epithelium with Calu-3 cell line.

The Calu-3 human adenocarcinoma epithelial cell line (ATCC HTB-55, LGC Standard, France) was used for the experiment at cell passage 24–40. All products used for cell culture were provided by Thermo Fisher Scientific unless stated otherwise. Calu-3 cells were cultured in Eagle's Minimum Essential Medium (MEM) supplemented with 10% v/v fetal bovine serum (FBS) (F7524, Sigma-Aldrich), 1% non-essential amino acids (NEAA) 100×, 1% sodium pyruvate, 1% Glutamax, 1% penicillin streptomycin 100×, and 1% HEPES buffer 100×. Cells were culture at a density of 40,000 cells/cm^2 in 25 or 75 cm^2 culture flasks (Corning) at 37 °C in a humidified 5% CO_2 atmosphere and passaged weekly before confluence. To form the epithelial barrier, Calu-3 cells were seeded on Transwell polyester inserts with a 3 µm pore diameter (Corning Costar) at a density of 500,000 cells/insert (with 500 µL of cell suspension in the apical compartment and 1.5 mL of medium in the basolateral compartment). The culture medium was changed every 2–3 days in both compartments until TEER $> 700\ \Omega\ cm^2$. The medium was removed from the apical compartment to create an air–liquid interface. The medium in the basolateral compartment was replaced by 0, 2, 4 or 8% FBS one day after ALI. Calu-3 cells cultured on Transwell membrane were maintained for 21 days after ALI.

MucilAir 3D lung tissue model.

MucilAir 3D lung tissue model is a fully differentiated bronchial epithelium reconstituted from human bronchial airway epithelial cells of healthy donors. The MucilAir cultures were purchased from Epithelix (Genève, Switzerland). Cells were obtained from 3 healthy non-smoking Caucasian donors, two men and one woman, of different ages. The primary cells were cultured on Transwell polyester inserts with 0.4 µm pore diameter using MucilAir serum-free cell culture medium with penicillin/streptomycin (EP04MM, Epithelix).

Trans-epithelial electrical resistance.

To assess the integrity of the epithelial barrier, the trans-epithelial electrical resistance (TEER) was measured with an EVOM2 ohmmeter (World Precision Instruments, Sarasota, USA) with STX2 electrodes. First, the culture medium was replaced by 1.5 mL and 0.5 mL Hanks' Balanced Salt Solutions supplemented with calcium and magnesium (HBSS$^{Ca2+/Mg2+}$, ThermoFisher Scientific, France) in the basal and apical compartment, respectively. HBSS was warmed at 37 °C before addition. For each experiment, the TEER was also measured in a cell-free Transwell (blank) and subtracted to values measured in cell seeded Transwell. Final TEER values are multiplied by the surface area of the inserts and expressed in Ω cm^2. We considered that a tight epithelium was formed if TEER $> 200\ \Omega\ cm^2$ for MucilAir following the provider's guidelines, and $> 300\ \Omega\ cm^2$ for Calu-3 cells. This latter value was determined by combining TEER and Lucifer Yellow permeability assay results in our cell culture conditions (Fig. S2).

Lucifer Yellow permeability assay.

The integrity of the barrier formed by Calu-3 cells at the air–liquid interface was checked with the Lucifer Yellow (LY) paracellular permeability assay (Sigma-Aldrich). LY is a 452 Da fluorescence dye which paracellular transport through the epithelium is prevented when tight junctions are formed (in the case of a short exposure time of the cell layer to LY). 0.5 mL LY (0.1 mg/mL), diluted in HBSS$^{Ca2+/Mg2+}$, were added to the apical compartment. The basal compartment was filled with 1 mL HBSS$^{Ca2+/Mg2+}$. LY was also added to a cell free well (blank). Following 1 h incubation at 37 °C, 0.1 mL of the apical and basal solutions were transferred to a 96-well microplate (µClear, Greiner Bio-One, Germany). The fluorescence intensity was measured with $\lambda_{exc} = 485$ nm and $\lambda_{em} = 535$ nm on a Flex microplate reader (Molecular Devices). This analysis was performed in triplicate. The permeability was calculated as follow:

$$Permeability\ (\%) = \frac{I_{sample} - I_{Blank}}{I_{LY} - I_{Blank}} \times 100$$

where I_{LY}, I_{sample}, and I_{blank} are the fluorescence intensities of the dye, the sample and the blank (cell-free sample) respectively. A permeability of < 2% was used as a threshold to define a tight epithelium.

BCA assay. The total protein concentration of the apical secretome was measured by the bicinchoninic acid (BCA) protein assay (Pierce BCA protein assay kit, ThermoFisher Scientific) following the manufacturer's protocol. Briefly, all samples were diluted in $HBSS^{Ca2+/Mg2+}$. After 30 min incubation at 37 °C, the absorbance at 562 nm was measured on the Flex microplate reader. The analysis was performed in duplicate.

Enzyme-linked lectin assay. The glycoprotein concentration of the apical secretome of Calu-3 cells and MucilAir was measured by the enzyme-linked lectin assay (ELLA). A 96-well plate (9018, Corning) was coated with 6 µg/mL lectin from *Triticum vulgaris* (L0636, Sigma-Aldrich) in PBS (ET330-A, Euromedex) and incubated for 1 h incubation at 37 °C. After washing the plates with PBS buffer supplemented with 0.5 M NaCl (S3014, Sigma-Aldrich) and 0.1% Tween 20 (P1379, Sigma-Aldrich), 50 µL of the apical secretome were added and incubated for 1 h at 37 °C. Known concentration of porcine stomach mucin (2378, Sigma-Aldrich) were added to the same plate to measure the calibration curve [78.1 ng/mL–10 µg/mL]. After washing, the detection solution composed of 1 µg/mL lectin peroxidase conjugated (L2650 Sigma-Aldrich) was added to each well and incubated for 1 h at 37 °C. Finally, tetramethylbenzidine (TMB) substrate reagent (555214 BD OptEIA, BD Bioscience) was added and incubated for 20 min in the dark at room temperature. The enzymatic reaction was stopped with 2 N H_2SO_4 (84727, Sigma-Aldrich) and the absorbance at 490 nm was measured. Each analysis was performed in duplicates.

MUC5AC and ZO-1 immunolabelling. Cells were fixed with 4% paraformaldehyde, washed with PBS, permeabilized with a 0.02% Triton X-100 (2000B, Euromedex), and blocked with 2% BSA (A7906, Sigma-Aldrich) in PBS. After washing, cells were incubated with mouse monoclonal anti-MUC5AC (dilution 1/500) (45M1-12178, Thermo Fisher scientific) and rabbit polyclonal anti-ZO-1 (SC-10804, Santa Cruz Biotechnology) antibodies at 4 °C overnight. Donkey anti-mouse-AF594 (715-585-150) and goat anti-rabbit-AF488 (111-545-144) secondary antibodies (Jackson ImmunoResearch) were used (dilution 1/1000). Cells were mounted with Fluoroshield (F6057, Sigma-Aldrich) before observation by confocal ZEISS LSM 700 fluorescence microscope with a 63× objective lens. Version 2.3 of the ZEISS ZEN software was used.

Transmission electron microscopy. Calu-3 cells cultured on Transwell were fixed with 2.5% glutaraldehyde and 2% paraformaldehyde in 0.1 M sodium cacodylate pH 7.3 for 45 min at room temperature. The samples were then treated with 1% osmium tetroxide for 45 min at 4 °C, and incubated in 1% aqueous uranyl acetate solution for 2 h at room temperature. They were dehydrated in ethanol solutions of increasing percentage (30%, 50%, 70%, 95% and 100%, 3 × 10 min each), in ethanol:propylene oxide mix (1:1 v), and in propylene oxide 3 × 10 min. Each sample was embedded in Epon epoxy resin. Ultrathin sections of 80 nm thickness were cut with a Leica Ultracut S microtome fitted with a diamond knife (Diatome ultra 45), transferred on Cu grids and post-stained with lead citrate. Samples were imaged with a JEM-100S microscope (Jeol Ltd Tokyo, Japan) operating at 80 kV. Images were acquired with an Orius 200 digital camera (Gatan-Roper Scientific, Evry, France) using Gatan software.

qRT-PCR. RNA was isolated from Calu-3 cells 20 days after ALI using NucleoSpin RNA kit (740955.250, Macherey–Nagel) and converted to cDNA using the high-capacity cDNA reverse transcription kits (4368814, Applied Biosystems). Primers for the selected genes of interest (*muc5ac, muc5b, zo1, alb*) were designed with Primer-Blast software (NCBI) and synthesized by Eurofins Genomics (*zo-1, hprt, muc5ac*), Oligo (*tbp*) and Invitrogen (*muc5b*). The sequence of the primers is detailed in Table S1. qRT-PCR was performed on a LightCycler 480 instrument II (Roche Diagnostics, France). Gene expression was analyzed by $2^{-\Delta\Delta Ct}$ method and normalized to RP19 and TBP housekeeping genes. Fold change was expressed using 10% FBS cell culture condition as the reference. Results are expressed as mean fold change ± standard deviation for three biological replicates.

LC–MS/MS. Label-free quantitative proteomic analysis of the Calu-3 and NHBE apical secretome was performed by LC–MS/MS following protein digestion with trypsin. 3 biological replicates were analyzed at day 4 and day 11, 2 biological replicates were analyzed at day 18. One biological replicate corresponds to the secretome collected from three different Transwell from the same donor pulled together in the case of the NHBE model, and to the secretome collected from three different Transwell from two different culture batches in the case of the Calu-3 model. Briefly, 16 µg of protein were precipitated in cold acetone, then resuspended in 25 mM NH_4HCO_3 buffer prior to tryptic digestion overnight (sequencing-grade Trypsin, Promega). Peptides were desalted and concentrated with 10 µL ZipTip µ-C18 Pipette Tips (Millipore,). Peptides were analyzed on a Q-Exactive Plus mass spectrometer coupled to a Proxeon 1000 Nano-LC (ThermoFisher). Peptides were separated by chromatography using the following specifications: acclaim PepMap100 C18 pre-column (2 cm, 75 µm i.d., 3 µm, 100 Å); Pepmap-RSLC Proxeon C18 column (50 cm, 75 µm i.d., 2 µm, 100 Å); 300 nL/min flow rate, 98 min gradient going from 95% solvent A (water, 0.1% formic acid) to 35% solvent B (100% acetonitrile, 0.1% formic acid) followed by column regeneration (total time 120 min). Peptides were first analyzed in positive mode in the Orbitrap cell at a 70,000 resolution with a m/z range of 375–1500. MS/MS data were acquired in the Orbitrap cell in a Top20 mode with an AGC target of 3.10^6 for full MS. Fragments were obtained by Higher-energy C-trap Dissociation (HCD) activation with a collisional energy of 27%, a quadrupole isolation window of 1.4 Da, and an AGC target of 2.10^5. MS/MS data were acquired in a data-dependent mode with a dynamic exclusion of 30 s.

Monovalent peptides or peptides with unassigned charge state were excluded from the analysis. The maximum ion accumulation times were set to 50 ms and 45 ms for MS and MS/MS acquisition respectively. Label Free quantitation was performed with Progenesis QI (Waters) using HI-3 method for protein quantification. Data were processed with Proteome Discoverer 2.2 software (ThermoFisher Scientific). The mass tolerance was set to 6 ppm for precursor ions and 0.02 Da for fragments.

Proteomic data analysis. The MASCOT software (Matrix Science, v. 2.4) was used for protein identification on the *Homo sapiens* and *Bos Taurus* Swissprot databases (2019). Post-translational modifications were searched in dynamics parameters: oxidation (M) phosphorylation (S/T/Y), acetylation (Protein N-terminal). The maximum number of missed cleavages was limited to two for trypsin digestion. P-values of peptides were calculated using the percolator algorithm and a 5% threshold was applied. Filters used in the MASCOT software correspond to: proteins identified with a minimum of 2 peptides, AND a MASCOT score > 40, AND $P < 0.05$. Extracellular proteins were identified using the extracellular compartment database of the Proteome Discoverer software. Bioinformatics analysis and figures were developed with R Software (v.3.6.2)[75]. Heat maps were generated with the 'pheatmap' package[76], where correlation clustering distance row was applied. PCA was calculated from the abundance of the extracellular proteins identified in each replicate and the results presented using the 'ggbiplot' package[77]. The 'packcircles' package[78] was used to represent protein abundance, where the circle area is proportional to each protein abundance. The Reactome pathway fold enrichment analysis was performed with PANTHER (v15.0) software using Fisher's test and Bonferroni correction for multiple testing. Statistically significant results were selected using $P < 0.05$.

Statistical analysis. The statistical analysis was performed with Prism GraphPad Software (v. 7.0). Data are expressed as mean ± standard deviation. All data passed the D'Agostino and Pearson or the Shapiro–Wilk normality test ($\alpha = 0.05$). When comparing groups, multiple comparison two-way ANOVA corrected with Benjamini, Krieger and Yekutieli test were used. For comparing time variability within group, three-way ANOVA corrected with Benjamini, Krieger and Yekutieli test were used. For Lucifer yellow assay, Boneferroni-Dunn t-test method was applied. $P < 0.05$ was used as a threshold for statistically significant results.

Data availability

The mass spectrometry proteomics data have been deposited to the ProteomeXchange Consortium via the PRIDE partner repository[79] with the dataset identifier PXD024242. The full protein lists are also available in the Excel file WS1 in the "SI".

Received: 30 November 2020; Accepted: 10 March 2021
Published online: 23 March 2021

References

1. Webster, M. J. & Tarran, R. *Slippery When Wet: Airway Surface Liquid Homeostasis and Mucus Hydration. Current Topics in Membranes* Vol. 81 (Elsevier Ltd, 2018).
2. Salvi, S. *et al.* Acute inflammatory responses in the airways and peripheral blood after short-term exposure to diesel exhaust in healthy human volunteers. *Am. J. Respir. Crit. Care Med.* **159**, 702–709 (1999).
3. Donaldson, K. *et al.* Combustion-derived nanoparticles: A review of their toxicology following inhalation exposure. *Part. Fibre Toxicol.* **2**, 1–14 (2005).
4. Calderón-Garcidueñas, L. *et al.* Long-term air pollution exposure is associated with neuroinflammation, an altered innate immune response, disruption of the blood-brain barrier, ultrafine particulate deposition, and accumulation of amyloid β-42 and α-synuclein in children and young adult. *Toxicol. Pathol.* **36**, 289–310 (2008).
5. Pope, C. A. *et al.* Exposure to fine particulate air pollution is associated with endothelial injury and systemic inflammation. *Circ. Res.* **119**, 1204–1214 (2016).
6. Seagrave, J. C. *et al.* Lung toxicity of ambient particulate matter from southeastern US sites with different contributing sources: Relationships between composition and effects. *Environ. Health Perspect.* **114**, 1387–1393 (2006).
7. Schwotzer, D. *et al.* Effects from a 90-day inhalation toxicity study with cerium oxide and barium sulfate nanoparticles in rats. *Part. Fibre Toxicol.* **14**, 1–20 (2017).
8. Upadhyay, S. & Palmberg, L. Air–liquid interface: Relevant in vitro models for investigating air pollutant-induced pulmonary toxicity. *Toxicol. Sci.* **164**, 21–30 (2018).
9. George, I., Vranic, S., Boland, S., Courtois, A. & Baeza-Squiban, A. Development of an in vitro model of human bronchial epithelial barrier to study nanoparticle translocation. *Toxicol. Vitr.* **29**, 51–58 (2015).
10. Zhou, J. *et al.* Differentiated human airway organoids to assess infectivity of emerging influenza virus. *Proc. Natl. Acad. Sci. USA* **115**, 6822–6827 (2018).
11. Fang, Y. & Eglen, R. M. Three-dimensional cell cultures in drug discovery and development. *SLAS Discov.* **22**, 456–472 (2017).
12. Boublil, L. *et al.* Development of a repeated exposure protocol of human bronchial epithelium in vitro to study the long-term effects of atmospheric particles. *Toxicol. Vitr.* **27**, 533–542 (2013).
13. Jeong, M. H. *et al.* In vitro model for predicting acute inhalation toxicity by using a Calu-3 epithelium cytotoxicity assay. *J. Pharmacol. Toxicol. Methods* **98**, 106576 (2019).
14. Braakhuis, H. M. *et al.* Simple in vitro models can predict pulmonary toxicity of silver nanoparticles. *Nanotoxicology* **10**, 770–779 (2016).
15. Cao, X. *et al.* Human air-liquid-interface organotypic airway tissue models derived from primary tracheobronchial epithelial cells—Overview and perspectives. *Vitr. Cell. Dev. Biol. Anim.* https://doi.org/10.1007/s11626-020-00517-7 (2020).
16. Rayner, R. E., Makena, P., Prasad, G. L. & Cormet-boyaka, E. Optimization of normal human bronchial epithelial (NHBE) cell 3D cultures for in vitro lung model studies. *Sci. Rep.* https://doi.org/10.1038/s41598-018-36735-z (2019).
17. Bovard, D. *et al.* Current research in toxicology comparison of the basic morphology and function of 3D lung epithelial cultures derived from several donors. *Curr. Res. Toxicol.* **1**, 56–69 (2020).
18. Grainger, C. I., Greenwell, L. L., Lockley, D. J., Martin, G. P. & Forbes, B. Culture of Calu-3 cells at the air interface provides a representative model of the airway epithelial barrier. *Pharm. Res.* **23**, 1482–1490 (2006).

19. Kreft, M. E. *et al.* The characterization of the human cell line Calu-3 under different culture conditions and its use as an optimized in vitro model to investigate bronchial epithelial function. *Eur. J. Pharm. Sci.* **69**, 1–9 (2015).
20. Zhu, Y., Chidekel, A. & Shaffer, T. H. Cultured human airway epithelial cells (Calu-3): A model of human respiratory function, structure, and inflammatory responses. *Crit. Care Res. Pract.* **2010**, 1–8 (2010).
21. He, R. W. *et al.* Comparative toxicity of ultrafine particles around a major airport in human bronchial epithelial (Calu-3) cell model at the air–liquid interface. *Toxicol. Vitr.* **68**, 104950 (2020).
22. Mathias, N. R. *et al.* Permeability characteristics of Calu-3 human bronchial epithelial cells: In vitro-in vitro correlation to predict lung absorption in rats. *J. Drug Target.* **10**, 31–40 (2002).
23. Foster, K. A., Avery, M. L., Yazdanian, M. & Audus, K. L. Characterization of the Calu-3 cell line as a tool to screen pulmonary drug delivery. *Int. J. Pharm.* **208**, 1–11 (2000).
24. Ihekwereme, C., Esimone, C., Di, S. & Agu, R. U. Preliminary studies on validation of Calu-3 cell line as a model for screening respiratory mucosa irritation and toxicity. *Pharmaceutics* **6**, 268–280 (2014).
25. Hynes, J. *et al. Advanced Non-animal Models in Biomedical Research: Respiratory Tract Diseases. EUR 30334 EN* (Publication Office of the European Union, 2020). https://doi.org/10.2760/52671.
26. Gordon, S. *et al.* Non-animal models of epithelial barriers (skin, intestine and lung) in Research, industrial applications and regulatory toxicology. *Altex* **32**, 327–378 (2015).
27. Hiemstra, P. S., Grootaers, G., van der Does, A. M., Krul, C. A. M. & Kooter, I. M. Human lung epithelial cell cultures for analysis of inhaled toxicants: Lessons learned and future directions. *Toxicol. Vitr.* **47**, 137–146 (2018).
28. Shan, J., Huang, J., Liao, J., Robert, R. & Hanrahan, J. W. Anion secretion by a model epithelium: More lessons from Calu-3. *Acta Physiol.* **202**, 523–531 (2011).
29. Ong, H. X., Traini, D. & Young, P. M. Pharmaceutical applications of the Calu-3 lung epithelia cell line. *Expert Opin. Drug Deliv.* **10**, 1287–1302 (2013).
30. Bloemen, P. G. M. *et al.* Expression and modulation of adhesion molecules on human bronchial epithelial cells. *Am. J. Respir. Cell Mol. Biol.* **9**, 586–593 (1993).
31. Han, X., Na, T., Wu, T. & Yuan, B. Z. Human lung epithelial BEAS-2B cells exhibit characteristics of mesenchymal stem cells. *PLoS ONE* **15**, 1–18 (2020).
32. Sakamoto, A. *et al.* Drug transporter protein quantification of immortalized human lung Cell lines derived from tracheobronchial epithelial cells (Calu-3 and BEAS2-B), bronchiolar-alveolar cells (NCI-H292 and NCI-H441), and alveolar type II-like cells (A549) by liquid chromat. *J. Pharm. Sci.* **104**, 3029–3038 (2015).
33. Kreda, S. M. *et al.* Coordinated release of nucleotides and mucin from human airway epithelial Calu-3 cells. *J. Physiol.* **584**, 245–259 (2007).
34. Bals, R., Weiner, D. J. & Wilson, J. M. The innate immune system in cystic fibrosis lung disease. *J. Clin. Invest.* **103**, 303–307 (1999).
35. Gupta, R. *et al.* Intercellular communication between airway epithelial cells is mediated by exosome-like vesicles. *Am. J. Respir. Cell Mol. Biol.* **60**, 209–220 (2019).
36. Rose, M. C. & Voynow, J. A. Respiratory tract mucin genes and mucin glycoproteins in health and disease. *Physiol. Rev.* **86**, 245–278 (2006).
37. Fahy, J. V. & Dickey, B. F. Airway mucus function and dysfunction. *N. Engl. J. Med.* **363**, 2233–2247 (2010).
38. Babu, P. B. R., Chidekel, A. & Shaffer, T. H. Protein composition of apical surface fluid from the human airway cell line Calu-3: Effect of ion transport mediators. *Clin. Chim. Acta* **347**, 81–88 (2004).
39. Gstraunthaler, G., Lindl, T. & Van Der Valk, J. A plea to reduce or replace fetal bovine serum in cell culture media. *Cytotechnology* **65**, 791–793 (2013).
40. Shaw, C. A. *et al.* Protein corona formation in bronchoalveolar fluid enhances diesel exhaust nanoparticle uptake and pro-inflammatory responses in macrophages. *Nanotoxicology* **10**, 981–991 (2016).
41. Konduru, N. V. *et al.* Protein corona: Implications for nanoparticle interactions with pulmonary cells. *Part. Fibre Toxicol.* **14**, 1–12 (2017).
42. Pisani, C. *et al.* The species origin of the serum in the culture medium influences the in vitro toxicity of silica nanoparticles to HepG2 cells. *PLoS ONE* **12**, 1–17 (2017).
43. Srinivasan, B. *et al.* TEER measurement techniques for in vitro barrier model systems. *J. Lab. Autom*. **20**, 107–126 (2015).
44. Ridley, C. & Thornton, D. J. Mucins: The frontline defence of the lung. *Biochem. Soc. Trans.* **46**, 1099–1106 (2018).
45. Rogers, D. F. The airway goblet cell. *Int. J. Biochem. Cell Biol.* **35**, 1–6 (2003).
46. Turner, J. & Jones, C. E. Regulation of mucin expression in respiratory diseases. *Biochem. Soc. Trans.* **37**, 877–881 (2009).
47. Olmeda, B. *et al.* Effect of hypoxia on lung gene expression and proteomic profile: Insights into the pulmonary surfactant response. *J. Proteomics* **101**, 179–191 (2014).
48. Tsutsumi, S. & Neckers, L. Extracellular heat shock protein 90: A role for a molecular chaperone in cell motility and cancer metastasis. *Cancer Sci.* **98**, 1536–1539 (2007).
49. Loimaranta, V., Hepojoki, J., Laaksoaho, O. & Pulliainen, A. T. Galectin-3-binding protein: A multitask glycoprotein with innate immunity functions in viral and bacterial infections. *J. Leukoc. Biol.* **104**, 777–786 (2018).
50. Popa, S. J., Stewart, S. E. & Moreau, K. Seminars in cell & developmental biology unconventional secretion of annexins and galectins. *Semin. Cell Dev. Biol.* **83**, 42–50 (2018).
51. Candiano, G. *et al.* Gelsolin secretion in interleukin-4-treated bronchial epithelia and in asthmatic airways. *Am. J. Respir. Crit. Care Med.* **172**, 1090–1096 (2005).
52. Lin, W. *et al.* Peptidyl prolyl cis/trans isomerase activity on the cell surface correlates with extracellular matrix development. *Commun. Biol.* **2**, 1–8 (2019).
53. Kitada, M. *et al.* Alpha-fetoprotein-producing primary lung carcinoma: A case report. *World J. Surg. Oncol.* **9**, 2–5 (2011).
54. Yao, X., Gordon, E. M., Figueroa, D. M., Barochia, A. V. & Levine, S. J. Emerging roles of apolipoprotein e and apolipoprotein A-I in the pathogenesis and treatment of lung disease. *Am. J. Respir. Cell Mol. Biol.* **55**, 159–169 (2016).
55. Bansil, R. & Turner, B. S. The biology of mucus: Composition, synthesis and organization. *Adv. Drug Deliv. Rev.* **124**, 3–15 (2018).
56. Chan, Y. R. *et al.* Lipocalin 2 is required for pulmonary host defense against klebsiella infection. *J. Immunol.* **182**, 4947–4956 (2009).
57. Xue, R. *et al.* Whole transcriptome sequencing analysis of the synergistic antimicrobial effect of metal oxide nanoparticles and ajoene on *Campylobacter jejuni*. *Front. Microbiol.* **9**, 2074 (2018).
58. Guglani, L. *et al.* Lipocalin 2 Regulates Inflammation during Pulmonary Mycobacterial Infections. *PLoS One* **7**, 1–11 (2012).
59. Yu, C. *et al.* Arrhythmogenic calmodulin mutations impede activation of small-conductance calcium-activated potassium current. *Hear. Rhythm* **13**, 1716–1723 (2016).
60. Matsuyama, S. *et al.* Enhanced isolation of SARS-CoV-2 by TMPRSS2-expressing cells. *Proc. Natl. Acad. Sci. USA* **117**, 7001–7003 (2020).
61. Banerjee, A. *et al.* Isolation, sequence, infectivity, and replication kinetics of severe acute respiratory syndrome coronavirus 2. *Emerg. Infect. Dis.* **26**, 2054–2063 (2020).
62. Zhang, H., Penninger, J. M., Li, Y., Zhong, N. & Slutsky, A. S. Angiotensin-converting enzyme 2 (ACE2) as a SARS-CoV-2 receptor: Molecular mechanisms and potential therapeutic target. *Intensive Care Med.* **46**, 586–590 (2020).
63. Cantuti-Castelvetri, L. *et al.* Neuropilin-1 facilitates SARS-CoV-2 cell entry and infectivity. *Science (80-).* **860**, 1–5 (2020).
64. Hoffmann, M. *et al.* Chloroquine does not inhibit infection of human lung cells with SARS-CoV-2. *Nature* **585**, 588–590 (2020).

65. Tseng, C.-T.K. *et al.* Apical entry and release of severe acute respiratory syndrome-associated coronavirus in polarized Calu-3 lung epithelial cells. *J. Virol.* **79**, 9470–9479 (2005).
66. Sims, A. C., Burkett, S. E., Yount, B. & Pickles, R. J. SARS-CoV replication and pathogenesis in an in vitro model of the human conducting airway epithelium. *Virus Res.* **133**, 33–44 (2008).
67. Furubayashi, T. *et al.* Comparison of various cell lines and three-dimensional mucociliary tissue model systems to estimate drug permeability using an in vitro transport study to predict nasal drug absorption in rats. *Pharmaceutics* **12**, 1–14 (2020).
68. Clippinger, A. J. *et al.* Expert consensus on an in vitro approach to assess pulmonary fibrogenic potential of aerosolized nanomaterials. *Arch. Toxicol.* **90**, 1769–1783 (2016).
69. Wagner, C. E., Wheeler, K. M. & Ribbeck, K. Mucins and their role in shaping the functions of mucus barriers. *Annu. Rev. Cell Dev. Biol.* **34**, 189–215 (2018).
70. Foster, M. W. *et al.* Proteomic analysis of human bronchoalveolar lavage fluid after subsgemental exposure. *J. Proteome Res.* **12**, 2194–2205 (2013).
71. Kumar, A. *et al.* Differences in the coronal proteome acquired by particles depositing in the lungs of asthmatic versus healthy humans. *Nanomed. Nanotechnol. Biol. Med.* **13**, 2517–2521 (2017).
72. Huh, D. *et al.* Reconstituting organ-level lung. *Science (80-).* **238**, 1662–1668 (2010).
73. Tenenbaum-Katan, J., Artzy-Schnirman, A., Fishler, R., Korin, N. & Sznitman, J. Biomimetics of the pulmonary environment in vitro: A microfluidics perspective. *Biomicrofluidics* **12**, 1–18 (2018).
74. Walters, M. S. *et al.* Generation of a human airway epithelium derived basal cell line with multipotent differentiation capacity. *Respir. Res.* **14**, 26–30 (2013).
75. R Core Team. R: A Language and Environment for Statistical Computing. R Foundation for Statistical Computing. Vienna, Austria (2019).
76. Kolde, R. Pheatmap: Pretty Heatmaps. R package version 1.0.12. 1–8 (2019).
77. Vu, V. Q. ggbiplot: A ggplot2 based biplot. R package version 0.55. (2011).
78. Bedward, M., Eppstein, D. & Menzel Peter. Package ' packcircles ' R package version 0.3.3. (2018).
79. Perez-Riverol, Y. *et al.* The PRIDE database and related tools and resources in 2019: Improving support for quantification data. *Nucleic Acids Res.* **47**, D442–D450 (2019).

Acknowledgements

This project received funding from the European Union's Horizon 2020 research and innovation program under Grant agreement no. 760928 (BIORIMA). DSG was supported by a fellowship from the Ecole Doctorale MTCI, Université de Paris. Confocal microscopy images were performed at the Plateau Imagerie, BFA, Université de Paris. We acknowledge the Proteomics platform at Institut Jacques Monod, Université de Paris, for support with mass spectrometry analysis.

Author contributions

A.B.S. and S.D. designed the study. D.S.G. performed and analyzed the experiments. O.B., C.M.C., V.S. assisted with cell culture experiments. S.B. contributed to the development of the long-term cell culture model. R.L.K. prepared samples for TEM imaging. D.S.G. and S.D. analyzed the proteomic data. D.S.G., S.D., A.B.S. wrote the manuscript. All authors reviewed the manuscript.

Competing interests

The authors declare no competing interests.

Additional information

Supplementary Information The online version contains supplementary material available at https://doi.org/10.1038/s41598-021-86037-0.

Correspondence and requests for materials should be addressed to S.D.

Reprints and permissions information is available at www.nature.com/reprints.

Annex II

Résumé long en française

Au cours des dernières années, la production industrielle de nanomatériaux (NM) et leur utilisation pour diverses applications ont augmenté de façon exponentielle accroissant ainsi la probabilité que l'homme y soit exposé. Les NM possèdent des propriétés spécifiques qui font craindre un danger potentiel pour la santé humaine. L'utilisation de modèles *in vitro* apparaît comme une solution pour évaluer la toxicité des NM tout en réduisant les tests expérimentaux sur les animaux.

L'exposition aux NM peut se produire par contact cutané, ingestion et/ou inhalation, cette dernière étant la voie d'exposition la plus courante, notamment lors d'une exposition professionnelle. L'épithélium des voies respiratoires constitue la première barrière du poumon contre les NM inhalés et la compréhension du mécanisme d'entrée dans l'épithélium des voies respiratoires pourrait nous aider à élucider la façon de prévenir la toxicité des NM.

L'objectif de cette thèse a été d'étudier les interactions NM-protéines qui se produisent dès que les NM arrivent au contact de l'épithélium respiratoire, en développant un modèle 3D d'épithélium bronchique humain permettant l'exposition aux NM à l'interface air-liquide.

Des nanoparticules d'argent (AgNP) ont été utilisées comme NM modèle dans cette étude. La lignée épithéliale bronchique humaine Calu-3 a été sélectionnée et son mode de culture adapté pour disposer d'un modèle de culture cellulaire 3D pertinent pour les études de nanotoxicologie. Il s'agissait d'avoir un mode de culture qui permette l'établissement d'une barrière épithéliale avec une différenciation muqueuse et le maintien de ces propriétés sur plusieurs semaines de culture. Cette barrière peut alors être utilisée pour étudier l'internalisation des nanoparticules (NP), et les interactions protéines-NP et NP-cellule, pour des expositions aigües et chroniques. Les cellules Calu-3 ont été cultivées à l'interface air-liquide (IAL) dans des chambres à 2 compartiments délimités par une membrane poreuse. 2 nouvelles modalités de culture ont été introduites pour répondre aux enjeux de la nanotoxicologie : i) l'utilisation d'inserts de large porosité (diamètre des pores de 3 µm au lieu de 0.4 µm) pour permettre les études futures d'évaluation de la translocation des NP ; ii) une réduction de la supplémentation en sérum de veau fœtal (SVF) afin de diminuer l'impact de protéines exogènes dans les interactions NP-protéines et NP-cellules.

L'intégrité de la barrière épithéliale a été mesurée pendant 17 jours de culture en IAL en utilisant une supplémentation de 0, 2, 4 et 8% de SVF dans le compartiment basal. La mesure de la résistance électrique trans-épithéliale (TEER) et de la perméabilité au jaune de Lucifer (LY) n'a pas montré de différences significatives entre les conditions, montrant que la culture sur un insert de large porosité n'empêchait pas l'établissement d'une barrière. Seuls de légers changements de TEER ont été observés, la condition 2% SVF présentant les valeurs de TEER les plus élevées. La formation de jonctions serrées a été confirmée par l'immunomarquage de la protéine zonula occludens-1 (ZO-1) associée aux jonctions serrées, ce qui montre que l'intégrité de l'épithélium a été maintenue pendant les 17 jours de culture en IAL. Par ailleurs, la sécrétion des protéines vers le compartiment apical a été étudiée en rinçant le pôle apical des cellules avec 200 µL de tampon HBSS. Dans ce sécrétome, nous avons observé que la concentration de protéines était plus élevée lorsque le pourcentage de SVF était plus élevé. Les cellules Calu-3 se différenciant *in vitro* en un phénotype muqueux, les mucines ont été dosées dans le sécrétome par un test ELLA. De manière surprenante, une sécrétion exacerbée de glycoprotéines a été mesurée dans les cultures sans supplémentation de SVF qui s'accentuait avec le temps. En revanche, alors que les cultures en présence de 4% et 8% de SVF n'ont pas présentées de changements dans la production de glycoprotéines, celles réalisées en présence de 2% de SVF produisaient moins de glycoprotéines au fil du temps. La sécrétion de mucines a été confirmée par l'immunomarquage de MUC5AC, une des principales mucines au niveau bronchique avec cependant un profil d'expression différencié. En effet, les cultures en l'absence de SVF présentaient un réseau de mucus très dense alors que celles réalisées en présence de 2%, 4% et 8% de SVF montraient un marquage punctiforme avec des différences dans les intensités de marquage.

Pour poursuivre nos travaux, nous avons sélectionné la culture complémentée avec 4 % de SVF qui permet de réduire l'apport en protéines exogènes sans affecter la sécrétion de protéines par les cellules Calu-3 ni l'intégrité de la barrière épithéliale, et ce sur plusieurs semaines de culture. La caractérisation du modèle Calu-3 a été poursuivie en le comparant à des épithéliums bronchiques humains normaux (MucilAir^{TM} de chez Epithelix) provenant de 3 donneurs différents. Une analyse protéomique par LC-MS/MS a été réalisée pour déterminer la composition du sécrétome apical des 2 types de cultures et son évolution pendant les 18 jours de culture en IAL. Au total, 408 protéines extracellulaires communes ont été identifiées dans les modèles Calu-3 et MucilAir^{TM}, soit 100% de similitude entre les protéines sécrétées dans les deux modèles. Parmi les protéines extracellulaires, des mucines gélifiantes (MUC5AC, MUC5B) et associées à la membrane (MUC1, MUC4 et MUC16), ainsi que des peptides antimicrobiens (lysozyme, lipocaline-2, lactotransferrine et clusterine) ont été identifiés. La présence de ces protéines a permis de démontrer la fonctionnalité du modèle Calu-3. Cependant, des différences dans les abondances relatives des protéines ont été observées entre les 2 modèles. Alors qu'aucune différence n'a été observée entre les 3 donneurs pour le modèle MucilAir^{TM}, des différences dans les abondances relatives ont été observées dans les sécrétomes des cultures Calu-3 selon le temps de culture en IAL. Une évolution entre les cultures récemment placées en IAL et celles y étant depuis plus de 11 jours est observée en lien avec la différenciation cellulaire en cours. Après 11 jours, la composition du sécrétome se stabilise, traduisant un sécrétome mature.

Afin d'aller plus loin dans l'interprétation des données de protéomique, nous avons utilisé la base de données *Reactome Pathway* pour identifier un enrichissement fonctionnel de certaines voies au niveau des sécrétomes matures de Calu-3 et de MucilAir^{TM}. Ceci nous a permis d'identifier un enrichissement en protéines impliquées dans les réponses immunitaires innées, soulignant le rôle de défense du sécrétome dans l'épithélium des voies respiratoires. Nous avons également pu faire une analyse LC-MS/MS d'un lavage broncho-alvéolaire (LBA) humain où nous avons retrouvé les protéines identifiées dans les sécrétomes *in vitro*, sans pouvoir toutefois réaliser une comparaison quantitative n'ayant pu disposer que d'un seul LBA. Néanmoins, les données de la littérature confirment ce que nous avons retrouvé dans les modèles *in vitro* d'épithélium bronchiques humains, avec la présence de protéines impliquées dans le système immunitaire inné dans différents LBA.

Lorsque les NP entrent en contact avec un fluide biologique, elles interagissent avec les différentes biomolécules présentes et notamment les protéines. Une couronne de biomolécules adsorbées à la surface des particules se forme qu'on appelle traditionnellement « corona ». Cette couronne protéique fournit une nouvelle identité biologique à la NP. Les protéines adsorbées peuvent modifier les interactions entre les NP et les cellules, augmenter ou diminuer leur internalisation, et jouent un rôle important dans la toxicité des NP. L'étude de la composition de la corona protéique a surtout été réalisée ces dernières années en utilisant du sérum ou du plasma sanguin comme fluide biologique pour déterminer le rôle des propriétés physico-chimiques des NP et celles des protéines disponibles dans le fluide dans leur adsorption. Par contre, la nature de la corona qui se forme sur les NP inhalées a fait l'objet de très peu de travaux. C'est la raison pour laquelle nous avons exploité notre modèle cellulaire 3D pour étudier les interactions entre NP et protéines du fluide respiratoire, riche en mucines. Nous avons analysé la composition de la couronne de protéines qui se forme sur les AgNP lorsqu'elles sont incubées dans le sécrétome apical des cellules Calu-3. Cette analyse a nécessité de tester différentes approches pour isoler les NP avec leur corona du sécrétome (protéines libres). Une séparation efficace est rendue difficile par la viscosité du sécrétome due à la présence de mucus. Nous avons adapté un protocole de séparation utilisant la centrifugation en ajoutant une étape de congélation à -80°C.

La formation de la couronne protéique sur les AgNP a ensuite été étudiée en utilisant deux stratégies :

i) la première nous a permis d'analyser ce que nous avons appelé la « couronne acellulaire » : les AgNP ont été incubées dans un sécrétome qui avait été préalablement récolté sur des cultures Calu-3 non exposées à des NP. Dans ces conditions, l'incubation est dite statique car la composition du sécrétome est stable dans le temps et les NP interagissent avec les protéines préexistantes. La composition de la corona peut toutefois évoluer au cours du temps en fonction de l'affinité des protéines pour la surface ;

ii) la seconde nous a permis d'étudier la « couronne cellulaire » qui s'est formée sur les NP après qu'elles aient été utilisées pour traiter les cultures de Calu-3 pendant 1 h ou 24 h. Dans ces conditions, le système est dynamique car la composition et/ou l'abondance des protéines dans le sécrétome évoluent du fait des réponses cellulaires à l'exposition aux AgNP. Les effets liés aux interactions NP-cellule et NP-protéines se combinent alors pour façonner et remanier la corona, ce qui se rapproche des conditions réelles d'exposition.

La « couronne acellulaire » formée sur les AgNP après 1 h d'incubation est composée de 73 ou 90 protéines, selon que l'expérience est réalisée en présence de 10 µg ou 50 µg d'AgNP. La diversité protéique est donc plus faible lorsque la surface disponible est la plus faible et la compétition pour l'adsorption la plus élevée (ratio protéines/NP le plus élevé correspondant à 50 µg protéines pour 10 µg AgNP, soit une surface de 3.8 10^{-4} m^2). La composition de la couronne protéique change également selon le ratio protéines/NP. Ainsi quand il est faible, la couronne présente un enrichissement en protéines impliquées dans le métabolisme des ARN et des acides aminés, tandis que lorsque la surface disponible augmente, nous observons également des protéines impliquées dans la signalisation induite par le récepteur des cellules B.

Enfin, quel que soit le ratio, un enrichissement en différentes sous-unités du protéasome (PSMB3, PSMB4 et PSM7), en cytokines (IL-18) entre autres est observé.

La « couronne cellulaire » formée lors de l'exposition des cellules Calu-3 aux AgNP est composée de 100 et 104 protéines, selon que l'expérience est réalisée en présence de 10 µg ou 50 µg d'AgNP après 1 h d'exposition. Au contraire, après 24 h d'exposition, la couronne protéique est composée de 367 et 377 protéines en présence de 10 µg ou 50 µg d'AgNP respectivement. Des différences dans la composition de la couronne de protéines ont été observées après 1 ou 24 h d'exposition de Calu-3 indépendamment de la concentration en NPs. Cela suggère une évolution de la composition du sécrétome et/ou un remaniement de la couronne protéique. Après 1 h d'incubation, la couronne « cellulaire » présente un enrichissement en protéines associées au métabolisme de l'ARN, mais aussi d'autres liées au cycle cellulaire, à la réplication de l'ADN (DEK), entre autres. Après 24 h d'exposition, nous avons observé un enrichissement des protéines associées aux microtubules (TUB8), des protéines impliquées dans le métabolisme des xénobiotiques et des protéines (CYB5B, famille RPL), et des protéines associées aux mitochondries (TXN2, PPA2).

De plus, des protéines extracellulaires et intracellulaires ont été identifiées aussi bien dans la couronne acellulaire que cellulaire. Les protéines intracellulaires pourraient provenir du renouvellement de l'épithélium (extrusion de cellules au pôle apical) (conditions sans exposition) et du remaniement de l'épithélium suite à une exposition aux AgNP.

La comparaison de la composition de la couronne protéique formée sur les AgNP dans le sécrétome en présence ou non de cellules a mis en évidence plusieurs éléments : i) la couronne protéique est plus riche, en termes de diversité protéique, lorsqu'elle se forme en présence de cellules ; ii) la fraction de protéines intracellulaires et issues d'organelles augmente avec le temps dans la couronne protéique cellulaire, iii) cette diversité augmente avec le temps. Ces résultats suggèrent que la réponse cellulaire aux AgNP a induit des changements dans la composition de la couronne protéique, qui pourraient être liés à la modification du sécrétome induite par l'exposition. Nous avons vérifié que les concentrations d'AgNP (10 µg/cm^2 et 50 µg/cm^2) utilisées pour exposer les cellules n'avaient aucun effet sur la viabilité des cellules ni sur l'intégrité de la barrière épithéliale jusqu'à 48 h.

Cependant, une surexpression des gènes impliqués dans la défense antioxydant, la réponse pro-inflammatoire et le stress métallique telles que l'hème-oxygénase, les cytokines IL-6 et IL-8, et la métallothionéine respectivement, a été observée, suggérant que l'exposition aux AgNP stimule les mécanismes de défenses cellulaires, probablement accompagnés de mécanismes sécrétoires. La composition du sécrétome des cellules exposées aux AgNP est actuellement en cours d'analyse afin de déterminer dans quelle mesure le traitement affecte celle-ci.

Des macrophages dérivés de THP-1 ont été utilisés pour étudier le rôle de la couronne de protéines sur les AgNP dans les interactions cellulaires. Les macrophages ont été exposés dans le milieu HBSS:RPMI aux AgNP seules, ou pré-incubées dans le sécrétome des cellules Calu-3 ou dans le SVF (4%). Les AgNP pré-incubées dans le sécrétome ont induit une activité métabolique plus élevée et une réponse pro-inflammatoire différente dans les cellules THP-1 par rapport aux AgNP nues ou incubées dans le SVF. La nouvelle identité biologique des AgNP acquise dans le sécrétome bronchique pourrait ainsi favoriser l'activation des cellules immunitaires et faciliter l'internalisation des NP par les macrophages. L'internalisation des AgNP par les macrophages a été confirmée dans toutes les conditions par microscopie électronique à transmission. Toutefois une analyse quantitative serait nécessaire pour déterminer dans quelle mesure la nature de la couronne protéique influence l'internalisation. Des expériences supplémentaires seront aussi nécessaires pour élucider son rôle sur la toxicité des AgNP et les mécanismes sous-jacents.

En conclusion, un modèle fonctionnel *in vitro* de culture 3D d'épithélium bronchique humain a été développé à partir de la lignée Calu-3. Il est actuellement mis en œuvre pour évaluer la toxicité à long terme des NM *in vitro* puisque nous avons pu établir des conditions de culture permettant le maintien de la barrière épithéliale sur plusieurs semaines. Nous avons montré que les cellules Calu-3 produisent un sécrétome ayant une fonction protectrice liée à l'immunité innée, très similaire à celui produit par l'épithélium bronchique humain normal et à celui produit *in vivo*. Nous avons décrit pour la première fois la composition et l'évolution de la couronne protéique qui se forme sur des AgNP au contact des secrétions épithéliales des voies aériennes et mis en évidence un effet spécifique de cette couronne protéique sur la réponse des macrophages aux AgNP Ce travail met en lumière la nécessité de poursuivre l'analyse de la couronne protéine dans le cadre de son implication dans la réponse immunitaire aux NM dans le poumon.

Valorization

Oral presentations:

NanoTox2021 |10th International Conference on Nanotoxicology | Virtual Conference | April 2021

Sanchez-Guzman et al.: *Investigating protein-nanoparticles interaction in 3D model of the human bronchial epithelium for long-term toxicity study of inhaled nanoparticles*

11th World Congress on Alternatives and Animal uses in Life sciences | Virtual Conference | August 2021

Sanchez-Guzman et al.: *Secretome characterization of 3D bronchial epithelial cultures to study the role of protein corona on the fate and long-term effects of nanoparticles*

MTCI Scientific days | Paris (France) | October 2021

Sanchez-Guzman et al.: *Characterization of the secretome of 3D bronchial epithelium model to study biomolecular corona formation on nanoparticles*

C'Nano 2020 | Toulouse (France) | November 2021

Sanchez-Guzman et al.: *Investigating protein-nanoparticles interactions in 3D cell culture models for the long -term toxicity study of inhaled silver nanoparticles.*

Poster presentations:

MTCI retreat | Saint-Rémy-lès-Chevreuse (France) | October 2019

Poster: Sanchez-Guzman D., et al. *Role of the protein corona in determining the fate and the long-term effects of nanoparticles on a 3D bronchial epithelial model*

"La Toxicologie vers la 3éme Dimension | Paris (France) | June 2019

Poster: Sanchez-Guzman D., et al. *Development of a 3D bronchial epithelial model for chronic exposure to nanomaterials*

International research stays:

Visiting PhD student | February 2020 – March 2020

Department of Chemistry, Royal College of Surgeons in Ireland (RCSI), Dublin, Ireland

Principal Investigator: Dr Marco Monopoli

Topic: Comparison of protocols for the isolation of protein corona on iron oxide nanoparticles

List of publications:

Long-Term Evolution of the Epithelial Cell Secretome in Preclinical 3D Models of the Human Bronchial Epithelium

Sanchez-Guzman, Daniel, Sonja Boland, Oliver Brookes, Claire Mc Cord, René Lai Kuen, Valentina Sirri, Armelle Baeza Squiban, and Stéphanie Devineau. 2021. Scientific Reports 11 (1): 1–14. https://doi.org/10.1038/s41598-021-86037-0

In Situ Analysis of Weakly Bound Proteins Reveals Molecular Basis of Soft Corona Formation

Sanchez-Guzman, Daniel, Gaël Giraudon--Colas, Laurent Marichal, Yves Boulard, Frank Wien, Jéril Degrouard, Armelle Baeza-Squiban, Serge Pin, Jean Philippe Renault, and Stéphanie Devineau. 2020. ACS Nano 14 (7): 9073–88. https://doi.org/10.1021/acsnano.0c04165.

Silver Nanoparticle-Adjuvanted Vaccine Protects against Lethal Influenza Infection through Inducing BALT and IgA-Mediated Mucosal Immunity

Sanchez-Guzman, Daniel, Pierre Le Guen, Berengere Villeret, Nuria Sola, Remi Le Borgne, Alice Guyard, Alix Kemmel, Bruno Crestani, Jean-Michel Sallenave, and Ignacio Garcia-Verdugo. 2019. Biomaterials. https://doi.org/10.1016/j.biomaterials.2019.119308.